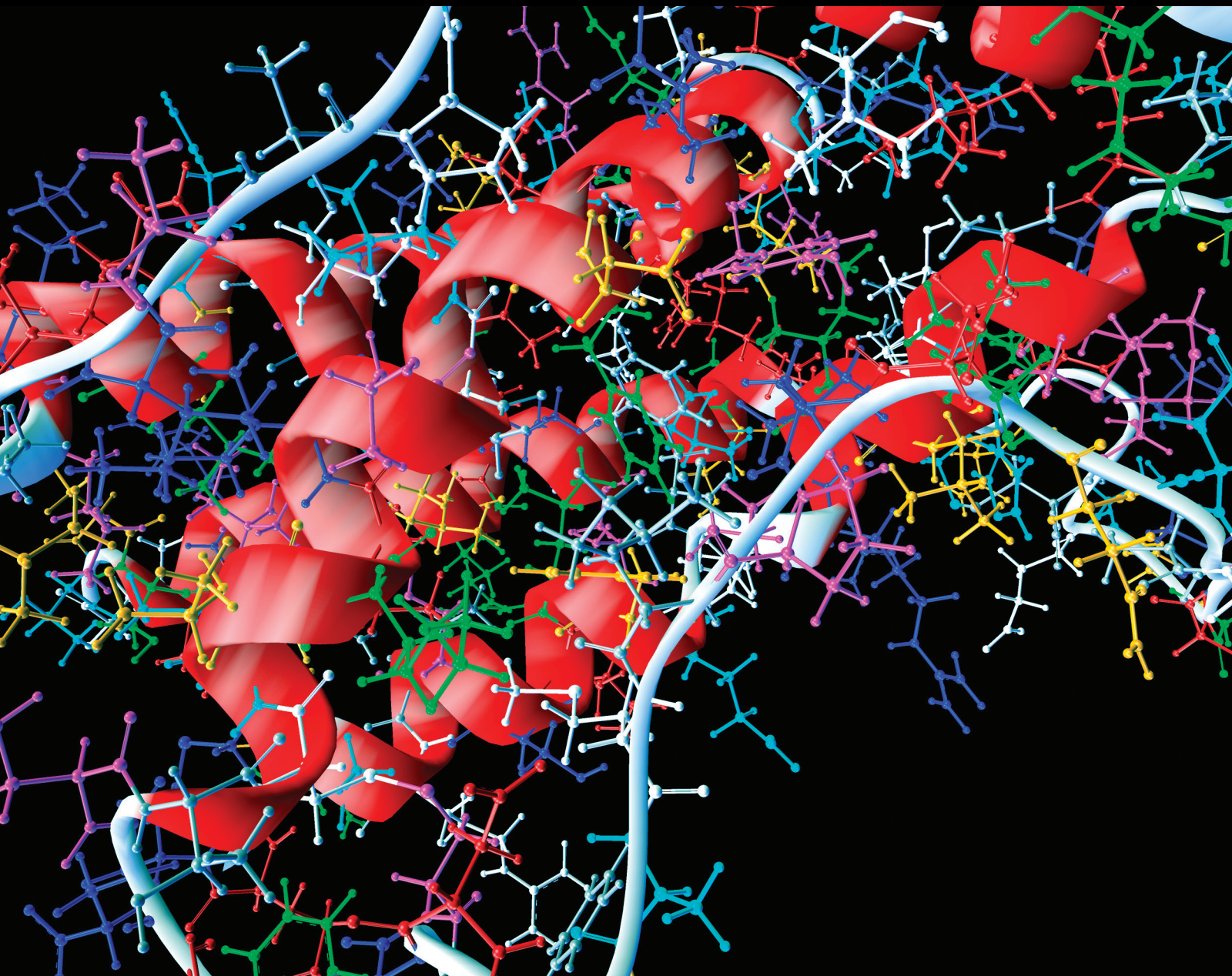


Computational and Mathematical Methods in Medicine

# Multiscale Computational Models for Respiratory Aerosol Dynamics with Medical Applications

Lead Guest Editor: Yu Feng

Guest Editors: Ming-shi Yang, Ke-jun Dong, and Xiaole Chen





---

**Multiscale Computational Models for  
Respiratory Aerosol Dynamics with  
Medical Applications**



Computational and Mathematical Methods in Medicine

---

**Multiscale Computational Models for  
Respiratory Aerosol Dynamics with  
Medical Applications**

Lead Guest Editor: Yu Feng

Guest Editors: Ming-shi Yang, Ke-jun Dong, and Xiaole Chen



---

Copyright © 2019 Hindawi. All rights reserved.

This is a special issue published in “Computational and Mathematical Methods in Medicine.” All articles are open access articles distributed under the Creative Commons Attribution License, which permits unrestricted use, distribution, and reproduction in any medium, provided the original work is properly cited.

## Editorial Board

Raul Alcaraz, Spain  
Emil Alexov, USA  
Konstantin G. Arbeev, USA  
Georgios Archontis, Cyprus  
Enrique Berjano, Spain  
Junguo Bian, USA  
Elia Biganzoli, Italy  
Konstantin Blyuss, UK  
Hans A. Braun, Germany  
Zoran Bursac, USA  
Thierry Busso, France  
Guy Carrault, France  
Filippo Castiglione, Italy  
Carlos Castillo-Chavez, USA  
Prem Chapagain, USA  
Hsiu-Hsi Chen, Taiwan  
Wai-Ki Ching, Hong Kong  
Nadia A. Chuzhanova, UK  
Maria N. D.S. Cordeiro, Portugal  
Cristiana Corsi, Italy  
Irena Cosic, Australia  
Qi Dai, China  
Chuangyin Dang, Hong Kong  
Didier Delignières, France  
Jun Deng, USA  
Thomas Desaive, Belgium  
David Diller, USA  
Michel Dojat, France  
Irina Doytchinova, Bulgaria  
Esmail Ebrahimie, Australia  
Georges El Fakhri, USA  
Issam El Naqa, USA  
Angelo Facchiano, Italy

Luca Faes, Italy  
Maria E. Fantacci, Italy  
Giancarlo Ferrigno, Italy  
Marc Thilo Figge, Germany  
Alfonso T. García-Sosa, Estonia  
Humberto González-Díaz, Spain  
Igor I. Goryanin, Japan  
Marko Gosak, Slovenia  
Damien Hall, Australia  
Roberto Hornero, Spain  
Tingjun Hou, China  
Seiya Imoto, Japan  
Hsueh-Fen Juan, Taiwan  
Martti Juhola, Finland  
Rafik Karaman, Palestine  
Andrzej Kloczkowski, USA  
Chung-Min Liao, Taiwan  
Ezequiel López-Rubio, Spain  
Pinyi Lu, USA  
Reinoud Maex, Belgium  
Valeri Makarov, Spain  
Kostas Marias, Greece  
Juan Pablo Martínez, Spain  
Richard J. Maude, Thailand  
Michele Migliore, Italy  
John Mitchell, UK  
Luminita Moraru, Romania  
Chee M. Ng, USA  
Michele Nichelatti, Italy  
Kazuhisa Nishizawa, Japan  
Francesco Pappalardo, Italy  
Manuel F. G. Penedo, Spain  
Jesús Picó, Spain

Kemal Polat, Turkey  
Alberto Policriti, Italy  
Giuseppe Pontrelli, Italy  
Jesús Poza, Spain  
Christopher Pretty, New Zealand  
Mihai V. Putz, Romania  
Jose Joaquin Rieta, Spain  
Jan Rychtar, USA  
Vinod Scaria, India  
Simon A. Sherman, USA  
Dong Song, USA  
Xinyuan Song, Hong Kong  
João M. Tavares, Portugal  
Jlenia Toppi, Italy  
Nelson J. Trujillo-Barreto, UK  
Anna Tsantili-Kakoulidou, Greece  
Markos G. Tsipouras, Greece  
Po-Hsiang Tsui, Taiwan  
Gabriel Turinici, France  
Liangjiang Wang, USA  
Ruisheng Wang, USA  
David A. Winkler, Australia  
Gabriel Wittum, Germany  
Yu Xue, China  
Yongqing Yang, China  
Chen Yanover, Israel  
Xiaojun Yao, China  
Kaan Yetilmezsoy, Turkey  
Hiro Yoshida, USA  
Henggui Zhang, UK  
Yuhai Zhao, China  
Xiaoqi Zheng, China

# Contents

## **Multiscale Computational Models for Respiratory Aerosol Dynamics with Medical Applications**

Yu Feng , Xiaole Chen, Mingshi Yang, and Ke-jun Dong  
Editorial (2 pages), Article ID 4304139, Volume 2019 (2019)

## **State-Dependent Pulse Vaccination and Therapeutic Strategy in an SI Epidemic Model with Nonlinear Incidence Rate**

Kaiyuan Liu , Tongqian Zhang , and Lansun Chen   
Research Article (10 pages), Article ID 3859815, Volume 2019 (2019)

## **Modeling Airflow and Particle Deposition in a Human Acinar Region**

Arun V. Kolanjiyil  and Clement Kleinstreuer   
Research Article (13 pages), Article ID 5952941, Volume 2019 (2019)

## **Airflow and Particle Deposition in Acinar Models with Inter-alveolar Septal Walls and Different Alveolar Numbers**

Jinxiang Xi , Mohamed Talaat, Hesham Tanbour, and Khaled Talaat  
Research Article (18 pages), Article ID 3649391, Volume 2018 (2019)

## **Modeling Inhibitory Effect on the Growth of Uninfected T Cells Caused by Infected T Cells: Stability and Hopf Bifurcation**

Yahui Ji, Wanbiao Ma , and Keying Song  
Research Article (10 pages), Article ID 3176893, Volume 2018 (2019)

## **A Feasible Computational Fluid Dynamics Study for Relationships of Structural and Functional Alterations with Particle Depositions in Severe Asthmatic Lungs**

Sanghun Choi , Shinjiro Miyawaki, and Ching-Long Lin   
Research Article (12 pages), Article ID 6564854, Volume 2018 (2019)

## **Numerical Simulations of the Motion and Deformation of Three RBCs during Poiseuille Flow through a Constricted Vessel Using IB-LBM**

Rongyang Wang , Yikun Wei , Chuanyu Wu , Liang Sun, and Wenguang Zheng  
Research Article (12 pages), Article ID 9425375, Volume 2018 (2019)

## **Analysis and Numerical Simulations of a Stochastic SEIQR Epidemic System with Quarantine-Adjusted Incidence and Imperfect Vaccination**

Fei Li, Xinzhu Meng , and Xinzeng Wang  
Research Article (14 pages), Article ID 7873902, Volume 2018 (2019)

## Editorial

# Multiscale Computational Models for Respiratory Aerosol Dynamics with Medical Applications

Yu Feng <sup>1</sup>, Xiaole Chen,<sup>2</sup> Mingshi Yang,<sup>3</sup> and Ke-jun Dong<sup>4</sup>

<sup>1</sup>School of Chemical Engineering, Oklahoma State University, Stillwater, Oklahoma, USA

<sup>2</sup>School of Energy and Environment, Southeast University, Nanjing, Jiangsu, China

<sup>3</sup>Department of Pharmacy, University of Copenhagen, Copenhagen, Denmark

<sup>4</sup>Centre for Infrastructure Engineering, Western Sydney University, Penrith, Australia

Correspondence should be addressed to Yu Feng; [yu.feng@okstate.edu](mailto:yu.feng@okstate.edu)

Received 10 February 2019; Accepted 10 February 2019; Published 3 March 2019

Copyright © 2019 Yu Feng et al. This is an open access article distributed under the Creative Commons Attribution License, which permits unrestricted use, distribution, and reproduction in any medium, provided the original work is properly cited.

## 1. Introduction

Inhalation of therapeutic drug aerosols is now becoming a novel way to administer micro/nanoparticles or vapors to treat lung and systemic diseases. Several attempts of such deliveries have been made at least in experimental analyses on asthma, chronic obstructive pulmonary disease (COPD), lung hypoxia, edema, lung injury, lung transplantation fungal infection, pulmonary fibrosis, and lung cancer. However, due to certain design deficiencies, existing pulmonary drug delivery devices still have poor efficiencies for delivering drugs to designated sites. Significant portions of the aggressive medicine deposit on healthy tissues, which causes severe side effects and induces extra healthcare expenses. Therefore, it is an urgent need to understand the aerosol drug dynamics better and develop a revolutionary patient-specific pulmonary drug delivery method and device to improve therapeutic outcomes by significantly improving drug delivery efficacy significantly. Due to the invasive nature and imaging resolution limitations, clinical and animal studies are not able to provide the high-resolution data for the researcher to understand the particle dynamics in human lung airways. Compared to experimental investigations, accurate and realistic computer simulation models would significantly contribute to reducing the research time and cost and visualize drug transport and translocation to multiple health endpoints via the pulmonary route.

To pave the way to developing the next-generation computational model and advance the scientific knowledge

of respiratory aerosol dynamics, this special issue covers a wide range of multiscale computational models with different medical applications. Seven exciting papers are included, and they might be broadly categorized into three levels: (a) respiratory system level, (b) cell level, and (c) disease level.

## 2. Overview of the Works Published in This Special Issue

**2.1. Respiratory System Level.** The focus of the first group which consists of 3 papers, which advance the fundamental understanding on how to more realistically model the inhaled aerosol transport and deposition in human respiratory systems and how different physiological factors can influence the deposition patterns. These factors include preexisting lung disease conditions, alveolar movements, breathing patterns, and aerosol size distributions. Specifically, A. V. Kolanjiyil and C. Kleinstreuer created an elastic “whole acinar model” which covers the entire alveolated distal airways and alveolar sacs and simulates particle transport and deposition *via* CFPD coupled with the fluid-structure interaction (FSI) method. Their results indicate that the alveolar wall motion significantly increases particle deposition, and particle deposition efficiency increases with higher inhalation tidal volume and aerosol size. The acinar model can efficiently simulate aerosol dynamics in the deep lung and is ready to be incorporated into the next-generation whole-lung model. Also, focusing on the aerosol dynamics in alveolar regions, J. Xi et al. investigated the impact of Kohn structures on particle depositions in their elastic

alveolar models for both healthy people and emphysema patients. Temporal and spatial deposition variations in multialveoli pore-communicated acinar models were numerically simulated. They found the size of the pores of Kohn, inhalation depth, and gravity orientation angle had insignificant effects on acinar deposition but had dramatic impact on the spatial distribution of particle deposition among alveoli. Furthermore, S. Choi et al. also used the CFPD-based model and explored the effect of altered structures and functions in severe asthma on particle deposition in subject-specific human respiratory systems. CFD results show that the induced constricted airways by asthma contribute to high wall shear stress, elevated pressure drop, and significantly increased particle deposition, compared to normal airways of healthy people.

*2.2. Disease Level.* The second group consists of 2 papers which developed mathematical models to investigate the transmission and control of infectious disease caused by inhalable bioaerosols (e.g., bacteria and virus). F. Li et al. investigated the infectious disease, e.g., the severe acute respiratory syndrome (SARS), via a stochastic susceptible-exposed-infected-quarantined-recovered (SEIQR) epidemic model with quarantine-adjusted incidence and the imperfect vaccination. Their theoretical analysis and simulations show that the stochastic disturbance is conducive to epidemic diseases control. K. Liu et al. analyzed the system dynamics of the state-dependent pulse vaccination and therapeutic strategy, which is described based on an SI ordinary differential equation model. Their results indicate that the state-dependent impulsive vaccination strategy could be used as a supplementary approach or under the situation when vaccine stockpile is limited.

*2.3. Cell Level.* The third group also consists of 2 papers, modeling transport and reproduction of cells. Y. Ji et al. studied the virus infection dynamics using a mathematical model. This model included a time delay term standing for the growth of the uninfected cells. The mathematical analysis indicates that the growth of the uninfected cells can complicate the infection results, e.g., relapse of the infection. From the biological aspect, it suggests that adequate drug treatment should be employed to avoid relapse or oscillation in the immune response. R. Wang et al. examined the transport and deformation of red blood cells through constricted microchannels using the immersed boundary-lattice Boltzmann method. Their simulations found that greater deformation and longer travel time were required to squeeze through the narrower channel.

### 3. Conclusions

This special issue documents some new studies and provides state-of-art advanced multiscale numerical modeling efforts for respiratory aerosol dynamics in pulmonary drug delivery device, human respiratory systems, and systemic regions, as well as other induced kinetics and dynamics in the human body. The accepted papers show a diversity of new findings

and overviews of the recent research and development. We hope this special issue will foster a wider interest in finding the most feasible way for the development of the next-generation multiscale model, to bring the computational respiratory aerosol dynamics simulations to health endpoints with the details never undertaken before in the near future.

### Conflicts of Interest

Editors report no conflicts of interest in this work.

### Acknowledgments

The editors are grateful to the participants of this special issue for their inspiring contributions and the anonymous reviewers for their helpful and constructive comments which greatly improved the content of the papers published in this special issue.

Yu Feng  
Xiaole Chen  
Mingshi Yang  
Ke-jun Dong

## Research Article

# State-Dependent Pulse Vaccination and Therapeutic Strategy in an SI Epidemic Model with Nonlinear Incidence Rate

Kaiyuan Liu <sup>1</sup>, Tongqian Zhang <sup>2,3</sup> and Lansun Chen <sup>4</sup>

<sup>1</sup>College of Mathematics and Information Science, Anshan Normal University, Anshan 114016, China

<sup>2</sup>College of Mathematics and Systems Science, Shandong University of Science and Technology, Qingdao 266590, China

<sup>3</sup>State Key Laboratory of Mining Disaster Prevention and Control Co-founded by Shandong Province and the Ministry of Science and Technology, Shandong University of Science and Technology, Qingdao 266590, China

<sup>4</sup>Academy of Mathematics and Systems Science, Chinese Academy of Sciences, Beijing 100190, China

Correspondence should be addressed to Tongqian Zhang; zhangtongqian@sdu.edu.cn

Received 26 July 2018; Revised 18 November 2018; Accepted 22 November 2018; Published 6 February 2019

Guest Editor: Ke-jun Dong

Copyright © 2019 Kaiyuan Liu et al. This is an open access article distributed under the Creative Commons Attribution License, which permits unrestricted use, distribution, and reproduction in any medium, provided the original work is properly cited.

In this paper, the state-dependent pulse vaccination and therapeutic strategy are considered in the control of the disease. A pulse system is built to model this process based on an SI ordinary differential equation model. At first, for the system neglecting the impulse effect, we give the classification of singular points. Then for the pulse system, by using the theory of the semicontinuous dynamic system, the dynamics is analyzed. Our analysis shows that the pulse system exhibits rich dynamics and the system has a unique order-1 homoclinic cycle, and by choosing  $p$  as the control parameter, the order-1 homoclinic cycle disappears and bifurcates an orbitally asymptotical stable order-1 periodic solution when  $p$  changes. Numerical simulations by maple 18 are carried out to illustrate the theoretical results.

## 1. Introduction

Infectious diseases are caused by various pathogens that can be transmitted from person to person, animal to animal, or human to animal. The ever-changing changes in the pathogens of ancient infectious diseases and the emergence of new pathogens have brought new challenges to the discovery, diagnosis, and prevention of infectious diseases. According to the 2016 report of the World Health Organization [1], about 36.7 million people have been infected with HIV/AIDS, 1.0 million people died of HIV/AIDS, and more than 18 million people worldwide living with HIV are receiving antiviral drugs. And tuberculosis is currently the biggest “killer” caused by a single infectious pathogen after AIDS in the world. As of the end of 2016, there were 10.4 million new tuberculosis cases [2]. Therefore, the control and elimination of infectious diseases has attracted wide

attention of people. Various dynamic models have been proposed by mathematicians to investigate the spread and evolution of infectious diseases [3–14]. In particular, mathematical models of differential equations have been extensively investigated, and among them, the most classical well-known model is SIR model [15] or SIS model [16], which have been widely investigated [17–23].

It is well known that vaccination is mostly a medical behavior that can evoke the individual’s natural defense mechanism to prevent possible future diseases. This kind of vaccination is known as prophylactic vaccination. Diphtheria, whooping cough, polio, tetanus, herpes, rubella, and mumps are the most common types of vaccines. There are many types of vaccination, the two common types are continuous vaccination and pulsed vaccination. Continuous vaccination is when people are vaccinated at birth to protect themselves from illness, while pulsed vaccination is when

people are vaccinated at a fixed period of time in all age groups which was firstly investigated by Agur et al in [24]. Pulse vaccination strategy (PVS) has been studied by many scholars [25, 26]. For example, Lu et al. [27] studied the pulse epidemic model with bilinear incidence and compared the effectiveness of the continuous and pulsed vaccination strategies. Liu et al. [28] investigated the SIR epidemic model with the saturated transmission rate. However, the strategy is taken at certain fixed times and does not depend on the status of infectious diseases. In general, taking into account the limited medical resources and costs, vaccines to susceptible people or infected people are more reasonable than continuous vaccination and fixed time pulse vaccination. This control strategy relies on the individual (or susceptible individuals) of the infection state and is called a state-dependent pulse vaccination strategy. Based on this idea, Tang et al. [29], Nie et al. [30], Guo et al. [31], and Qin et al. [32] have considered a state-dependent pulse strategy in SIR model and SIRS model. In fact, using state-dependent feedback control strategies to simulate real-world problems is more reasonable. Therefore, the impulsive state feedback control is also widely applied to the population dynamics model [33–46], chemostat model [47], and turbidostat model [48].

Firstly, we consider an SI epidemic model with nonlinear incidence rate  $\beta SI^2$  described by the ordinary differential equations as follows:

$$\begin{cases} \frac{dS}{dt} = \theta - \beta SI^2 - \gamma S, \\ \frac{dI}{dt} = \beta SI^2 - \gamma I, \end{cases} \quad (1)$$

which is a special case in the study of Liu et al. [49] and  $S(t)$  and  $I(t)$  represents the number of susceptible and infected individuals at time  $t$ , respectively.  $\theta$  is the birth rate,  $\beta$  is the contact rate, and  $\gamma$  is the natural death rate.

Motivated by the studies of Tang et al. [29], Nie et al. [30], and Zhang et al. [50], we consider state-dependent pulse vaccination and treatment strategy in model (1) and get the following model:

$$\begin{cases} \left. \begin{cases} \frac{dS}{dt} = \theta - \beta SI^2 - \gamma S, \\ \frac{dI}{dt} = \beta SI^2 - \gamma I, \end{cases} \right\} I < h_1, \\ \left. \begin{cases} \Delta S = -pS, \\ \Delta I = -qI, \end{cases} \right\} I < h_1, \end{cases} \quad (2)$$

where  $\Delta S(t) = S(t^+) - S(t)$  and  $\Delta I(t) = I(t^+) - I(t)$ . When the amount of infected reaches the hazardous threshold value  $h_1 (> 0)$ , vaccination and treatment are taken into account, and the number of susceptible and infected

suddenly turn to  $(1-p)S(t)$  and  $(1-q)I(t)$ , respectively, where  $0 < p$  and  $q < 1$  denote the vaccination rate of susceptible individuals and treatment rate of infected individuals, respectively. By the scaling,

$$\begin{aligned} S &= k_1 x, \\ I &= k_2 y, \\ t &= k_3 \tau, \\ \frac{k_3}{k_1} \theta &= a, \\ \beta k_2^2 k_3 &= 1, \\ k_3 &= \frac{1}{\gamma} \end{aligned} \quad (3)$$

then, model (2) transforms into the following form:

$$\begin{cases} \left. \begin{cases} \frac{dx}{d\tau} = a - y^2 x - x, \\ \frac{dy}{d\tau} = y^2 x - y, \end{cases} \right\} \Delta y = -qy, \\ \left. \begin{cases} \Delta x = -px, \\ \Delta y = -qy, \end{cases} \right\} y = h_2, \end{cases} \quad (4)$$

where  $h_2 = h_1/k_2$ . In the following, according to the actual condition, we always suppose that  $h \leq y_2$ , and based on practical significance, our research scope is limited to the first quadrant, i.e.,  $R_+^2 = \{(x, y) | x \geq 0, y \geq 0\}$ .

The purpose of this paper is to study the dynamic behavior under the effect of state-dependent pulse vaccination and treatment strategy. This article is organized as follows. In Section 2, we introduce some definitions and notations of the geometric theory of semicontinuous dynamic systems, which will be useful for the latter discussion. In Section 3, we qualitatively analyze the dynamics of model (3). In Section 4, the existence of the homoclinic cycle is studied by using the geometrical theory of semicontinuous dynamical systems. At last, we present some numerical simulations.

## 2. Preliminaries

In this section, we introduce some notations, definitions, and lemmas of the geometric theory of semicontinuous dynamic system, which will be useful for the following discussions. The following definitions and lemmas of semicontinuous dynamic system come from the studies of Chen et al. [51] and Wei and Chen [36].

*Definition 1.* Consider the following state-dependent impulsive differential system

$$\begin{cases} \frac{dx}{dt} = P(x, y), & \frac{dy}{dt} = Q(x, y), & (x, y) \notin M\{x, y\}, \\ \Delta x = \alpha(x, y), & \Delta y = \beta(x, y), & (x, y) \in M\{x, y\}. \end{cases} \quad (5)$$

The solution mapping of system (4) is called the semi-continuous dynamical system denoted by  $\Omega, f, \varphi$ , and  $M$ , where  $(x, y) \in \Omega \subset \mathbb{R}_+^2$  and  $f = f(p; t)$  is the semi-continuous dynamical system mapping with initial point  $p = (x_0, y_0) \notin M$ ; the sets  $M$  and  $N$  are called the impulse set and phase set, which are lines or curves on  $\mathbb{R}_+^2$ . The continuous function  $\varphi : M \rightarrow N$  is called impulse mapping.

*Remark 1.* System (4) constitutes a semicontinuous dynamic system  $(\Omega, f, \varphi, M)$ , where  $\Omega = \mathbb{R}_+^2 = \{(x, y) | x \geq 0, y \geq 0\}$ ,  $M = \{(x, y) \in \mathbb{R}_+^2 | x \geq 0, y = h_2\}$ ,  $\varphi : (x, y) \in M \rightarrow ((1-p)x, (1-q)h_2) \in \mathbb{R}_+^2$ ,  $N = \varphi(M) = \{(x, y) \in \mathbb{R}_+^2 | x \geq 0, y = (1-q)h_2\}$ .

*Definition 2.* If there exists a point  $P \in N$  and  $T > 0$  such that  $f(P, T) = Q \in M$  and  $\varphi(Q) = \varphi(f(P, T)) = P \in N$ , then  $f(P, t)$  is called order-1 periodic solution.

*Definition 3.* The trajectory  $f(P, t)$  combining with impulse line QP is called the order-1 cycle. If the order-1 cycle has a singularity, then the order-1 cycle is called the order-1 singular cycle. Furthermore, if the order-1 cycle only has a saddle, then the order-1 singular cycle is called the order-1 homoclinic cycle.

*Definition 4.* We assume that  $G$  is a bounded closed simple connected region, which has the following properties:

- (i) Impulse set  $M$  is a simple connected bounded closed straight line segments or curve segments which do not contain closed branch
- (ii) The boundaries AD, BC, and AB of region  $G$  are nontangent arcs of semicontinuous dynamical system (4). The boundary CD is the impulse set of system (4), and its phase set satisfies  $\varphi(CD) \subseteq AB$ ;
- (iii) The orientation of the vector fields of semicontinuous dynamical system (4) on the AD, BC, and AB points of the internal of region  $G$ . There are no equilibriums on the boundaries and also in the internal of region  $G$  of semicontinuous dynamical system (4).

Then region  $G$  is called Bendixson's region of semicontinuous dynamical system (4).

**Lemma 1.** (*Bendixson theorem of semicontinuous dynamical system.*) *If region  $G$  is Bendixson's region of semicontinuous dynamical system (4), then there exists at least an order-1 periodic solution in the internal of region  $G$  (Figure 1).*

Next, we will give the definition of successor function of system (4). Firstly, we define a new number axis in set  $N$ . On

straight line  $y = (1-q)h_2$ , take the origin at point  $(0, (1-q)h_2)$  of coordinate axis  $y$  and define the positive direction and unit length to be consistent with coordinate axis  $x$ , then we obtain a number axis  $l$ . For any  $A \in l$ , let  $l(A)$  be the coordinate of point  $A$  which is defined as the distance between point  $A$  and the  $y$ -axis, i.e.,  $l(A) = x_A$ .

*Definition 5.* Suppose  $g : N \rightarrow N$  be a map. Let  $P \in N$  be the initial mapping point, for any  $P \in N$ , there exists a  $t_1 > 0$  such that  $F(P) = f(P, t_1) = P_1 \in M, P_1^+ = \varphi(P_1) \in N$ . Then, function  $g(P) = l(P_1^+) - l(P)$  is the successor function of point  $P$ , and the point  $P_1^+$  is called the successor point of  $P$  (Figure 2).

*Definition 6.* Suppose  $\Gamma = f(P, t)$  is an order-1 periodic solution of system (4). If for any  $\varepsilon > 0$ , there must exist  $\delta > 0$  and  $t_0 \geq 0$  such that, for any point  $P_1 \in \cup (P, \delta) \cap N$ , we have  $\rho(f(P_1, t), \Gamma) < \varepsilon$  for  $t > t_0$ ; then we call the order-1 periodic solution  $\Gamma$  is orbitally asymptotically stable.

### 3. Qualitative Analysis of System Neglecting the Impulse Effect

First, we consider the classification of singular points of the system neglecting the impulse effect. Neglecting the impulse effects, system (3) reduces to

$$\begin{cases} \frac{dx}{dt} = a - y^2x - x, \\ \frac{dy}{dt} = y^2x - y, \end{cases} \quad (6)$$

system (5) always has one equilibrium  $E_0(a, 0)$ . Denote  $R_0 = a^2/4$ ; if  $R_0 > 1$ , the system (5) has two positive equilibria  $E_1(x_1, y_1)$  and  $E_2(x_2, y_2)$ , where  $x_1 = (a + \sqrt{a^2 - 4}/2)$ ,  $y_1 = (a - \sqrt{a^2 - 4}/2)$  and  $x_2 = (a - \sqrt{a^2 - 4}/2)$ ,  $y_2 = (a + \sqrt{a^2 - 4}/2)$ .

Next, we will analysis of the stability of the equilibria of system (5). For equilibrium  $E_0$ , we have

$$J_{E_0} = \begin{pmatrix} -1 & 0 \\ 0 & -1 \end{pmatrix}, \quad (7)$$

obviously  $E_0$  is a stable node.

For  $E_1$ , we have

$$J_{E_1} = \begin{pmatrix} -1 - y_1^2 & -2x_1y_1 \\ y_1^2 & -1 + 2x_1y_1 \end{pmatrix}, \quad (8)$$

and the characteristic equation is  $\lambda^2 + y_1^2\lambda + y_1^2 - 1 = 0$ . Let  $\lambda_1$  and  $\lambda_2$  be the two characteristic roots of the characteristic equation, then we have

$$\begin{aligned} \lambda_1 + \lambda_2 &= -y_1^2 < 0, \\ \lambda_1\lambda_2 &= y_1^2 - 1 = \frac{y_1}{x_1} - 1 \\ &= \frac{-2\sqrt{a^2 - 4}}{a + \sqrt{a^2 - 4}} < 0, \end{aligned} \quad (9)$$

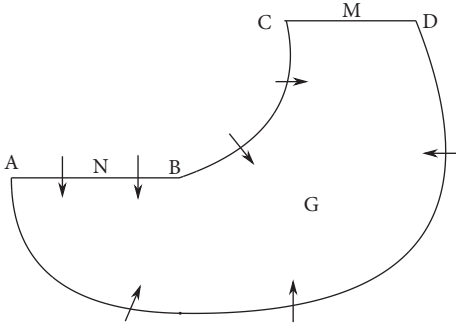


FIGURE 1: Bendixon region of the semicontinuous dynamical system. This figure is reproduced from the study of Wei and Chen [36] (under the Creative Commons Attribution License/public domain).

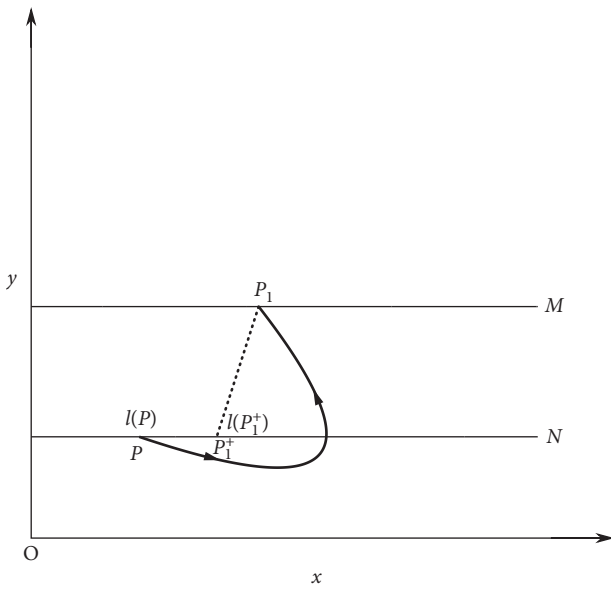


FIGURE 2: Successor function.

obviously  $E_1$  is a saddle.

For  $E_2$ , we have

$$J_{E_2} = \begin{pmatrix} -1 - y_2^2 & -2x_2y_2 \\ y_2^2 & -1 + 2x_2y_2 \end{pmatrix}, \quad (10)$$

and by calculations, we get

$$\lambda_1 + \lambda_2 = -y_2^2 < 0, \quad (11)$$

$$\lambda_1\lambda_2 = y_2^2 - 1 = \frac{y_2}{x_2} - 1 = \frac{2\sqrt{a^2 - 4}}{a - \sqrt{a^2 - 4}} > 0,$$

obviously  $E_2$  is a stable node (Figure 3).

**Lemma 2.** *System (5) is uniformly bounded.*

*Proof.* Firstly, if we have the isoclines  $L_1 : dx/dt = 0$  and  $L_2 : dy/dt = 0$  (Figure 4) and the straight line  $l_1 : x - a = 0$ , then we get  $dl_1/dt = dx/dt|_{x=a} = -ay^2 < 0$ ; thus, according to the qualitative theory of ordinary

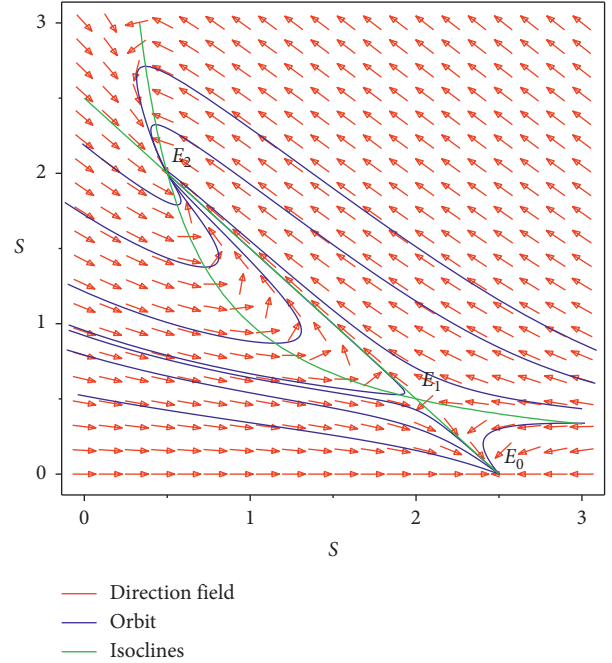


FIGURE 3: Phase diagram of system (3) with  $\theta = 2.5$ ,  $\beta = 1$ , and  $\gamma = 1$ .

differential equations, the trajectory of the system (5) passes through  $l_1$  and goes from the right side of  $l_1$  to the left side of  $l_1$ . Consider the straight line  $l_2 : x + y - M = 0$ , where  $M$  is large enough and  $0 \leq x \leq a$ . Then, we obtain  $dl_2/dt|_{l_2=0} = a - M < 0$ , and thus, the straight line  $l_2$  is nontangent; then, according to the qualitative theory of ordinary differential equations, the trajectory of the system (5) passes through  $l_2$  and goes from the upper right side of  $l_2$  to the lower left side of  $l_2$ . Let us denote the intersections of  $l_2$  and  $L_2$  be  $H(x_H, y_H)$  and consider the straight line  $l_3 : y - y_H = 0$ , obviously, we have  $dy/dt|_{l_3=0} < 0$ , and then, the trajectory of model (5) passes through  $l_3$  and goes from the top side of  $l_3$  to the bottom side of  $l_3$ . Thus, the model (5) is uniformly upper bounded. This completes the proof.  $\square$

#### 4. Homoclinic Cycle of Model about Parameter $p$

In this section, we will discuss the existence of order-1 homoclinic cycle of model (3) by choosing  $p$  as the control parameter.

**Theorem 1.** *If  $R_0 > 1$ , then there exists  $p' \in (0, 1)$  such that model (3) has an order-1 homoclinic cycle.*

*Proof.* In model (3), since the point  $E_1$  is a saddle point, then there exist two manifolds which will enter or leave the saddle point  $E_1$ , one is the unstable manifold  $\Gamma_A$  and another is the stable manifold  $\Gamma_B$ . According to Lemma 2 and the qualitative theory of ordinary differential equations,  $\Gamma_A$  and impulse set  $M$  must intersect, and the intersection is denoted as  $A(x_A, y_A)$ . If we denote the intersection of impulse

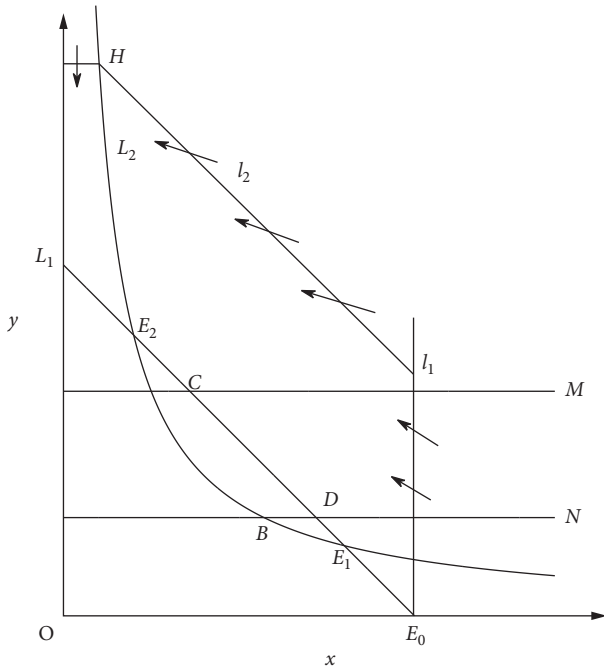


FIGURE 4: System (3) is the uniformly bounded.

set  $M$  and the isocline  $L_1$  as point  $C(x_C, y_C)$ , the intersection of image set  $N$  and isoclines  $L_1$  as point  $D(x_D, y_D)$ , and the intersection of image set  $N$  and  $\Gamma_B$  as point  $B(x_B, y_B)$ , by the qualitative theory of ordinary differential equations, the unstable manifold  $\Gamma_A$  is above of the isoclines  $L_1$ , and the stable manifold  $\Gamma_B$  is below the isoclines  $L_2$  ( $dy/dt = 0$ ) (Figure 5). Because the monotonicity of the impulsive function  $\varphi(x, p) = (1-p)x$  with respect to  $x$  and  $p$ , there must exist  $p' \in (0, 1)$  such that  $\varphi(x_A, p') = (1-p')x_A = x_B$ , and then the stable manifold  $\Gamma_B$  starting form the point  $B$ , the unstable manifold  $\Gamma_A$  starting form the point  $E_1$ , and the impulse line  $AB$  formed a homoclinic cycle.  $\square$

*Remark 2.* If  $p > p'$ , according to the theory of differential equations, the trajectory tends to  $E_0$ , and in a biological sense, the disease eventually extincts. However, the relatively high vaccination rate will waste medical resources. So, we always assume that  $p < p'$  in the following theorem.

**Theorem 2.** *If  $R_0 > 1$ ,  $p < p'$ , and  $p' - p \ll 1$ , then the homoclinic cycle of model (3) disappears and bifurcates an unique order-1 periodic solution.*

*Proof.* By Theorem 1, if  $R_0 > 1$ , then there exists  $p' \in (0, 1)$  such that model (3) has an order-1 homoclinic cycle, i.e., the stable manifold  $\Gamma_B$  starting form the point  $B$ , the unstable manifold  $\Gamma_A$  starting form the point  $E_1$ , and the impulse line  $AB$  formed a homoclinic cycle. Now, we consider whether there will be a periodic solution that bifurcates out of the homoclinic cycle when  $p$  changes. In fact, consider the unstable manifold  $\Gamma_A$  starting form the point  $E_1$ , when  $\Gamma_A$  touches the impulsive set  $M$  (the intersection is denoted as  $A$ ), then a pulse happens and then the impulsive function transfers the point  $A$  into  $D_1$  and the point  $C$  into  $B_1$ , and

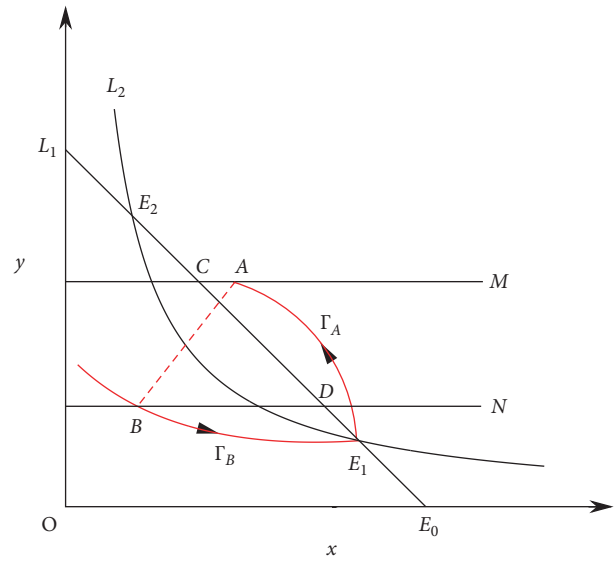


FIGURE 5: The existence of the order-1 homoclinic cycle.

according the definition of impulsive function, we have  $\varphi(x_A, p) = (1-p)x_A = x_{D_1}$ ,  $\varphi(x_C, p) = (1-p)x_C = x_{B_1}$ . If  $p < p'$ , we obtain  $x_{D_1} > x_B$ . Since  $x_B \leq \varphi(x_C, p) = x_{B_1}$  and  $x_D \geq \varphi(x_A, p) = x_{D_1}$ , then we get  $x_D \geq x_{D_1} \geq x_{B_1} \geq x_B$ , and then by the definition of Bendixon region of semi-continuous dynamics system,  $AC$ ,  $CD$  (part of isoclin  $L_1$ ),  $DB$  ( $B_1D_1 \subset BD$ ),  $BE_1$  (part of the  $\Gamma_B$ ), and  $E_1A$  (part of the  $\Gamma_A$ ) constitute the Bendixon region  $G$  of the system (3). According to Lemma 1 and Lemma 2 in [36], system (3) must exist an order-1 periodic solution, initial point of which is between  $B_1$  and  $D_1$  in image set  $N$  (Figure 6).

Next, we show the order-1 periodic solution of system (3) is unique if it exists. The idea of the proof comes from the study of Wei and Chen [36]. Select two points  $I$  and  $J$  in phase set  $B_1D_1$  arbitrarily, where  $x_{B_1} < x_J < x_I < x_{D_1}$ . Let  $F(I) = I_1 \in M$  and  $F(J) = J_1 \in M$ , after that due to the impulsive effects, points  $I_1$  and  $J_1$  jump to  $I_1^+$ ,  $J_1^+ \in N$ . For  $x_J < x_I$ , we have  $x_{I_1} < x_{J_1}$  and  $x_{I_1^+} = (1-p)x_{I_1}$ ,  $x_{J_1^+} = (1-p)x_{J_1}$ ; hence, we have  $x_{I_1^+} < x_{J_1^+}$ . Using Definition 5 and Definition 6 in [36], we obtain  $g(I) = x_{I_1^+} - x_I$  and  $g(J) = x_{J_1^+} - x_J$ . Hence, we have  $g(I) - g(J) = (x_{I_1^+} - x_I) - (x_{J_1^+} - x_J) = (x_J - x_I) + (x_{I_1^+} - x_{J_1^+}) < 0$ ; that is, the successor function  $g(p)$  is monotonic in  $B_1D_1$ . Therefore, there is an unique point  $H$  such that  $g(H) = 0$ ; thus, system (3) has an unique order-1 periodic solution (Figure 7).  $\square$

**Theorem 3.** *If  $R_0 > 1$ ,  $p < p'$ , and  $p' - p \ll 1$ , then the order-1 periodic solution of model (3) is orbitally asymptotically stable.*

*Proof.* By Theorem 2, we have that the order-1 periodic solution in system (3) is unique. Let the initial point of the order-1 periodic solution is  $H \in B_1D_1$ , where  $x_{B_1} < x_H < x_{D_1}$ . Set  $F(D_1) = C_1 \in M$ , then due to the impulsive effects  $C_1$  jumps to  $C_1^+$  which is the successor point of  $D_1$  (Figure 8). We have  $x_{B_1} < x_{C_1^+} < x_H$ . Set  $F(C_1^+) = C_2 \in M$ . Owing to



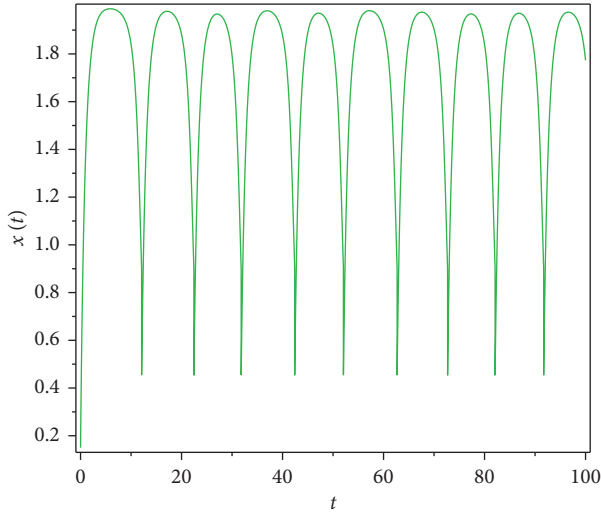


FIGURE 10: Time series diagram of  $x(t)$  of system (3) with  $p = 0.496$  and  $q = 0.5$ .

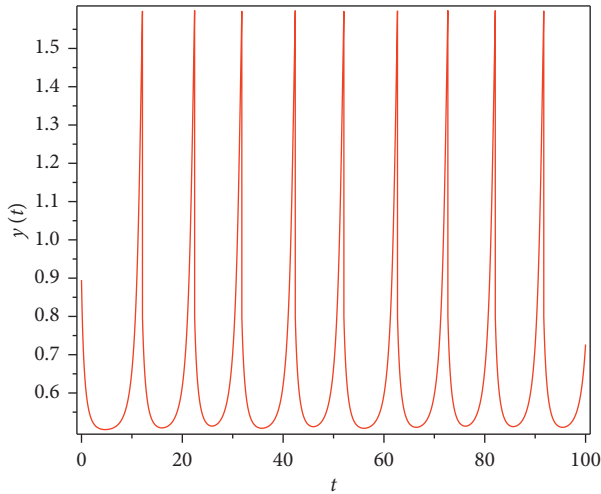


FIGURE 11: Time series diagram of  $y(t)$  of system (3) with  $p = 0.496$  and  $q = 0.5$ .

impulsive effect. Then for any  $l$ , we have  $x_{C_{2(k+l+1)}^+} < x_{H_{2l}} < x_{C_{2(k+l)}^+}$  and  $x_{C_{2(k+l+1)}^+} < x_{H_{2l+1}} < x_{C_{2(k+l+1)+1}^+}$ . Hence,  $\{x_{H_{2l}}\}, l = 0, 1, 2, \dots$ , is monotonically decreasing, and  $\{x_{H_{2l+1}}\}, i = 0, 1, 2, \dots$ , is monotonically increasing. Thus, after the pulse effects the successor points are attracted to the point  $H$ , which means that the order-1 periodic solution of the system (3) is orbitally asymptotically stable.  $\square$

### 5. Numerical Simulations

In this section, we give some numerical simulations to illustrate the theoretical results we previously obtained. First, we consider the system neglecting state-dependent pulse strategy, let  $\theta = 2.5, \beta = 1, \gamma = 1$ , and  $h = 1.6$ , and simple calculations show  $R_0 = 1.5625$ ; then system (3) has three

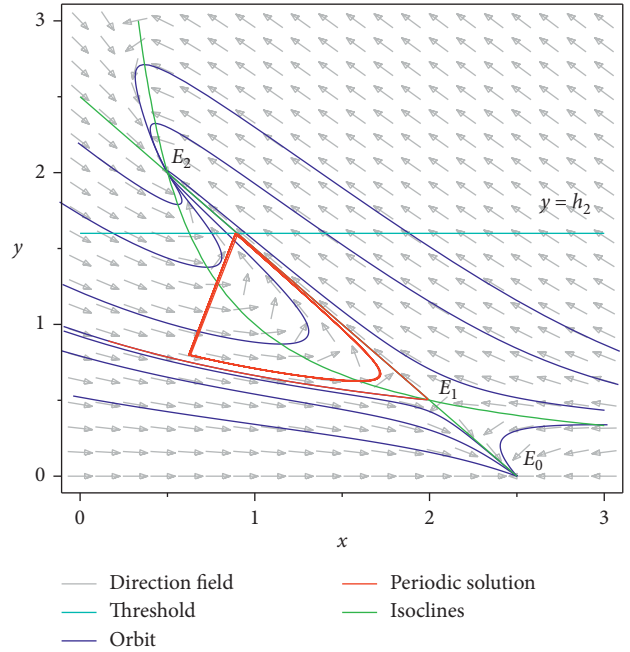


FIGURE 12: Order-1 homoclinic bifurcation of system (3) with  $p = 0.3$ .

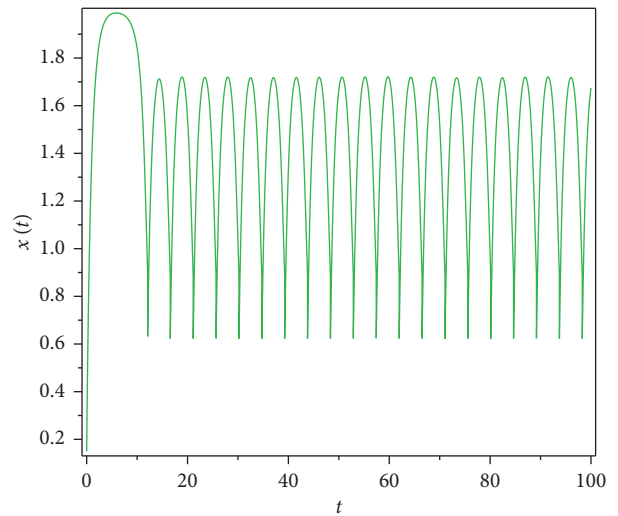


FIGURE 13: Time series diagram of  $x(t)$  of system (3) with  $p = 0.3$ .

equilibria, i.e.,  $E_0 = (2.5, 0)$ ,  $E_1 = (2, 0.5)$ , and  $E_2 = (0.5, 2)$  (Figure 3), and among them,  $E_0$  is a stable node,  $E_1$  is a saddle, and  $E_2$  is a stable node.

Then, we consider the state-dependent pulse control strategy in system (3). First, we take more moderate preventive and therapeutic measures, and let  $p = 0.496, q = 0.5$ , then system (3) has a homoclinic cycle composed of the unstable manifold ( $\Gamma_A$ ), the stable manifold ( $\Gamma_B$ ), and the pulse straight line (Figure 9, the initial value is  $S_0 = 0.15$  and  $I_0 = 0.895$ ). And from the time series diagrams, we can see that  $x$  and  $y$  show periodic oscillations over time (Figures 10 and 11). If we maintain a certain intensity of treatment (fix parameter  $q = 0.5$ ) and reduce the

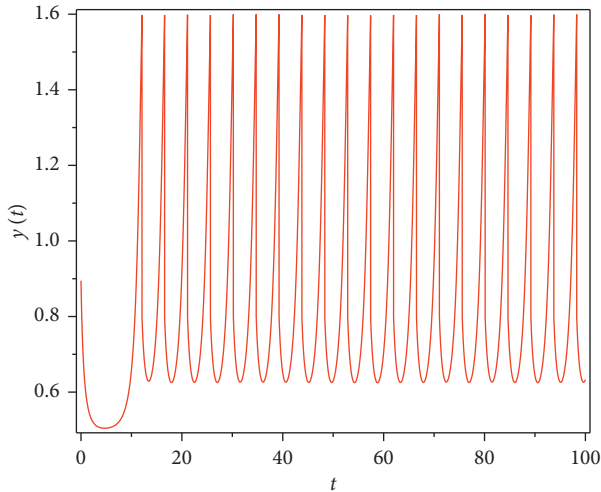


FIGURE 14: Time series diagram of  $y(t)$  of system (3) with  $p = 0.3$ .

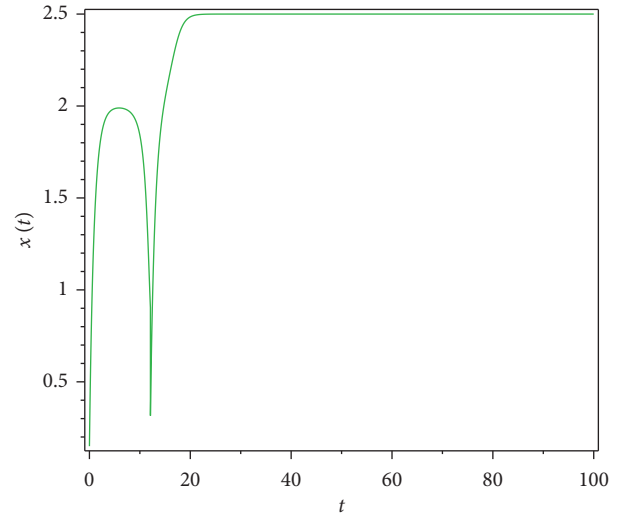


FIGURE 16: Time series diagram of  $x(t)$  of system (3) with  $p = 0.65$ .

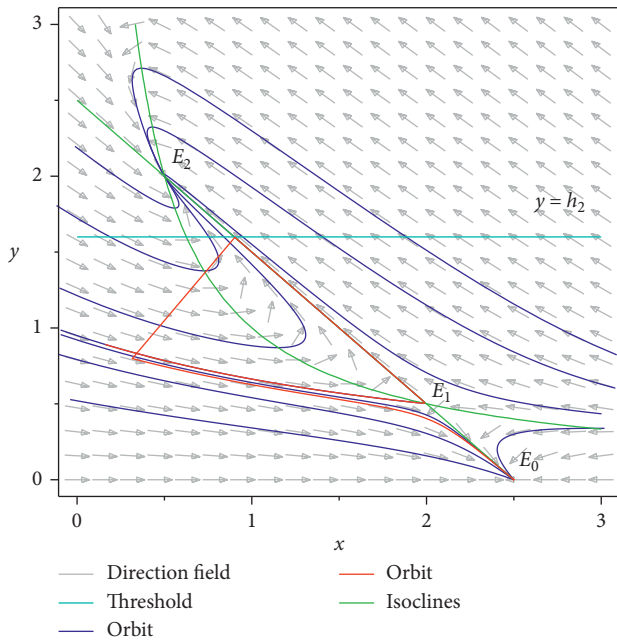


FIGURE 15: Phase diagram of system (3) with  $p = 0.65$ .

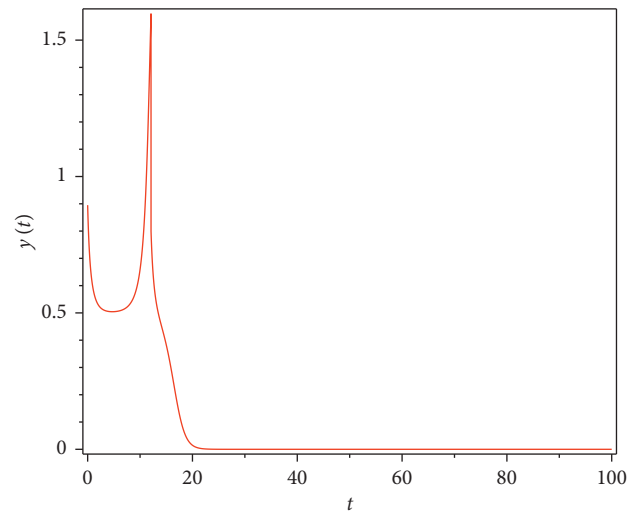


FIGURE 17: Time series diagram of  $y(t)$  of system (3) with  $p = 0.65$ .

intensity of prevention, for example, let  $p = 0.3$ , by Theorem 2, the order-1 homoclinic cycle disappears and bifurcates an order-1 periodic solution, which is shown in Figures 12–14. And if we take more stringent preventive measures which means a larger vaccination rate, for example, let  $p = 0.65$ , then the disease will become extinct, which is shown in Figures 15–17.

### 6. Conclusion

In this paper, a different strategy from tradition, i.e., the state-dependent pulse vaccination and therapeutic strategy, is considered in the control of the disease. A pulse system is built to model this process based on an SI ordinary differential equation model. By using the theory of semi-continuous dynamic system, the dynamics of the pulse

system is analyzed. Our results show the pulse system exhibits rich dynamics; for example, the system has a unique order-1 homoclinic cycle, and by choosing  $p$  as the control parameter, we prove that when  $p$  changes, the order-1 homoclinic cycle disappears and bifurcates an orbitally asymptotical stable order-1 periodic solution. However, it should be pointed out here that, in this work, we focused on the theoretical framework and realistic parameters can be incorporated into our model. State-dependent impulsive vaccination strategy may be used a supplementary control measure besides routine vaccination, or it may be used in the situation when vaccine stockpile is limited (for example, the yellow fever outbreaks in Nigeria and Congo in 2017 [52]). The realistic approach in childhood infection and other infections will be conducted in future work.

### Data Availability

All data are hypothetical to verify the theoretical results of this study.

## Conflicts of Interest

The authors declare that there are no conflicts of interest regarding the publication of this paper.

## Acknowledgments

This work was supported by the National Natural Science Foundation of China (No. 11671346 and 61751317), SDUST Research Fund (No. 2014TDJH102), and Scientific Research Foundation of Shandong University of Science and Technology for Recruited Talents.

## References

- [1] WHO: World health organization, <http://www.who.int/gho/hiv/en/>, 2016.
- [2] WHO: World health organization, <http://www.who.int/gho/tb/en/>, 2016.
- [3] R. Xu and Z. Ma, "Global stability of a SIR epidemic model with nonlinear incidence rate and time delay," *Nonlinear Analysis: Real World Applications*, vol. 10, no. 5, pp. 3175–3189, 2009.
- [4] W. Wang and T. Zhang, "Caspase-1-Mediated pyroptosis of the predominance for driving CD4<sup>+</sup> T cells death: a nonlocal spatial mathematical model," *Bulletin of Mathematical Biology*, vol. 80, no. 3, pp. 540–582, 2018.
- [5] Z. Chang, X. Meng, and T. Zhang, "A new way of investigating the asymptotic behaviour of a stochastic SIS system with multiplicative noise," *Applied Mathematics Letters*, vol. 87, pp. 80–86, 2019.
- [6] T. Zhang, X. Meng, and T. Zhang, "Global analysis for a delayed SIV model with direct and environmental transmissions," *Journal of Applied Analysis and Computation*, vol. 6, no. 2, pp. 479–491, 2016.
- [7] S. Zhang, X. Meng, and X. Wang, "Application of stochastic inequalities to global analysis of a nonlinear stochastic SIRS epidemic model with saturated treatment function," *Advances in Difference Equations*, vol. 2018, no. 1, p. 50, 2018.
- [8] K. Li, J. Li, and W. Wang, "Epidemic reaction-diffusion systems with two types of boundary conditions," *Electronic Journal of Differential Equations*, vol. 2018, pp. 1–21, 2018.
- [9] Y. Zhou, S. Yuan, and D. Zhao, "Threshold behavior of a stochastic SIS model with," *Applied Mathematics and Computation*, vol. 275, pp. 255–267, 2016.
- [10] Q. Liu, D. Jiang, N. Shi, T. Hayat, and A. Alsaedi, "Stationary distribution and extinction of a stochastic SIRS epidemic model with standard incidence," *Physica A: Statistical Mechanics and its Applications*, vol. 469, pp. 510–517, 2017.
- [11] F. Li, X. Meng, and X. Wang, "Analysis and numerical simulations of a stochastic SEIQR epidemic system with quarantine-adjusted incidence and imperfect vaccination," *Computational and Mathematical Methods in Medicine*, vol. 2018, Article ID 7873902, 14 pages, 2018.
- [12] Y. Song, A. Miao, and T. Zhang, "Extinction and persistence of a stochastic SIRS epidemic model with saturated incidence rate and transfer from infectious to susceptible," *Advances in Difference Equations*, vol. 2018, no. 1, p. 293, 2018.
- [13] X. Fan, Y. Song, and W. Zhao, "Modeling cell-to-cell spread of HIV-1 with nonlocal infections," *Complexity*, vol. 2018, article 2139290, 10 pages, 2018.
- [14] T. Zhang, X. Meng, and T. Zhang, "Global dynamics of a virus dynamical model with cell-to-cell transmission and cure rate," *Computational and Mathematical Methods in Medicine*, vol. 2015, Article ID 758362, 8 pages, 2015.
- [15] W. O. Kermack and A. G. McKendrick, "A contribution to the mathematical theory of epidemics," *Proceedings of the Royal Society of London. Series A, Containing Papers of a Mathematical and Physical Character*, vol. 115, no. 772, pp. 700–721, 1927.
- [16] W. O. Kermack and A. G. McKendrick, "Contributions to the mathematical theory of epidemics," *Proceedings of the Royal Society of London A: Mathematical, Physical and Engineering Sciences*, vol. 138, no. 834, pp. 55–83, 1932.
- [17] T. Zhang, X. Meng, Y. Song, and T. Zhang, "A stage-structured predator-prey si model with disease in the prey and impulsive effects," *Mathematical Modelling and Analysis*, vol. 18, no. 4, pp. 505–528, 2013.
- [18] X. Leng, T. Feng, and X. Meng, "Stochastic inequalities and applications to dynamics analysis of a novel SIVS epidemic model with jumps," *Journal of Inequalities and Applications*, vol. 2017, no. 1, p. 138, 2017.
- [19] T. Zhang, X. Meng, T. Zhang, and Y. Song, "Global dynamics for a new high-dimensional SIR model with distributed delay," *Applied Mathematics and Computation*, vol. 218, no. 24, pp. 11806–11819, 2012.
- [20] A. Miao, J. Zhang, T. Zhang, and B. G. S. A. Pradeep, "Threshold dynamics of a stochastic SIR model with vertical transmission and vaccination," *Computational and Mathematical Methods in Medicine*, vol. 2017, Article ID 4820183, 10 pages, 2017.
- [21] A. Miao, X. Wang, T. Zhang, W. Wang, and B. Sampath Aruna Pradeep, "Dynamical analysis of a stochastic SIS epidemic model with nonlinear incidence rate and double epidemic hypothesis," *Advances in Difference Equations*, vol. 2017, no. 1, p. 226, 2017.
- [22] A. Miao, T. Zhang, J. Zhang, and C. Wang, "Dynamics of a stochastic SIR model with both horizontal and vertical transmission," *Journal of Applied Analysis and Computation*, vol. 2018, no. 4, pp. 1108–1121, 2018.
- [23] X. Meng, S. Zhao, T. Feng, and T. Zhang, "Dynamics of a novel nonlinear stochastic SIS epidemic model with double epidemic hypothesis," *Journal of Mathematical Analysis and Applications*, vol. 433, no. 1, pp. 227–242, 2016.
- [24] Z. Agur, L. Cojocaru, G. Mazor, R. M. Anderson, and Y. L. Danon, "Pulse mass measles vaccination across age cohorts," *Proceedings of the National Academy of Sciences of the United States of America*, vol. 90, no. 24, pp. 11698–11702, 1993.
- [25] A. D'Onofrio, "On pulse vaccination strategy in the SIR epidemic model with vertical transmission," *Applied Mathematics Letters*, vol. 18, no. 7, pp. 729–732, 2005.
- [26] C. Wei and L. Chen, "A delayed epidemic model with pulse vaccination," *Discrete Dynamics in Nature and Society*, article 746951, p. 12, 2008.
- [27] Z. Lu, X. Chi, and L. Chen, "The effect of constant and pulse vaccination on SIR epidemic model with horizontal and vertical transmission," *Mathematical and Computer Modelling*, vol. 36, no. 9–10, pp. 1039–1057, 2006.
- [28] S. Liu, Y. Pei, C. Li, and L. Chen, "Three kinds of TVS in a SIR epidemic model with saturated infectious force and vertical transmission," *Applied Mathematical Modelling*, vol. 33, no. 4, pp. 1923–1932, 2009.
- [29] S. Tang, Y. Xiao, and D. Clancy, "New modelling approach concerning integrated disease control and cost-effectivity," *Nonlinear Analysis: Theory, Methods and Applications*, vol. 63, no. 3, pp. 439–471, 2005.

- [30] L. Nie, Z. Teng, and A. Torres, "Dynamic analysis of an SIR epidemic model with state dependent pulse vaccination," *Nonlinear Analysis: Real World Applications*, vol. 13, no. 4, pp. 1621–1629, 2012.
- [31] H. Guo, L. Chen, and X. Song, "Dynamical properties of a kind of SIR model with constant vaccination rate and impulsive state feedback control," *International Journal of Biomathematics*, vol. 10, no. 7, p. 21, 2017.
- [32] W. Qin, S. Tang, C. Xiang, and Y. Yang, "Effects of limited medical resource on a filippov infectious disease model induced by selection pressure," *Applied Mathematics and Computation*, vol. 283, pp. 339–354, 2016.
- [33] T. Zhang, W. Ma, X. Meng, and T. Zhang, "Periodic solution of a prey-predator model with nonlinear state feedback control," *Applied Mathematics and computation*, vol. 266, pp. 95–107, 2015.
- [34] J. Wang, H. Cheng, Y. Li, and X. Zhang, "The geometrical analysis of a predator-prey model with multi-state dependent impulsive," *Journal of Applied Analysis and Computation*, vol. 8, no. 2, pp. 427–442, 2018.
- [35] J. Wang, H. Cheng, H. Liu, and Y. Wang, "Periodic solution and control optimization of a prey-predator model with two types of harvesting," *Advances in Difference Equations*, vol. 2018, no. 1, p. 41, 2018.
- [36] C. Wei and L. Chen, "Homoclinic bifurcation of prey-predator model with impulsive state feedback control," *Applied Mathematics and Computation*, vol. 237, pp. 282–292, 2014.
- [37] H. Cheng, F. Wang, and T. Zhang, "Multi-state dependent impulsive control for holling I predator-prey model," *Discrete Dynamics in Nature and Society*, vol. 2012, Article ID 181752, 21 pages, 2012.
- [38] M. Huang, S. Liu, X. Song, and L. Chen, "Periodic solutions and homoclinic bifurcation of a predator-prey system with two types of harvesting," *Nonlinear Dynamics*, vol. 73, no. 1–2, pp. 815–826, 2013.
- [39] Y. Li, H. Cheng, J. Wang, and Y. Wang, "Dynamic analysis of unilateral diffusion gompertz model with impulsive control strategy," *Advances in Difference Equations*, vol. 2018, no. 1, p. 32, 2018.
- [40] H. Cheng, F. Wang, and T. Zhang, "Multi-state dependent impulsive control for pest management," *Journal of Applied Mathematics*, vol. 2012, Article ID 381503, 25 pages, 2012.
- [41] G. Pang and L. Chen, "Periodic solution of the system with impulsive state feedback control," *Nonlinear Dynamics*, vol. 78, no. 1, pp. 743–753, 2014.
- [42] G. Wang and S. Tang, "Qualitative analysis of prey-predator model with nonlinear impulsive effects," *Applied Mathematics and Mechanics*, vol. 34, no. 5, pp. 496–505, 2013.
- [43] J. Liang, S. Tang, and R. A. Cheke, "Beverton-holt discrete pest management models with pulsed chemical control and evolution of pesticide resistance," *Communications in Nonlinear Science and Numerical Simulation*, vol. 36, pp. 327–341, 2016.
- [44] H. Cheng, T. Zhang, and F. Wang, "Existence and attractiveness of order one periodic solution of a holling I predator-prey model," *Abstract and Applied Analysis*, vol. 2012, Article ID 126018, 18 pages, 2012.
- [45] H. Liu and H. Cheng, "Dynamic analysis of a prey-predator model with state-dependent control strategy and square root response function," *Advances in Difference Equations*, vol. 2018, no. 1, p. 63, 2018.
- [46] J. Wang, H. Cheng, X. Meng, and B. S. A. Pradeep, "Geometrical analysis and control optimization of a predator-prey model with multi state-dependent impulse," *Advances in Difference Equations*, vol. 2017, no. 1, p. 252, 2017.
- [47] Z. Li, T. Wang, and L. Chen, "Periodic solution of a chemostat model with beddington-deanglis uptake function and impulsive state feedback control," *Journal of Theoretical Biology*, vol. 261, no. 1, pp. 23–32, 2009.
- [48] Z. Li and L. Chen, "Periodic solution of a turbidostat model with impulsive state feedback control," *Nonlinear Dynamics*, vol. 58, no. 3, p. 525, 2009.
- [49] W. Liu, S. A. Levin, and Y. Iwasa, "Influence of nonlinear incidence rates upon the behavior of SIRS epidemiological models," *Journal of Mathematical Biology*, vol. 23, no. 2, pp. 187–204, 1986.
- [50] M. Zhang, G. Song, and L. Chen, "A state feedback impulse model for computer worm control," *Nonlinear Dynamics*, vol. 85, no. 3, pp. 1561–1569, 2016.
- [51] L. Chen, X. Liang, and Y. Pei, "The periodic solutions of the impulsive state feedback dynamical system," *Communications in Mathematical Biology and Neuroscience*, article 14, 2018.
- [52] S. Zhao, L. Stone, D. Gao, and D. He, "Modelling the large-scale yellow fever outbreak in luanda, angola, and the impact of vaccination," *Plos Neglected Tropical Diseases*, vol. 12, no. 1, article e0006158, 2018.

## Research Article

# Modeling Airflow and Particle Deposition in a Human Acinar Region

Arun V. Kolanjiyil <sup>1</sup> and Clement Kleinstreuer <sup>1,2</sup>

<sup>1</sup>Department of Mechanical & Aerospace Engineering, North Carolina State University, Raleigh, NC 27695, USA

<sup>2</sup>Joint UNC-NCSU Department of Biomedical Engineering, North Carolina State University, Raleigh, NC 27695, USA

Correspondence should be addressed to Clement Kleinstreuer; ck@ncsu.edu

Received 25 July 2018; Revised 8 November 2018; Accepted 26 December 2018; Published 14 January 2019

Guest Editor: Yu Feng

Copyright © 2019 Arun V. Kolanjiyil and Clement Kleinstreuer. This is an open access article distributed under the Creative Commons Attribution License, which permits unrestricted use, distribution, and reproduction in any medium, provided the original work is properly cited.

The alveolar region, encompassing millions of alveoli, is the most vital part of the lung. However, airflow behavior and particle deposition in that region are not fully understood because of the complex geometrical structure and intricate wall movement. Although recent investigations using 3D computer simulations have provided some valuable information, a realistic analysis of the air-particle dynamics in the acinar region is still lacking. So, to gain better physical insight, a physiologically inspired *whole acinar model* has been developed. Specifically, air sacs (i.e., alveoli) were attached as partial spheroids to the bifurcating airway ducts, while breathing-related wall deformation was included to simulate actual alveolar expansion and contraction. Current model predictions confirm previous notions that the location of the alveoli greatly influences the alveolar flow pattern, with recirculating flow dominant in the proximal lung region. In the midalveolar lung generations, the intensity of the recirculating flow inside alveoli decreases while radial flow increases. In the distal alveolar region, the flow pattern is completely radial. The micron/submicron particle simulation results, employing the Euler-Lagrange modeling approach, indicate that deposition depends on the inhalation conditions and particle size. Specifically, the particle deposition rate in the alveolar region increases with higher inhalation tidal volume and particle diameter. Compared to previous acinar models, the present system takes into account the entire acinar region, including both partially alveolated respiratory bronchioles as well the fully alveolated distal airways and alveolar sacs. In addition, the alveolar expansion and contraction have been calculated based on physiological breathing conditions which make it easy to compare and validate model results with in vivo lung deposition measurements. Thus, the current work can be readily incorporated into human whole-lung airway models to simulate/predict the flow dynamics of toxic or therapeutic aerosols.

## 1. Introduction

The alveolar region encompasses millions of alveoli specifically designed to allow efficient gas diffusion during the normal breathing process [1]. Flow behavior and particle deposition in the alveolar region are not yet fully understood because of the complex geometrical structure [2, 3]. Understanding the flow and particle behavior in the alveolar region is important because inhaled aerosols depositing in the alveoli can lead to severe lung diseases [4–6]. In case of therapeutic drug targeting [7, 8], the prediction of airflow and particle deposition in the alveolar region is necessary for the treatment of pulmonary diseases as well as drug-aerosol transfer to systemic regions.

Although the acinar region is the most vital part of the lung, only limited information is available regarding its geometry because of its inaccessibility. Current limitations in obtaining detailed images of these micron structures also restrict detailed fluid-particle dynamics studies [5, 9]. Similar to the conducting region, the acinar region is composed of repeating bifurcating alveolar ducts with alveoli arranged around the conduits [10, 11]. Each alveolus may be approximated as a spherically shaped cup [12], with one opening to the airway, tightly packed around the alveolar ducts in order to optimize the alveolar surface area [11]. These alveoli are separated by a thin tissue layer called septa which contain a multitude of blood vessels [10]. Several studies have used lung casts to analyze the geometrical structure of the

acinus, and the reported alveoli topology varies from study to study [1, 10–14]. Recently, micro X-ray computed tomography (micro-CT) has been used to study morphology and geometric structure of rodent acinar lung airways [14, 15]. Three-dimensional (3D) reconstructions of acinar airways from high-resolution CT images show the irregular nature of the alveolar topology but closely resemble the spheroidal topology [13]. Polygonal space-filling structure of the alveoli has also been suggested in several studies [4, 16–19]. However, with these sac shapes, it is difficult to assess the bifurcation characteristics of the alveolar ducts, and it may not be able to replicate the partially alveolated transitional respiratory bronchioles. Furthermore, recent studies indicate that the topological features of alveoli may not be significant in distal airways and sacs [17, 20].

Traditionally it has been thought that the low Reynolds number flow in the alveolar region is completely reversible. However, this assumption was reexamined after the bolus inhalation experiments by Heyder et al. [21] in which they showed that irreversible convective mixing exists in the peripheral lung airways. This may lead to high deposition of inhaled particles deep inside the lung. In spite of the evidence showing convective mixing of acinar airflow, these *in vivo* experiments could not provide detailed information regarding trajectories and local deposition of particles in sub-millimeter alveolar structures. As an alternative, numerical analyses were used, based on simplified alveolar configurations, still highlighting the prominent flow characteristics in the alveolar region, including recirculation and chaotic mixing [22]. These earlier findings were again confirmed based on additional experimental and numerical results [5, 13, 23, 24]. Nevertheless, it is still not clear how the alveolar structure at the microlevel changes during breathing [25]. Several explanations have been put forward to explain the mechanism; yet, no consensus exists [26]. The common hypotheses are the following: (1) isotropic balloon-like expansion of alveoli; (2) expansion followed by shape change; (3) recruitment and derecruitment of alveoli; and (4) anisotropic accordion-like shape changes [27, 28]. Studies have pointed out that the deforming alveoli primarily contribute to changes in lung volume, while the deformations of airways and ducts have a considerably lower influence [29].

In addition to the airflow, several studies have indicated that the particle transport and deposition in the alveolar airways are significantly affected by the alveolar-wall motion [30, 31], predominantly affecting submicron particles [32]. In these investigations, it was noticed that the particle deposition pattern in the alveoli was mostly heterogeneous; however, the alveolar entrance ring was an important site for particle deposition [32, 33]. Similarly, heterogeneous deposition of particles on the duct and alveolar walls was observed in multigenerational, bifurcating alveolar models [34, 35]. However, concentrated particle deposition was noticed at the bifurcation ridge, indicating the significance of alveolar airway bifurcation [36–38]. Recently, 3D space-filling alveolar models have been used in alveolar airway simulations [4, 5, 17, 20, 39–41]. The alveolar airways were developed using repeated polyhedral units assuming equal space-filling alveoli and the interconnecting faces were

removed to form the alveolar ducts. Most of these simulations were conducted assuming uniform ventilation in all alveoli; however, anisotropic ventilation due to heterogeneous alveolar-wall expansion may also contribute to the chaotic nature of the alveolar flow [39]. Even though the space-filling polyhedral models can accommodate multiple alveolated ducts, these models cannot account for the variation in airway bifurcations. Additionally, these models have not been shown to predict whole acinar lung deposition; hence, they have not been incorporated to study the deposition in a whole-lung model, with the exception of Khajeh-Hosseini-Dalasm and Longest [41]. More recently, microfluidic lab-on-chip models of the acinar generations have been developed to study the rhythmic motion of the alveoli as well as its impact on alveolar flow pattern and particle transport [42, 43]. Initial results have shown streamline crossing of particles due to the dominant effects of gravity and diffusion, leading to site-specific deposition depending on particle size.

The objective of the present study was to develop a *full* human acinar airway model to simulate and analyze micron/submicron particle transport/deposition in these lower lung airways. The current acinar model simulates the inhalation-exhalation process, i.e., the expanding and contracting motions of the alveoli. Hence, it can replicate all physiological breathing modes. Furthermore, the current comprehensive model takes into account the variation of alveolar tissue dynamics for each airway generation. Of special interest is the interplay between alveolar-wall deformation and particle deposition due to gravity and secondary flow. As mentioned, the comprehensive acinar model can be readily incorporated into human whole-lung airway models to simulate/predict the fate of inhaled toxic or therapeutic aerosols.

## 2. Methods

**2.1. Model Geometry.** For the comprehensive acinar model, spherical alveoli were attached to triple bifurcation units (TBUs), where the alveoli were separated by a minimum distance to allow for expansion, representing the septa that separate the alveoli (Figure 1). The spherical shape of the alveoli was selected based on observations by Hansen and Ampaya [12] and Harding and Robinson [13]. A cylindrical projection from the lumen was used to anchor the spherical alveolus to the duct. The final alveolus has a 3/4 spheroid shape. The partial spheroid with the neck was arbitrarily assembled on the surface of the duct so that the alveolar neck opens to the duct. A single alveolus can be described using four parameters: alveolus radius (AR), neck radius (NR), alveolus depth ( $D$ ), and the duct diameter (DD) (Figure 1(e)). The geometrical assumptions have been verified by the morphometric study using human lung casts and images (Figures 1(b)–1(e)) ([13]). In general, the initial dimensions (at time  $t=0$  or at functional residual capacity (FRC)) of the alveoli are given in Table 1 [44]. Depending on the inhalation condition, the alveolus radius and alveolus depth may change with time; however, alveolar neck and airway duct were assumed to be rigid. This assumption is based on previous investigations which pointed out that at shallow breathing

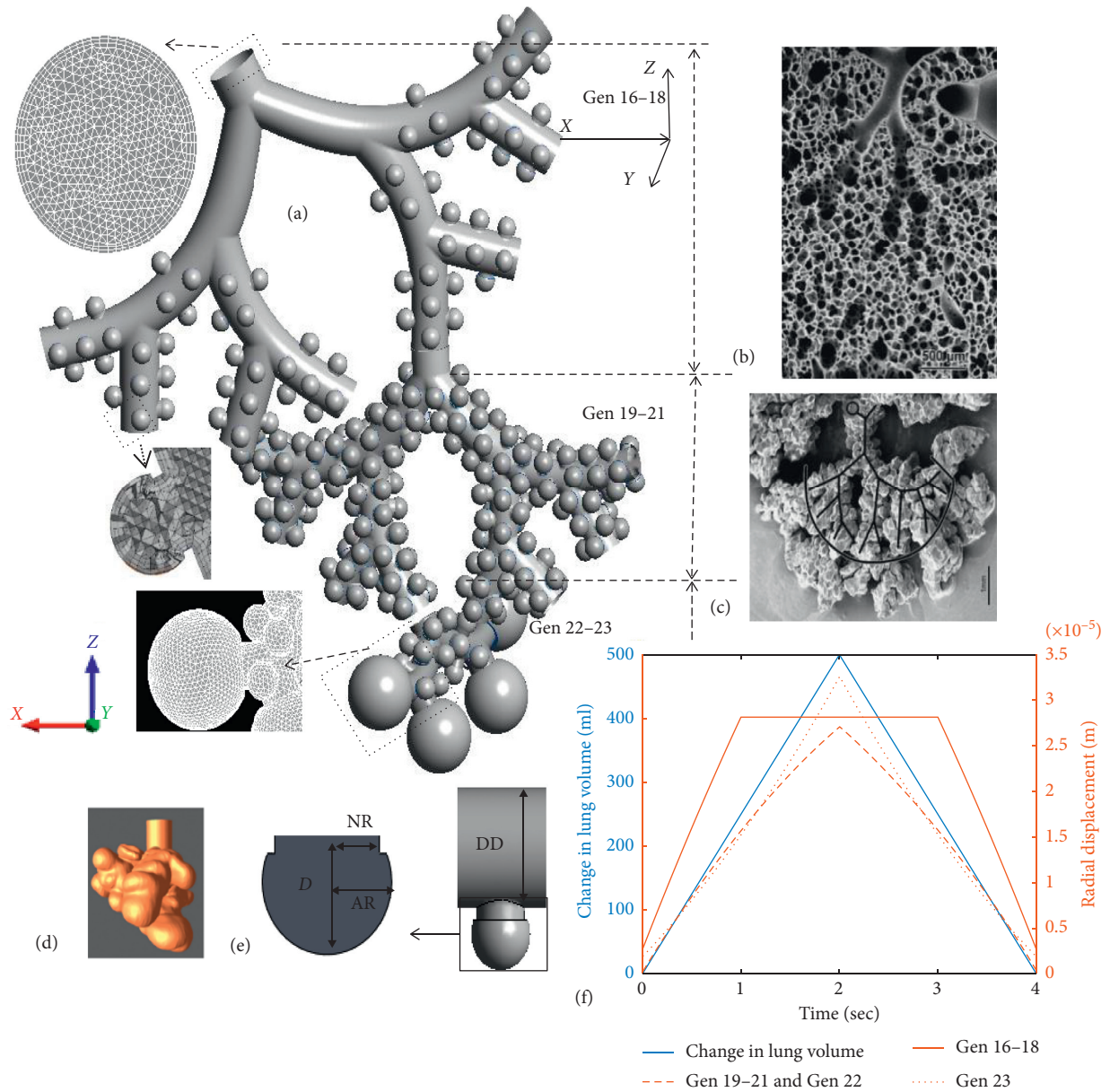


FIGURE 1: (a) Final assembled full alveolar model; (b) image of terminal conducting airways ending in an acinar region from a lung cast (source [45]); (c) image of fully alveolated airways from a lung cast (source [45]); (d) image of a lung airway sac (source [46]) republished with permission of ASME and permission conveyed through Copyright Clearance Center, Inc.); (e) representative alveoli attached duct; and (f) change in lung volume for a 15 LPM breathing flow rate with inhalation period of 2 s, tidal volume of 500 ml, and the corresponding radial displacement vectors for the alveoli in each lung generations.

conditions, the deforming alveoli primarily contribute to changes in lung volume, while the deformation of airways and ducts are considerably less when compared to the alveoli [29]. The duct diameter for each model was based on the scaled Weibel’s symmetrical lung model. The size of the alveoli has not been varied with generation; however, variation in duct diameter with lung generation number was considered. Additionally, the deformation scale of each alveolus depends on the generation number of the airway, which resulted in variation in alveolar size with respect to the airway generation. These alveolar designs were further modified in terms of triple bifurcation units (TBUs) in order to represent alveolar airway generations from 16 to 18 and 19 to 21. A double bifurcation

unit (DBU) was used to represent the airway generations 22 and 23. This design of the acinar airways follows a symmetric dichotomous branching structure as reported in many lung-cast studies [10, 11, 45, 46]. The first TBU represents a partially alveolated respiratory or transitional airways. Details regarding the duct dimensions and the number of alveoli per generation are given in [44]. Instead of using separate alveoli, a quasispherical alveolus (closed sac) was used to represent generation 23. The total volume of the 23<sup>rd</sup> generation was conserved in the model by creating a partial spheroid with the same total volume as in generation 23 (i.e., duct with 17 alveoli). As reported previously, in the terminal alveolar airways, the demarcation of alveoli is not obvious, i.e., they

TABLE 1: Geometric model parameters for a single alveolus.

		Literature comparison	Reference
Alveolus radius (AR)	0.105 mm	0.1–0.14 mm	Weibel [10] Harding and Robinson [13]
Neck radius (NR)	0.085 mm	0.085 mm	Ma and Darquenne [35] Harding and Robinson [13]
Alveolus depth ( $D$ )	0.2–0.22 mm	0.23 mm	Weibel [10] Harding and Robinson [13]
$D$ /NR ratio	1.17–1.3	0.48–1.44	Harding and Robinson [13]

rather form clusters, which results in reduced surface areas. Additionally, recent studies have reported larger sizes for terminal alveoli [47]. The final assembled human acinus and images of human lung casts are shown in Figure 1. Following previous analyses, only one TBU per generation was modeled and the TBU for generations 19–21 and DBU for 22–23 were fitted to one of the outlets of the previous generation [48–50].

**2.2. Wall Motion and Boundary Conditions.** The wall motion of the alveoli surface was incorporated so that the breathing mechanism due to the negative alveolar pressure can be reproduced. The alveoli were assumed to deform isotropically, i.e., balloon-like with preserving shape, while the deformation rates determine the inhalation and exhalation flow rates [26, 27, 29]. The increase or decrease in volume of the alveoli produces a differential pressure which pulls in or expels air, allowing for the simulation of any realistic waveform. Depending on the flow rates, a deformation vector for the alveoli was estimated to produce the required volume changes. For example, the increase in volume from the initial functional residual capacity (FRC) can be represented using the following equations:

$$V_{\text{FRC}} = f \frac{4}{3} \pi r^3, \quad (1)$$

$$\begin{aligned} V_{\text{FRC}} + dV &= f \frac{4}{3} \pi (r + dr)^3 \\ &= f \frac{4}{3} \pi (r^3 + dr^3 + 3r dr (r + dr)), \end{aligned} \quad (2)$$

$$dV = f \frac{4}{3} \pi (dr^3 + 3r dr (r + dr)), \quad (3)$$

where  $V_{\text{FRC}}$  is the alveolus volume at FRC,  $f$  is the fractional volume of the spherical cap representing an alveolus ( $f=0.75$ ) and the alveolar sac ( $f=0.97$ ), and  $dV$  is the differential increase in volume due to the radial expansion  $dr$ .

Assuming a symmetric dichotomous branching structure of the lung, the inhalation flow rate through any generation will be the flow rate measured at the oral inlet divided by the number of airways in that generation. This can be represented as follows:

$$\begin{aligned} \dot{M}_g &= \frac{\dot{M}_{\text{inlet}}}{2^g}, \\ \dot{V}_g &= \frac{\dot{V}_{\text{inlet}}}{2^g}, \end{aligned} \quad (4)$$

where  $\dot{M}_{\text{inlet}}$  is the mass flow rate at the oral inlet,  $\dot{M}_g$  is the mass flow rate through the airway generation  $g$ ,  $\dot{V}_{\text{inlet}}$  is the volume flow rate at oral inlet, and  $\dot{V}_g$  is the volume flow rate through the airway generation  $g$ .

As mentioned, the airflow rate is generated via the alveolar deformation and the deformation rate varies with the local TBU. The total number of alveoli is 84, 182, 25, 4 in TBU 16–18, 19–21, 22, and 23, respectively, and their corresponding alveolar volume fraction per TBU is 0.03, 0.25, 0.27, and 0.45. The alveoli in each TBU deform in order to produce a fraction of the oral inhalation flow rate which is equal to the total flow rate times the alveolar volume fraction in the TBU. This can be mathematically represented using

$$\dot{V}_{\text{TBU}}(t) = V_{\text{TBU}}^{\text{FRC}} + \dot{V}_{\text{inlet}} \frac{V_{\text{TBU}}^{\text{FRC}}}{\sum_{g=17}^{23} V_g^{\text{FRC}}}, \quad (5)$$

where  $\dot{V}_{\text{TBU}}(t)$  is the instantaneous volume of the TBU at any time  $t$ ,  $V_{\text{TBU}}^{\text{FRC}}$  is the volume of the TBU at FRC, and  $V_g^{\text{FRC}}$  is the volume of the airway generation  $g$ . The alveolar volume fraction within a TBU is represented using the ratio  $V_{\text{TBU}}^{\text{FRC}} / \sum_{g=17}^{23} V_g^{\text{FRC}}$ .

Additionally, the individual alveolus wall deformation can be estimated by dividing the fractional volume flow rate per TBU with the number of alveoli in that TBU. The instantaneous flow rate  $dV/dt$  in a particular lung generation for any given inhalation condition can be predetermined, and hence the corresponding alveolar deformation can be estimated by solving equation (3) for  $dr/dt$ . Figure 1(f) shows the change in lung volume with respect to a breathing cycle as well as the corresponding radial displacement vectors for the alveoli in each lung generations. The breathing conditions included a flow rate of 15 LPM, inhalation period of 2 s, and a corresponding tidal volume (TV) of 500 ml. The contraction of the alveoli was modeled by following a reverse path from the expanded volume to the original FRC volume at an identical deformation rate, assuming isotropic volume expansion/contraction, i.e., with negligible geometrical hysteresis.

As suggested in previous studies, the rhythmic expansion and contraction of the lung is assumed to be geometrically self-similar in nature [19]. The presence of surfactant also helps the alveoli to expand and contract at the same rate. The control of liquid surface tension by the surfactants and nonlinear elasticity of the lung tissue prohibits expansion of alveoli beyond a specific radius [51]. In order to replicate the physiological breathing motion of the alveoli, the deformation of the alveoli was restricted after a specified increase in alveolar radius. This final radius was estimated based on the self-similarity assumption. For an average human adult with FRC of 3000 ml and total lung capacity of 6000 ml, the maximum increase in alveolar radius is estimated to be 0.26 times the initial radius (Figure 1(f)). Measured alveolar distention values are in close range with

the assumed values [26]. It is quite difficult to measure the exact stress-strain relationship in the alveoli during different levels of inflation. The nonlinear alveolar tissue dynamics and the presence of liquid lining layer and surfactants inside alveoli may limit the stretching of the alveolar walls after an initial expansion [52]. So, in the present study, this effect was simulated by assuming that after 500 ml of tidal volume, the expansion rate was reduced to half due to strain-stiffening of the biological tissue. Once the alveoli reached their maximum capacity of deformation, the rates of the alveoli in distal generation 23 were increased proportionally to satisfy the required total inhalation flow rate. A similar behavior has been noticed where the volume redistributes from over-distended alveoli with reduced compliance to larger alveoli [26, 53].

**2.3. Numerical Method.** Following our previous, experimentally validated fluid-particle dynamics modeling [49], the alveolar fluid flow was simulated by solving the 3D Navier–Stokes equations on a moving mesh using an unsteady incompressible laminar flow solver with a user-enhanced commercial CF-PD package (CFX, Version 15 from ANSYS, Inc.; Canonsburg, PA). The particle transport was modeled using a Lagrangian approach assuming a dilute particle suspension. The major point forces acting on each particle are the drag (with Schiller–Naumann drag coefficient) and gravity [54]. The regional deposition of micron particles in human airways can be quantified in terms of the deposition fraction (DF):

$$DF = \frac{\text{number of deposited particles in a specific region}}{\text{number of particles entering the generation 16 inlet}} \quad (6)$$

In order to reduce the computational effort and resources required for simulating the full alveolar model, each individual TBU/DBU was simulated independently. At the inlet of these TBUs/DBUs, an opening, i.e., entrainment, boundary condition was applied. The opening boundary condition, applying constant pressure, will allow flow in both directions. It will ensure that the physiological breathing mechanism (air being sucked in during inspirations and air being pushed out during expiration) is enforced. A wall deformation vector (depending on the local TBU/DBU) was applied on the alveoli surface and the rest of the airway wall was assumed to be rigid. At the outlet of the TBUs, a mass flow rate boundary condition was enforced in such a way that the outlet flow rate  $Q_D$  and flow rate due to the alveolar-wall motion  $Q_A$  together result in the inlet flow rate  $Q_G$  (i.e., flow rate per generation). The no-slip boundary condition was invoked at the wall boundaries (duct and alveoli) so that the fluid velocity matches with the wall velocity at the fluid wall interface. User-defined CFX Expression Language (CEL) functions were used to apply the wall deformation vector. In order to study the effects of inhalation and exhalation conditions on alveolar flow pattern, transient breathing profile with constant oral inhalation flow rates were assumed. Simulations were conducted for rest (15 LPM) breathing conditions with

inhalation periods of 2 s and 4 s, corresponding to tidal volumes (TVs) of 500 ml and 1000 ml (Figure 1(f)). A simple breathing waveform was selected in order to compare the model predictions with experimental data sets in which subjects inhaled and exhaled at quasiconstant airflow rates. Clearly, *by controlling the alveolar-wall displacement, any inhalation waveform can be simulated, which implies that the model is capable of simulating actual breathing patterns.*

The geometrical models were meshed using ICEM from ANSYS, Inc. (Canonsburg, PA). The fluid domain of the single-generation alveolated models and the TBUs were discretized using tetrahedral elements with three prism layers. Prism layers were added to accurately capture the near wall gradients, while the DBU fluid domain consisted of only tetrahedral elements. A mesh convergence study was performed to ensure grid independent results by comparing the velocities at different cross sections as well as regional particle deposition values. Increasing the number of elements by a factor of 1.5 showed less than 1% of differences in these results. The final mesh for the single-generation, single-alveolated and multialveolated models had 100k and 280k elements while the TBUs had 2 million elements. In order to avoid large elemental deformation leading to negative volume, a coarser mesh was used for the 23<sup>rd</sup> generation. The final mesh for the DBU had 400k elements.

Particles were distributed uniformly at the inlet with an initial velocity being the same as the inlet-air velocity. The outlet measurements (i.e., particle distributions) from the upper TBU outlets were exported at each time step to become the inlet condition for the next generation TBU, and the process was continued for all TBUs/DBU attached later on. During the exhalation phase, particle tracking starts from the suspended position at the end of inspiration, while the particles exiting the TBUs or DBUs were randomly injected into one of the outlets of the upper TBU, i.e., the outlets of the parent unit are considered as a single-injection plane from which the exited particles are reinjected. 20,000 particles per second were injected at the inlet of TBU 16–18. Particles were assumed to deposit on the walls on contact. Increasing the number of particles by a factor of 2 showed less than a 2% difference in the total acinar deposition results.

### 3. Results and Discussion

**3.1. Alveolar Flow Pattern.** The airflow through an alveolated duct depends on the rhythmic expansion and contraction rate of the alveoli. The flow patterns through different generations of the TBUs 16–18, TBUs 19–21, and DBUs 22–23 during inhalation with an inhalation flow rate of 15 LPM are shown in Figure 2. Enlarged views of the flow streamlines and velocity vectors inside alveolus are also displayed. The results indicate that the air in the alveolus of the proximal alveolar airways is strongly recirculating with substantially lower velocities when compared to the duct flow. Thus, only a very small fraction of the duct flow enters the alveoli; however, the shear flow across the alveolar mouth generates the recirculation region in the alveolar cavity. The presence of alveoli around the duct in conjunction with the alveolar pulling force generated from the alveolar-wall motion

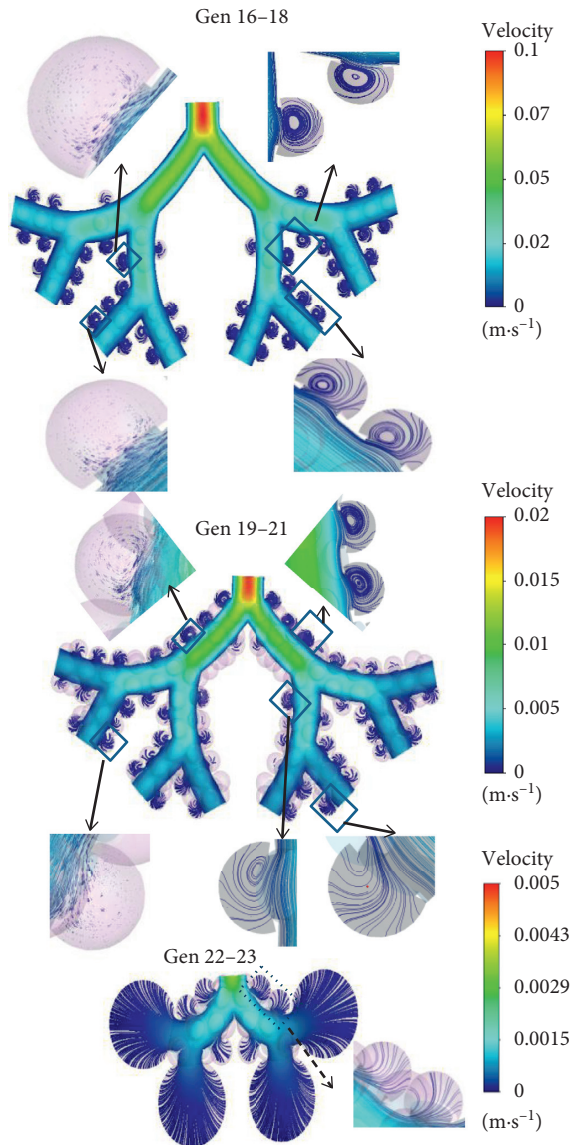


FIGURE 2: Enlarged view of the flow streamlines and velocity vectors inside alveolar airways [48].

produces a deflection of a small amount of duct flow into the alveolar cavity. In the proximal alveolar airways, the size of the alveolar cavity is much less compared to the duct diameter. Hence, the amount of duct air entering the alveoli is also lower. However, within the TBUs, variations in recirculating flow intensity were noticed. As shown in Figure 2, the velocity vectors inside the alveolus in generation 17 shows rotating flow while the flow inside the alveolus of generation 18 exhibits a mixed radial-recirculating flow field. This is due to the decreased shear flow through the ducts. As the generation number increases, the flow is divided by half which in turn reduces the shear flow through the duct and hence the recirculating alveolar flow, thereby increasing the radial flow into the alveolus. The flow characteristics in TBUs 19–21 indicate that the intensity of the recirculating flow inside the alveolus is decreasing, while the radial flow is increasing. As a result, the flow inside an alveolus in

generation 21 is mostly radial. Hence, it is expected that the mass transfer from the duct to the alveoli will increase in the distal lung generations. In DBUs 22–23, the flow pattern inside the alveolus is fully radial. The expansion of the alveolar sac model representing generation 23 generates a larger proportion of the inhalation flow rate into the lung so that the flow into the alveolar sac is fully radial. The Reynolds number in these distal lung regions under the assumed inhalation flow rate of 15 LPM is very low; hence, it can be assumed that the flow is quasisteady. The flow characteristics during exhalation were almost identical to the inhalation phase, other than that the direction of the flow was reversed. At the distal generations, the radial flow was directed from the alveolar cavity into the duct. Similarly, the direction of the recirculating flow in the proximal alveolar cavities was reversed with the change in phase. During the flow reversal from inhalation to exhalation, unsteady flow characteristics were not evident which may be due to the low inhalation flow rate.

**3.2. Particle Transport and Deposition.** Trajectories of particles with diameters  $2\ \mu\text{m}$  to  $10\ \mu\text{m}$  were simulated using the full acinar model. Gravity was assumed to act in the negative  $z$ -direction (Figure 1). Particle deposition results during inhalation phase are shown in Figure 3. The particle deposition was significantly influenced by particle size and tidal volume. The deposition fraction increased with the particle size and the tidal volume. There is an exponential increase in deposition for the lower-micron-size particles and as the particle size increased above  $5\ \mu\text{m}$ , the increase in deposition reduces. Except for  $2\ \mu\text{m}$ , more than 50% of the particles deposited during the inhalation phase itself. Even though total deposition trend showed an increase with particle size, segmental deposition varied over airway generations. Particle deposition increased with particle size in the proximal alveolar region (generation 16 to 18), increased with lower micron particle size, and decreased with upper micron particle size in the midalveolar region, but decreased with particle size in the distal alveolar region. The results also show that with the increase in tidal volume, more particles are being pulled into the distal lung airways, and hence the deposition in these distal lung generations increases. The number of particles deposited is higher in the midalveolar airways compared to other airway generations. The deposition in the proximal alveolar region (generation 16 to 18) is constant, for all the inhalation conditions considered. The results indicate that the increase of particle deposition with an increase in inhalation tidal volume is mostly due to the increased deposition in the distal alveolar airways.

The particle deposition results during exhalation phase are shown in Figure 4. The deposition fraction decreased with the particle size and did not show much variation with the tidal volume. Contrary to the inhalation phase, during exhalation phase particle deposition is higher in the mid-alveolar airways and in the distal alveolar airways. Lower-micron-sized particles have higher deposition in the mid- and distal airways, while larger micron particles tend to deposit in the proximal airways themselves. This can be

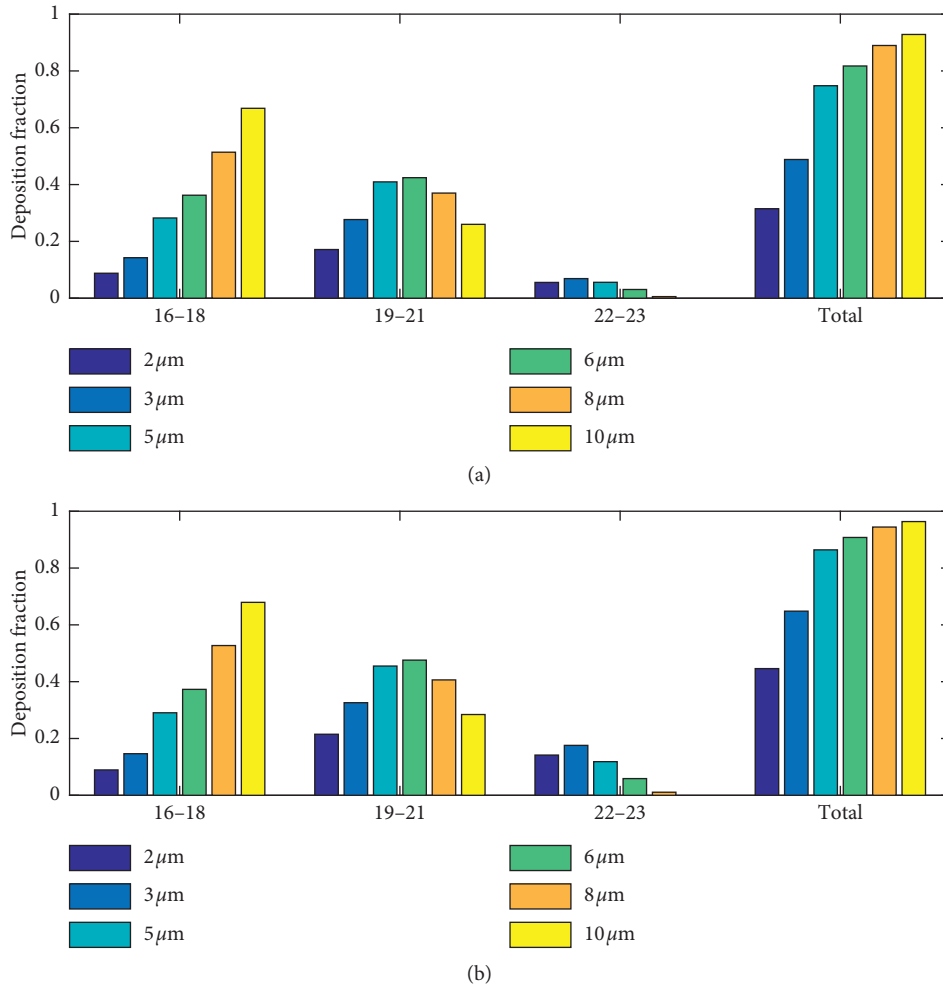


FIGURE 3: Particle deposition results for (a) TV 500 ml and (b) TV 1000 ml during inhalation phase.

attributed to the higher number of suspended larger micron particles in the proximal airways. These suspended particles are mostly particles that are being inhaled during the final inhalation phase. Due to the low inhalation flow rate, they reach the midalveolar airways so that during exhalation, these particles tend to deposit in the proximal alveolar airways due to sedimentation. Similar to the inhalation phase, the number of lower micron particles reaching the distal airways increased with tidal volume and hence the deposition in these airways.

The positions of the 3  $\mu\text{m}$  particles at selected time levels during inhalation and exhalation phase with flow rate 15 LPM and tidal volume 1000 ml are shown in Figure 5. The particles were continuously injected at the inlet during the inhalation phase, and the particles were tracked until they were deposited or exhaled. Majority of the particles were convected with the duct flow during their transport through the lower lung generations. The particle front reached the second-level TBU within 0.2 s; however, due to the reduced flow velocity, the particle front penetrated into the DBU after 1 s. The transport and deposition of the particles were significantly influenced by the gravitational force. With the increase in generation number, more particles were found to enter the alveolar cavities which are oriented in the direction

of the gravitational vector. Over time, a small number of particles were found to enter the alveoli in the proximal generations. These particles were mostly injected close to the lower airway surface which increased their chance to enter the alveoli. It is evident from the figure that with the increase in inhalation tidal volume, more particles tend to reach the distal alveolar generations. The 3  $\mu\text{m}$  particle-front reached generation 19 at around 0.15 s, while the 5  $\mu\text{m}$  particle-front took less time to reach the same generation. This is due to the higher gravitational pull. During the exhalation phase, the particles were pulled back into the upper lung generations. Particles present inside the alveolus were pulled out due to the contracting motion of the alveolus. However, the trajectories of the particles during exhalation were different when compared to inhalation, due to the effect of gravity. The gravitational pull during the exhalation phase has resulted in increased particle residence times of the particles and hence a higher deposition fraction.

**3.3. Total Acinar Deposition and Comparison with In Vivo Measurements.** The total particle deposition results during a full breathing cycle are plotted in Figure 6(a). The number of particles remaining in suspension at the end of the first

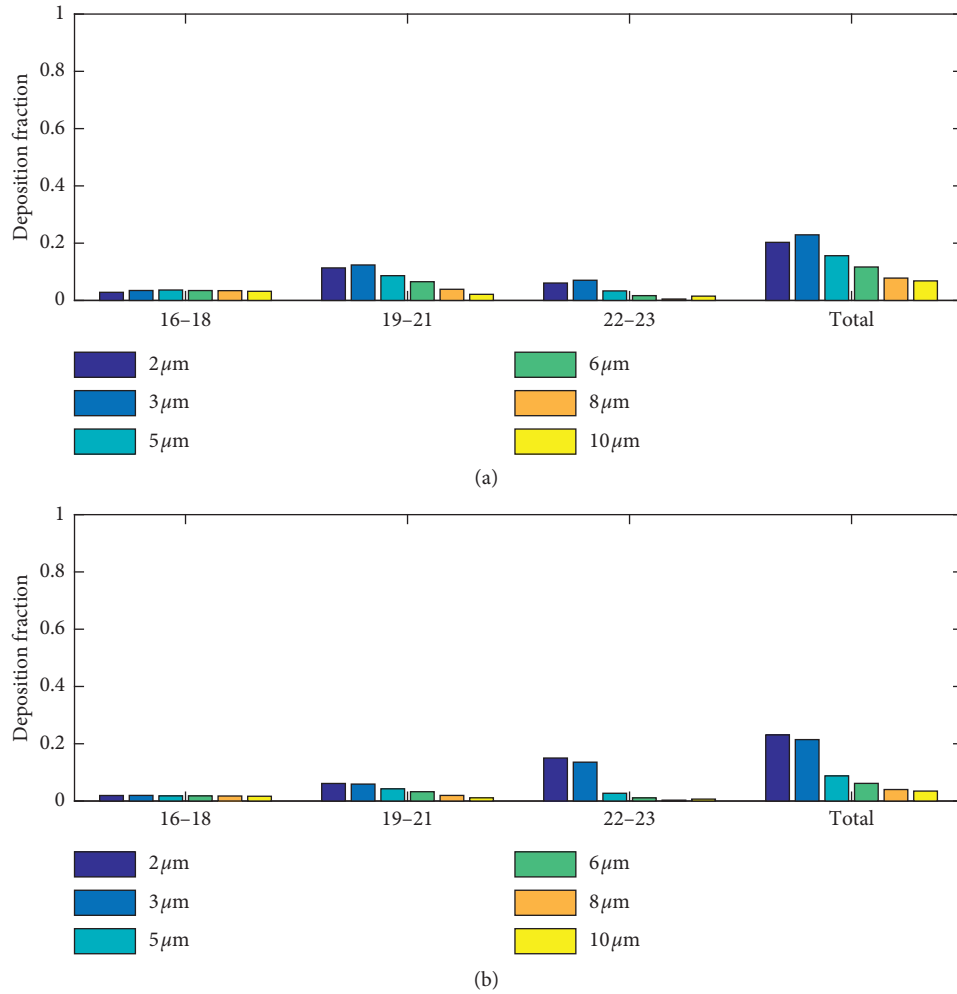


FIGURE 4: Particle deposition results for (a) TV 500 ml and (b) TV 1000 ml during exhalation phase.

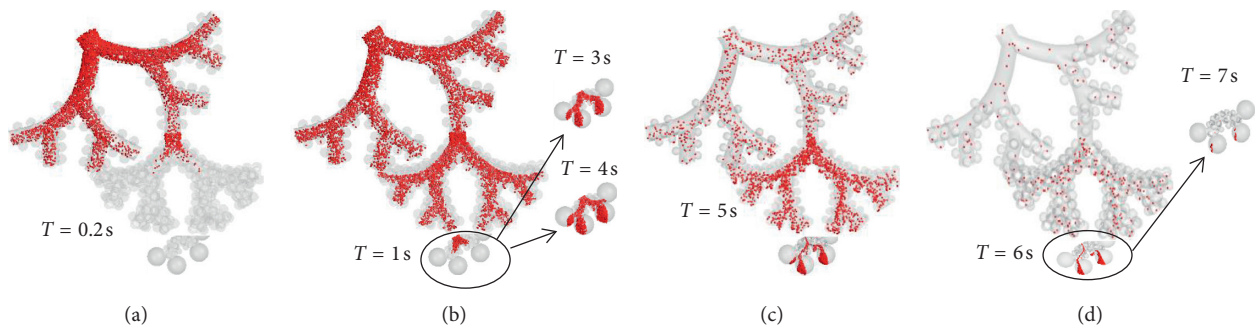


FIGURE 5: Position of the 3  $\mu\text{m}$  particles at selected time levels during an inhalation and exhalation phase with flow rate 15 LPM and tidal volume 1000 ml.

inhalation cycle was 3.75% of the total particles injected for 2  $\mu\text{m}$  and was less than 0.05% for other particle sizes. It is evident from the results that an increase in tidal volume and/or an increase in particle diameter will result in higher deposition in the acinar model.

Considering the deposition in the extra-thoracic and tracheobronchial region, particle deposition fraction in the alveolar region can be approximated from the model

predicted deposition using the relation  $DF = \phi(1 - \eta_E)(1 - \eta_F)\eta_A$ . Based on these reported in vivo measurements [55] for deposition fraction in the extra-thoracic region ( $\eta_E$ ), tracheobronchial region ( $\eta_F$ ) (mean experimental deposition values for extra-thoracic region ( $\eta_E$ ), tracheobronchial region ( $\eta_F$ ) are reported in [55]), the volume fraction of the air coming to rest in the alveolar region ( $\phi$ ), and the present model predicted deposition  $\eta_A$ , we

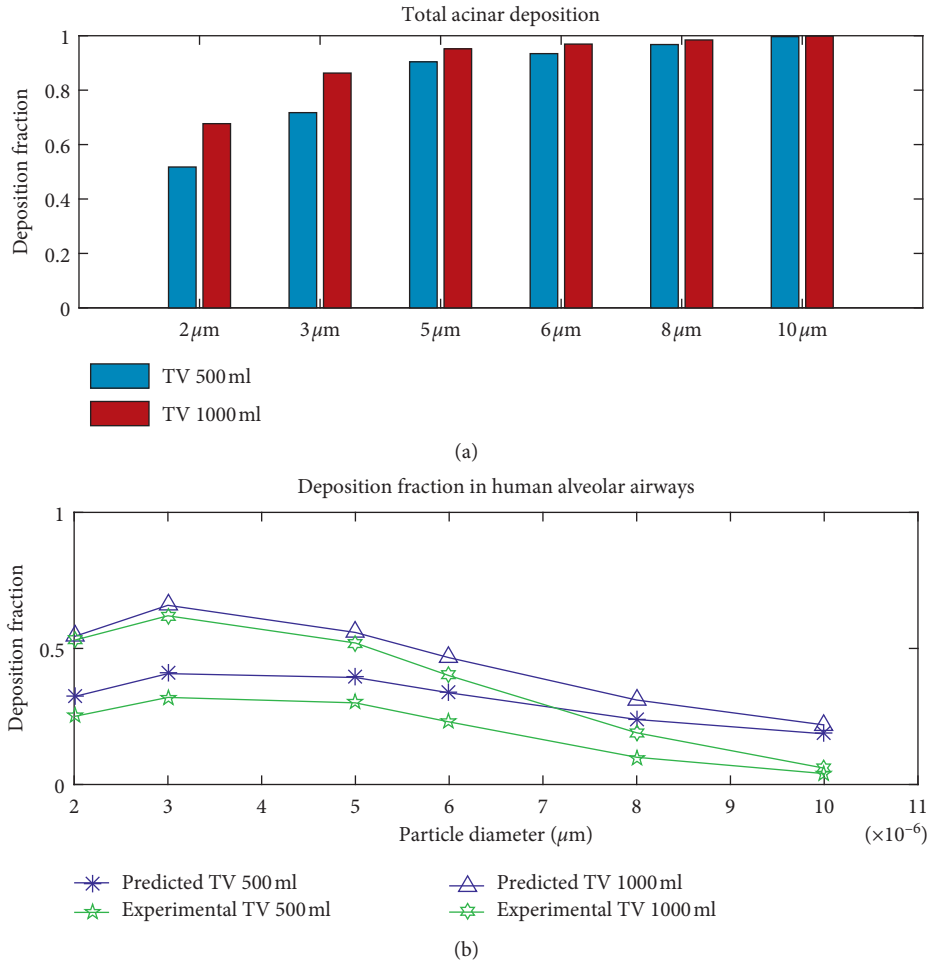


FIGURE 6: (a) Total acinar particle deposition results during a full breathing cycle (b) Comparison with in vivo measurements [55].

translated the model predicted deposition  $\eta_A$ , in the alveolar region into DF. This DF values were compared with the experimental measurements of alveolar deposition (Figure 6(b)) [55, 56]. The model predicted deposition results follow a similar trend and are in agreement with the in vivo alveolar deposition measurements [55]. Slight overprediction of alveolar deposition in the upper micron particle size range (around 10  $\mu\text{m}$ ) could be either because of the underestimation of in vivo particle deposition in the upper airways. Other in vivo measurements have indicated higher deposition and large subject variability for upper micron particle around 10  $\mu\text{m}$  in the extra-thoracic and tracheobronchial deposition [56]. Considering that significant intersubject variability exists between measured human alveolar deposition data [56], the present model provides good approximation of deposition in human acinar region.

The location of the deposited particles in the comprehensive alveolar model during inhalation with a tidal volume of 1000 ml is shown in Figure 7. The results indicate that the majority of the particles are deposited in the direction of the gravitational vector and the deposition is localized as the particles have predominantly entered into the alveolus with an opening in the direction of the gravitational vector. The deposition trends for the 3  $\mu\text{m}$  and 5  $\mu\text{m}$  particles are similar.

As mentioned, the full acinar model developed in this study is an anatomically inspired human alveolar model with eight generations of lung airways represented, using alveolated bifurcating tubular models, mimicking a full human acinar region. Among these, the first three generations are partially alveolated lung airways, and the rest are fully alveolated. In the present acinus model, the number of alveoli per triple bifurcation unit (TBU) is 84, 182, 25, and 4 in 16–18, 19–21, 22, and 23, respectively. One TBU was modeled per level with a mass flow rate boundary condition at the unresolved outlets. Specifically, in the acinar model there is one TBU representing generations 16–18, eight 19–21 TBUs, and sixty-four 22–23 DBUs. Hence, the total number of alveoli in this acinus model is 3396. In a symmetric lung model, there will be  $2^{15}$  similar acini, which would result in more than 111 million alveoli per lung in the present model. If the 17 individual alveoli in the 23<sup>rd</sup> generation, which was represented as a single spheroid is considered, there will be 7492 alveoli in total in the acinus model. For a symmetric lung model, there will be more than 245 million alveoli per lung. These digits are in close range with the recent estimations of the total number of alveoli in a human lung [1]. Recent numerical studies using multigenerational alveolar models [41] have indicated that

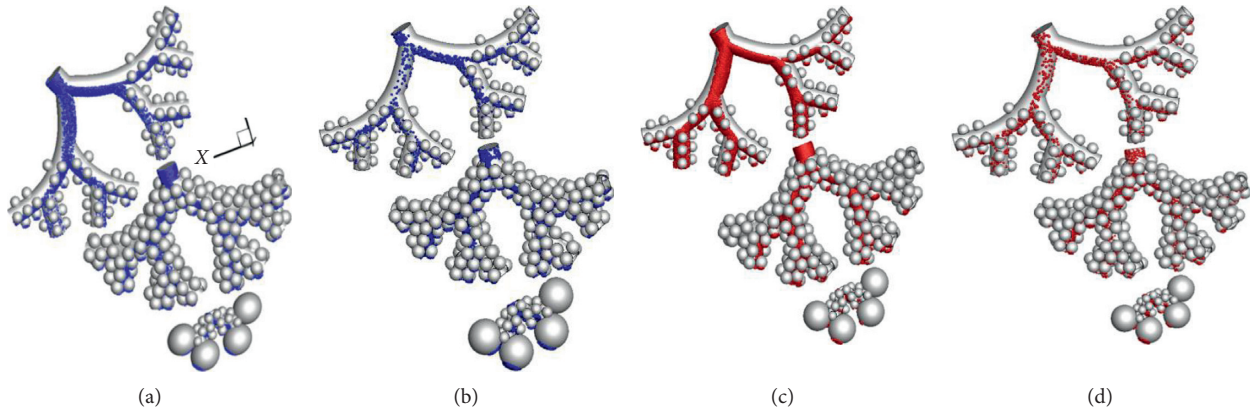


FIGURE 7: Location of the deposited particles ( $3\ \mu\text{m}$  and  $5\ \mu\text{m}$ ) in the full alveolar model during inhalation and exhalation phases with a tidal volume of 1000 ml. (a)  $3\ \mu\text{m}$  inhalation. (b)  $3\ \mu\text{m}$  exhalation. (c)  $5\ \mu\text{m}$  inhalation. (d)  $5\ \mu\text{m}$  exhalation.

a minimum number of fully alveolated airways (usually three) can predict realistic particle deposition results, i.e., adding additional generations had negligible impact on total acinar deposition. Therefore, the current model is reasonably accurate in representing a full acinar model and at the same time is computationally efficient. In this study, we used the ratio of alveolar flow to the airflow at the oral inlet, which is equal to the fractional alveolar volume in each generation. This approach makes it easy to incorporate the current acinar model into human whole-lung airway models, to simulate/predict the fate of inhaled toxic or therapeutic aerosols [48].

Previous multigenerational alveolar models have assumed homogeneous alveolar airway deformation without considering the variation in deformation rate with generation and in the number of alveoli per generation [19, 35, 41]. Model results from the present study have shown that the alveolar flow varies with airway generation and inhalation flow rate. The position of the alveolus determines the alveolus-wall deformation rate and the amount of convective mixing. The alveolar deformation rate in the current model depends on the mass flow rate through the TBUs and the alveolar volume fraction per TBU. Hence, the current model captures the variation in alveolar flow characteristics with airway generation number with respect to the number of alveoli per generation.

The particle deposition locations highlight the predominant deposition in the alveolar airway bifurcations. Although sedimentation is the dominant mechanism influencing particle deposition in the acinar region, the deposition trend indicates hotspots of particle deposition around the bifurcation ridges in the direction of gravitational orientation. While the gravitational orientation in the present study is fixed, recent investigations [41] showed that the total acinar deposition is independent of gravitational orientation; however, deposition hotspots were influenced by it [35].

The model results shows that light micron particles around  $2\ \mu\text{m}$  are not completely expelled during one inhalation cycle and after each inhalation cycle, the suspended particles may reach deeper axial locations, while heavier

particles ( $\geq 3\ \mu\text{m}$ ) tend to deposit or exit within one inhalation cycle. The number of particles remaining suspended in the airway model at the end of the first inhalation cycle was around 3.75% of the total particles injected for  $2\ \mu\text{m}$  and was less than 0.05% for other particle sizes. As expected, the number of particles that remain suspended in the domain reduced with increase in particle size and inhalation tidal volume [19, 35]. This indicates that once the smaller-micron-sized particles reach the alveolar region, it may not be completely expelled out within one inhalation cycle and it may remain there for longer duration providing higher particle residence time. These results are valuable insights for targeted delivery of therapeutic aerosols to distal lung regions.

#### 4. Conclusions

A comprehensive, physiologically inspired acinar model has been developed which can efficiently simulate the physiological breathing mechanism and can predict variations in local alveolar flow pattern and particle deposition. The simulation results show that the alveolar flow pattern depends on the location of the alveoli. Dominant recirculating flow structures were noticed inside proximal lung generation alveoli, while intensity of the recirculating flow decreases while the radial flow increases in the midalveolar lung generations. In the distal alveoli, the airflow is completely radial. The particle simulation results indicate that microsphere deposition depends on the inhalation conditions and particle size. The particle deposition rate in the alveolar region increases with higher inhalation tidal volume and particle diameter. When the tidal volume is increased, more particles are pulled into the distal lung airways and hence the deposition in these distal lung generations increases. Irrespective of the tidal volume, the particle deposition fraction in the proximal alveolar region (i.e., generations 16 to 18) is constant, and the number of particles deposited is higher in the midalveolar airways compared to other airway generations. Contrary to the deposition results during the inhalation phase, particle deposition during exhalation is higher when the tidal

volume is lower. This can be attributed to the large number of suspended particles depositing during the exhalation phase in the upper alveolar airways. The key mechanism for micron particle deposition in the alveolar lung airways is due to gravitational effects. However, the interplay between the breathing-induced wall motion and sedimentation significantly increases particle deposition.

## 5. Model Limitation and Future Work

The primary objectives were to develop a predictive modeling framework and provide computer simulation results for air-particle flow in a physiologically inspired whole acinar model. Presently, only one level of TBU is in-plane, i.e., it is rotated when connecting the next level. However, it has been noticed that the orientation of gravitational vector influences the deposition hot spots; hence, more detailed analyses may be required to study the effects of local airway orientation with respect to the gravitational vector on particle deposition. While relatively large nanoparticle transport and deposition can be accommodated with the present model, a separate analysis will focus on nanoparticles with  $d_p < 100$  nm as part of the whole-lung airway simulation project. There are many uncertainties regarding the alveolar and duct biomechanics, e.g., recent studies have pointed out that the alveolar deformation is anisotropic [26]. Hence, further analyses are required considering neck and duct anisotropic deformations. Additionally, simulations with different inhalation conditions considering subject variability in breathing profiles will be carried out in future.

The limitations of this study also include the assumption of symmetric alveolar airways as well as the shape and size of the alveoli. Even though human lung-cast and tissue studies have indicated that there exist variations in the alveolar size and topology [11, 12], recent investigations have shown that these variations in alveolar topology might not significantly influence distal alveolar particle transport [30]; however, it may be significant in the upper alveolar airways [17, 20]. Indeed, with appropriate modifications such variations in alveolar topology and size could be incorporated into the current acinar model. The structural changes of the alveoli are still under debate. To reach a unifying hypothesis, further investigations are required. Additionally, we will build on the current modeling framework to study the influence of the lobar volumes on acinar deposition, using scaled models representing different lung lobes. A separate analysis will also focus on the effects of lung pathological conditions, such as emphysema, on alveolar airflow dynamics and particle deposition.

## Data Availability

The data used to support the findings of this study are available from the corresponding author upon request.

## Conflicts of Interest

The authors report no conflicts of interest.

## Acknowledgments

The authors gratefully acknowledge the use of ANSYS, Inc. (Canonsburg, PA) software, based on the NCSU-ANSYS Professional Partnership.

## References

- [1] M. Ochs, J. R. Nyengaard, A. Jung et al., "The number of alveoli in the human lung," *American Journal of Respiratory and Critical Care Medicine*, vol. 169, no. 1, pp. 120–124, 2004.
- [2] K. L. Zeman and W. D. Bennett, "Growth of the small airways and alveoli from childhood to the adult lung measured by aerosol-derived airway morphometry," *Journal of Applied Physiology*, vol. 100, no. 3, pp. 965–971, 2006.
- [3] J. Sznitman, F. Heimsch, T. Heimsch, D. Rusch, and T. Rösgen, "Three-dimensional convective alveolar flow induced by rhythmic breathing motion of the pulmonary acinus," *Journal of Biomechanical Engineering*, vol. 129, no. 5, pp. 658–665, 2007.
- [4] J. M. Oakes, P. Hofemeier, I. E. Vignon-Clementel, and J. Sznitman, "Aerosols in healthy and emphysematous in silico pulmonary acinar rat models," *Journal of Biomechanics*, vol. 49, no. 11, pp. 2213–2220, 2016.
- [5] J. Sznitman, "Respiratory microflows in the pulmonary acinus," *Journal of Biomechanics*, vol. 46, no. 2, pp. 284–298, 2013.
- [6] A. V. Kolanjiyil and C. Kleinstreuer, "Nanoparticle mass transfer from lung airways to systemic regions—Part II: multi-compartmental modeling," *Journal of Biomechanical Engineering*, vol. 135, no. 12, article 121004, 2013.
- [7] C. Kleinstreuer, Y. Feng, and E. Childress, "Drug-targeting methodologies with applications: a review," *World Journal of Clinical Cases*, vol. 2, no. 12, pp. 742–756, 2014.
- [8] A. V. Kolanjiyil, C. Kleinstreuer, and R. T. Sadikot, "Computationally efficient analysis of particle transport and deposition in a human whole-lung-airway model. Part II: dry powder inhaler application," *Computers in Biology and Medicine*, vol. 84, pp. 247–253, 2016.
- [9] A. V. Kolanjiyil and C. Kleinstreuer, "Computationally efficient analysis of particle transport and deposition in a human whole-lung-airway model. Part I: theory and model validation," *Computers in Biology and Medicine*, vol. 79, pp. 193–204, 2016.
- [10] E. Weibel, *Morphometry of the Human Lung*, Academic Press, New York, NY, USA, 1963.
- [11] B. Haefeli-Bleuer and E. R. Weibel, "Morphometry of the human pulmonary acinus," *Anatomical Record*, vol. 220, no. 4, pp. 401–414, 1988.
- [12] J. E. Hansen and E. P. Ampaya, "Human air space shapes, sizes, areas, and volumes," *Journal of Applied Physiology*, vol. 38, no. 6, pp. 990–995, 1975.
- [13] E. M. Harding Jr. and R. J. Robinson, "Flow in a terminal alveolar sac model with expanding walls using computational fluid dynamics," *Inhalation Toxicology*, vol. 22, no. 8, pp. 669–678, 2010.
- [14] J. Sznitman, R. Sutter, D. Altorfer, M. Stampanoni, T. Rösgen, and J. C. Schittny, "Visualization of respiratory flows from 3D reconstructed alveolar airspaces using X-ray tomographic microscopy," *Journal of Visualization*, vol. 13, no. 4, pp. 337–345, 2010.
- [15] A. Tsuda, N. Filipovic, D. Haberthür et al., "Finite element 3D reconstruction of the pulmonary acinus imaged by

- synchrotron X-ray tomography,” *Journal of Applied Physiology*, vol. 105, no. 3, pp. 964–976, 2008.
- [16] Y. C. Fung, “A model of the lung structure and its validation,” *Journal of Applied Physiology*, vol. 64, no. 5, pp. 2132–2141, 1988.
- [17] P. Hofemeier and J. Sznitman, “Role of alveolar topology on acinar flows and convective mixing,” *Journal of Biomechanical Engineering*, vol. 136, no. 6, article 061007, 2014.
- [18] P. W. Longest, G. Tian, N. Khajeh-Hosseini-Dalasm, and M. Hindle, “Validating whole-airway CFD predictions of DPI aerosol deposition at multiple flow rates,” *Journal of Aerosol Medicine and Pulmonary Drug Delivery*, vol. 29, no. 6, pp. 461–481, 2016.
- [19] J. Sznitman, T. Heimsch, J. H. Wildhaber, A. Tsuda, and T. Rosgen, “Respiratory flow phenomena and gravitational deposition in a three-dimensional space-filling model of the pulmonary acinar tree,” *Journal of Biomechanical Engineering*, vol. 131, no. 3, article 031010, 2009.
- [20] H. Kumar, M. H. Tawhai, E. A. Hoffman, and C.-L. Lin, “The effects of geometry on airflow in the acinar region of the human lung,” *Journal of Biomechanics*, vol. 42, no. 11, pp. 1635–1642, 2009.
- [21] J. Heyder, J. D. Blanchard, H. A. Feldman, and J. D. Brain, “Convective mixing in human respiratory tract: estimates with aerosol boli,” *Journal of Applied Physiology*, vol. 64, no. 3, pp. 1273–1278, 1988.
- [22] A. Tsuda, R. A. Rogers, P. E. Hydon, and J. P. Butler, “Chaotic mixing deep in the lung,” *Proceedings of the National Academy of Sciences*, vol. 99, no. 15, pp. 10173–10178, 2002.
- [23] J. M. Oakes, S. Day, S. J. Weinstein, and R. J. Robinson, “Flow field analysis in expanding healthy and emphysematous alveolar models using particle image velocimetry,” *Journal of Biomechanical Engineering*, vol. 132, no. 2, article 021008, 2010.
- [24] E. J. Berg, J. L. Weisman, M. J. Oldham, and R. J. Robinson, “Flow field analysis in a compliant acinus replica model using particle image velocimetry (PIV),” *Journal of Biomechanics*, vol. 43, no. 6, pp. 1039–1047, 2010.
- [25] G. C. Smaldone, W. Mitzner, and H. Itoh, “Role of alveolar recruitment in lung inflation: influence on pressure-volume hysteresis,” *Journal of Applied Physiology*, vol. 55, no. 4, pp. 1321–1332, 1983.
- [26] E. Roan and C. M. Waters, “What do we know about mechanical strain in lung alveoli?,” *American Journal of Physiology-Lung Cellular and Molecular Physiology*, vol. 301, no. 5, pp. L625–L635, 2011.
- [27] J. Gil, H. Bachofen, P. Gehr, and E. R. Weibel, “Alveolar volume-surface area relation in air- and saline-filled lungs fixed by vascular perfusion,” *Journal of Applied Physiology*, vol. 47, no. 5, pp. 990–1001, 1979.
- [28] G. C. Smaldone and W. Mitzner, “Viewpoint: unresolved mysteries,” *Journal of Applied Physiology*, vol. 113, no. 12, pp. 1945–1947, 2012.
- [29] J. B. Forrest, “The effect of changes in lung volume on the size and shape of alveoli,” *Journal of Physiology*, vol. 210, no. 3, pp. 533–547, 1970.
- [30] A. Tsuda, F. S. Henry, and J. P. Butler, “Particle transport and deposition: basic physics of particle kinetics,” *Comprehensive Physiology*, vol. 3, no. 4, pp. 1437–1471, 2013.
- [31] F. S. Henry, S. Haber, D. Haberthor et al., “The simultaneous role of an alveolus as flow mixer and flow feeder for the deposition of inhaled submicron particles,” *Journal of Biomechanical Engineering*, vol. 134, no. 12, article 121001, 2012.
- [32] S. Haber, D. Yitzhak, and A. Tsuda, “Gravitational deposition in a rhythmically expanding and contracting alveolus,” *Journal of Applied Physiology*, vol. 95, no. 2, pp. 657–671, 2003.
- [33] P. Hofemeier and J. Sznitman, “Revisiting pulmonary acinar particle transport: convection, sedimentation, diffusion and their interplay,” *Journal of Applied Physiology*, vol. 118, no. 11, pp. 1375–1385, 2015.
- [34] K. E. Pinkerton, F. H. Y. Green, C. Saiki et al., “Distribution of particulate matter and tissue remodeling in the human lung,” *Environmental Health Perspectives*, vol. 108, no. 11, p. 1063, 2000.
- [35] B. Ma and C. Darquenne, “Aerosol deposition characteristics in distal acinar airways under cyclic breathing conditions,” *Journal of Applied Physiology*, vol. 110, no. 5, pp. 1271–1282, 2011.
- [36] C. Darquenne, “Heterogeneity of aerosol deposition in a two-dimensional model of human alveolated ducts,” *Journal of Aerosol Science*, vol. 33, no. 9, pp. 1261–1278, 2002.
- [37] L. Harrington, G. Kim Prisk, and C. Darquenne, “Importance of the bifurcation zone and branch orientation in simulated aerosol deposition in the alveolar zone of the human lung,” *Journal of Aerosol Science*, vol. 37, no. 1, pp. 37–62, 2006.
- [38] C. Darquenne, L. Harrington, and G. K. Prisk, “Alveolar duct expansion greatly enhances aerosol deposition: a three-dimensional computational fluid dynamics study,” *Philosophical Transactions of the Royal Society A: Mathematical, Physical and Engineering Sciences*, vol. 367, no. 1896, pp. 2333–2346, 2009.
- [39] P. Hofemeier and J. Sznitman, “The role of anisotropic expansion for pulmonary acinar aerosol deposition,” *Journal of Biomechanics*, vol. 49, no. 14, pp. 3543–3548, 2016.
- [40] H. Kumar, M. H. Tawhai, E. A. Hoffman, and C. Lin, “Steady streaming: a key mixing mechanism in low-Reynolds-number acinar flows,” *Physics of Fluids*, vol. 23, no. 4, article 041902, 2011.
- [41] N. Khajeh-Hosseini-Dalasm and P. W. Longest, “Deposition of particles in the alveolar airways: inhalation and breath-hold with pharmaceutical aerosols,” *Journal of Aerosol Science*, vol. 79, pp. 15–30, 2015.
- [42] R. Fishler, M. K. Mulligan, and J. Sznitman, “Acinus-on-a-chip: a microfluidic platform for pulmonary acinar flows,” *Journal of Biomechanics*, vol. 46, no. 16, pp. 2817–2823, 2013.
- [43] R. Fishler, P. Hofemeier, Y. Etzion, Y. Dubowski, and J. Sznitman, “Particle dynamics and deposition in true-scale pulmonary acinar models,” *Scientific Reports*, vol. 5, no. 1, 2015.
- [44] A. V. Kolanjiyil, *Whole-lung airflow and particle transport/deposition modeling and simulation*, Ph.D. dissertation, North Carolina State University, Raleigh, NC, USA, 2016.
- [45] E. R. Weibel, “What makes a good lung?,” *Swiss Medical Weekly*, vol. 139, no. 27–28, pp. 375–386, 2009.
- [46] E. J. Berg and R. J. Robinson, “Stereoscopic particle image velocimetry analysis of healthy and emphysemic alveolar sac models,” *Journal of Biomechanical Engineering*, vol. 133, no. 6, article 061004, 2011.
- [47] K. Talaat and J. Xi, “Computational modeling of aerosol transport, dispersion, and deposition in rhythmically expanding and contracting terminal alveoli,” *Journal of Aerosol Science*, vol. 112, pp. 19–33, 2017.
- [48] A. V. Kolanjiyil and C. Kleinstreuer, “Computational analysis of aerosol-dynamics in a human whole-lung airway model,” *Journal of Aerosol Science*, vol. 114, pp. 301–316, 2017.
- [49] A. V. Kolanjiyil and C. Kleinstreuer, “Nanoparticle mass transfer from lung airways to systemic regions-Part I:

- whole-lung aerosol dynamics,” *Journal of Biomechanical Engineering*, vol. 135, no. 12, article 121003, 2013.
- [50] P. G. Koullapis, P. Hofemeier, J. Sznitman, and S. C. Kassinos, “An efficient computational fluid-particle dynamics method to predict deposition in a simplified approximation of the deep lung,” *European Journal of Pharmaceutical Sciences*, vol. 113, pp. 132–144, 2018.
- [51] C. B. Daniels and S. Orgeig, “Pulmonary surfactant: the key to the evolution of air breathing,” *Physiology*, vol. 18, no. 4, pp. 151–157, 2003.
- [52] C. E. Perlman and J. Bhattacharya, “Alveolar expansion imaged by optical sectioning microscopy,” *Journal of Applied Physiology*, vol. 103, no. 3, pp. 1037–1044, 2007.
- [53] C. E. Perlman, D. J. Lederer, and J. Bhattacharya, “Micro-mechanics of alveolar edema,” *American Journal of Respiratory Cell and Molecular Biology*, vol. 44, no. 1, pp. 34–39, 2011.
- [54] Y. Feng, *Non-spherical particle dynamics analysis with applications to inhaled aerosol transport and deposition in human upper airway models*, Ph.D. dissertation, North Carolina State University, Raleigh, NC, USA, 2013.
- [55] J. Heyder, J. Gebhart, G. Rudolf, C. F. Schiller, and W. Stahlhofen, “Deposition of particles in the human respiratory tract in the size range 0.005–15  $\mu\text{m}$ ,” *Journal of Aerosol Science*, vol. 17, no. 5, pp. 811–825, 1986.
- [56] W. Stahlhofen, G. Rudolf, and A. C. James, “Intercomparison of experimental regional aerosol deposition data,” *Journal of Aerosol Medicine*, vol. 2, no. 3, pp. 285–308, 1989.

## Research Article

# Airflow and Particle Deposition in Acinar Models with Interalveolar Septal Walls and Different Alveolar Numbers

Jinxiang Xi <sup>1,2,3</sup>, Mohamed Talaat,<sup>2</sup> Hesham Tanbour,<sup>3</sup> and Khaled Talaat<sup>4</sup>

<sup>1</sup>Department of Biomedical Engineering, California Baptist University, Riverside, CA 92504, USA

<sup>2</sup>Department of Aerospace, Industrial, and Mechanical Engineering, California Baptist University, Riverside, CA 92504, USA

<sup>3</sup>School of Engineering and Technology, Central Michigan University, Mt. Pleasant, MI 48858, USA

<sup>4</sup>Department of Nuclear Engineering, The University of New Mexico, Albuquerque, NM 87131, USA

Correspondence should be addressed to Jinxiang Xi; [xilj@cmich.edu](mailto:xilj@cmich.edu)

Received 31 May 2018; Accepted 27 August 2018; Published 25 September 2018

Academic Editor: Yu Feng

Copyright © 2018 Jinxiang Xi et al. This is an open access article distributed under the Creative Commons Attribution License, which permits unrestricted use, distribution, and reproduction in any medium, provided the original work is properly cited.

Unique features exist in acinar units such as multiple alveoli, interalveolar septal walls, and pores of Kohn. However, the effects of such features on airflow and particle deposition remain not well quantified due to their structural complexity. This study aims to numerically investigate particle dynamics in acinar models with interalveolar septal walls and pores of Kohn. A simplified 4-alveoli model with well-defined geometries and a physiologically realistic 45-alveoli model was developed. A well-validated Lagrangian tracking model was used to simulate particle trajectories in the acinar models with rhythmically expanding and contracting wall motions. Both spatial and temporal dosimetries in the acinar models were analyzed. Results show that collateral ventilation exists among alveoli due to pressure imbalance. The size of interalveolar septal aperture significantly alters the spatial deposition pattern, while it has an insignificant effect on the total deposition rate. Surprisingly, the deposition rate in the 45-alveoli model is lower than that in the 4-alveoli model, indicating a stronger particle dispersion in more complex models. The gravity orientation angle has a decreasing effect on acinar deposition rates with an increasing number of alveoli retained in the model; such an effect is nearly negligible in the 45-alveoli model. Breath-holding increased particle deposition in the acinar region, which was most significant in the alveoli proximal to the duct. Increasing inhalation depth only slightly increases the fraction of deposited particles over particles entering the alveolar model but has a large influence on dispensing particles to the peripheral alveoli. Results of this study indicate that an empirical correlation for acinar deposition can be developed based on alveolar models with reduced complexity; however, what level of geometry complexity would be sufficient is yet to be determined.

## 1. Introduction

Alveolar sacs are the ends of the respiratory tree and the smallest respiration units. The alveoli have a complex framework and are supported by interalveolar septa [1]. Pores of Kohn are apertures in the alveolar septum, which are circular or oval in shape and allow communications among adjacent alveoli [2]. This collateral ventilation helps equalize pressures across alveoli and plays an important role in preventing lung collapse (i.e., atelectasis) [3] and promoting alveolar recruitment [4]. In the case of emphysema, the number and size of pores increase in early stages [5–7]. In later stages, destruction of septa and even framework breakdown have been observed, leading to a decrease of the

elasticity and an increase of the sac airspace [8]. Aging can also cause the breakdown of interalveolar septa and increase the number and sizes of alveolar pores of Kohn, thereby decreasing the collateral flow resistance among alveoli [9, 10]. Understanding the effects of alveolar septum and pore on alveolar airflow and particle dynamics is fundamental for understanding the pathology of pulmonary diseases, improving ventilator management, and devising more effective treatment strategies.

Due to the extremely large number of alveoli in the lungs (~480 million), it is impossible to construct a complete model of the acinar airspace. Even to construct a single acinar unit will be a formidable task, considering that each acinar unit consists of more than 10,000 alveoli [1]. As

a result, alveolar models with varying realism and complexities had been proposed to understand particle dynamics inside the alveoli. These included alveolus models comprising a single hemisphere attached to a duct (i.e., respiratory bronchiole) [11–16], an alveolar duct with multiple alveoli (i.e., alveolated duct) [17, 18], and space-filling-based models with honeycomb or polygonal structures (i.e., terminal alveolar sacs) [19–23]. Based on *in vivo* microscopy observations, Kitaoka et al. [19] proposed that the alveolar mouth closes at minimum volume and gradually opens during inhalation. Based on a series of acinar models, Khajeh-Hosseini-Dalasm and Longest [22] investigated the effect of geometry complexity on acinar deposition. It was observed that when the acinar models consisted of more than three alveolar duct generations, the total acinar deposition rates were similar among models and were not affected by gravity orientation either. However, the effects of pores of Kohn on acinar deposition remain unclear and underinvestigated. More recently, Hofemeier et al. [23] proposed an algorithm to construct generic heterogeneous acinar models ranging from 372 to 2361 alveoli. They observed that variance in acinar heterogeneity played a minor role in determining alveolar deposition while the deposition rate increased for deeper inhalations.

General findings from previous studies are summarized as follows: classical alveolar deposition correlations are less accurate and need to be improved; wall motion is essential in determining the alveolar flows and aerosol dynamics; geometry complexity and realism strongly affect the predictions of alveolar deposition. Classical alveolar deposition correlations were typically based on particle sedimentation in steady tubular flows [24, 25] and used analytical approximations of particle deposition mechanisms [26]. Such corrections neglected a number of factors that are crucial in accurately determining particle transport and deposition, such as tidal breathing, wall motion, and geometry details. Kojic and Tsuda [27] showed that using steady-flow solutions to approximate oscillatory flows underestimated local particle deposition densities, and this error increased quickly for increasing oscillation frequencies. When the oscillation period became equivalent to the characteristic time for gravitational sedimentation, particle deposition would no longer be approximated by the classical solution based on steady flows as proposed in [28]. Alveolar wall motion has been demonstrated to be essential to match single-path-transport model predictions with *in vivo* alveolar deposition data [29, 30]. It is noted that wall kinematics, such as symmetric vs. anisotropic oscillations, played a negligible role in the alveolar deposition [15, 31]. On the contrary, the type and complexity of the acinar airway yield unique features of airflow and particle transport patterns. Kumar et al. [20] simulated airflow in acinar models with honeycomb structures and reported recirculation inside the alveoli induced by oscillatory wall motions. Talaat and Xi [15] numerically investigated aerosol deposition in a single terminal alveolus with rhythmical oscillations and found significantly different particle dynamics in comparison to that in alveolated ducts or respiratory bronchioles [12, 21, 32, 33]. Particles move back and forth driven by the oscillating walls

of the terminal alveolus and form multifolding trajectories [15]; by contrast, particles in an alveolated duct or respiratory bronchiole geometry remain suspended in the alveolus for several breathing cycles, rotating clockwise during exhalation and counterclockwise during inhalation [12, 21].

Several controversial observations have been reported regarding the influences from gravity orientation angle, airway realism, and breathing depth. Haber et al. [12] and Sznitman et al. [21] reported that particle deposition efficiencies are strongly related to the gravity orientation in both alveolated ducts and space-filling geometries. By contrast, Khajeh-Hosseini-Dalasm and Longest [22] suggested that total acinar deposition rates were insensitive to the gravity orientation when the geometry had more than three alveolar duct generations. While some studies [18, 34, 35] found that the geometry complexity significantly affected acinar aerosol deposition, Hofemeier et al. [23] recently observed that heterogeneity in acinar geometry had little effect on alveolar deposition. Similarly, while Hofemeier et al. [23] reported that the acinar deposition rate increased for deeper inhalations, Talaat and Xi [15] reported that the deposition was relatively insensitive to the breathing depth in single terminal alveolar models.

Unique features exist in the acinar airspace. Structurally, there are septal walls and pores of Kohn between neighboring alveoli, which are expected to strongly affect airflow and particle deposition, but whose influences have rarely been studied. Dynamically, the contribution of particle-wall interception to deposition can be important due to the geometrical complexity. But its importance relative to other deposition mechanisms, such as oscillatory convection, gravitational sedimentation, and particle dispersion, is unclear. Moreover, interalveolar septa and pores of Kohn can change in shape and size due to diseases or aging. As a result of these complexities, most space-filling-based honeycomb or polyhedral models to date have neglected the interalveolar septa and pores.

The objective of this study is to investigate the effects of acinar geometrical details, such as the interalveolar septum and pore size, on acinus airflow and particle dynamics in both a simplified 4-alveoli model and a 45-alveoli model. There are four specific aims in this study: (1) to develop acinar models with different number of alveoli and with septa and pores of different sizes, (2) to characterize airflows and particle motions in these acinar geometries, (3) to quantify the effect of pore size on surface doses both temporally and spatially, and (4) to evaluate the acinar deposition in simplified and complex models under the influence of the following factors: particle size, geometrical complexity, gravity orientation angle, and inhalation depth.

## 2. Methods

**2.1. Study Design.** Pulmonary alveoli are composed of a myriad of alveolar sacs arranged in a fractal manner. To study particle deposition in these regions, we started with a simplified four-sac alveolar model, with septal walls and pores of Kohn between adjacent sacs. Due to its well-defined

shape and dimension, this model allowed controlled testing of influential parameters such as particle diameter, breathing conditions, and pore sizes. As a result, a comprehensive understanding of deposition mechanisms in alveolar sacs can be obtained. By doing so, airflow and particle dynamics in a control case with rhythmic wall motions were examined; the resulting particle deposition was characterized both temporally (dynamic deposition growth) and spatially (in each alveolus). Six controlled tests were then conducted. To study the effects of rhythmic wall motions, Test 1 compared particle deposition in alveolar models with dynamic and rigid walls. For the model with rigid walls, the flow was stagnant (i.e., zero velocity), and particles moved due to gravity. Test 2 investigated the effect of particle size on alveolar deposition, which was  $0.5\ \mu\text{m}$ ,  $1\ \mu\text{m}$ ,  $2\ \mu\text{m}$ , and  $3\ \mu\text{m}$ . Test 3 investigated alveolar deposition under four gravity orientation angles ( $0^\circ$ ,  $45^\circ$ ,  $90^\circ$ , and  $135^\circ$  from the gravity). The effects of breath-holding and respiration depth were studied in Tests 4 and 5, respectively. The breath holding durations included 0.5, 1, 2, 3, and 4 seconds following the inhalation. The respiration depths included 1, 2, 3, and 4 times of the standard tidal volumes, which is 23.3% of the functional residual capacity (FRC). The last test (Test 6) studied the effects of pore sizes on particle deposition that included three different pore sizes and one model without the septal wall.

A more complex and physiologically realistic model was then developed that contained 45 alveolar sacs. Airflow and particle deposition in this model were compared to the simplified 4-alveoli (or 4-sac) model to determine the feasibility of using simplified alveolar models for inhalation dosimetry predictions and to evaluate the impact from gravitational orientation and inhalation depth. Model development, fluid-particle tracking algorithms, and numerical methods are detailed below.

**2.2. Computational Acinar Model and Kinematics.** To model an acinar cluster, four alveoli were retained in the simplified model. Individual alveolus was approximated using a  $0.3\ \text{mm}$  diameter sphere. The alveolar cluster was joined to a duct with a length of  $0.2\ \text{mm}$  and a diameter of  $0.1\ \text{mm}$ . The left panel of Figure 1(a) shows the air-filled geometry of the above duct-alveoli model, while the middle panel of Figure 1(a) shows the cut-open view of the hollow duct-alveoli model. There were openings (i.e., pores of Kohn) connecting any two neighboring alveoli, and thus totally five pores existed in this model geometry (Figure 1(a), middle panel). To facilitate later reference to the four alveolar sacs, the upper alveolus was termed as Sac 1, the lower alveolus as Sac 4, and the left and right alveoli as Sac 2 and Sac 3, respectively (Figure 1(a), left panel).

The wall kinematics of the acinar model followed the anisotropic motion of the chest [36, 37], which reported a smaller expansion in the arm-arm ( $z$ ) direction than the head-foot ( $x$ ) and back-front ( $y$ ) directions (i.e.,  $z:y:x = 0.375:1:1$ ). Under normal breathing conditions, the volume expansion was assumed to be the standard tidal volume, that is,  $V_T/\text{FRC} = 0.233$ , where  $V_T$  represents the

standard tidal volume [38]. A user-defined function (UDF) was written that specified the oscillatory wall motions (right panel of Figure 1(a)). More details of the UDF can be found in Talaat and Xi [15].

To investigate the effects of pore sizes on alveolar deposition, three geometrically similar models with different pore sizes were developed, that is,  $40\ \mu\text{m}$ ,  $100\ \mu\text{m}$ , and  $160\ \mu\text{m}$ , as shown in Figures 1(a), 1(b), and 1(c), respectively. For comparison purposes, an alveolar model with no septal wall was also developed (Figure 1(d)).

To investigate the model complexity effects, the second model consisted of 45 alveoli. Similar to the 4-alveoli model, septal walls existed between contiguous alveoli and pores of Kohn existed in the septal walls (Figure 1(e)). Even though spheres were initially used to approximate the alveoli, they naturally evolved into polygonal shapes when multiple spheres intersected each other (Figure 1(e)). The airway volume is  $4.32 \times 10^{-11}\ \text{m}^3$  for the 4-alveoli model and  $4.20 \times 10^{-10}\ \text{m}^3$  for the 45-alveoli model in comparison to  $1.48 \times 10^{-11}\ \text{m}^3$  for the single alveolus model in Talaat and Xi [15].

**2.3. Airflow and Particle Transport Models.** Particles ranging from  $0.5$  to  $3\ \mu\text{m}$  in diameter were investigated because smaller submicron particles deposited in the pulmonary region with different mechanisms (i.e., diffusion), and larger micrometer particles were captured by the upper respiratory tract and could not reach the pulmonary acinus. For each numerical test, multiple (3–24) respiration cycles were modeled, with the first cycle to create the unsteady flow field. An amount of 10,000 particles was inhaled at  $0.20\ \text{s}$  of the second cycle to simulate the inhalation of a bolus of pharmaceutical particles and was tracked until all particles deposited or exited the geometry with the expiratory flow.

The airflow was isothermal and incompressible in this study. The flow regime is laminar because the Reynolds number is much smaller than one even during peak inhalations [39]. Therefore, the laminar flow model was used to solve the airflow field. A well-tested direct Lagrangian algorithm was used to track particle motions [40, 41]. This algorithm, enhanced by the near-wall treatment algorithm [42], has been shown in our previous studies to agree with *in vitro* deposition results in human upper airways for both nanoparticles [43] and micrometer particles [44, 45].

**2.4. Numerical Methods.** ANSYS Fluent (Canonsburg, PA) with dynamic mesh and discrete phase models was used to simulate the transient airflow and particle deposition. User-defined Fortran and C modules were used to specify alveolar wall kinematics and calculate temporal and spatial surface deposition rates [46, 47]. ANSYS ICEM CFD (Ansys, Inc) was utilized for computational mesh generation. One-way coupling from the airflow to particles was assumed. A grid sensitivity analysis was conducted by testing a range of mesh densities, and grid independent result was considered to be achieved when the difference in total particle deposition was less than 1%. The final mesh was chosen to be 1.2 million cells for the 4-alveoli model and 6.0 million for the 45-alveoli model.

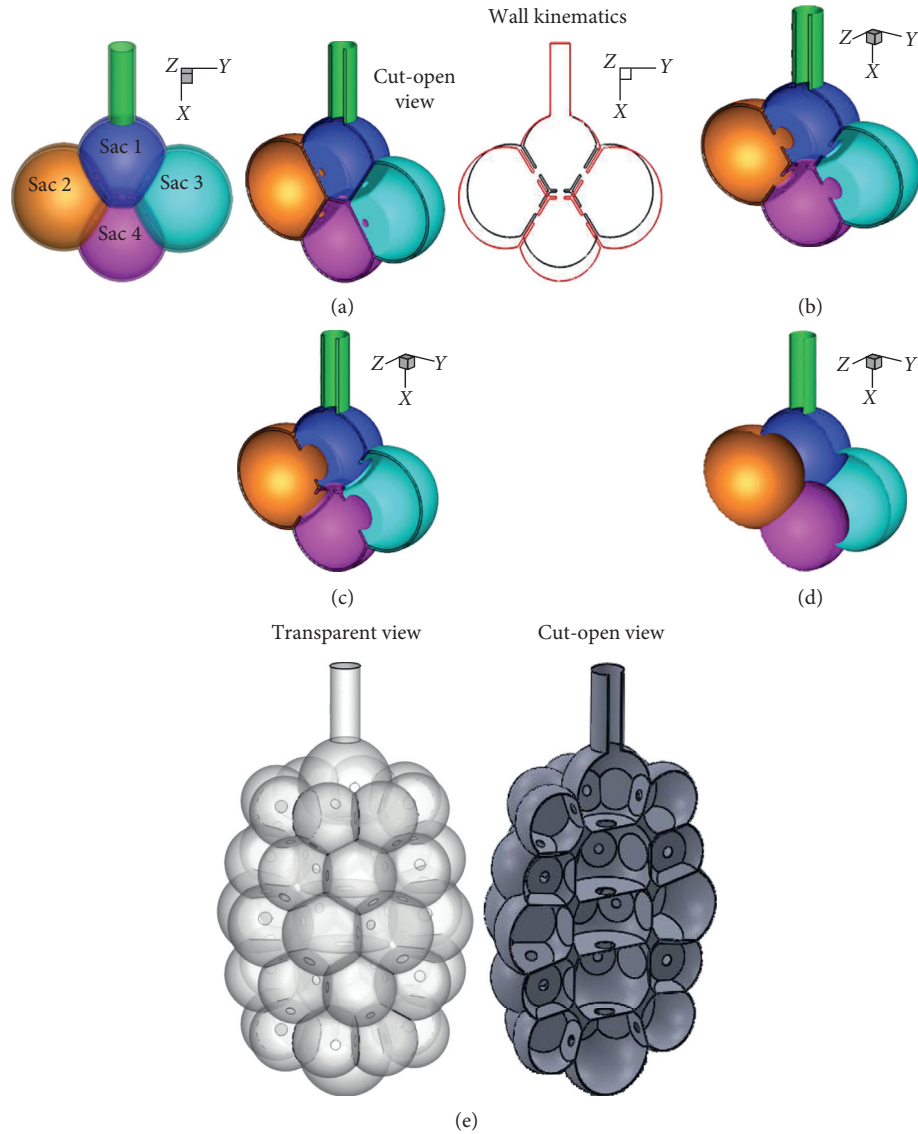


FIGURE 1: Simplified and complex multiple-alveoli models with septa and pores: (a) simplified 4-alveoli (or 4-sac) model with pores (septal apertures) of  $40\ \mu\text{m}$  in diameter; (b) 4-alveoli model with  $100\ \mu\text{m}$  pores; (c) 4-alveoli model with  $160\ \mu\text{m}$  pores; (d) 4-alveoli model with no spectrum; and (e) 45-alveoli model with  $40\ \mu\text{m}$  pores.

### 3. Results

**3.1. Airflow Field and Particle Motion.** Instantaneous airflow fields at the middle of inhalation and exhalation cycles are shown in Figure 2 in the 4-alveoli model with different pore sizes. Under the normal tidal breathing condition ( $23.3\%$  FRC, or  $1\ V_T$ ), the peak velocity at the inlet is around  $1\ \text{mm/s}$ . In the model with a pore size of  $40\ \mu\text{m}$  ((A) in Figure 2), Venturi effect at the pores was observed, which increased the penetration depth of particles into the peripheral alveoli. This effect, however, was absent when the pore sizes were large ((B) in Figure 2) or when the septal wall was missing ((C) in Figure 2). Overall symmetric flow patterns were noted for all of the three models considered (at their peak inhalation and exhalation speeds herein). Interesting discrepancies were also discerned among the three

models. In (A) in Figure 2, streamlines flowed from the lower alveolus to the two lateral alveoli during inhalation and reversed their directions during exhalation. By contrast, streamlines in (B) in Figure 2 flowed from the two lateral alveoli to the lower one during inhalation and vice versa. These collateral ventilations were presumably associated with the pressure imbalance between neighboring alveoli.

Particle dynamics in the oscillating alveoli are visualized in Figures 3 and 4. Figure 3 shows the snapshots of particle positions during the first cycle at ten different instants. Particles were inhaled into the geometry approximately at the beginning of inhalation. Depending on local velocities, the swarm of particles exhibits a parabolic pattern in the alveolar duct ( $T = 0.25\ \text{s}$ ) and a spherical shape after entering the top alveolus (i.e., Sac 1,  $T = 0.50\ \text{s}$ ). Around the middle of inhalation cycle ( $T = 0.75$  and  $1.0\ \text{s}$ ), particles start entering

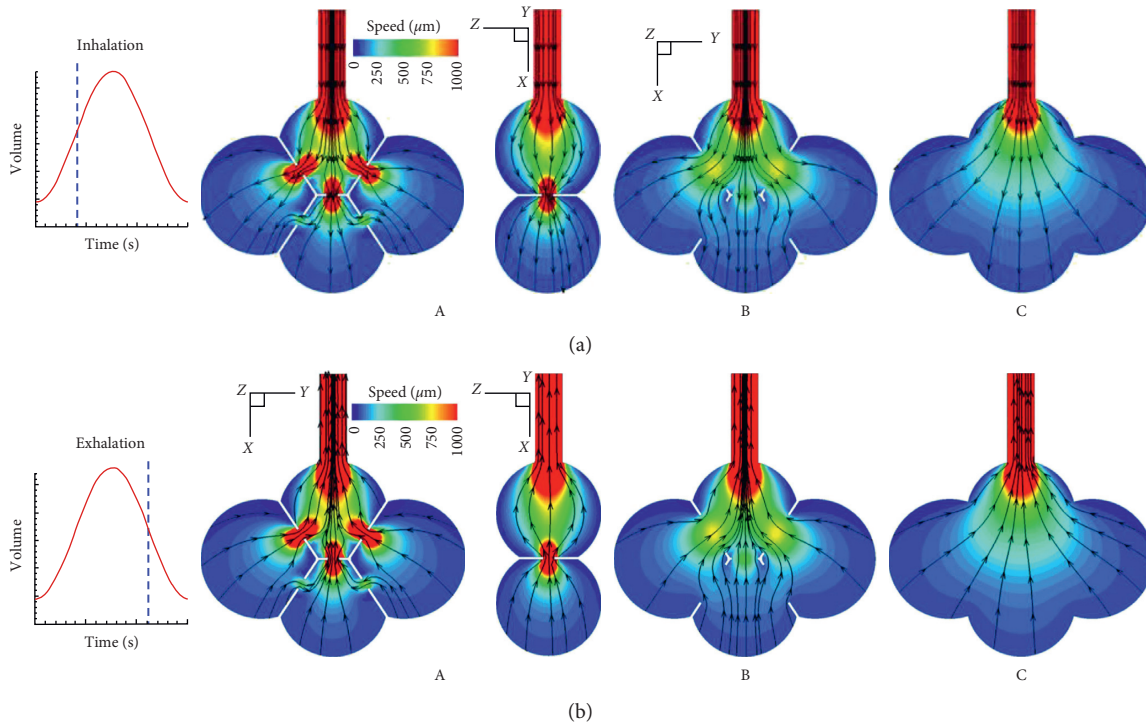


FIGURE 2: Airflow contour and stream traces in the 4-alveoli models with a pore size of (A)  $40 \mu\text{m}$ , (B)  $160 \mu\text{m}$ , and (C) no septal wall during (a) inhalation and (b) exhalation.

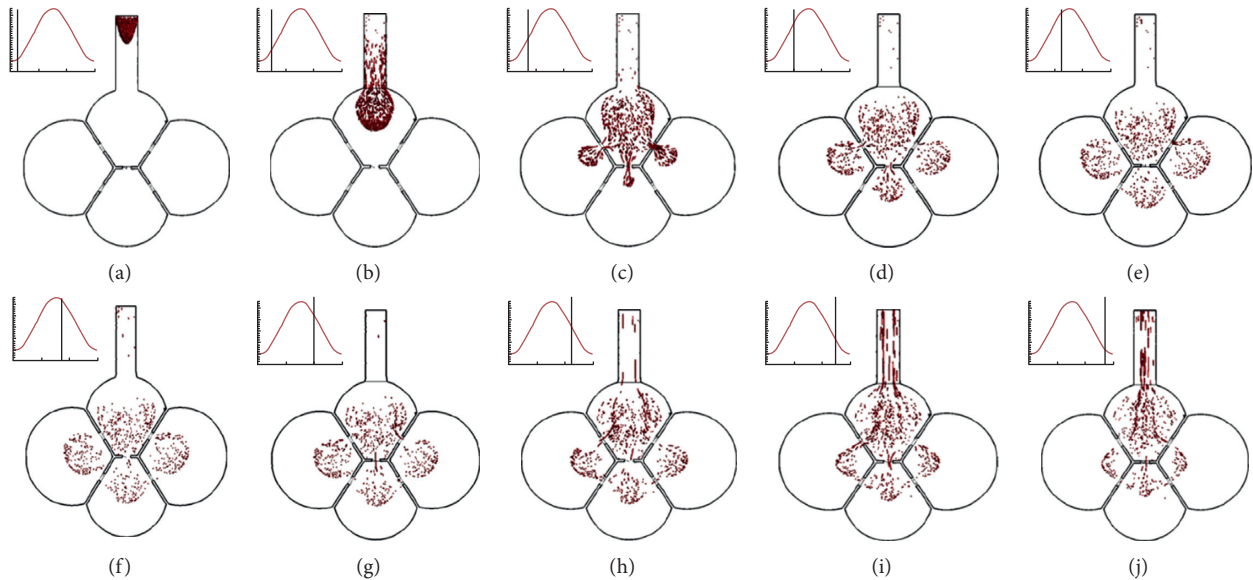


FIGURE 3: Instantaneous snapshots of particle positions in the 4-alveoli model during the first cycle after particle inhalation. Particles were  $1 \mu\text{m}$  in diameter. Due to particle dispersion, some particles exited the geometry with expiratory airflow. (a)  $T=0.25 \text{ s}$ . (b)  $T=0.50 \text{ s}$ . (c)  $T=0.75 \text{ s}$ . (d)  $T=1.00 \text{ s}$ . (e)  $T=1.25 \text{ s}$ . (f)  $T=1.75 \text{ s}$ . (g)  $T=2.00 \text{ s}$ . (h)  $T=2.25 \text{ s}$ . (i)  $T=2.50 \text{ s}$ . (j)  $T=2.75 \text{ s}$ .

the adjacent alveoli through the pores of Kohn and deposit on the septal walls in Sac 1. In contrast, the particle fronts in the three adjacent alveoli only reached half of the airspace at the end of the first inhalation cycle ( $T=1.25 \text{ s}$ ).

During expiration, particles gradually reversed their direction and started to move upward ( $T=1.75\text{--}2.75 \text{ s}$ ).

Particles that returned to Sac 1 from the three peripheral alveoli (Sacs 2–4) gained momentum due to the pores’ accelerating effect. They mixed with the relatively slow-moving particles in the top alveoli, which enhanced particle dispersion. At the end of the first cycle, some particles were exhaled out of the alveoli, as displayed at  $T=2.50\text{--}2.75 \text{ s}$ . In

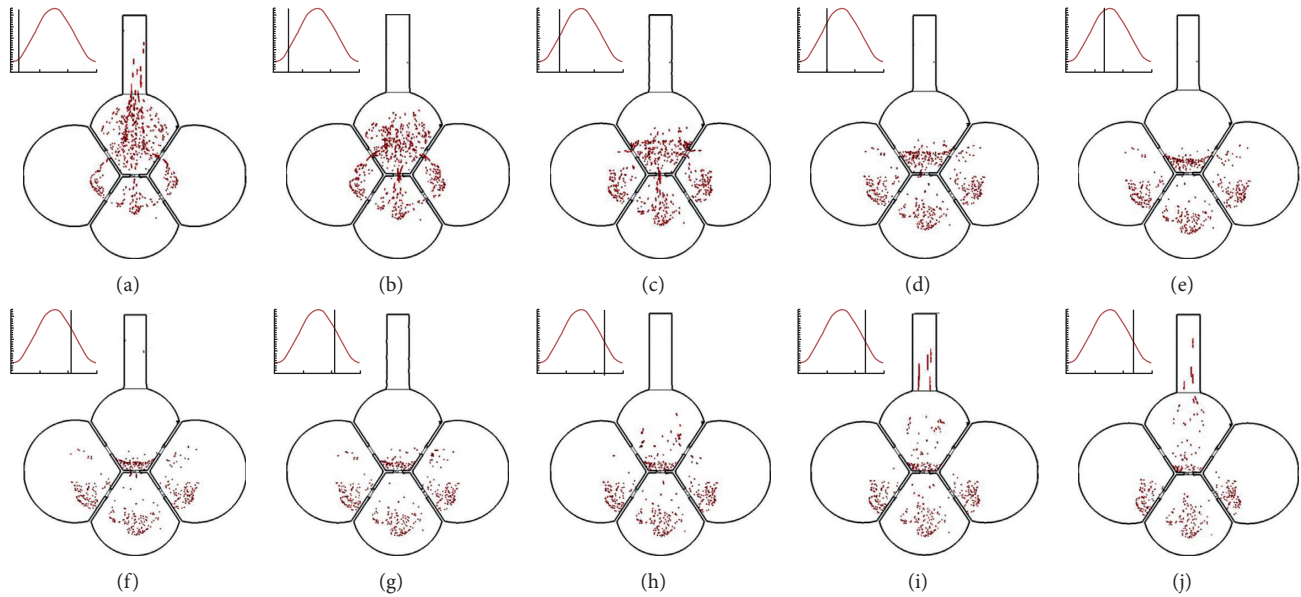


FIGURE 4: Instantaneous snapshots of particle positions in the 4-alveoli model during the second cycle after particle inhalation. All the remaining particles will deposit eventually due to particle interception or gravitational sedimentation. (a)  $T = 3.25$  s. (b)  $T = 3.50$  s. (c)  $T = 3.75$  s. (d)  $T = 4.00$  s. (e)  $T = 4.25$  s. (f)  $T = 4.75$  s. (g)  $T = 5.00$  s. (h)  $T = 5.25$  s. (i)  $T = 5.50$  s. (j)  $T = 5.75$  s.

principle, these particles would not be able to re-enter the geometry.

The instantaneous snapshots of particles during the second respiration cycle are shown in Figure 4 at ten instants. Similar as in the first cycle, the particle swarm oscillated with the expanding-contracting wall motion. However, a negligible number of particles was observed to leave the geometry. Instead, all these particles eventually deposited on the septal walls due to oscillatory convection and gravitational sedimentation. In the following sections, we would study the distribution of particles among individual alveoli as well as the influences of breathing conditions and pore size on these distributions.

Figure 5 shows the surface deposition pattern of  $1\ \mu\text{m}$  particles. Most particles deposited on the septal walls of the top and two lateral alveoli, indicating that gravitational sedimentation is still the predominant deposition mechanism. It was noted that the deposition pattern in Figure 5 displayed the positions of the particles when they deposited on the moving walls of the alveoli; therefore, particle deposition was not limited to one surface but was possible on any surface in a range spanned by the oscillating wall motion.

From Figure 5, a large portion of particles deposited at the end of exhalation (wall contraction) when alveoli have the smallest volume. This was because that, near the end of the exhalation, gravitational sedimentation overtook the upward-moving momentum from the contracting wall. As a result, particles moved downward and collided with the upward-moving wall. Moreover, at the start of the subsequent inhalation, particles still outran the expanding walls and deposited there. As a result, a seemingly suspending layer of deposited particles was observed in the top and lower alveoli (solid arrow in Figure 5(a)). Considering the

two lateral alveoli, no particles were observed on the distal walls, indicating a limited contribution from convective deposition. By contrast, most particles deposited on the interalveolar septal walls that bordered with the lower alveolus (i.e., Sac 4), with even more concentrated deposition in the lower position of the septal walls (dashed ellipse in Figure 5(b)).

Three major differences were observed when comparing temporal deposition profiles between dynamic and static models (Figure 6). First, the cumulative deposition rates were different, with 100% in the static model versus 76.2% in the dynamic model for  $1\ \mu\text{m}$  particles. Second, the spatial distributions of particle deposition among alveoli were different. Heterogeneous doses were predicted in the dynamic model, with 26.8% in the upper alveolus (Sac 1), 14.4% in the lower alveolus (Sac 4), and about  $12.3 \pm 1\%$  in each of the two lateral alveoli (Sac 2 and 3). In addition, there was also an appreciable fraction of particles that deposited in the alveolar duct (8.9%) and the canals of the pores (1.4%), as shown in Figure 6(a). By contrast, no particle deposited in the two lateral alveoli of the static model (Figure 6(b)). The third difference was the time required for deposition. It took about 24 seconds to start deposition in the static model, which was dictated by the alveolar size over particle settling velocity; while in the dynamic model, deposition started almost immediately after particles enter the alveoli. Furthermore, once the deposition started, it took only a short period time for the deposition to complete in the static model; in contrast, the deposition in the dynamic model took about three cycles to complete in the upper alveolus and more than four cycles in the lower and lateral alveoli. Further, a multistage staggering profile of the deposition fraction (DF) versus time was observed in each alveolus of the dynamic model. These three differences clearly demonstrated that

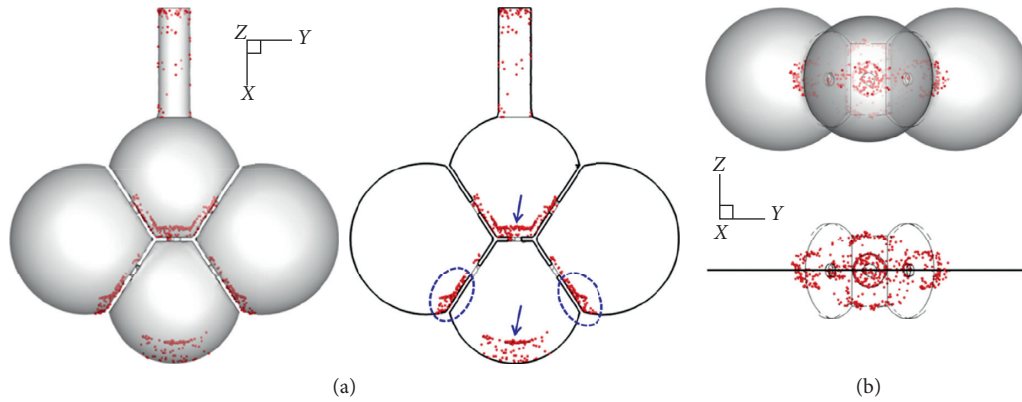


FIGURE 5: Surface deposition of  $1\ \mu\text{m}$  particles in the 4-alveoli model with a pore size of  $40\ \mu\text{m}$ : (a) side view and (b) bottom view.

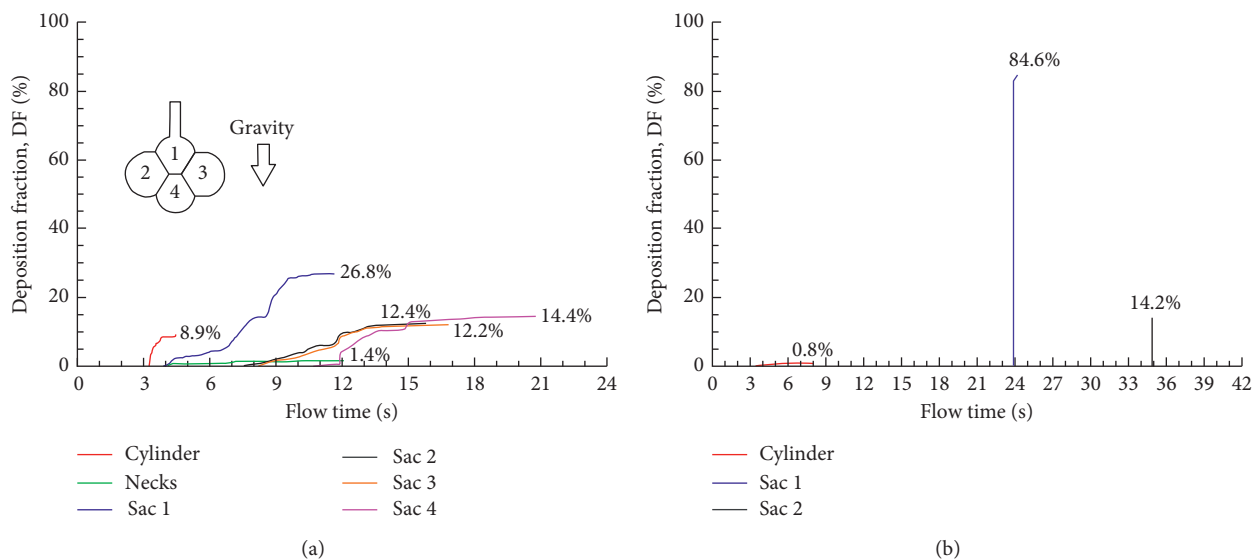


FIGURE 6: Cumulative deposition rate with time for  $1\ \mu\text{m}$  particles in the 4-alveoli model: (a) dynamic model with rhythmic wall motions and (b) static model. Each respiration cycle has a period of  $3.0\ \text{s}$ .

analyses that neglected the dynamic nature of the alveoli would miss the particle behaviors in the acinar region.

Deposition fractions for different sized particles are shown in Figure 7, which increases quickly with particle sizes. It is about 51.5% for  $0.5\ \mu\text{m}$  particles and 76.1% for  $1\ \mu\text{m}$  particles. For particles larger than  $2\ \mu\text{m}$ , nearly all deposits are in the alveolar airspace (i.e., 98.4% for  $2\ \mu\text{m}$  particles and 100% for  $3\ \mu\text{m}$  particles). It is noted that, in this study, a particle bolus was inhaled into the geometry at the start of the inhalation. Particle boluses inhaled at later instants will have lower deposition rates [16].

To gain a better understanding of particle behaviors at different sizes, temporal variation of DFs was quantified in each section of the alveolar sacs (i.e., alveolar duct, four alveoli, and interalveolar pores, Figures 7(b)–7(d)). Similar to the dynamic case in Figure 6, heterogeneous and continuous particle deposition was observed for all sized particles, with the upper alveolus receiving the highest deposition. The time required for deposition was very

different between different particle sizes. It took around 45 s (i.e., 48–3 in Figure 7(b)) for  $0.5\ \mu\text{m}$  particles to complete the deposition, while it took 12 s (i.e., 15–3 in Figure 7(c)) for  $1\ \mu\text{m}$  particles, 4 s for  $2\ \mu\text{m}$  particles, and 2 s for  $3\ \mu\text{m}$  particles. These decreases are due to the increasing particle settling velocity, which is proportional to the square of the particle diameter (i.e.,  $v_{\text{settling}} = 18(\rho_p - \rho_f)gd_p^2/18\mu$ ). Furthermore, deposition of  $0.5\ \mu\text{m}$  particles started 21 s after administration in the two lateral alveoli and 33 s in the lower alveoli. By contrast, much shorter periods of time were needed for larger particles. For instance, it took 1 s for  $2\ \mu\text{m}$  particles to start deposition in the lateral alveoli and 1.5 s in the lower alveoli (Figure 7(d)).

The effects of gravity orientation angle on particle deposition in the alveolar sacs are shown in Figure 8. For the four cases considered ( $0^\circ$ ,  $45^\circ$ ,  $90^\circ$ , and  $135^\circ$ ), the total DF ranged from 60.3 to 77.2%. The highest subregional DF still occurred in Sac 1 (26.8–31.5%). However, the distribution of DFs in the other three alveoli changed significantly,

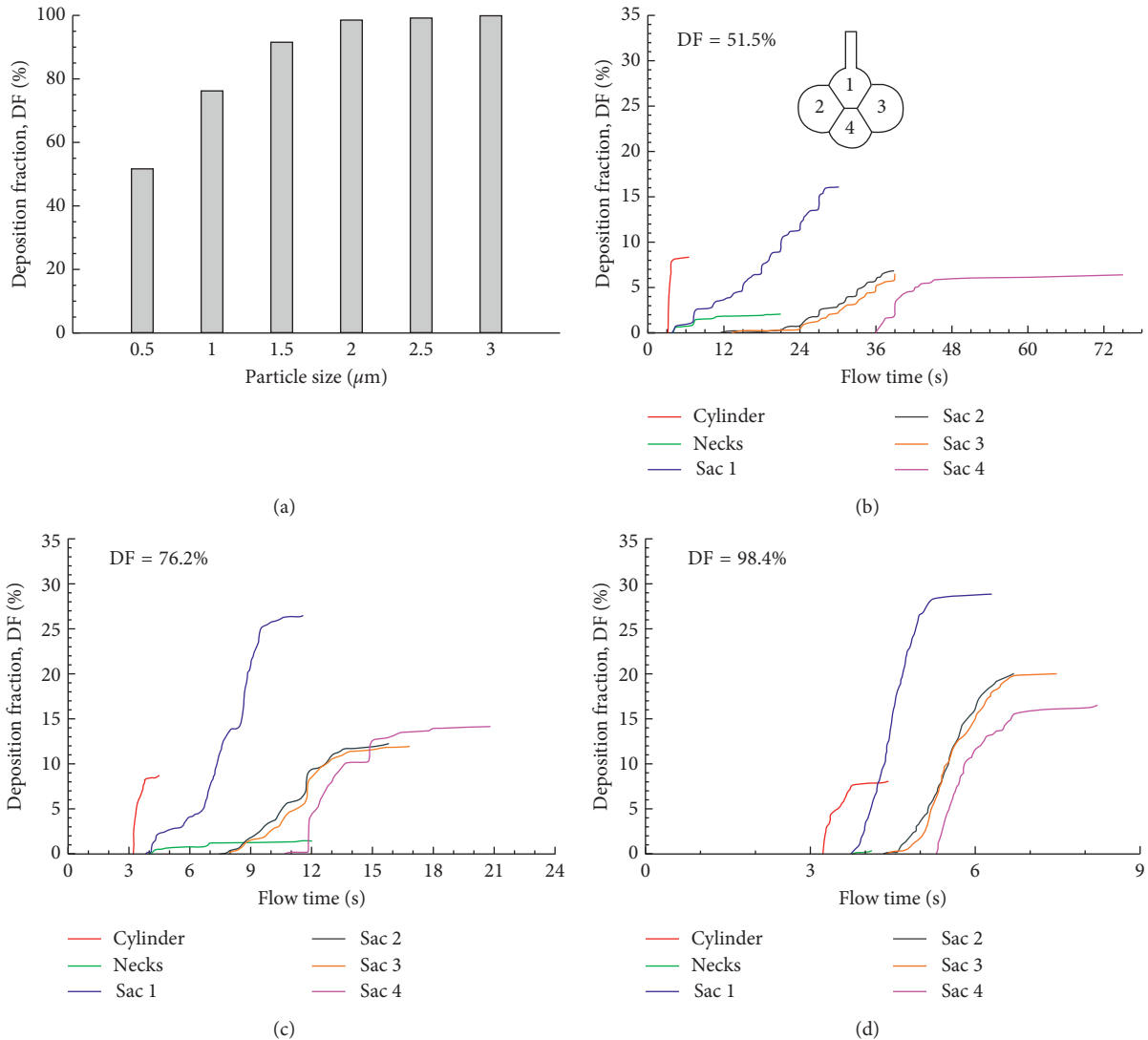


FIGURE 7: Comparison of particle deposition between different particle sizes in the 4-alveoli model: (a) total deposition fractions for 0.5–3  $\mu\text{m}$  particles and the time resolution of sectional cumulative deposition for (b) 0.5  $\mu\text{m}$ , (c) 1  $\mu\text{m}$ , and (d) 2  $\mu\text{m}$ . Deposition was quantified in each section of the model, that is, cylinder, the four alveoli (sacs), and the interalveolar pores (necks).

depending on the alveolar orientation relative to the gravity. For instance, the DF in Sac 2 changed from 12.4% at  $0^\circ$  to  $\sim 17\%$  at  $45^\circ$  and  $90^\circ$  and 11.8% at  $135^\circ$ , while the DF in Sac 3 changed from 12.2% at  $0^\circ$  to  $2\sim 4\%$  at  $45^\circ\text{--}135^\circ$ . Considering that the major deposition mechanisms herein were gravitational sedimentation and oscillatory convection, the orientation-induced DF variation was closely associated to the projected area normal to the gravity, as well as the convective penetration depth of particles into the distal alveoli. Similarly, DF in the alveolar duct was the highest at  $90^\circ$  (16.3%, Figure 8(c)) due to its largest projected area normal to the gravity and was lowest at  $0^\circ$  (8.9%, Figure 8(a)).

Breath-holding after inhalation can significantly enhance alveolar deposition. Figure 9(a) shows the predicted DF of 1  $\mu\text{m}$  particles with different periods of breath-holding. Four seconds or longer hold of breath allowed all inhaled particles to deposit. Figure 9(b) shows the

temporal and spatial variation of DFs in the alveolar sacs for breath-holding of 4 seconds. Compared to the case without breath-holding (Figure 8(a)), subregional DF in Sac 1 increased significantly, for example, from 26.8% to 36.5%. Subregional DFs in the three peripheral alveoli also increased with the breathing-holding due to the prolonged action period of gravitational sedimentation relative to the particle dispersion from oscillatory convection.

The effects of inhalation depth on alveolar deposition and its distribution in the 4-alveoli model are shown in Figure 10. Increasing the inhalation depth had a negligible effect on total DF. However, it notably changed particle distributions among alveoli, with deeper inhalations being associated with less heterogeneous subregional depositions. For instance, at higher tidal volumes, the DF in Sac 1 decreased while DF in Sac 4 increased, reducing the difference between them (Figures 10(b) vs. 10(d)). A subtle variation in

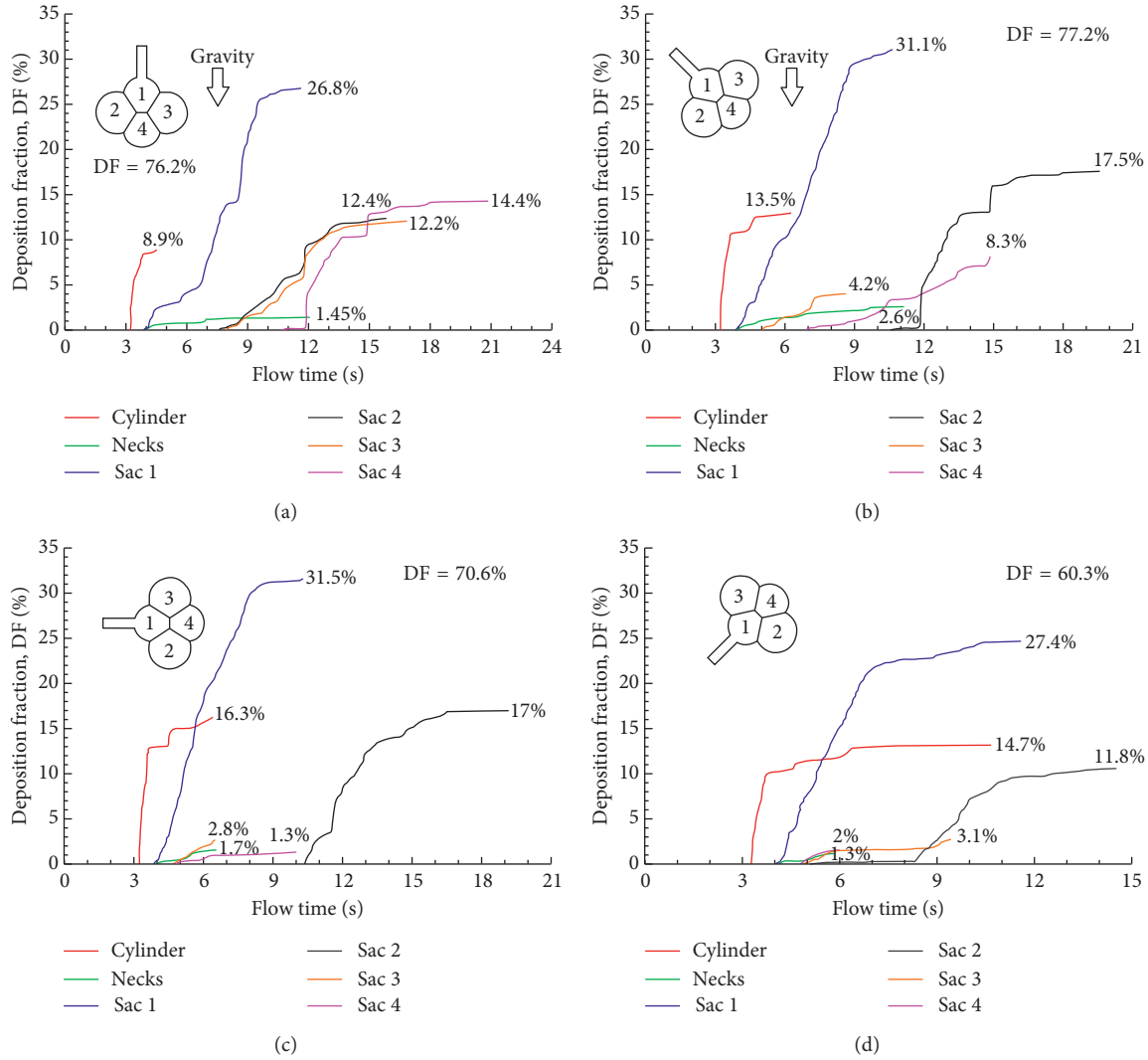


FIGURE 8: Comparison of the cumulative deposition with time for different gravity orientation angles in the 4-alveoli model: (a) 0°, (b) 45°, (c) 90°, and (d) 135° counterclockwise from the gravity.

DF was also noted in the alveolar duct, which increased slightly but persistently with increasing tidal volumes.

One significant issue of pulmonary pathology is the breakdown of interalveolar septal walls and associated collateral ventilation. To investigate their effects on acinar deposition, models with different sizes of septal apertures (pores) were simulated and compared in Figure 11(a). Surprisingly, total DF was found to be insensitive to the pore size. For all pore sizes considered (40 μm, 100 μm, 160 μm, and no septal wall), the total DF for 1 μm particles varied within a narrow range of 71.3~74.4% (Figures 11(b)–11(e)). Dramatic changes in the spatial deposition distribution with the pore size were predicted. Considering the cases of pore size from 40 μm (Figure 8(a)) to 160 μm (Figures 11(c) and 11(d)), the DF in Sac 4 constantly increased with pore size, while DFs in the two lateral alveoli (Sac 2 and 3) decreased with pore size. This trend was reasonable because a larger pore allowed more particles to enter the lower alveolus (due to gravity) but at the same time, decreased the Venturi effect

of pore aperture and therefore reduced the particle penetration depth to the lateral alveoli. When there was no septal wall, the alveolar sacs behave more like a single alveolus, as in Talaat and Xi [15], where particle deposition concentrated at the bottom of the alveolus (Figures 11(b) and 11(e)). This phenomenon was even more pronounced for 3 μm particles, where the majority of particles deposited in the lower alveolus (Sac 4, Figures 11(b) and 11(f)).

Airflow and particle deposition in the 45-alveoli model was also simulated. Figure 12(a) shows the inspiratory airflow in the 45-alveoli model. Complex flow fields are observed as the inhaled airflow enters the alveolar sacs sequentially from top to bottom and from central to peripheral. Airflow is stronger in the axial direction (i.e., positive *x*-direction, Figure 12(a)) and decreases progressively in the lateral compartments. Surface deposition of inhaled particles is shown in Figure 12(b). Overall symmetric surface deposition patterns are observed. Due to the multiple alveolar generations retained in this model, particle deposition exhibits a cascading pattern for all particle

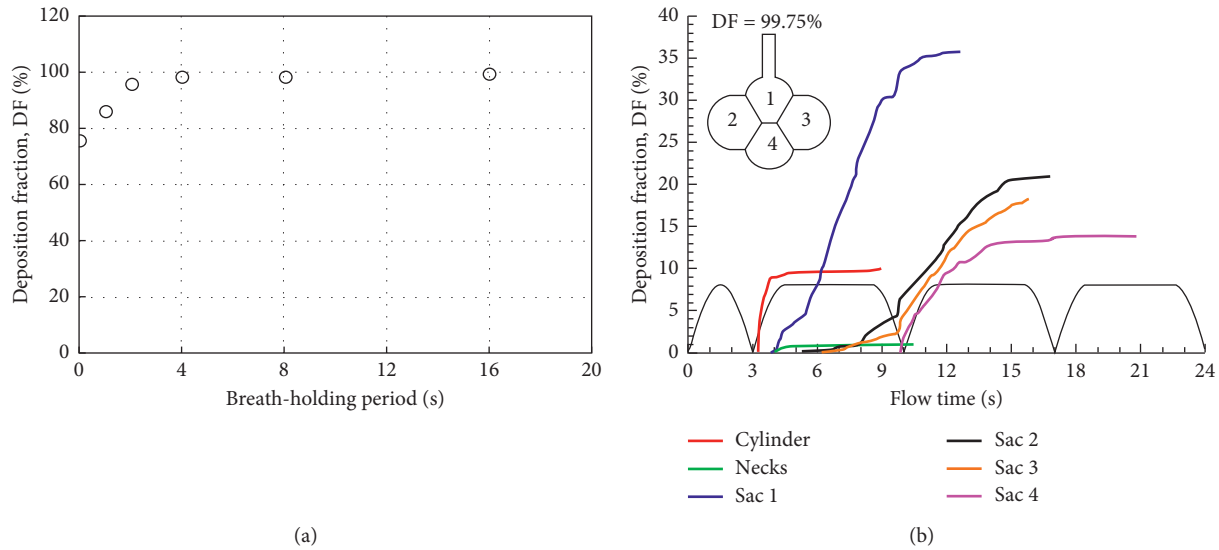


FIGURE 9: Comparison of total deposition rates for different breath-holding periods in the 4-alveoli model: (a) total deposition and (b) temporal deposition for 4 s breath-holding.

sizes ( $0.5\text{--}3.0\ \mu\text{m}$ ) considered (Figure 12(b)). However, deposition is more dispersed for small particles and more concentrated for large particles.

Figure 12(c) compares the deposition fractions as a function of particle size between the 45-alveoli and 4-alveoli models, as well as the single-alveolus model in [15]. Surprisingly, for  $0.5\text{--}1.5\ \mu\text{m}$  particles, lower deposition fractions were predicted in the complex 45-alveoli model than the highly simplified 4-alveoli and single-alveolus models, indicating a negative correlation of acinar deposition with the number of alveoli retained in the model. The cumulative deposition profiles with time were displayed in Figure 12(d) for  $0.5\text{--}3.0\ \mu\text{m}$  particles. The time required for complete deposition decreased dramatically from  $0.5\ \mu\text{m}$  to  $3.0\ \mu\text{m}$  (Figure 12(d)).

Effects of gravity orientation angle on particle deposition in the 45-alveoli model are shown in Figure 13. It appears that the total DF is not sensitive to the gravity orientation angle, as demonstrated by the close similarity of temporal deposition profiles among the four angles considered (i.e.,  $0^\circ$ ,  $45^\circ$ ,  $90^\circ$ , and  $135^\circ$  counterclockwise from the gravity, Figure 13(e)). The spatial deposition distributions, however, exhibit high levels of heterogeneity. In contrast to the symmetric distribution in the  $0^\circ$  case (Figure 13(a)), particles in the other three models deposit preferentially in the central alveoli or alveoli along the gravity (Figures 13(b)–13(d)). Particle deposition decreases quickly in the distal alveoli; very few particles are observed in the alveoli opposite to the gravity direction (Figures 13(b)–13(d)).

Effects of inhalation depth on particle deposition in the 45-alveoli model are shown in Figure 14. The inhalation depth ranges from 0.5 to 1.05 standard  $V_T$  (i.e., one standard  $V_T = 0.233\ \text{FRC}$ ), and the particle size is  $1\ \mu\text{m}$ . Very different deposition patterns are noted for different inhalation depths. At very shallow breath (i.e., 0.5 standard  $V_T$  or volume expansion ratio = 0.117), particles concentrate in the central alveoli along the gravity direction while very few particles

deposit in the peripheral alveoli. As the breath depth increases, particle deposition becomes progressively more dispersed (Figures 14(a)–14(d)). This is caused by the deeper ventilation and stronger flow irregularity at a higher flow rate, both of which will lead to enhanced particle mixing. This phenomenon is most pronounced in the highest breath depth considered ( $1.05\ V_T$ ), where particles are spread in all compartments of the 45-alveoli model geometry (Figure 14(d)). Figure 14(e) shows the cumulative deposition with time for  $1\ \mu\text{m}$  particles at varying inhalation depths. Similar temporal profiles are observed among the four inhalation depths considered, all with a steep slope during the first two cycles and approaching asymptotic thereafter. The final DF slightly increases with the breath depth, for instance, from 62.6% at  $0.5\ V_T$  to 70.5% at  $1.05\ V_T$  (Figure 14(e)).

#### 4. Discussion and Summary

A systematic study of acinar deposition of inertial particles was conducted in a well-defined 4-alveoli model and a more realistic 45-alveoli model. Airflow and particle dynamics driven by oscillating wall motions were visualized. A parametric study of various respiratory and structural factors was conducted, which included alveolar wall kinematics, particle size, model orientation, breath-holding, inhalation depth, and size of interalveolar pores.

Similar to the single-alveolus model as considered in [15], oscillatory wall motion was essential for the multi-alveoli models to capture particle dynamics and acinar deposition. A static multialveoli model that neglected oscillatory wall motions failed to predict neither the deposition fraction nor the particle lifetime before deposition. Much longer time was needed for particles to start deposition in a static alveolar model (about seven respiration cycles, Figure 5) than in a dynamic model (less than three cycles) [15]. This observation called into question of the using aerosols to estimate the alveolar size *in vivo* [48].

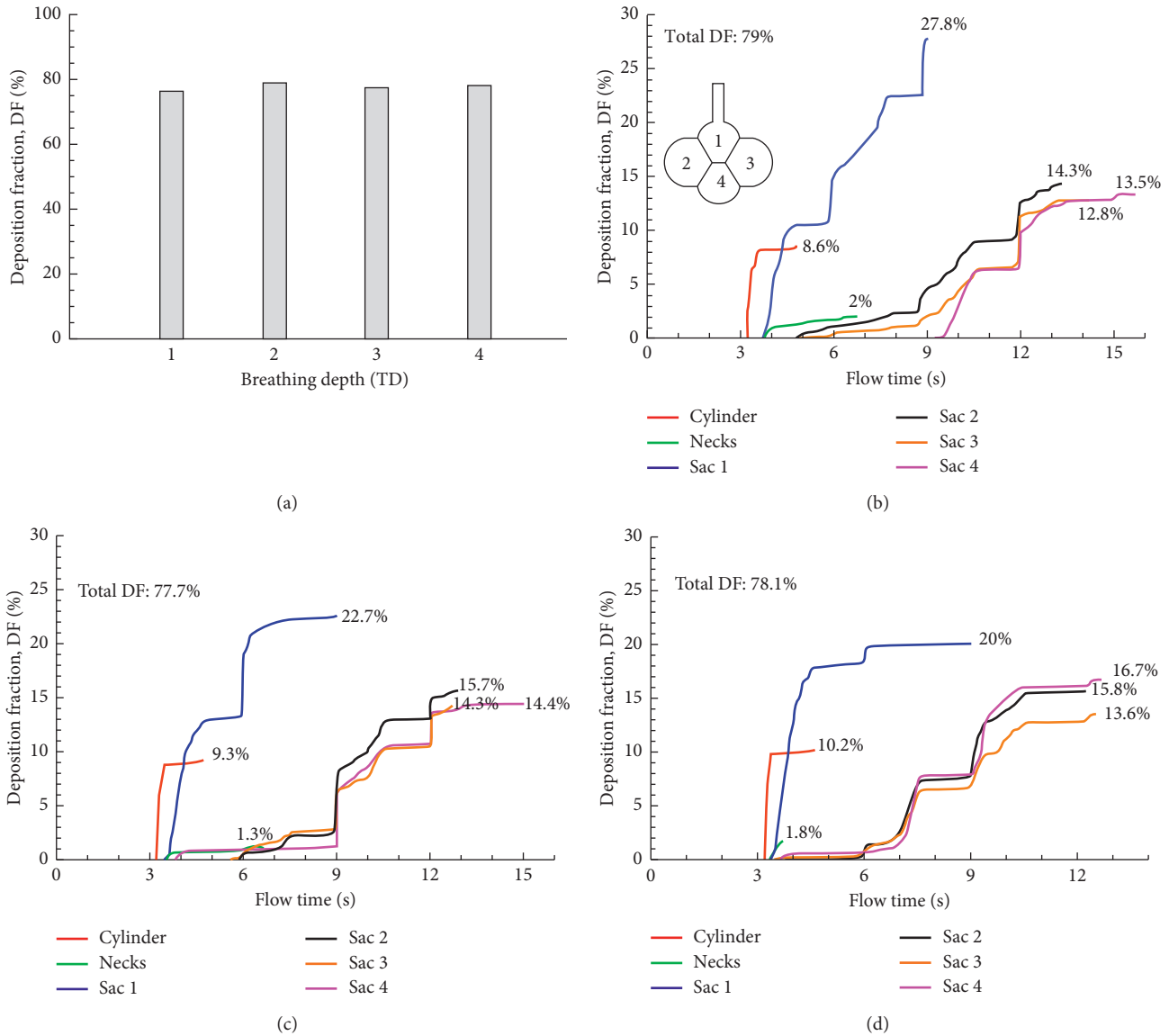


FIGURE 10: Comparison of particle deposition rates between different inhalation depths in the 4-alveoli model: (a) total deposition at different tidal volumes ( $V_T$ ) and the time resolution of sectional cumulative deposition for (b) 2 standard  $V_T$  (i.e., volume expansion factor: 0.466), (c) 3 standard  $V_T$  (i.e., volume expansion factor: 0.699), and (d) 4  $V_T$  (i.e., volume expansion factor: 0.932). Each respiration cycle has a period of 3.0 s.

In comparison to a single-alveolus model [15], interesting differences were observed in multiple-alveoli (i.e., 4-alveoli and 45-alveoli) models. One difference between the single-alveolus model and multialveoli model is the time to start deposition after inhalation. In a terminal single-alveolus model, inhaled particles cannot reach the airway wall during the first inhalation cycle due to the resident air, as observed both experimentally by Berg et al. [49] and in numerical studies by Sera et al. [50] and Talaat and Xi [15]. It took about three breathing cycles for  $1 \mu\text{m}$  particles to start deposition and even longer for submicron particles [15]. In contrast, particle deposition in multialveoli models started during the first inhalation cycle. As shown in Figures 3(d) and 3(e), inhaled particles reached the septal walls of the upper

alveolus (Sac 1) around the middle of the cycle. Due to the interalveolar communication in multialveoli models, all residual air in Sac 1 was displaced into the peripheral alveoli, transporting particles to Sac 1's septa; while the residual air in the single-alveolus model remained in the airspace during wall expansion, which restrained particles' forward motion and kept particles from reaching the alveolar wall.

The acinar deposition was found to be considerably sensitive to the number of alveoli retained in the model. In this study, the total DF for  $0.5\text{--}1.5 \mu\text{m}$  particles was lower in the 45-alveoli model than that in the 4-alveoli model, which in turn was slightly lower than that in the single-alveolus model. This might be counterintuitive at first sight, as complex structures are generally expected to capture more

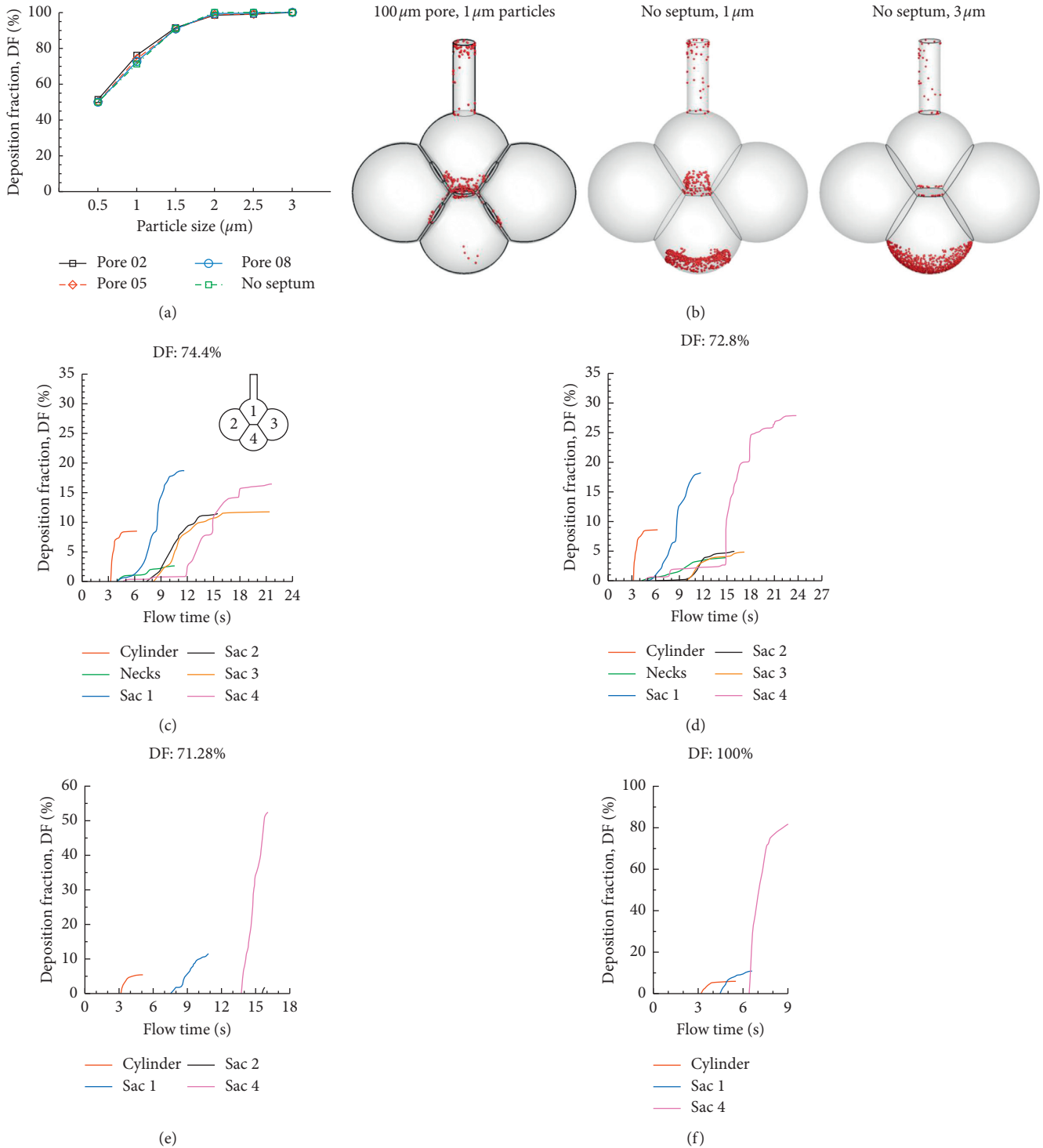


FIGURE 11: Pore size effects on alveolar deposition in the 4-alveoli model: (a) total deposition rates in the alveoli with different pore sizes, (b) surface deposition in different alveoli models, and the time resolution of sectional cumulative deposition for (c) pore size: 100  $\mu\text{m}$ , particles: 1  $\mu\text{m}$ , (d) pore size: 160  $\mu\text{m}$ , particles: 1  $\mu\text{m}$ , (e) no septum, particles: 1  $\mu\text{m}$ , and (f) no septum, particles: 3  $\mu\text{m}$ .

inhaled particles. This is mostly true for throughout flows with inlets and outlets. However, the terminal acinar region is a blind-end airspace, where airflow is driven by the rhythmical wall motion, which enters and exits the geometry through the same inlet. Some particles will be exhaled out of

the geometry during expiration, leading to incomplete deposition. The escaping particles are primarily due to dispersion. Particles that remain in the geometry will eventually deposit either by convection impaction or gravitational sedimentation. Concerning the geometrical complexity

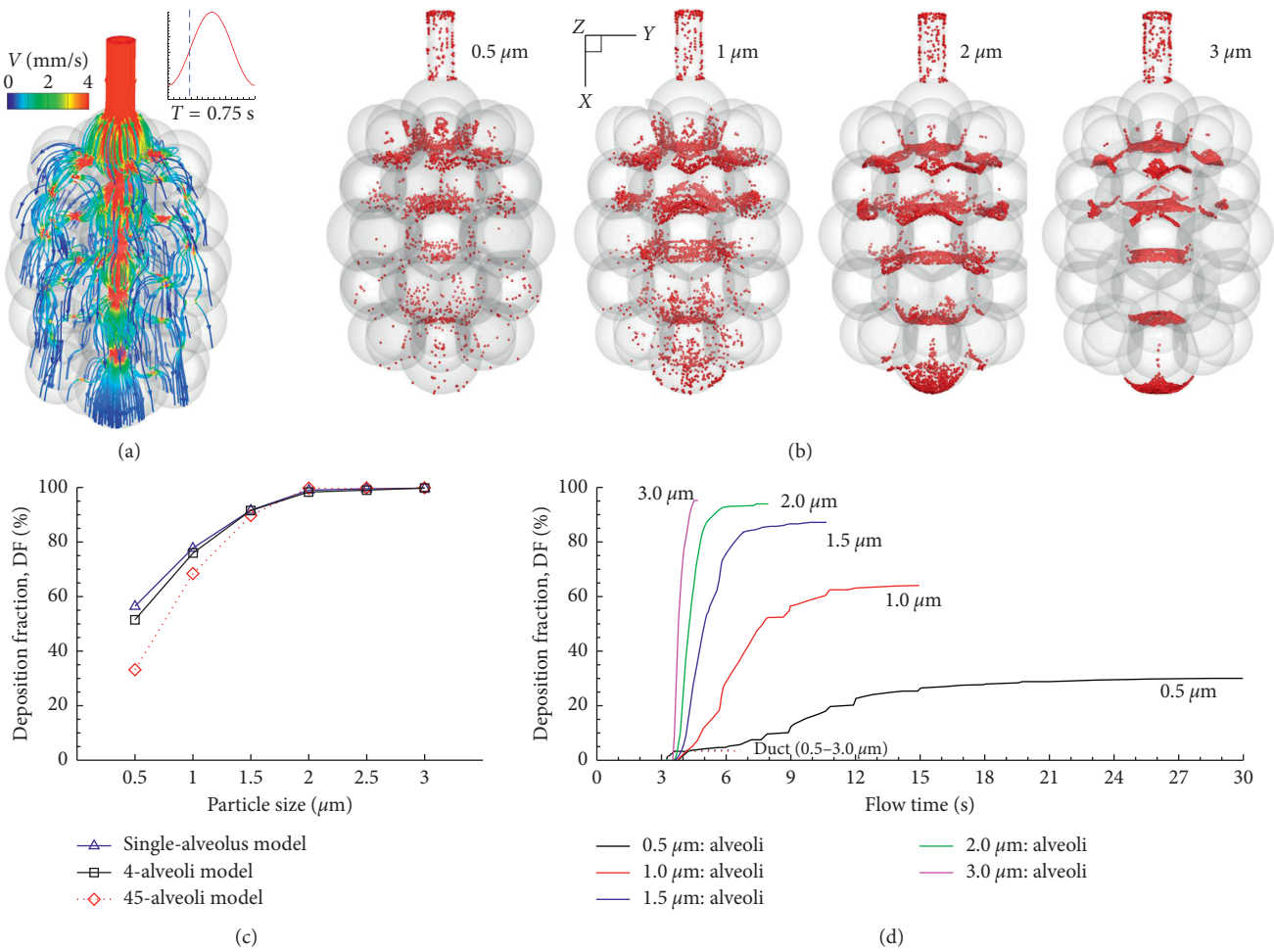


FIGURE 12: Airflow and particle deposition in the 45-alveoli model: (a) airflow, (b) surface deposition, (c) comparison of deposition rate between the 45-alveoli model and 4-alveoli and single-alveolus models, and (d) deposition with time.

effect, the 45-sac model will filter more particles for a given period of time, but meanwhile causes much stronger dispersion, overall giving rise to a lower total DF.

Second, self-similarities exist of particle dynamics in different generations of alveolar sacs. Particles in the central alveoli are more likely to deposit via convective impaction or interception, whereas particles in the peripheral alveoli will deposit via sedimentation, where the flow is slower. For a given tidal volume (i.e., 23.3% FRC), the 45-alveoli model draws in about ten times of air than the 4-alveoli model, inducing stronger inertia impaction in the central alveoli and higher particle deposition. As the inhaled flow bifurcates into the more distal compartments, the inertial impaction effect quickly decreases yielding much lower deposition. Overall, the total DF in the 45-alveoli model can be lower than a simpler 4-alveoli or single-alveolus model.

Particle deposition of these models (i.e., 1-, 4-, and 45-alveoli) reacted differently to the model orientation relative to the gravity. The DF was found to be relatively sensitive to the gravity orientation angle in the single-alveolus model (62.6%–80.0% from  $0^\circ$  to  $135^\circ$ ) [15] and the 4-alveoli model (60.3%–77.2% from  $0^\circ$  to  $135^\circ$ ), but was insensitive in the

45-alveoli model (67.5%–71.6% from  $0^\circ$  to  $135^\circ$ ). The lowest DF occurred at  $135^\circ$  for all of the three models considered. Considering that gravitational sedimentation was one dominating deposition mechanism, the above variation was most likely attributed to area ratio of the duct inlet over the projected area of the alveoli normal to the gravity, which decreased as the model become more complex. Accordingly, it was anticipated that particle dose in more complex acinus should be orientationally insensitive too. A similar observation was also reported in Khajeh-Hosseini-Dalasm and Longest [22] that acinar deposition was not affected by gravity orientation angle when the number of alveolar duct generations was more than three.

The inhalation depth was found to have an insignificant effect on the acinar DF in both the single-alveolus model [15] and the two multialveoli models herein. However, inhalation depth significantly altered the spatial distribution of the particle deposition, with more deposition rates in peripheral alveoli at deeper inhalations. A higher inhalation depth means a higher airflow speed and stronger wall-flow-particle interaction, which further lead to an enhanced deposition from convection and interception, as well as an intensified

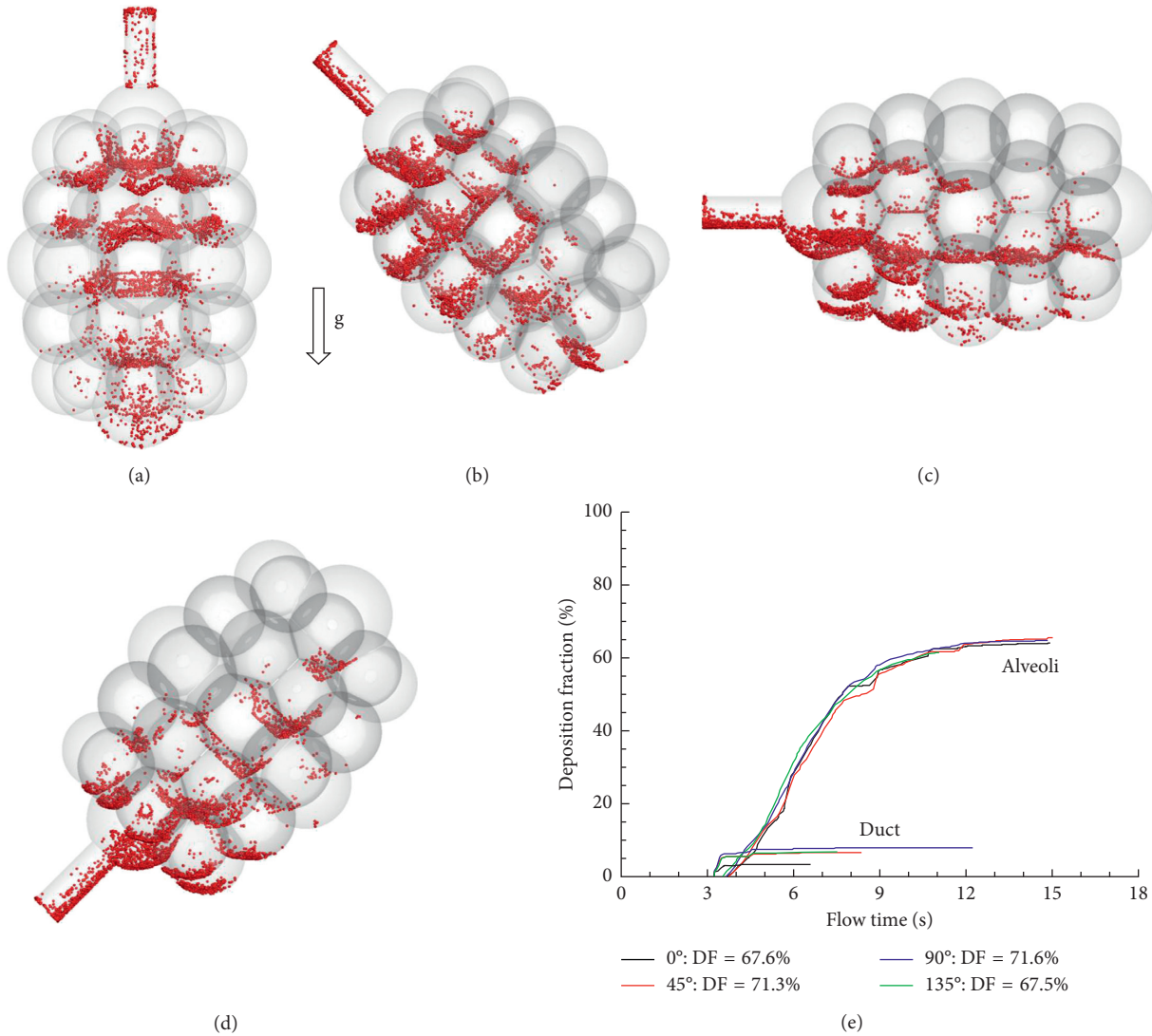


FIGURE 13: Comparison of the cumulative deposition with time for different gravity orientation angles in the 45-alveoli model: (a) 0°, (b) 45°, (c) 90°, and (d) 135° counterclockwise from the gravity, and (e) deposition.

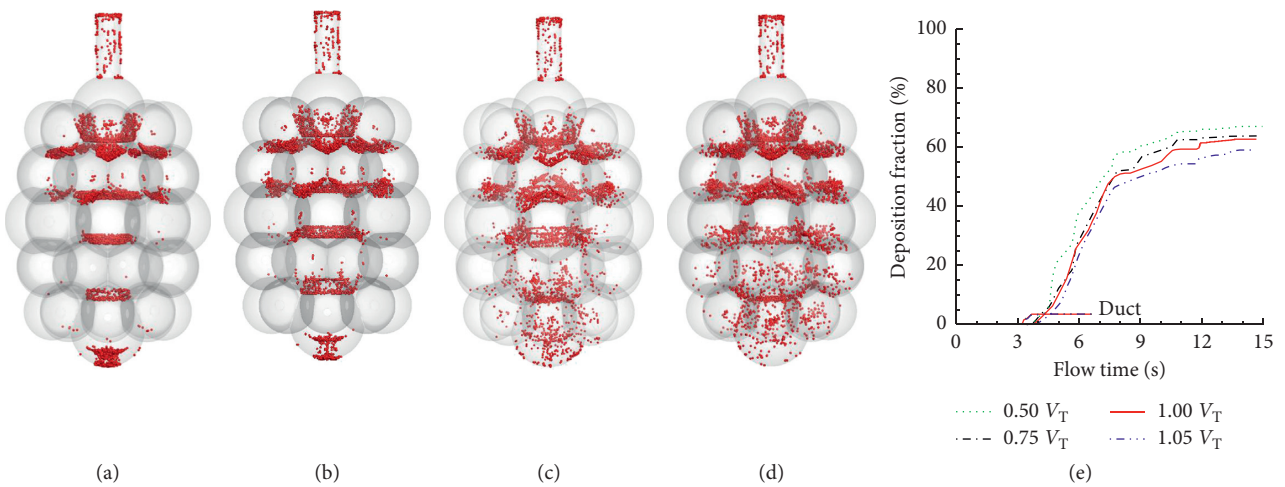


FIGURE 14: Comparison of particle deposition with different breath depths in the 45-alveoli model: (a) total deposition vs. inhalation depth and the time resolution of sectional cumulative deposition for (b) 0.5 standard  $V_T$  (i.e., volume expansion factor: 0.117), (c) 0.75 standard  $V_T$  (i.e., volume expansion factor: 0.175), (d) 1.05 standard  $V_T$  (i.e., volume expansion factor: 0.245), and (e) 1.1 standard  $V_T$  (i.e., volume expansion factor: 0.256).

particle dispersion. As discussed earlier, particle dispersion can cause more particles to escape the geometry during exhalation. Overall, the acinar DFs remain similar between different inhalation depths for a given acinar model. It is acknowledged that the acinar deposition fraction presented in this study was calculated as the number of particles deposited in the alveoli over the number of particles entering the alveolar model. The fraction of orally inhaled particles that entered the alveolar airways was not considered. Increasing inhalation depth will convey more particles to the alveolar airways and lead to higher doses in the acinar region.

In a recent study, Hofemeier et al. [23] also reported that that variance in acinar heterogeneity had little effect on total deposition. When comparing the DF between different acinar models (Figure 12(c)), the DF-particle profiles exhibit a similar asymptotic pattern among the three models, despite the difference in DF magnitude for particles ranging from 0.5 to 1.5  $\mu\text{m}$ . This similarity was to a large extent due to the similar oscillating flows and the associated particle dynamics. Taken other similarities altogether, this agreement suggests a possibility of a generic deposition correlation to estimate the dosimetry in the intricate alveoli using relatively simple geometries even though what level of geometry complexity would be sufficient is yet to be determined. It is emphasized that Khajeh-Hosseini-Dalasm and Longest [22] pursued this question in multigeneration space-filling models with no septal walls and reported a relatively constant acinar deposition rate when more than three alveolar duct generations were retained in the acinar model. Furthermore, correlations of alveolar dose were proposed for different ventilation waveforms such as quick-and-deep and slow-and-deep inhalations [22].

Results of the airflow and particle deposition in alveoli with different pore sizes have meaningful implications in emphysema, which is featured by pore size increase and septum destruction. Varying the pore size was found to exert an insignificant impact on the alveolar deposition, indicating that the emphysematous terminal sacs might receive a similar amount of inhaled aerosols. It is noted that the above results were obtained with the remaining parameters being kept constant, while an emphysematous alveolus might also experience other changes, such as size increase, more compliant (i.e., longer exhalation time), and structure remodeling.

Besides interalveolar pores, collateral ventilation can also occur via bronchiole-alveolar communications (Lambert's channels), interbronchiolar communications (Martin's channels), and even interlobular respiratory bronchioles, depending on the alveolar location and emphysema severity [3]. This study focused on the terminal alveolar sac, where the bronchiole-alveolar and interbronchiolar channels are scarce and the interalveolar pores are prevalent [3, 51]. As a result, results of this study should only be applicable in the terminal alveoli or apical acinar regions where pores of Kohn were found in greatest numbers [3].

Other limitations of this study include simplified model geometry, ideal breathing conditions, noncontinuous aerosol inhalation, and one-way (wall-flow-particle) interaction. For simplicity, particle charge [52, 53], size [54], and hygroscopy effect [55] were also excluded. *In vivo*

pulmonary alveoli have complicated morphology as revealed by histology and microscopy studies [49, 56–58], which appear as a polyhedral complex with varying-sized alveoli grouped in a fractal form [59]. In this study, both the 4-alveoli and 45-alveoli models were constructed from regular geometries such as a cylindrical duct, spheres, and circular pores. Anatomically, the interalveolar septal wall was demonstrated to have a variable thickness from the alveolar mouth to distal walls [60]; a constant wall thickness was assumed herein for computational simplicity. Likewise, there was no more than one pore in one septum in this study, while there can be one to seven pores in life conditions [61]. Even though scanning electron microscope (SEM) evidence has confirmed that pores of Kohn are normal structures in healthy lungs, it is not clear whether they are open all the time or are mostly covered by surfactant that ruptures during expansion or at high differential pressures. Because SEM samples are *ex vivo*, to the authors' knowledge, there is no literature that tracked the size and shape of *in vivo* pores in human lungs, despite recent attempts that utilized confocal microscopy [4] and optical coherence tomography (OCT) imaging to visualize alveolar structure dynamics [62] in mouse models. Moreover, surface tension of the fluids/surfactant mixture lining the alveolar wall varies during the expansion and contraction of the alveoli (roughly proportional to the surface area) [63]. Along with the nonlinear alveolar tissue elasticity, this surface tension variation further complicates the alveolar kinematics, for instance, by slowing down or constraining the wall stretching as it approaches the end of inhalation [64]. However, essential geometrical features of the alveoli were retained in these two models, such as the septa between alveoli and the pores in the septa, both of which had been neglected in previous numerical studies. The sphere was also naturally reshaped into a polyhedron when several spheres cross-cut each other, as displayed by the polyhedrons inside the 45-alveoli model, as well as the semipolyhedrons in the outer layers of both models (Figure 1). More importantly, well-defined shape and size allowed controlled parametric studies and hence identification of major factors that dictate airflow and particle deposition in alveolar sacs. The second physiological parameter to be improved is the breathing profile, which can have different waveforms and inhalation : exhalation (I : E) ratios. In life conditions, a normal breathing in a healthy subject generally has an I : E ratio of 1 : 2. [65] In emphysematous patients, the loss of alveolar elasticity leads to even longer exhalation time [8]. Compared to an I : E ratio of 1 : 1, this means a longer period of exhalation, a slower expiratory speed, a further downward motion, and therefore a higher deposition rate. This scenario should be close to the case with a postinhalation breath-holding of 1 or 2 seconds. Thirdly, particles were inhaled only at the beginning of the inhalation, and results of this study cannot be applied in scenarios with continuous aerosol exposures. Lastly, kinematics of the alveolar wall was modeled based on experimentally measured chest motions [37], and the amplitude of the alveolar wall motion was based on the tidal volume [66]. Direct measurements of *in vivo* alveolar motion using the imaging method should be used in future studies. It is also

noted that pores of Kohn is 2–15  $\mu\text{m}$  in diameter in normal healthy lungs [2, 61], but can constantly increase in size till septal wall breakdown in emphysematous alveoli [59]. Further studies of the influences of smaller and multiple pores on acinar flow and particle deposition are needed.

In Summary, temporal and spatial deposition variations in multialveoli pore-communicated acinar models were numerically investigated under the influences of various physiological factors. Specific findings are listed as follows:

- (1) Collateral ventilation existed in multialveoli acinar models
- (2) Heterogeneous deposition distributions were found among alveoli, with the highest deposition in the central alveoli and decreasing deposition in more peripheral alveoli
- (3) The acinar deposition was highly sensitive to particle size; for particles that were larger than 2  $\mu\text{m}$  and administered at the beginning of the inhalation, nearly 100% alveolar deposition fraction (i.e., particles deposited in the alveolar model over particles entering the alveolar model) was predicted
- (4) The number of alveoli retained in the model affected the total deposition, with the 45-alveoli model having lower deposition than the 4-alveoli and single-alveolus models
- (5) The size of the pores of Kohn, inhalation depth, and gravity orientation angle had insignificant effects on the acinar deposition fraction but had a dramatic impact on the spatial distribution of particle deposition among alveoli

## Data Availability

The data used to support the findings of this study are available from the corresponding author upon request.

## Conflicts of Interest

The authors report no conflicts of interest in this work.

## Acknowledgments

This study was funded by the NSF Grant (CBET 1745602).

## References

- [1] M. Ochs, J. R. Nyengaard, A. Jung et al., “The number of alveoli in the human lung,” *American Journal of Respiratory and Critical Care Medicine*, vol. 169, no. 1, pp. 120–124, 2004.
- [2] C. Desplechain, B. Foliguet, E. Barrat, G. Grignon, and F. Touati, “The pores of Kohn in pulmonary alveoli,” *Bulletin Européen de Physiopathologie Respiratoire*, vol. 19, no. 1, pp. 59–68, 1983.
- [3] P. B. Terry and R. J. Traystman, “The clinical significance of collateral ventilation,” *Annals of the American Thoracic Society*, vol. 13, no. 12, pp. 2251–2257, 2016.
- [4] E. Namati, J. Thiesse, J. de Ryk, and G. McLennan, “Alveolar dynamics during respiration: are the pores of Kohn a pathway to recruitment?,” *American Journal of Respiratory Cell and Molecular Biology*, vol. 38, no. 5, pp. 572–578, 2008.
- [5] A. Nagai, H. Inano, K. Matsuba, and W. M. Thurlbeck, “Scanning electronmicroscopic morphometry of emphysema in humans,” *American Journal of Respiratory and Critical Care Medicine*, vol. 150, no. 5, pp. 1411–1415, 1994.
- [6] C. M. Van Allen, G. E. Lindskog, and H. G. Richter, “Gaseous interchange between adjacent lung lobules,” *Yale Journal of Biology and Medicine*, vol. 2, no. 4, pp. 297–300, 1930.
- [7] P. B. Terry, R. J. Traystman, H. H. Newball, G. Batra, and H. A. Menkes, “Collateral ventilation in man,” *New England Journal of Medicine*, vol. 298, no. 1, pp. 10–15, 1978.
- [8] J. C. Hogg, “Pathophysiology of airflow limitation in chronic obstructive pulmonary disease,” *The Lancet*, vol. 364, no. 9435, pp. 709–721, 2004.
- [9] S. Shimura, E. S. Boatman, and C. J. Martin, “Effects of ageing on the alveolar pores of Kohn and on the cytoplasmic components of alveolar type II cells in monkey lungs,” *Journal of Pathology*, vol. 148, no. 1, pp. 1–11, 1986.
- [10] N. A. Gillett, R. F. Gerlach, B. A. Muggenburg, J. R. Harkema, W. C. Griffith, and J. L. Mauderly, “Relationship between collateral flow resistance and alveolar pores in the aging beagle dog,” *Experimental Lung Research*, vol. 15, no. 5, pp. 709–719, 1989.
- [11] I. Balashazy, W. Hofmann, A. Farkas, and B. G. Madas, “Three-dimensional model for aerosol transport and deposition in expanding and contracting alveoli,” *Inhalation Toxicology*, vol. 20, no. 6, pp. 611–621, 2008.
- [12] S. Haber, D. Yitzhak, and A. Tsuda, “Gravitational deposition in a rhythmically expanding and contracting alveolus,” *Journal of Applied Physiology*, vol. 95, no. 2, pp. 657–671, 2003.
- [13] D. Y. Lee and J. W. Lee, “Characteristics of particle transport in an expanding or contracting alveolated tube,” *Journal of Aerosol Science*, vol. 34, no. 9, pp. 1193–1215, 2003.
- [14] J. Sznitman, F. Heimsch, T. Heimsch, D. Rusch, and T. Rösigen, “Three-dimensional convective alveolar flow induced by rhythmic breathing motion of the pulmonary acinus,” *Journal of Biomechanical Engineering*, vol. 129, no. 5, pp. 658–665, 2007.
- [15] K. Talaat and J. Xi, “Computational modeling of aerosol transport, dispersion, and deposition in rhythmically expanding and contracting terminal alveoli,” *Journal of Aerosol Science*, vol. 112, pp. 19–33, 2017.
- [16] J. Xi, K. Talaat, and X. Si, “Deposition of bolus and continuously inhaled aerosols in rhythmically moving terminal alveoli,” *Journal of Computational Multiphase Flows*, 2018.
- [17] C. Darquenne and M. Paiva, “Two- and three dimensional simulations of aerosol transport and deposition in alveolar zone of human lung,” *Journal of Applied Physiology*, vol. 80, no. 4, pp. 1401–1414, 1996.
- [18] A. Karl, F. S. Henry, and A. Tsuda, “Low reynolds number viscous flow in an alveolated duct,” *Journal of Biomechanical Engineering*, vol. 126, no. 4, pp. 420–429, 2004.
- [19] H. Kitaoka, G. F. Nieman, Y. Fujino, D. Carney, J. DiRocco, and I. Kawase, “A 4-dimensional model of the alveolar structure,” *Journal of Physiological Sciences*, vol. 57, no. 3, pp. 175–185, 2007.
- [20] H. Kumar, M. H. Tawhai, E. A. Hoffman, and C. L. Lin, “The effects of geometry on airflow in the acinar region of the human lung,” *Journal of Biomechanics*, vol. 42, no. 11, pp. 1635–1642, 2009.
- [21] J. Sznitman, T. Heimsch, J. H. Wildhaber, A. Tsuda, and T. Rösigen, “Respiratory flow phenomena and gravitational deposition in a three-dimensional space-filling model of the

- pulmonary acinar tree,” *Journal of Biomechanical Engineering*, vol. 131, no. 3, article 031010, 2009.
- [22] N. Khajeh-Hosseini-Dalasm and P. W. Longest, “Deposition of particles in the alveolar airways: inhalation and breath-hold with pharmaceutical aerosols,” *Journal of Aerosol Science*, vol. 79, no. 1, pp. 15–30, 2015.
- [23] P. Hofemeier, K. Koshiyama, S. Wada, and J. Sznitman, “One (sub-)acinus for all: fate of inhaled aerosols in heterogeneous pulmonary acinar structures,” *European Journal of Pharmaceutical Sciences*, vol. 113, no. 2, pp. 53–63, 2018.
- [24] W. H. Finlay, *The Mechanics of Inhaled Pharmaceutical Aerosols*, Academic Press, San Diego, CA, USA, 2001.
- [25] G. Rudolf, J. Gebhart, J. Heyder, C. F. Schiller, and W. Stahlhofen, “An empirical formula describing aerosol deposition in man for any particle size,” *Journal of Aerosol Science*, vol. 17, no. 3, pp. 350–355, 1986.
- [26] K. K. Isaacs, J. A. Rosati, and T. B. Martonen, “Mechanisms of particle deposition,” in *Aerosols Handbook*, L. S. Ruzer and N. H. Harley, Eds., pp. 75–99, CRC Press, New York, NY, USA, 2005.
- [27] M. Kojic and A. Tsuda, “A simple model for gravitational deposition of non-diffusing particles in oscillatory laminar pipe flow and its application to small airways,” *Journal of Aerosol Science*, vol. 35, no. 2, pp. 245–261, 2004.
- [28] J. Pich, “Theory of gravitational deposition of particles from laminar flows in channels,” *Journal of Aerosol Science*, vol. 3, no. 5, pp. 351–361, 1972.
- [29] J. I. Choi and C. S. Kim, “Mathematical analysis of particle deposition in human lungs: an improved single path transport model,” *Inhalation Toxicology*, vol. 19, no. 11, pp. 925–939, 2007.
- [30] C. S. Kim, “Deposition of aerosol particles in human lungs: in vivo measurement and modelling,” *Biomarkers*, vol. 14, no. 1, pp. 54–58, 2009.
- [31] P. Hofemeier and J. Sznitman, “The role of anisotropic expansion for pulmonary acinar aerosol deposition,” *Journal of Biomechanics*, vol. 49, no. 14, pp. 3543–3548, 2016.
- [32] S. Haber, J. P. Butler, H. Brenner, I. Emanuel, and A. Tsuda, “Shear flow over a self-similar expanding pulmonary alveolus during rhythmical breathing,” *Journal of Fluid Mechanics*, vol. 405, no. 2, pp. 243–268, 2000.
- [33] S. Chhabra and A. K. Prasad, “Flow and particle dispersion in a pulmonary alveolus—part I: velocity measurements and convective particle transport,” *Journal of Biomechanical Engineering*, vol. 132, no. 5, article 4001112, 2010.
- [34] E. J. Berg and R. J. Robinson, “Stereoscopic particle image velocimetry analysis of healthy and emphysemic alveolar sac models,” *Journal of Biomechanical Engineering*, vol. 133, no. 6, article 061004, 2011.
- [35] B. Ma and C. Darquenne, “Aerosol bolus dispersion in acinar airways—-influence of gravity and airway asymmetry,” *Journal of Applied Physiology*, vol. 113, no. 3, pp. 442–450, 2012.
- [36] C. Plathow, S. Ley, C. Fink et al., “Evaluation of chest motion and volumetry during the breathing cycle by dynamic MRI in healthy subjects: comparison with pulmonary function tests,” *Investigative Radiology*, vol. 39, no. 4, pp. 202–209, 2004.
- [37] A. De Groote, M. Wantier, G. Cheron, M. Estenne, and M. Paiva, “Chest wall motion during tidal breathing,” *Journal of Applied Physiology*, vol. 83, no. 5, pp. 1531–1537, 1997.
- [38] R. L. Jones and M. M. Nzekwu, “The effects of body mass index on lung volumes,” *Chest*, vol. 130, no. 3, pp. 827–833, 2006.
- [39] E. M. Harding and R. J. Robinson, “Flow in a terminal alveolar sac model with expanding walls using computational fluid dynamics,” *Inhalation Toxicology*, vol. 22, no. 8, pp. 669–678, 2010.
- [40] J. Xi, X. Si, J. Kim, G. Su, and H. Dong, “Modeling the pharyngeal anatomical effects on breathing resistance and aerodynamically generated sound,” *Medical & Biological Engineering & Computing*, vol. 52, no. 7, pp. 567–577, 2014.
- [41] X. Si, J. Xi, and J. Kim, “Effect of laryngopharyngeal anatomy on expiratory airflow and submicrometer particle deposition in human extrathoracic airways,” *Open Journal of Fluid Dynamics*, vol. 3, no. 4, 2013.
- [42] P. W. Longest and J. Xi, “Computational investigation of particle inertia effects on submicron aerosol deposition in the respiratory tract,” *Journal of Aerosol Science*, vol. 38, no. 1, pp. 111–130, 2007.
- [43] P. W. Longest and J. Xi, “Effectiveness of direct Lagrangian tracking models for simulating nanoparticle deposition in the upper airways,” *Aerosol Science and Technology*, vol. 41, no. 4, pp. 380–397, 2007.
- [44] J. Kim, J. Xi, X. Si, A. Berlinski, and W. C. Su, “Hood nebulization: effects of head direction and breathing mode on particle inhalability and deposition in a 7-month-old infant model,” *Journal of Aerosol Medicine and Pulmonary Drug Delivery*, vol. 27, no. 3, pp. 209–218, 2014.
- [45] Z. Li, C. Kleinstreuer, and Z. Zhang, “Simulation of airflow fields and microparticle deposition in realistic human lung airway models. Part II: particle transport and deposition,” *European Journal of Mechanics-B/Fluids*, vol. 26, no. 5, pp. 650–668, 2007.
- [46] J. Xi and P. W. Longest, “Transport and deposition of micro-aerosols in realistic and simplified models of the oral airway,” *Annals of Biomedical Engineering*, vol. 35, no. 4, pp. 560–581, 2007.
- [47] J. Xi, J. E. Yuan, M. Yang, X. Si, Y. Zhou, and Y.-S. Cheng, “Parametric study on mouth–throat geometrical factors on deposition of orally inhaled aerosols,” *Journal of Aerosol Science*, vol. 99, pp. 94–106, 2016.
- [48] W. D. Bennett and G. C. Smaldone, “Use of aerosols to estimate mean air-space size in chronic obstructive pulmonary disease,” *Journal of Applied Physiology*, vol. 64, no. 4, pp. 1554–1560, 1985.
- [49] E. J. Berg, J. L. Weisman, M. J. Oldham, and R. J. Robinson, “Flow field analysis in a compliant acinus replica model using particle image velocimetry (PIV),” *Journal of Biomechanics*, vol. 43, no. 6, pp. 1039–1047, 2010.
- [50] T. Sera, K. Uesugi, N. Yagi, and H. Yokota, “Numerical simulation of airflow and microparticle deposition in a synchrotron micro-CT-based pulmonary acinus model,” *Computer Methods in Biomechanics and Biomedical Engineering*, vol. 18, no. 13, pp. 1427–1435, 2015.
- [51] E. J. Cetti, A. J. Moore, and D. M. Geddes, “Collateral ventilation,” *Thorax*, vol. 61, no. 5, pp. 371–373, 2006.
- [52] J. Xi, X. Si, and P. W. Longest, “Electrostatic charge effects on pharmaceutical aerosol deposition in human nasal-laryngeal airways,” *Pharmaceutics*, vol. 6, no. 1, pp. 26–35, 2013.
- [53] J. Xi, X. A. Si, and R. Gaide, “Electrophoretic particle guidance significantly enhances olfactory drug delivery: a feasibility study,” *PLoS One*, vol. 9, no. 1, article e86593, 2014.
- [54] X. A. Si, J. Xi, J. Kim, Y. Zhou, and H. Zhong, “Modeling of release position and ventilation effects on olfactory aerosol drug delivery,” *Respiratory Physiology & Neurobiology*, vol. 186, no. 1, pp. 22–32, 2013.
- [55] J. W. Kim, J. Xi, and X. A. Si, “Dynamic growth and deposition of hygroscopic aerosols in the nasal airway of a 5-year-old

- child,” *International Journal for Numerical Methods in Biomedical Engineering*, vol. 29, no. 1, pp. 17–39, 2013.
- [56] G. C. Smaldone and W. Mitzner, “Viewpoint: unresolved mysteries,” *Journal of Applied Physiology*, vol. 113, no. 12, pp. 1945–1947, 2012.
- [57] B. Haefeli-Bleuer and E. R. Weibel, “Morphometry of the human pulmonary acinus,” *Anatomical Record*, vol. 220, no. 4, pp. 401–414, 1988.
- [58] H. Kumar, D. M. Vasilescu, Y. Yin, E. A. Hoffman, M. H. Tawhai, and C.-L. Lin, “Multiscale imaging and registration-driven model for pulmonary acinar mechanics in the mouse,” *Journal of Applied Physiology*, vol. 114, no. 8, pp. 971–978, 2013.
- [59] A. Yoshikawa, S. Sato, T. Tanaka et al., “Breakdown of lung framework and an increase in pores of Kohn as initial events of emphysema and a cause of reduction in diffusing capacity,” *International Journal of Chronic Obstructive Pulmonary Disease*, vol. 11, no. 1, pp. 2287–2294, 2016.
- [60] S. F. Ryan, “The structure of the interalveolar septum of the mammalian lung,” *Anatomical Record*, vol. 165, no. 4, pp. 467–483, 1969.
- [61] J. L. Cordingley, “Pores of Kohn,” *Thorax*, vol. 27, no. 4, pp. 433–441, 1972.
- [62] L. Kirsten, M. Gaertner, C. Schnabel, S. Meissner, and E. Koch, “Four-dimensional imaging of murine subpleural alveoli using high-speed optical coherence tomography,” *Journal of Biophotonics*, vol. 6, no. 2, pp. 148–152, 2013.
- [63] C. B. Daniels, S. Orgeig, A. W. Smits, and J. D. Miller, “The influence of temperature, phylogeny, and lung structure on the lipid composition of reptilian pulmonary surfactant,” *Experimental Lung Research*, vol. 22, no. 3, pp. 267–281, 1996.
- [64] E. J. A. Veldhuizen and H. P. Haagsman, “Role of pulmonary surfactant components in surface film formation and dynamics,” *Biochimica et Biophysica Acta (BBA)–Biomembranes*, vol. 1467, no. 2, pp. 255–270, 2000.
- [65] I. Van Diest, K. Verstappen, A. E. Aubert, D. Widjaja, D. Vansteenwegen, and E. Vlemincx, “Inhalation/exhalation ratio modulates the effect of slow breathing on heart rate variability and relaxation,” *Applied Psychophysiology and Biofeedback*, vol. 39, no. 3–4, pp. 171–180, 2014.
- [66] L. Porra, S. Monfraix, G. Berruyer, G. Le Duc, C. Nemoz, and S. Bayat, “Effect of tidal volume on distribution of ventilation assessed by synchrotron radiation CT in rabbit,” *Journal of Applied Physiology*, vol. 96, pp. 1899–1908, 2004.

## Research Article

# Modeling Inhibitory Effect on the Growth of Uninfected T Cells Caused by Infected T Cells: Stability and Hopf Bifurcation

Yahui Ji, Wanbiao Ma , and Keying Song

Department of Applied Mathematics, School of Mathematics and Physics,  
University of Science and Technology Beijing, 100083, Beijing, China

Correspondence should be addressed to Wanbiao Ma; [wanbiao\\_ma@ustb.edu.cn](mailto:wanbiao_ma@ustb.edu.cn)

Received 1 February 2018; Accepted 30 April 2018; Published 12 August 2018

Academic Editor: Ming-shi Yang

Copyright © 2018 Yahui Ji et al. This is an open access article distributed under the Creative Commons Attribution License, which permits unrestricted use, distribution, and reproduction in any medium, provided the original work is properly cited.

We consider a class of viral infection dynamic models with inhibitory effect on the growth of uninfected T cells caused by infected T cells and logistic target cell growth. The basic reproduction number  $R_0$  is derived. It is shown that the uninfected equilibrium is globally asymptotically stable if  $R_0 < 1$ . Sufficient conditions for the existence of Hopf bifurcation at the infected equilibrium are investigated by analyzing the distribution of eigenvalues. Furthermore, the properties of Hopf bifurcation are determined by the normal form theory and the center manifold. Numerical simulations are carried out to support the theoretical analysis.

## 1. Introduction

The human immunodeficiency virus (HIV) is a lentivirus, which replicates by infecting and destroying primarily  $CD4^+$  T cells. The end stage of HIV viral progression is acquired immune deficiency syndrome (AIDS) (see, for example, [1]), identified when the count of individual's  $CD4^+$  cells count falls below 200. Since AIDS was found in America in 1981, it spread worldwide and became the public health and social problem which causes serious damage to human survival and development. In 2016, there exist about 38 million people living with human immunodeficiency virus (HIV) (see, for example, [2]). Thus, it is a challenge to study and control the virus.

It is widely known that mathematical models have made considerable contributions to understanding the HIV infection dynamics. Nowak et al. have proposed a class of classic mathematical model to describe HIV infection dynamics (see, for example, [3–6]),

$$\begin{aligned}\dot{x}(t) &= s - dx(t) - \beta x(t)v(t), \\ \dot{y}(t) &= \beta x(t)v(t) - py(t), \\ \dot{v}(t) &= ky(t) - uv(t),\end{aligned}\tag{1}$$

where  $x(t)$ ,  $y(t)$ , and  $v(t)$  denote the concentrations of uninfected cells, infected cells, and free virus at time  $t$ , respectively. Uninfected cells are produced at the rate  $s$  ( $s > 0$ ), die at the rate  $d$  ( $d > 0$ ), and become infected at the rate  $\beta$  ( $\beta > 0$ ). The constant  $p$  ( $p > 0$ ) is the death rate of the infected cells due either to virus or to the immune system. The constant  $k$  ( $k > 0$ ) is the rate of production of virus by infected cells and the constant  $u$  ( $u > 0$ ) is the rate at which the virus is cleared.

Incorporating the life cycle of the virus in the cells, some researchers have considered that the HIV virus from HIV infection to produce new virus takes time. To make a better understanding for this phenomenon in mathematics, HIV models including time delay have been proposed (see, for example, [4, 7–9]). Several researchers have considered that when T cells stimulate by antigen or mitogen, this will differentiate and increase in the number. The HIV model with a full logistic mitosis term has been investigated (see, for example, [6, 10, 11]). Taking into account the growth of uninfected cells, they made a further investigation to add a full logistic term  $rx(t)(1 - (x(t) + y(t))/T)$  (see, for example, [12, 13]).

In the above model, there are two factors that accelerate the reduction of uninfected cells: one is the natural death of uninfected cells and the other is that uninfected

cells become infected cells. HIV gene expression products can be toxic and directly or indirectly induce apoptosis in uninfected cells. Some data show that viral proteins interact with uninfected cells and produce an apoptotic signals that accelerate the death of uninfected cells. Recently, Wang and Zhang proposed a spatial mathematical model to describe the predominance for driving CD4<sup>+</sup> T cells death, which is called caspase-1-mediated pyroptosis (see, for example, [14]).

Based on model (1), Guo and Ma have proposed a class of delay differential equations model of HIV infection dynamics with nonlinear transmissions and apoptosis induced by infected cells (see, for example, [15]). And then, Cheng et al. [16] have considered the following infection model with inhibitory effect on the growth of uninfected cells by infected cells:

$$\begin{aligned}\dot{x}(t) &= s - dx(t) - cx(t)y(t) - \beta x(t)v(t), \\ \dot{y}(t) &= \delta x(t - \tau)v(t - \tau) - py(t), \\ \dot{v}(t) &= ky(t) - uv(t),\end{aligned}\quad (2)$$

where the constant  $c$  ( $c > 0$ ) represents the rate of apoptosis at which infected cells induce uninfected cells.  $\delta$  ( $\delta > 0$ ) denotes the surviving rate of infected cells before they become productively infected. The biological meanings of the other parameters in the model (2) are similar to that in the model (1).

Motivated by the above models, in this paper, we will study a delay differential equation model of HIV infection with a full logistic term of uninfected cells,

$$\begin{aligned}\dot{x}(t) &= s + rx \left(1 - \frac{x(t) + y(t)}{T}\right) - dx(t) \\ &\quad - cx(t)y(t) - \beta x(t)v(t), \\ \dot{y}(t) &= \delta x(t - \tau)v(t - \tau) - py(t), \\ \dot{v}(t) &= ky(t) - uv(t).\end{aligned}\quad (3)$$

In this model, the logistic growth of the healthy CD4<sup>+</sup> T cells is described by  $rx(t)(1 - (x(t) + y(t))/T)$ . The total concentration of CD4<sup>+</sup> T cells is  $x(t) + y(t)$ , where  $x(t)$  denotes the concentration of uninfected cells,  $y(t)$  is the concentration of infected cells, and  $T$  is the maximum level of CD4<sup>+</sup> T cells.  $\delta$  ( $\delta > 0$ ) is the infection rate of infected cells. The biological meanings of the other parameters in the model (3) are similar to that in the model (2).

The main purpose of this paper is to carry out a pretty theoretical analysis on the stability of the equilibria of the model (3) and to analyze the Hopf bifurcation by related theories of the differential equations. The organization of this paper is as follows. In Section 2, we investigate the existence and the ultimate boundedness of the solutions of the model (3). Then we consider the global stability of the uninfected equilibrium and the Hopf bifurcation at the infected equilibrium. In Section 3, some properties of Hopf bifurcation such as direction, stability, and period are determined. In Section 4, the brief conclusions are given and sets of numerical simulations are provided to illustrate the main results.

## 2. Local and Global Stability of the Equilibria

According to biological meanings, we assume that the initial condition of the model (3) is given as follows:

$$\begin{aligned}x(\theta) &= \phi_1(\theta), \\ y(\theta) &= \phi_2(\theta), \\ v(\theta) &= \phi_3(\theta)\end{aligned}\quad (4)$$

$(\theta \in [-\tau, 0]),$

where  $\phi = (\phi_1, \phi_2, \phi_3)^T \in C$  such that  $\phi_i(\theta) \geq 0$  ( $i = 1, 2, 3$ ). Here,  $C = C([-\tau, 0]; R_+^3)$  denotes the Banach space of continuous functions mapping from the interval  $[-\tau, 0]$  to  $R_+^3$  equipped with the supnorm.

The existence and uniqueness, nonnegativity, and boundedness of the solutions of the model (3) with the initial condition (4) can be given as follows.

**Theorem 1.** *The solution  $(x(t), y(t), v(t))$  of the model (3) with the initial condition (4) is existent, unique, and nonnegative on  $[0, +\infty)$  and also has*

$$\begin{aligned}\limsup_{t \rightarrow +\infty} x(t) &\leq x_0, \\ \limsup_{t \rightarrow +\infty} (x(t) + y(t + \tau)) &\leq \frac{s + rx_0}{\tilde{d}}, \\ \limsup_{t \rightarrow +\infty} v(t) &\leq \frac{k(s + rx_0)}{u\tilde{d}},\end{aligned}\quad (5)$$

where  $\tilde{d} = \min\{d, p\}$  and  $x_0 = (T/2r)(r - d + \sqrt{(r - d)^2 + 4sr/T})$ .

In fact, by using standard theorems for existence and uniqueness of functional differential equations (see, for example, [17–19]), we can show that the solution  $(x(t), y(t), v(t))$  of the model (3) with the initial condition (4) is existent, unique and nonnegative on  $[0, +\infty)$ , easily. And the proving of ultimately bounded of the solution  $(x(t), y(t), v(t))$  is similar to [12, 16].

We can denote the basic reproduction number of the HIV virus for the model (3) as  $R_0 = (k\delta/pu)x_0$  (see, for example, [3]). For the existence of nonnegative equilibria of the model (3), we can obtain the following classifications:

(i) The model (3) always has the uninfected equilibrium  $E_0 = (x_0, 0, 0)$ .

(ii) If  $R_0 = (k\delta/pu)x_0 > 1$ , the model (3) has unique infected equilibrium  $E^* = (x^*, y^*, v^*)$ , where

$$\begin{aligned}x^* &= \frac{pu}{\delta k}, \\ y^* &= \frac{u}{k}v^*, \\ v^* &= \frac{-rx^{*2}/T + (r - d)x^* + s}{rx^*u/kT + (cu/k)x^* + \beta x^*}.\end{aligned}\quad (6)$$

**Theorem 2.** *If  $R_0 < 1$ , the uninfected equilibrium  $E_0$  of the model (3) is globally asymptotically stable.*

*Proof.* We consider linear system of the model (3) at  $E_0$ , we have

$$\begin{aligned} \dot{x}(t) &= \left(r - d - \frac{2r}{T}x_0\right)x(t) - \left(\frac{r}{T} + c\right)x_0y(t) \\ &\quad - \beta x_0v(t), \\ \dot{y}(t) &= \delta x_0v(t - \tau) - py(t), \\ \dot{v}(t) &= ky(t) - uv(t). \end{aligned} \quad (7)$$

The corresponding characteristic equation is given by

$$\left(\lambda - r + d + \frac{2r}{T}x_0\right) \left[(\lambda + p)(\lambda + u) - k\delta x_0 e^{-\lambda\tau}\right] = 0. \quad (8)$$

Clearly, one of the roots is  $\lambda_1 = r - d - (2r/T)x_0 = -\sqrt{(r-d)^2 + 4rs/T} < 0$ , so the local stability depends on the other two roots generated by

$$\lambda^2 + (p+u)\lambda + pu - k\delta x_0 e^{-\lambda\tau} = 0. \quad (9)$$

When  $R_0 < 1$ ,  $pu - k\delta x_0 \neq 0$ . Therefore,  $\lambda = 0$  is not root of (9). If (9) has pure imaginary root  $\lambda = i\omega$  ( $\omega > 0$ ) for some  $\tau > 0$ , substituting it into (9) and separating the real and imaginary parts, it has

$$\begin{aligned} pu - \omega^2 &= k\delta x_0 \cos \omega\tau, \\ (p+u)\omega &= -k\delta x_0 \sin \omega\tau. \end{aligned} \quad (10)$$

It follows that

$$f(\tilde{\omega}) \equiv \tilde{\omega}^2 + (p^2 + u^2)\tilde{\omega} + p^2u^2 - k^2\delta^2x_0^2 = 0, \quad (11)$$

where  $\tilde{\omega} = \omega^2$ . Since  $p^2 + u^2 > 0$ ,  $p^2u^2 - k^2\delta^2x_0^2 = p^2u^2(1 - R_0^2) > 0$ , we have  $f(\tilde{\omega}) > 0$ , which contradicts  $f(\tilde{\omega}) = 0$ . This suggests that all the roots of (8) have negative real parts for any time delay  $\tau \geq 0$ . Therefore, the uninfected equilibrium  $E_0$  of the model (3) is locally asymptotically stable.

Define

$$G = \{\phi = (\phi_1, \phi_2, \phi_3) \in C \mid 0 \leq \|\phi_1\| \leq x_0, \phi_2 \geq 0, \phi_3 \geq 0\}. \quad (12)$$

It is easy to show that  $G$  attracts all solutions of the model (3) and is also positively invariant with respect to the model (3).

Motivated by the methods in [20, 21], we choose the following Liapunov functional:

$$L(\phi) = \frac{1}{\delta}\phi_2(0) + \frac{p}{\delta k}\phi_3(0) + \int_{-\tau}^0 \phi_1(\theta)\phi_3(\theta) d\theta \quad (13)$$

for any  $\phi \in G$ . The time derivative of  $L$  along the solutions of the model (3) is

$$\begin{aligned} \dot{L} &= \frac{1}{\delta}y'(t) + \frac{p}{\delta k}v'(t) + x(t)v(t) - x(t-\tau)v(t-\tau) \\ &= \left(x(t) - \frac{up}{k\delta}\right)v(t) \leq \left(x_0 - \frac{up}{k\delta}\right)v(t) \\ &= \left(1 - \frac{1}{R_0}\right)x_0v(t) \leq 0, \end{aligned} \quad (14)$$

where  $t \geq 0$ . By using Liapunov-LaSalle invariance principle [18], the uninfected equilibrium  $E_0$  of the model (3) is globally asymptotically stable.

Next, let us study the stability of the infected equilibrium  $E^*$ . The linearized system of the model (3) at  $E^*$  is

$$\begin{aligned} \frac{d}{dt}x(t) &= -\left(\frac{s}{x^*} + \frac{rx^*}{T}\right)x(t) - \frac{rx^*}{T}y(t) - \beta x^*v(t) \\ &\quad - cx^*y(t), \\ \frac{d}{dt}y(t) &= \delta [x^*v(t-\tau) + x(t-\tau)v^*] - py(t), \\ \frac{d}{dt}v(t) &= ky(t) - uv(t). \end{aligned} \quad (15)$$

Denote

$$\begin{aligned} B &= \frac{s}{x^*} + \frac{rx^*}{T}, \\ E &= \left(\frac{r}{T} + c\right)x^*, \\ F &= \beta x^*, \\ G &= \delta v^*, \\ H &= \delta x^*. \end{aligned} \quad (16)$$

The corresponding characteristic equation is

$$\begin{aligned} \lambda^3 + (B+p+u)\lambda^2 + (Bp+uB+up)\lambda + uBp \\ + [(EG-kH)\lambda + (kGF+uEG-kBH)]e^{-\lambda\tau} \\ = 0. \end{aligned} \quad (17)$$

Define

$$\begin{aligned} a_1 &= B+p+u > 0, \\ a_2 &= Bp+uB+up > 0, \\ a_3 &= uBp > 0, \\ b_2 &= EG-kH, \\ b_3 &= kGF+uEG-kBH, \end{aligned} \quad (18)$$

where  $b_2 = pu(rv^*/kT - 1) + c\delta x^*v^*$  and  $b_3 = pu(\beta v^* + ruv^*/kT - B) + c\delta ux^*v^*$ .

Therefore, (17) becomes

$$\lambda^3 + a_1\lambda^2 + a_2\lambda + a_3 + [b_2\lambda + b_3]e^{-\lambda\tau} = 0. \quad (19)$$

When  $\tau = 0$ , (19) becomes  $\lambda^3 + a_1\lambda^2 + (a_2+b_2)\lambda + (a_3+b_3) = 0$ . Notice that  $a_1 > 0$ ,  $a_3+b_3 = pu(\beta v^* + ruv^*/kT) + c\delta ux^*v^* > 0$ . Thus, if  $R_0 > 1$  and  $\Delta_2 = a_1(a_2+b_2) - (a_3+b_3) > 0$  hold, by Routh-Hurwitz criterion, the infected equilibrium  $E^*$  is locally asymptotically stable when  $\tau = 0$ .

Now, let us investigate the stability of  $E^*$  when  $\tau > 0$ . Rewriting (19) as

$$P(\lambda) + Q(\lambda)e^{-\lambda\tau} = 0, \quad (20)$$

where

$$\begin{aligned} P(\lambda) &= \lambda^3 + a_1\lambda^2 + a_2\lambda + a_3, \\ Q(\lambda) &= b_2\lambda + b_3. \end{aligned} \quad (21)$$

Since  $a_3 + b_3 = uBp + pu(\beta v^* + ruv^*/kT - B) + c\delta ux^* v^* > 0$ ,  $\lambda = 0$  is not the root of (19). Assume that (19) has pure imaginary  $\lambda = iw$  ( $w > 0$ ) for some  $\tau > 0$ ; substituting it into (19), it has  $-iw^3 - a_1w^2 + ia_2w + a_3 + (ib_2w + b_3)(\cos w\tau - i \sin w\tau) = 0$ , and separating the real and imaginary parts, we have

$$\begin{aligned} w^3 - a_2w &= b_2w \cos w\tau - b_3 \sin w\tau, \\ a_1w^2 - a_3 &= b_2w \sin w\tau + b_3 \cos w\tau. \end{aligned} \quad (22)$$

Therefore, it has

$$w^6 + c_1w^4 + c_2w^2 + c_3 = 0, \quad (23)$$

where  $c_1 = a_1^2 - 2a_2$ ,  $c_2 = a_2^2 - 2a_1a_3 - b_2^2$ ,  $c_3 = a_3^2 - b_3^2$ . Denote  $v = w^2$ ; (23) becomes

$$v^3 + c_1v^2 + c_2v + c_3 = 0. \quad (24)$$

Define

$$h(v) = v^3 + c_1v^2 + c_2v + c_3, \quad (25)$$

hence  $h'(v) = 3v^2 + 2c_1v + c_2$ . Considering

$$3v^2 + 2c_1v + c_2 = 0. \quad (26)$$

It has two real roots, given as  $v_1 = (-c_1 + \sqrt{\Delta})/3$  and  $v_2 = (-c_1 - \sqrt{\Delta})/3$ , where  $\Delta = c_1^2 - 3c_2$ .

Now, we will illustrate the following conclusions, and it has been proved in [22].  $\square$

**Lemma 3.** For the polynomial (24), the following conclusions are given:

- (i) If  $c_3 < 0$ , (24) has at least one positive root.
- (ii) If  $c_3 \geq 0$  and  $\Delta < 0$ , (24) has no real root.
- (iii) If  $c_3 \geq 0$  and  $\Delta > 0$ , if and only if  $v_1 = (-c_1 + \sqrt{\Delta})/3 > 0$  and  $h(v_1) \leq 0$ , (24) has real roots.

Assume that  $h(v) = 0$  has positive real roots. Generally, we may suppose that (24) has  $k$  ( $1 \leq k \leq 3$ ) positive real roots, denoted as  $v_1, v_2$ , and  $v_3$ . Then, (23) has positive real roots  $\omega_k = \sqrt{v_k}$ . From (22), we attain

$$\cos w\tau = \frac{b_2w^4 + (a_1b_3 - a_2b_2)w^2 - a_3b_3}{b_2^2w^2 + b_3^2}. \quad (27)$$

Then, we get the corresponding  $\tau_k^{(n)} > 0$  such that (19) has pure imaginary  $\lambda = iw_k$ , where

$$\begin{aligned} \tau_k^{(n)} &= \frac{1}{w_k} \left\{ \arccos \left( \frac{b_2w_k^4 + (a_1b_3 - a_2b_2)w_k^2 - a_3b_3}{b_2^2w_k^2 + b_3^2} \right) \right. \\ &\quad \left. + 2n\pi \right\}, \quad k = 1, 2, 3, \quad n = 0, 1, 2, \dots \end{aligned} \quad (28)$$

Define

$$\tau^* = \min_{k \in [1, 2, 3]} \{ \tau_k^{(0)} \}. \quad (29)$$

Differentiating the two sides of (19) with respect to  $\tau$ , it follows that

$$\begin{aligned} (3\lambda^2 + 2a_1\lambda + a_2) \frac{d\lambda}{d\tau} + b_2e^{-\lambda\tau} \frac{d\lambda}{d\tau} \\ - \tau(b_2\lambda + b_3)e^{-\lambda\tau} \frac{d\lambda}{d\tau} - \lambda(b_2\lambda + b_3)e^{-\lambda\tau} = 0. \end{aligned} \quad (30)$$

Thus, we get

$$\begin{aligned} \left( \frac{d\lambda}{d\tau} \right)_{\lambda=iw_k}^{-1} &= \frac{(a_2 - 3w_k^2) + 2a_1w_k i}{(a_2w_k^2 - w_k^4) - (a_3w_k - a_1w_k^3) i} \\ &\quad + \frac{b_2}{-b_2w_k^2 + b_3w_k i}. \end{aligned} \quad (31)$$

Then

$$\begin{aligned} \left[ \frac{d(\text{Res}(\lambda))}{d\tau} \right]_{\lambda=iw_k}^{-1} \\ = \frac{(a_2 - 3w_k^2)(a_2w_k^2 - w_k^4) - 2a_1w_k(a_3w_k - a_1w_k^3)}{(a_2w_k^2 - w_k^4)^2 + (a_3w_k - a_1w_k^3)^2} \\ + \frac{-b_2^2w_k^2}{-b_2^2w_k^4 + b_3^2w_k^2}. \end{aligned} \quad (32)$$

From (22), we obtain  $b_2^2w^2 + b_3^2 = (w^3 - a_2w)^2 + (a_1w^2 - a_3)^2$ . Therefore,

$$\begin{aligned} \left[ \frac{d(\text{Res}(\lambda))}{d\tau} \right]_{\lambda=iw_k}^{-1} &= \frac{3v_k^3 + 2c_1v_k^2 + c_2v_k}{w_k^2 [b_2^2w_k^2 + b_3^2]} \\ &= \frac{v_k h'(v_k)}{w_k^2 [b_2^2w_k^2 + b_3^2]}. \end{aligned} \quad (L)$$

Since  $v_k > 0$ , we get  $\text{Re}(d\lambda(\tau)/d\tau)|_{\tau=\tau_k^{(n)}}$  and  $h'(v_k)$  have the same sign. Combining Lemma 3 with the above (L), we have the following conclusions.

**Theorem 4.**  $\tau_k^{(n)}$  and  $\tau^*$  are defined by (28) and (29). If  $R_0 > 1$ , the following results hold:

- (i) If  $c_3 \geq 0$  and  $\Delta \leq 0$ , then infected equilibrium  $E^*(x^*, y^*, v^*)$  is locally asymptotically stable.
- (ii) If  $c_3 < 0$  or  $c_3 \geq 0$  and  $\Delta > 0$ , then infected equilibrium  $E^*(x^*, y^*, v^*)$  is locally asymptotically stable when  $\tau \in [0, \tau^*)$  and unstable when  $\tau > \tau^*$ .
- (iii) If the conditions of (ii) are all satisfied and  $h'(v_k) \neq 0$ , then model (3) undergoes a Hopf bifurcation at  $E^*$  when  $\tau = \tau_k^{(n)}$  ( $n = 0, 1, 2, \dots$ ).

### 3. Properties of Hopf Bifurcation

In the above section, we have given the sufficient condition where the model (3) undergoes a Hopf bifurcation at  $E^*$ . In this section, we will use the normal form method and the center manifold theory provided in [23, 24] to analysis direction, stability, and the period of the bifurcating periodic solution. By setting  $\tau = \tau^* + \mu$ , then  $\mu = 0$  is a Hopf bifurcation value of the model (3). Let  $\mu_1 = x - x^*$ ,  $\mu_2 = y - y^*$ ,  $\mu_3 = v - v^*$ , and

$$\begin{aligned} u(t) &= (\mu_1(t), \mu_2(t), \mu_3(t))^T \in \mathbb{R}_+^3, \\ u_t(\theta) &= u(t + \theta) \quad (\theta \in [-\tau, 0]). \end{aligned} \quad (33)$$

Then, the model (3) is equivalent to the functional differential equations  $\dot{u}_t = L_\mu(u_t) + f(\mu, u_t)$ , defined in  $C := C([-\tau, 0], \mathbb{R}_+^3)$ , where

$$\begin{aligned} f(\mu, \varphi) &= \begin{pmatrix} -\frac{r}{T}\varphi_1^2(0) - \left(\frac{r}{T} + c\right)\varphi_1(0)\varphi_2(0) - \beta\varphi_1(0)\varphi_3(0) \\ \delta\varphi_1(-\tau)\varphi_3(-\tau) \\ 0 \end{pmatrix}. \end{aligned} \quad (34)$$

For  $\varphi = (\varphi_1, \varphi_2, \varphi_3)^T \in C$ , define  $L_\mu\varphi = A\varphi(0) + D\varphi(-\tau)$ . Here,

$$\begin{aligned} A &= \begin{pmatrix} -B & -E & -F \\ 0 & 0 & H \\ 0 & 0 & 0 \end{pmatrix}, \\ D &= \begin{pmatrix} 0 & 0 & 0 \\ G & -p & 0 \\ 0 & k & -u \end{pmatrix}. \end{aligned} \quad (35)$$

Using the Riesz representation theorem, there is a  $3 \times 3$  bounded variation matrix function  $\eta(\theta, \mu)$ , which exists for  $\theta \in [-\tau, 0]$ , such that  $L_\mu\varphi = \int_{-\tau}^0 d\eta(\theta, \mu)\varphi(\theta)$  holds for any  $\varphi \in C$ . We can choose  $\eta(\theta, \mu) = A\rho(\theta) - D\rho(\theta + \tau)$ , where

$$\rho(\theta) = \begin{cases} 1, & \theta = 0, \\ 0, & \theta \neq 0. \end{cases} \quad (36)$$

For  $\varphi \in C([-\tau, 0], \mathbb{R}^3)$ , define

$$\begin{aligned} A(\mu)\varphi &= \begin{cases} \frac{d\varphi(\theta)}{d\theta}, & \theta \in [-\tau, 0), \\ \int_{-\tau}^0 d\eta(s, \mu)\varphi(s), & \theta = 0, \end{cases} \\ R\varphi &= \begin{cases} 0, & \theta \in [-\tau, 0), \\ f(\mu, \varphi), & \theta = 0. \end{cases} \end{aligned} \quad (37)$$

Then, the system is equivalent to the following operator equation:

$$\dot{u}_t = A(\mu)u_t + Ru_t. \quad (38)$$

Let  $C^* = C([0, \tau], (\mathbb{R}^3)^*)$ , and adjoint operator  $A^*$  of  $A$  is defined by

$$A^*\psi(\xi) = \begin{cases} -\frac{d\psi(\xi)}{d\xi}, & \xi \in (0, \tau], \\ \int_{-\tau}^0 d\eta(s, 0)\psi(-s), & \xi = 0. \end{cases} \quad (39)$$

Define the bilinear inner product of  $\varphi \in C$  and  $\psi \in C^*$  as

$$\begin{aligned} \langle \psi(\xi), \varphi(\theta) \rangle &= \overline{\psi}(0)\varphi(0) \\ &\quad - \int_{\theta=-\tau}^0 \int_{s=0}^{\theta} \overline{\psi}(s-\theta)d\eta(\theta)\varphi(s)ds, \end{aligned} \quad (40)$$

where  $\eta(\theta) = \eta(\theta, 0)$ .

Since  $A(0)$  and  $A^*(0)$  are adjoint operator and  $\pm i\omega^*$  is the eigenvalue of  $A(0)$ , therefore  $\pm i\omega^*$  also is the eigenvalue of  $A^*$ . Suppose that the eigenvector of  $A(0)$  with respect to the eigenvalue  $i\omega^*$  is  $q(\theta)$ ; the eigenvector of  $A^*$  with respect to the eigenvalue  $-i\omega^*$  is  $q^*(\xi)$ , and they all satisfy  $\langle q^*(\xi), q(\theta) \rangle = 1$ .

We choose  $q(\theta) = (1, q_2, q_3)^T e^{i\omega^*\theta}$ ,  $\theta \in [-\tau, 0]$ , and  $q^*(\xi) = \overline{R}(1, \overline{q}_2^*, \overline{q}_3^*) e^{i\omega^*\xi}$ ,  $\xi \in [0, \tau]$ . Since  $A(0)q(\theta) = i\omega^*q(\theta)$ ,  $A^*q^*(\xi) = -i\omega^*q^*(\xi)$ , we get

$$\begin{aligned} q_2 &= -\frac{(i\omega^* + u)(i\omega^* + B)}{E(i\omega^* + u) + kF}, \\ q_3 &= -\frac{k(i\omega^* + B)}{E(i\omega^* + u) + kF}, \\ q_2^* &= -\frac{i\omega^* - B}{Ge^{i\omega^*\tau^*}}, \\ q_3^* &= \frac{E}{k} + \frac{(i\omega^* - B)(i\omega^* - s)}{kGe^{i\omega^*\tau^*}}. \end{aligned} \quad (41)$$

From  $\langle q^*(\xi), q(\theta) \rangle = 1$  and the similar arguments as in [20–22], we attain the following formula:

$$R = \left[ 1 + \overline{q}_2^*q_2 + \overline{q}_3^*q_3 + \overline{q}_2^*\tau^*(G + q_3H)e^{-i\omega^*\tau^*} \right]^{-1}. \quad (42)$$

Following the algorithms given in [23] (see, also [13, 24–26]), it then follows that

$$\begin{aligned} g_{20} &= 2R \left[ -\frac{r}{T}(1 + q_2) - cq_2 - \beta q_3 + \overline{q}_2^*q_3\delta e^{-2i\omega^*\tau^*} \right], \\ g_{11} &= R \left[ -\frac{r}{T}(2 + q_2 + \overline{q}_2) - c(q_2 + \overline{q}_2) - \beta(q_3 + \overline{q}_3) \right. \\ &\quad \left. + \overline{q}_2^*\delta(q_3 + \overline{q}_3) \right], \\ g_{02} &= 2R \left[ -\frac{r}{T}(1 + \overline{q}_2) - c\overline{q}_2 - \beta\overline{q}_3 + \overline{q}_2^*\overline{q}_3\delta e^{2i\omega^*\tau^*} \right], \end{aligned}$$

$$\begin{aligned}
g_{21} = 2R & \left\{ -\frac{r}{T} \left[ 2\omega_{11}^{(1)}(0) + \omega_{20}^{(1)}(0) + \omega_{11}^{(2)}(0) \right. \right. \\
& + \frac{\omega_{20}^{(2)}(0)}{2} + q_2 \frac{-\omega_{20}^{(1)}(0)}{2} + q_2 \omega_{11}^{(1)}(0) \left. \right] \\
& - c \left[ \omega_{11}^{(2)}(0) + \frac{\omega_{20}^{(2)}(0)}{2} + q_2 \frac{-\omega_{20}^{(1)}(0)}{2} \right. \\
& + q_2 \omega_{11}^{(1)}(0) \left. \right] - \beta \left[ \omega_{11}^{(3)}(0) + \frac{\omega_{20}^{(3)}(0)}{2} \right. \\
& + q_3 \frac{-\omega_{20}^{(1)}(0)}{2} + q_3 \omega_{11}^{(1)}(0) \left. \right] \\
& + \overline{q_2}^* \delta \left[ \frac{\omega_{20}^{(3)}(-\tau^*)}{2} e^{i\omega^* \tau^*} + \omega_{20}^{(3)}(-\tau^*) e^{i\omega^* \tau^*} \right. \\
& \left. + \overline{q_3}^* \omega_{11}^{(1)}(-\tau^*) e^{i\omega^* \tau^*} \right] \left. \right\}, \tag{43}
\end{aligned}$$

where

$$\begin{aligned}
\omega_{20}(\theta) &= \frac{i g_{20}}{\omega^*} q(0) e^{i\omega^* \theta} + \frac{i \overline{g_{02}}}{3\omega^*} \overline{q}(0) e^{-i\omega^* \theta} + E_1 e^{2i\omega^* \theta}, \\
\omega_{11}(\theta) &= \frac{i g_{11}}{\omega^*} q(0) e^{i\omega^* \theta} + \frac{i \overline{g_{11}}}{\omega^*} \overline{q}(0) e^{-i\omega^* \theta} + E_2, \\
E_1 &= 2 \begin{pmatrix} 2i\omega^* + B & E & F \\ -G e^{-2i\omega^* \tau^*} & -2i\omega^* + p & -H e^{-2i\omega^* \tau^*} \\ 0 & -k & 2i\omega^* + u \end{pmatrix}^{-1} \\
&\times \begin{pmatrix} -\frac{r}{T} - \frac{r}{T} q_2 - c q_2 - \beta q_3 \\ \delta q_3 e^{-2i\omega^* \tau^*} \\ 0 \end{pmatrix}, \tag{44} \\
E_2 &= \begin{pmatrix} B & E & F \\ -G & p & -H \\ 0 & -k & u \end{pmatrix}^{-1} \\
&\times \begin{pmatrix} -\frac{2r}{T} - \frac{r}{T} (q_2 + \overline{q_2}) - c (q_2 + \overline{q_2}) - \beta (q_3 + \overline{q_3}) \\ \delta (q_3 + \overline{q_3}) \\ 0 \end{pmatrix}.
\end{aligned}$$

Then we can obtain the following quantities:

$$\begin{aligned}
C_1(0) &= \frac{i}{2\omega^*} \left( g_{11} g_{20} - 2 |g_{11}|^2 - \frac{|g_{02}|^2}{3} \right) + \frac{g_{21}}{2}, \\
\mu_2 &= -\frac{\operatorname{Re}(C_1(0))}{\operatorname{Re}(\lambda'(\tau^*))}, \\
\beta_2 &= 2 \operatorname{Re}(C_1(0)),
\end{aligned}$$

$$T_2 = -\frac{\operatorname{Im}(C_1(0)) + \mu_2 \operatorname{Im}(\lambda'(\tau^*))}{\omega^*}. \tag{45}$$

These quantities determine the properties of bifurcating periodic solutions. From the previous discussions, we have the following conclusions.

**Theorem 5.** *Suppose that the conditions in (iii) of Theorem 4 hold, then the infected equilibrium  $E^*$  undergoes a Hopf bifurcation at  $\tau = \tau^*$ , and  $\mu_2, \beta_2, T_2$  determine the direction, stability, and period of the Hopf bifurcation, respectively,*

- (i) *If  $\mu_2 > 0$ , a bifurcating periodic solution exists in the sufficiently small  $\tau^*$ -neighbourhood.*
- (ii) *If  $\beta_2 < 0$  ( $\beta_2 > 0$ ), the bifurcating periodic solution is stable (unstable) when  $t \rightarrow +\infty$  ( $t \rightarrow -\infty$ ).*
- (iii) *If  $T_2 < 0$  ( $T_2 > 0$ ), the period of the bifurcating periodic solution decreases (increases).*

#### 4. Simulations and Conclusions

For the main results in Sections 2 and 3, we now give some numerical simulations.

Based on the numerical simulations in [16, 27–29], take the following data:

$$\begin{aligned}
s &= 0.1, \\
r &= 0.01, \\
T &= 200, \\
d &= 0.02, \\
c &= 0.001, \\
\beta &= 0.0027, \\
\delta &= 0.002, \\
p &= 0.3, \\
k &= 0.1, \\
u &= 0.01.
\end{aligned} \tag{46}$$

We can get  $R_0 = 0.6363 < 1$  and  $E_0 = (9.5445, 0, 0)$  by direct calculations. The uninfected equilibrium  $E_0$  is globally asymptotically stable by Theorem 2. Figure 1 gives the curves and orbits of the model (3) with appropriate initial condition.

Furthermore, we also simulate the occurrence of Hopf bifurcations as the time delay  $\tau$  increases. Take the following data:

$$\begin{aligned}
s &= 0.1, \\
r &= 1.01, \\
T &= 200, \\
d &= 0.02,
\end{aligned}$$

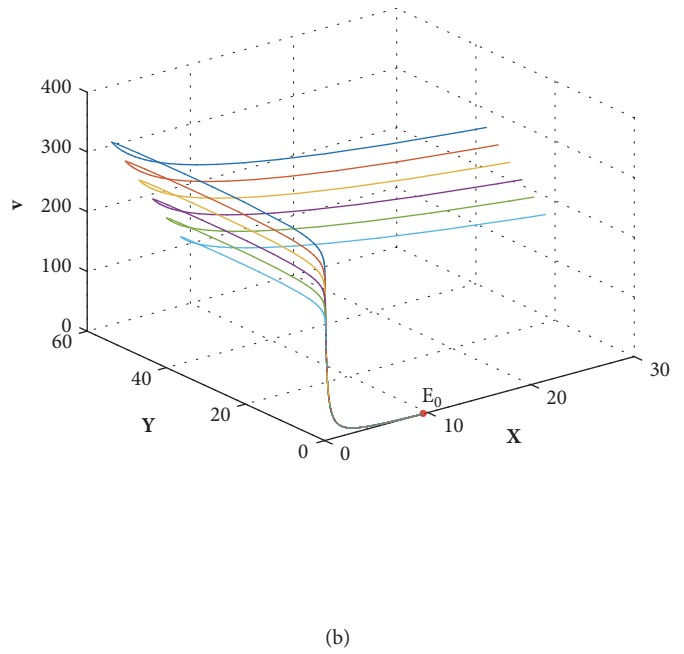
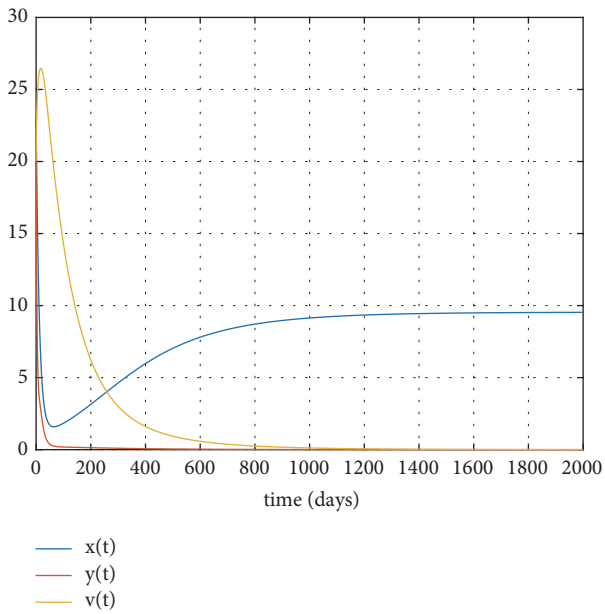


FIGURE 1: (a) The solution curves of the model (3) with  $R_0 < 1$ . (b) The orbits of the model (3) when  $R_0 < 1$ .

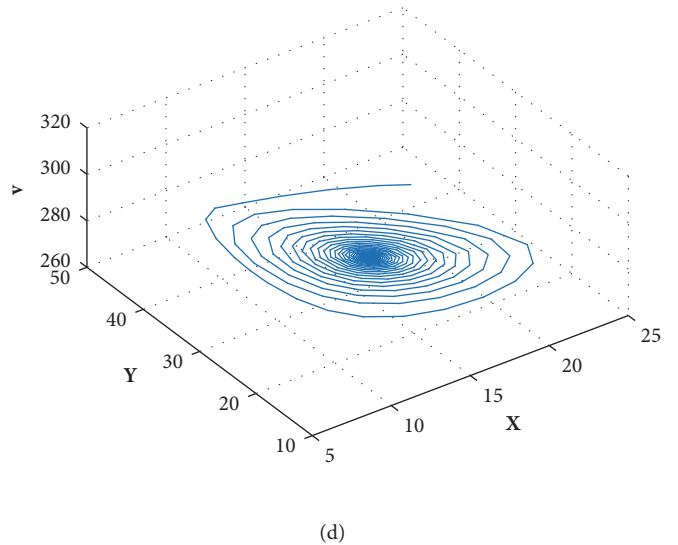
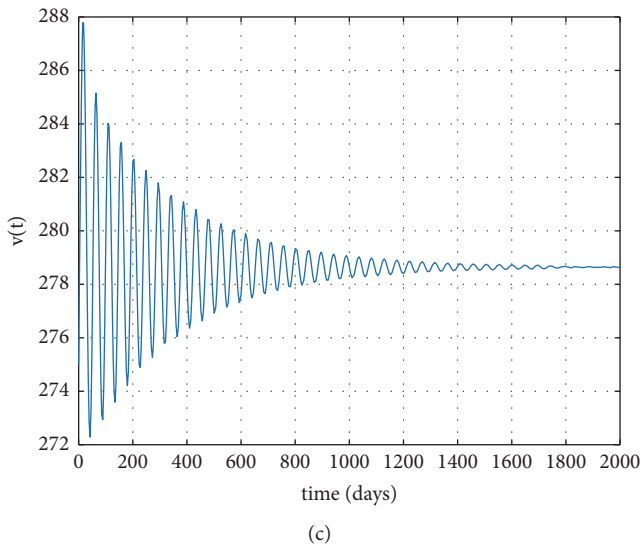
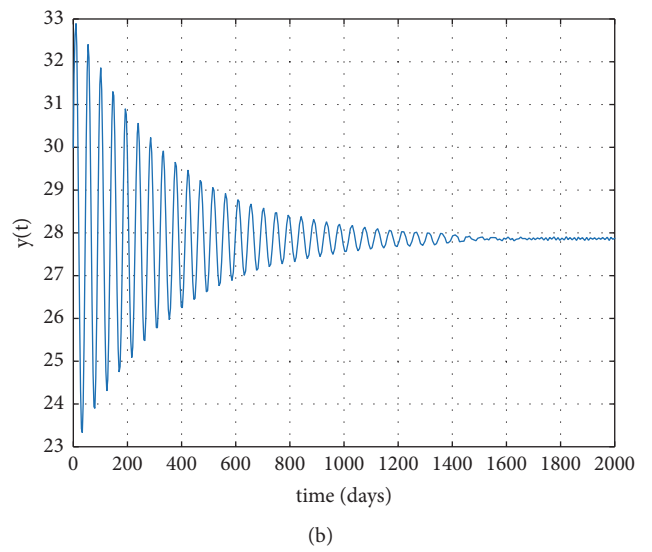
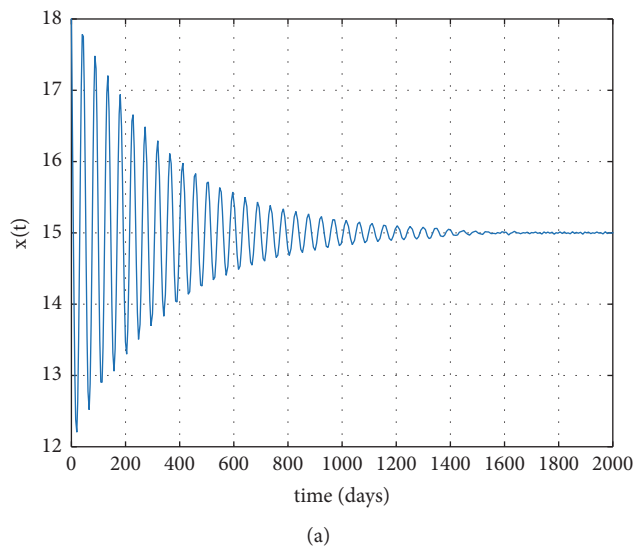


FIGURE 2: (a), (b), and (c) The solution curves of the model (3) with  $R_0 > 1$ ,  $\tau = 10 < \tau^*$ . (d) The orbits of the model (3) when  $R_0 > 1$ ,  $\tau = 10 < \tau^*$ .

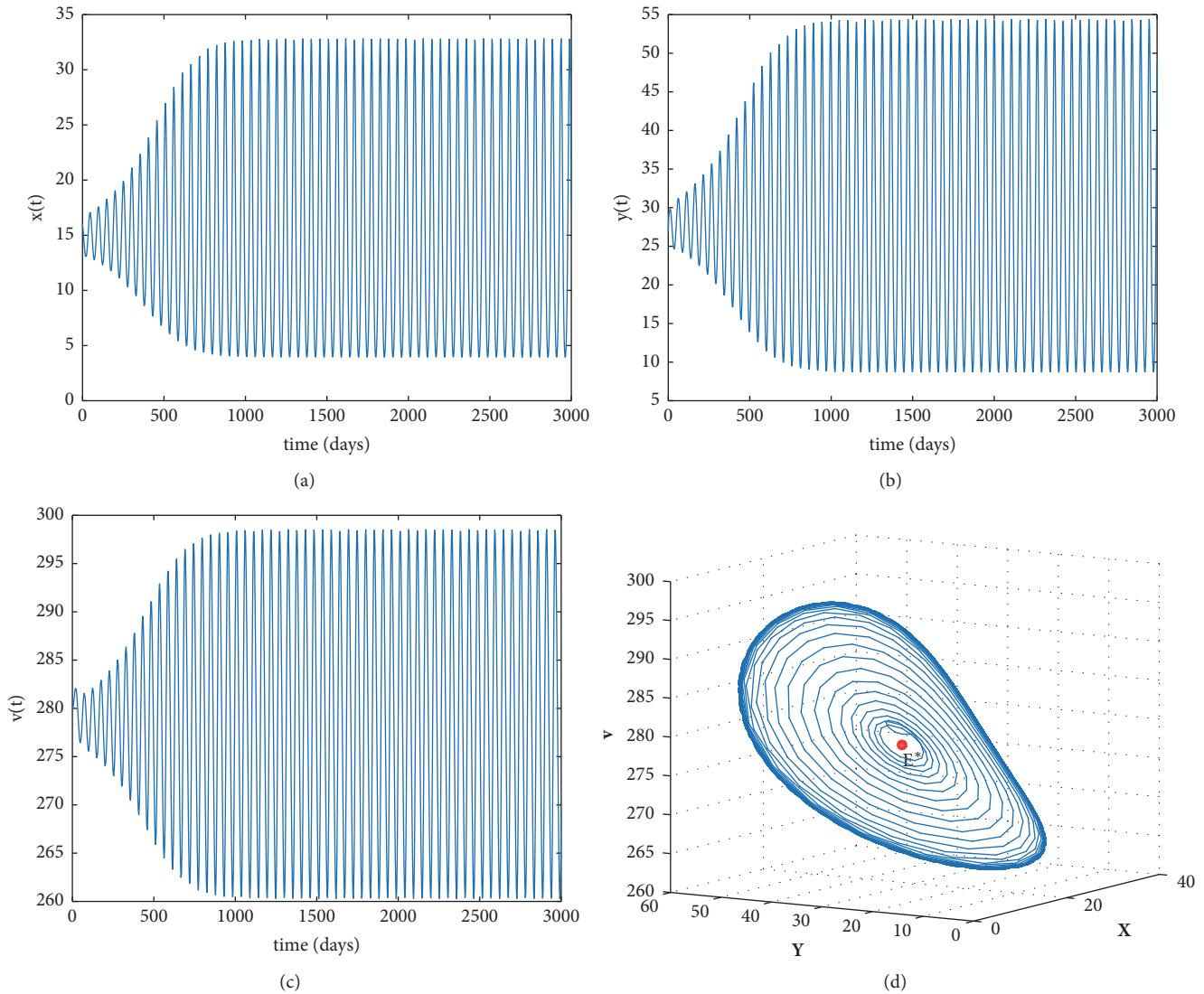


FIGURE 3: (a), (b), and (c) The solution curves of the model (3) with  $R_0 > 1$ ,  $\tau = 12 > \tau^*$ . (d) The orbits of the model (3) when  $R_0 > 1$ ,  $\tau = 12 > \tau^*$ .

$$\begin{aligned}
 c &= 0.001, \\
 \beta &= 0.0027, \\
 \delta &= 0.002, \\
 p &= 0.3, \\
 k &= 0.1, \\
 u &= 0.01.
 \end{aligned}
 \tag{47}$$

By direct calculations, we get that (24) has a positive root  $v^* = 0.0175 > 0$ ,  $R_0 = 13.0761 > 1$ , and  $E^* = (15, 27.8643, 278.6435)$ . And by simple computations, we attain  $\omega^* = 0.1322$ ,  $\tau^* = 10.6528$ , and  $h'(v^*) = 0.0027 \neq 0$ . From Theorem 4, the infected equilibrium  $E^*$  is locally asymptotically stable when  $0 < \tau < \tau^*$  and unstable when

$\tau > \tau^*$ . Figure 2 gives the stable phase trajectories and orbits of the model (3) when  $\tau = 10 < \tau^*$ . Figure 3 gives the phase trajectories and orbits of model (3) when  $\tau = 12 > \tau^*$  and it suggests that Hopf bifurcations occur. From (45), we obtain  $\text{Re}(C_1(0)) = -1.1035 \times 10^{-6} < 0$  for  $\tau = 12$ . Therefore, both bifurcating periodic solutions are stable.

In this paper, we have proposed a delay HIV infection model (3) with a full logistic term  $rx(1-(x(t)+y(t))/T)$ . Then, using the basic reproduction number  $R_0 = (k\delta/pu)x_0$ , we discuss the existence of the uninfected equilibrium  $E_0$  and the infected equilibrium  $E^* = (x^*, y^*, v^*)$ . By Routh-Hurwitz criterion, Liapunov-LaSalle invariance principle, and Hopf bifurcation method, we prove the following results.

If  $R_0 \leq 1$ , the uninfected equilibrium  $E_0$  is globally asymptotically stable when  $\tau \geq 0$ . That is to say, any solution  $(x(t), y(t), v(t))$  trends to  $E_0$ . Biologically, this means that the virus cannot successfully invade uninfected cells and will soon be cleared of the immune system. And as the time  $t$

increases, the virus will disappear. This suggests that we can control the disease by controlling the  $R_0$ .

If  $R_0 > 1$ , there exists a unique infected equilibrium  $E^*$ . The result of Theorem 4 implies that the time delay  $\tau$  can destabilize the stability of the infected equilibrium  $E^*$  and leads to the occurrence of Hopf bifurcations. And if  $\tau \in [0, \tau^*)$ , the infected equilibrium  $E^*$  is locally asymptotically stable. Biologically, this means that the HIV infection may become chronic. The infected equilibrium  $E^*$  will be unstable and Hopf bifurcation occurs under some conditions when the time delay  $\tau$  exceeds  $\tau^*$ . In biology, this implies that the concentrations of uninfected cells, infected cells, and free virus will first tend to be constants and then oscillate as the time delay  $\tau$  increases. In the immune response, this situation is very important for choosing the adequate drug treatment programs.

It can be found that the basic reproduction number  $R_0$  for the model (3) is not the same as that for model (2). It is independent on the constant  $c$ , which represents inhibitory effect on the growth of uninfected cells by infected cells. But  $R_0$  depends on the coefficient  $r$  of the full logistic term  $rx(1 - (x(t) + y(t))/T)$ . Furthermore, the value of  $x^*$  is independent on the coefficient  $r$ . And the values of  $y^*$  and  $v^*$  are the increasing functions with respect to  $r$ . And this paper shows that the time delay  $\tau$  can produce richer dynamic behavior. As the time delay increases, the stability changes and periodic oscillations occur.

## Data Availability

The data used to support the findings of this study are available from the corresponding author upon request.

## Conflicts of Interest

The authors declare that they have no conflicts of interest.

## Acknowledgments

This work is partly supported by the National Natural Science Foundation of China for W. Ma (no. 11471034).

## References

- [1] D. C. Douek, M. Roederer, and R. A. Koup, "Emerging concepts in the immunopathogenesis of AIDS," *Annual Review of Medicine*, vol. 60, pp. 471–484, 2009.
- [2] Y. Yan, P. Yan, L. Chen et al., "Research progress of AIDS treatment," *Chinese Journal of Zoonoses*, vol. 33, no. 5, pp. 383–388, 2017.
- [3] M. A. Nowak and C. R. M. Bangham, "Population dynamics of immune responses to persistent viruses," *Science*, vol. 272, no. 5258, pp. 74–79, 1996.
- [4] M. A. Nowak and R. M. May, *Virus Dynamics: Mathematics Principles of Immunology and Virology*, Oxford University Press, London, UK, 2000.
- [5] A. S. Perelson, A. U. Neumann, M. Markowitz, J. M. Leonard, and D. D. Ho, "HIV-1 dynamics in vivo: virion clearance rate, infected cell life-span, and viral generation time," *Science*, vol. 271, no. 5255, pp. 1582–1586, 1996.
- [6] A. S. Perelson and P. W. Nelson, "Mathematical analysis of HIV-1 dynamics in vivo," *SIAM Review*, vol. 41, no. 1, pp. 3–44, 1999.
- [7] A. V. M. Herz, S. Bonhoeffer, R. M. Anderson, R. M. May, and M. A. Nowak, "Viral dynamics in vivo: limitations on estimates of intracellular delay and virus decay," *Proceedings of the National Academy of Sciences of the United States of America*, vol. 93, no. 14, pp. 7247–7251, 1996.
- [8] J. Tam, "Delay effect in a model for virus replication," *Mathematical Medicine and Biology*, vol. 16, no. 1, pp. 29–37, 1999.
- [9] W. Wang and W. Ma, "A diffusive HIV infection model with nonlocal delayed transmission," *Applied Mathematics Letters*, vol. 75, pp. 96–101, 2018.
- [10] A. S. Perelson, D. E. Kirschner, and R. D. Boer, "Dynamics of HIV infection of CD4<sup>+</sup> T cells," *Mathematical Biosciences*, vol. 114, no. 1, pp. 81–125, 1993.
- [11] R. V. Culshaw and S. Ruan, "A delay-differential equation model of HIV infection of CD4<sup>+</sup> T-cells," *Mathematical Biosciences*, vol. 165, no. 1, pp. 27–39, 2000.
- [12] L. Wang and M. Y. Li, "Mathematical analysis of the global dynamics of a model for HIV infection of CD4<sup>+</sup> T cells," *Mathematical Biosciences*, vol. 200, no. 1, pp. 44–57, 2006.
- [13] P. Hao, D. Fan, J. Wei, and Q. Liu, "Dynamic behaviors of a delayed HIV model with stage-structure," *Communications in Nonlinear Science and Numerical Simulation*, vol. 17, no. 12, pp. 4753–4766, 2012.
- [14] W. Wang and T. Zhang, "Caspase-1-mediated pyroptosis of the predominance for driving CD4<sup>+</sup> T cells death: a nonlocal spatial mathematical model," *Bulletin of Mathematical Biology*, vol. 80, no. 3, pp. 540–582, 2018.
- [15] S. Guo and W. Ma, "Global behavior of delay differential equations model of HIV infection with apoptosis," *Discrete and Continuous Dynamical Systems - Series B*, vol. 21, no. 1, pp. 103–119, 2016.
- [16] W. Cheng, W. Ma, and S. Guo, "A class of virus dynamic model with inhibitory effect on the growth of uninfected T Cells caused by infected T Cells and its stability analysis," *Communications on Pure and Applied Analysis*, vol. 15, no. 3, pp. 795–806, 2016.
- [17] L. Chen, X. Meng, and J. Jiao, *Biodynamics*, Beijing Science Press, Beijing, China, 2009.
- [18] J. K. Hale and S. M. Verduyn Lunel, *Introduction to Functional-Differential Equations*, Springer, Berlin, Germany, 1993.
- [19] Y. Kuang, *Delay Differential Equations with Applications in Population Dynamics*, Academic Press, New York, NY, USA, 1993.
- [20] Y. Wang, Y. Zhou, J. Wu, and J. Heffernan, "Oscillatory viral dynamics in a delayed HIV pathogenesis model," *Mathematical Biosciences*, vol. 219, no. 2, pp. 104–112, 2009.
- [21] T. Zhang, X. Meng, and T. Zhang, "Global analysis for a delayed SIV model with direct and environmental transmissions," *Journal of Applied Analysis and Computation*, vol. 6, no. 2, pp. 479–491, 2016.
- [22] S. Ruan and J. Wei, "On the zeros of a third degree exponential polynomial with applications to a delayed model for the control of testosterone secretion," *IMA Journal of Mathematics Applied in Medicine and Biology*, vol. 18, no. 1, pp. 41–52, 2001.
- [23] B. D. Hassard, N. D. Kazarinoff, and Y.-H. Wan, *Theory and Applications of Hopf Bifurcation*, Cambridge University Press, 1981.

- [24] J. Wei, H. Wang, and W. Jiang, *Bifurcation Theory And Application of Delay Differential Equation*, Science Press, Beijing, China, 2012.
- [25] Z. Jiang and W. Ma, "Delayed feedback control and bifurcation analysis in a chaotic chemostat system," *International Journal of Bifurcation and Chaos*, vol. 25, no. 6, Art. ID 1550087, 13 pages, 2015.
- [26] J. Wei and S. Ruan, "Stability and global Hopf bifurcation for neutral differential equations," *Acta Mathematica Sinica*, vol. 45, no. 1, pp. 93–104, 2002.
- [27] F. Li, W. Ma, Z. Jiang, and D. Li, "Stability and Hopf bifurcation in a delayed HIV infection model with general incidence rate and immune impairment," *Computational and Mathematical Methods in Medicine*, vol. 2015, Art. ID 206205, 14 pages, 2015.
- [28] R. R. Regoes, D. Wodarz, and M. A. Nowak, "Virus dynamics: the effect of target cell limitation and immune responses on virus evolution," *Journal of Theoretical Biology*, vol. 191, no. 4, pp. 451–462, 1998.
- [29] A. Miao, X. Wang, T. Zhang, W. Wang, and B. G. Sampath Aruna Pradeep, "Dynamical analysis of a stochastic SIS epidemic model with nonlinear incidence rate and double epidemic hypothesis," *Advances in Difference Equations*, vol. 2017, Paper No. 226, 27 pages, 2017.

## Research Article

# A Feasible Computational Fluid Dynamics Study for Relationships of Structural and Functional Alterations with Particle Depositions in Severe Asthmatic Lungs

Sanghun Choi <sup>1</sup>, Shinjiro Miyawaki<sup>2,3</sup> and Ching-Long Lin <sup>3</sup>

<sup>1</sup>School of Mechanical Engineering, Kyungpook National University, Daegu, Republic of Korea

<sup>2</sup>Jacobs, 1100 NE Circle Blvd., Suite 300, Corvallis, Oregon 97330, USA

<sup>3</sup>Department of Mechanical and Industrial Engineering, IIHR-Hydrosience and Engineering, University of Iowa, Iowa City, Iowa, USA

Correspondence should be addressed to Ching-Long Lin; [ching-long-lin@uiowa.edu](mailto:ching-long-lin@uiowa.edu)

Received 2 February 2018; Accepted 26 March 2018; Published 22 July 2018

Academic Editor: Yu Feng

Copyright © 2018 Sanghun Choi et al. This is an open access article distributed under the Creative Commons Attribution License, which permits unrestricted use, distribution, and reproduction in any medium, provided the original work is properly cited.

This study aims to investigate the effect of altered structures and functions in severe asthma on particle deposition by using computational fluid dynamics (CFD) models. Airway geometrical models of two healthy subjects and two severe asthmatics were reconstructed from computed tomography (CT) images. Subject-specific flow boundary conditions were obtained by image registration to account for regional functional alterations of severe asthmatics. A large eddy simulation (LES) model for transitional and turbulent flows was applied to simulate airflows, and particle transport simulations were then performed for 2.5, 5, and 10  $\mu\text{m}$  particles using CFD-predicted flow fields. Compared to the healthy subjects, the severe asthmatics had a smaller air-volume change in the lower lobes and a larger air-volume change in the upper lobes. Both severe asthmatics had smaller airway circularity ( $Cr$ ), but one of them had a significant reduction of hydraulic diameter ( $D_h$ ). In severe asthmatics, the larger air-volume change in the upper lobes resulted in more particles in the upper lobes, especially for the small 2.5  $\mu\text{m}$  particles. The structural alterations measured by  $Cr$  and  $D_h$  were associated with a higher particle deposition.  $D_h$  was found to be the most important metric which affects the specific location of particle deposition. This study demonstrates the relationship of CT-based structural and functional alterations in severe asthma with flow and particle dynamics.

## 1. Introduction

Asthma is pathologically characterized by combined phenotypes of airflow obstruction, bronchial hyperresponsiveness, and airway inflammation [1]. However, how structural and functional alterations of asthma affect flow structure and particle deposition is yet to be investigated. In imaging studies of asthma, ventilation defects and airway structural changes have been investigated by using magnetic resonance image (MRI), positron emission tomography (PET), and single-photon emission computed tomography (SPECT) [2–4]. In addition, via quantitative computed tomography (QCT) imaging, several studies [5–8] have demonstrated significant alterations such as reduced airway diameter as well as increased wall thickness and air trapping. Although QCT

can provide structural measurements of the airways up to segmental airways ( $\sim 2$  mm), quantification of local functional variables is still limited.

Image registration technique has been utilized to provide functional information by matching images at different inflation levels [9]. The registration derived-variables were validated by comparing ventilation maps from different imaging modalities [10]. Furthermore, this technique has shown strengths when characterizing functional alterations of diseased lungs [11, 12]. For instance, a study used the technique to differentiate airway vs. parenchymal phenotypes in a chronic obstructive pulmonary disease (COPD) [11]. We have recently demonstrated that volume changes of severe asthmatic lungs are preferentially smaller near basal regions and the smaller volume changes are compensated with air-volume

change in apical regions [12]. We also demonstrated that severe asthmatics were characterized by the reduced airway diameters and noncircular shapes, unlike healthy and nonsevere asthmatics [13].

Computational fluid dynamics (CFD) technique has been used to analyze flow characteristics and particle depositions in the human lungs [14]. With regard to CFD simulations of asthmatic lungs, a study [15] showed alterations of particle depositions with an asthmatic subject before and after asthma attack, and another study [16] correlated forced expiratory volume in one second ( $FEV_1$ ) with CFD-based resistance before and after bronchodilator. However, both of them imposed parabolic velocity profiles to the trachea regions and uniform pressure boundary conditions to QCT-resolved ending branches, under the Reynolds-averaged Navier-Stokes equations (RANS) model or laminar assumption. Heenan et al. [17] and Jayaraju et al. [18] have compared CFD simulations using RANS model with experimental results, concluding that ones with RANS provided less accurate prediction in both flow structure and particle deposition. On the other hand, Longest et al. [19] and Tian et al. [20] have demonstrated that low-Reynolds number  $k-\omega$  approximation with near-wall correction improves the prediction of particle deposition. With five asthmatics, Vinchurkar et al. [21] have also demonstrated a good agreement of aerosol delivery between imaging-based CFD method and in vivo experimental data. Meanwhile, Backer et al. [22] have demonstrated that lobar distributions of air-volume change between SPECT and QCT are consistent, so they have emphasized the importance of subject-specific boundary conditions in CFD simulations.

The main objective of this study is to investigate how functional and structural alterations of severe asthmatic lungs affect flow structures and particle depositions. This study further evaluates clinical applications of CFD in localizing hot spots. According to our existing population-based analysis [8, 12, 13], severe asthmatics were characterized by the shifted lobar air-volume change from lower lobes to upper lobes, decreased airway circularity ( $Cr$ ), and reduced hydraulic diameter ( $D_h$ ). To reproduce regional air-volume change, we employed an image registration technique for a subject-specific boundary condition. Next, to reflect subject-specific airway features such as  $Cr$  and  $D_h$ , we employed a surface fitting method from 1D skeleton to 3D CT-resolved airways [23]. We then performed computational fluid-particle dynamics simulations to obtain local particle distribution and deposition. To achieve main objective, three major components in this study are (1) reproducing regional air-volume change, (2) quantifying subject-specific airway features, and (3) quantifying local particle distribution and deposition.

## 2. Methods

**2.1. Human Subjects.** The imaging study and protocols for acquiring QCT images at both total lung capacity (TLC) and functional residual capacity (FRC) were approved by Institutional Review Board (IRB) of University of Pittsburgh as a part of multicenter Severe Asthma Research Program (SARP) [24]. Four human subjects were employed in this study, among whom two subjects were healthy and two

subjects were severe asthmatic (Table 1). The CT images were taken via GE helical VCT-64 slice scanner with the slice thickness of 0.625 mm. Major criteria used to define severe asthma included treatments with oral corticosteroids and high-dose inhaled corticosteroids, besides several minor criteria [24]. At least, one major and two minor criteria were required to be classified as severe asthmatics. The CT scans were acquired in a supine position, and 3D airways, 1D skeletons, lungs, and lobes were segmented using Apollo software (VIDA Diagnostics, Coralville, Iowa).

**2.2. Flow Simulation and Boundary Condition.** Filtered continuity and incompressible Navier-Stokes equations read

$$\nabla \cdot \bar{\mathbf{u}} = 0, \quad (1a)$$

$$\frac{\partial \bar{\mathbf{u}}}{\partial t} + (\bar{\mathbf{u}} \cdot \nabla) \bar{\mathbf{u}} = -\frac{1}{\rho_f} \nabla \bar{p} + \nabla \cdot [(\nu_f + \nu_T) \nabla \bar{\mathbf{u}}] \quad (1b)$$

where  $\bar{\mathbf{u}}$ ,  $\rho_f$ ,  $\bar{p}$ ,  $\nu_f$ , and  $\nu_T$  are filtered velocity vector, fluid density, filtered pressure, fluid kinematic viscosity, and subgrid-scale turbulent eddy viscosity [25], respectively. A large eddy simulation (LES) model was adopted to resolve laminar-transitional-turbulent flows in the central airways. The properties of  $\rho_f$  and  $\nu_f$  were set to  $1.12 \text{ kg/m}^3$  and  $1.64 \times 10^{-5} \text{ m}^2/\text{s}$ , respectively. A characteristic Galerkin finite element method [26] was employed to discretize (1a) and (1b). A moderate steady-inspiratory flow-rate of  $3.27 \times 10^{-4} \text{ m}^3/\text{s}$  ( $\approx 20$  liters/min) was imposed as the inlet condition, being equivalent to the peak flow-rate of a sinusoidal waveform with a tidal volume of 500 mL and a period of 4.8 s. Reynolds numbers (Re) in trachea range from 1300 to 1700 in the given flow-rate and individual tracheal sizes of two healthy and two severe asthmatics.

Figure 1(a) shows a flow chart from the image segmentation and registration to a realistic CFD simulation. First, an image registration technique [9] was employed to estimate local air-volume change between TLC and FRC at lung parenchyma (top row), and one-dimensional (1D) centerline (CL) tree structures obtained by a volume filling method [27] bridged three-dimensional- (3D-) resolved ending branches and lung parenchyma (middle row). Air-volume change measured at parenchyma was summed at CT-resolved ending branch to estimate regional flow-rate ratios. With the flow-rate ratios, parabolic profiles of velocity were essentially imposed at the CT ending branch. Lastly, a surface fitting method [23] together with Gmesh [28] was used to fit an initial CL-based 3D surface geometry to CT-segmented airway surface and construct a CL-CT-based airway geometrical model (bottom row). The resulting model captured subject-specific airway features such as  $Cr$  and  $D_h$ . At this step, we created a synthetic turbulence [29] right above the glottal constricted regions, because the SARP study [24] did not gather oropharynx scans. The turbulent intensity and largest eddy size were set to 0.29 and 8 mm, respectively, to mimic the turbulent flows found in the CFD simulations with oropharynx [30]. The number of elements ranges from 3.9 to 5.0 million for four cases. Time steps of  $5.0 \times 10^{-6} \text{ s}$  (HS 1,

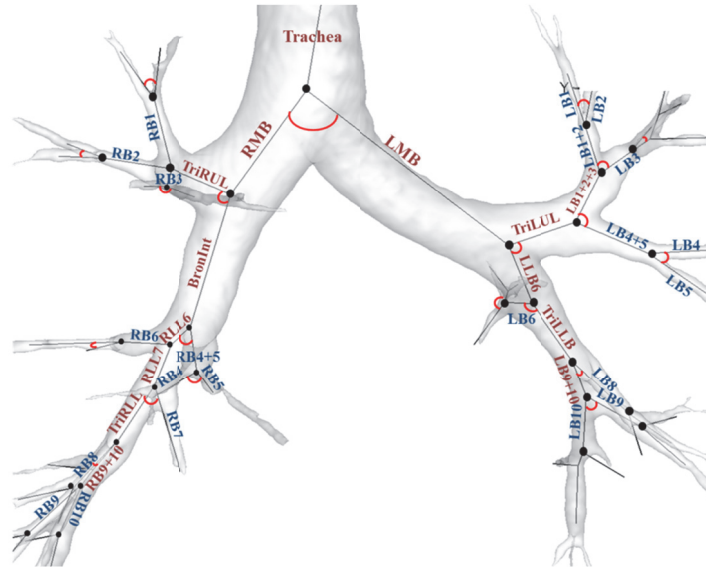
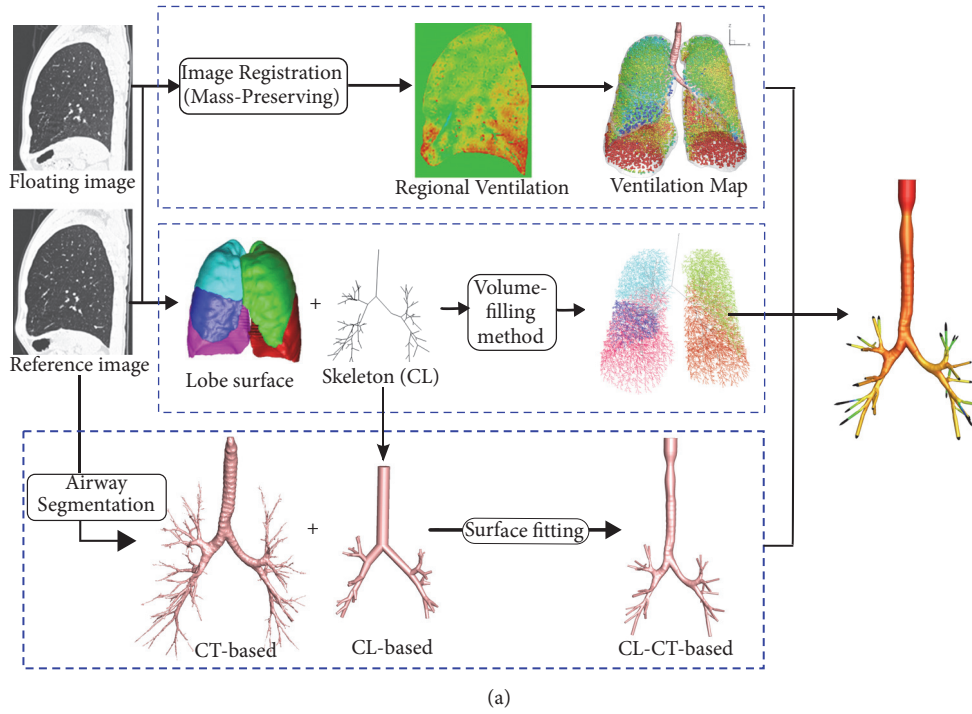


FIGURE 1: (a) Flow charts of connecting CT imaging-based structural and functional data for physiologically consistent CFD simulations. (b) Segmental names of airways: each angle of the segment represents the bifurcation angle between two daughter branches.

HS 2, and SA 1) and  $3.0 \times 10^{-6}$  s (SA 2) were chosen to satisfy Courant–Friedrichs–Lewy (CFL) number less than 1.

**2.3. Structural Metrics Associated with Aerosol Delivery.**  $Cr$  and  $D_h$  could be directly associated with airflows and particle delivery. In this study, we measured the structural metrics at 31 segmental airways (Figure 1(b)).  $Cr$  was computed to assess the degree of elliptical shape of an airway cross section as follows:

$$Cr = \frac{\text{Perimeter of an area-equivalent circle}}{\text{Perimeter of a luminal area}} = \frac{\pi D_{ave}}{P_e}, \quad (2)$$

where  $D_{ave}$  and  $P_e$  are average diameter and perimeter of an airway.  $D_{ave}$  was computed as follows:  $\sqrt{4 \times A_c / \pi}$ , where  $A_c$  is the cross-sectional area of the airway. Next, in order to assess a degree of airway narrowing,  $D_h$  was computed as follows:

$$D_h = \frac{4A_c}{P_e}. \quad (3)$$

TABLE 1: Demographic, PFT baseline (prebronchodilator), and maximal (postbronchodilator) lung functions and CT-based air-volumes of two healthy subjects and two severe asthmatics.

	Healthy subjects (HS)		Severe asthmatics (SA)	
	HS 1	HS 2	SA 1	SA 2
<b>Demographics</b>				
Gender (F, Female)	F	F	F	F
Age (yrs.)	59	29	61	48
BMI (kg/m <sup>2</sup> )	23.7	22.2	32.4	23.9
Asthma duration (yrs.)	-	-	10.6	19.7
<b>Baseline lung function (pre-bronchodilator)</b>				
FEV <sub>1</sub> (liters) (% predicted)	2.97 (100%)	3.15 (94%)	1.19 (34%)	1.02 (40%)
FVC (liters) (% predicted)	3.82 (100%)	4.00 (101%)	1.83 (39%)	2.52 (80%)
FEV1/FVC (%)	78%	79%	65%	41%
<b>Maximal lung function (post-bronchodilator)</b>				
FEV <sub>1</sub> (liters) (% predicted)	3.36 (107%)	3.17 (100%)	2.05 (72%)	1.17 (46%)
FVC (liters) (% predicted)	4.04 (103%)	3.94 (102%)	2.97 (74%)	3.11 (98%)
FEV1/FVC (%)	83%	80%	69%	38%
<b>CT-based air-volumes</b>				
TLC (liters)	5.37	4.31	5.64	4.33
FRC (liters)	2.04	1.79	2.85	1.77

All subjects are Caucasians and nonsmokers. PFT and CT measurements were obtained in upright and supine positions, respectively. CT scans were performed after bronchodilator.

Note that  $Cr$  decreases as airway lumen becomes elliptic, and  $D_h$  decreases as airway narrowing is dominant.  $Cr$  and  $D_h$  were decreased in severe asthmatics compared with healthy subjects, in a population-based comparison [13]. In this study,  $Cr$  decreases in both severe asthmatics (SA 1 and SA 2), but  $D_h$  only decreases in a severe asthmatic subject (SA 2). In Results, the effects of  $Cr$  and  $D_h$  on particle delivery are investigated.

**2.4. Particle Simulation.** To compare the characteristics of particle distribution and deposition such as pharmaceutical aerosols between healthy subjects and severe asthmatics, particle transport analysis was conducted using LES-predicted airflow fields. Quasi-steady airflow fields for 2.4 s were collected, e.g., 400 datasets  $\times$  0.006 s, after initial 2.4 s airflow fields. For particle simulation, Lagrangian particle tracking algorithm [31] was adopted to track particle trajectories as follows:

$$\frac{d\mathbf{u}_p}{dt} = \frac{U}{Stk \cdot D_{ave}} (\bar{\mathbf{u}} - \mathbf{u}_p) + \frac{\rho_p - \rho_f}{\rho_p} \mathbf{g}, \quad (4)$$

where  $\mathbf{u}_p$ ,  $\rho_p$ , and  $\mathbf{g}$  are particle velocity, particle density, and gravitational acceleration, respectively. In the equation, Stokes number (Stk) is defined as follows:

$$Stk = \frac{2Q\rho_p d^2}{9\pi\mu_f D_{ave}^3 C_c \alpha^{3.7}} \quad (5)$$

where  $Q$ ,  $d$ ,  $\mu_f$ ,  $C_c$ , and  $\alpha$  are the flow-rate of the branch, the diameter of particles, fluid dynamic viscosity, the Cunningham slip correction factor, and the particle-particle interaction factor, respectively. The detailed descriptions of particle transport simulation could be found in [30]. At the beginning of particle simulation, the spherical particles were uniformly distributed in a cylinder with a radius of 10 mm and a depth of 4 mm at the trachea inlet. They were then released 9 different times to obtain an ensemble average of particle deposition. The number of particles was set to 10,000, and three different spherical particle sizes of 2.5, 5, and 10  $\mu\text{m}$  were chosen in this study. The aerosol size was chosen with a general distribution of aerosols using dry powder inhaler (DPI) and soft mist inhaler (SMI) [32]. This is to investigate the relationship between aerosol size and airway structure. The particle density and mean free path were given as 1000 kg/m<sup>3</sup> and 68 nm, respectively. ‘‘Particle distribution’’, ‘‘deposition’’, and ‘‘advection’’ by lobe are defined as ‘‘particles entering each lobe’’, ‘‘those deposited in 3D segments of each lobe’’, and ‘‘those exiting 3D ending branches of each lobe without being deposited in 3D segments’’, respectively.

### 3. Results

**3.1. Pulmonary Function Test (PFT).** Table 1 shows demographic as well as PFT- and CT-based measurements. Bronchodilator was performed for both healthy subjects and

severe asthmatics to obtain maximal lung functions, and CT scans were acquired after bronchodilator because the aim of SARP study was to assess lung function of stable asthma [33]. First, the baseline and maximal FEV<sub>1</sub> and FVC %predicted values in two healthy subjects were close to normal ranges (~100% predicted). In contrast, baseline FEV<sub>1</sub> % predicted values of SA 1 (34%) and SA 2 (40%) were much smaller than normal ranges ( $\geq 80\%$ ). The maximal FEV<sub>1</sub> % predicted value (~46%) of SA 2 was still lower even with bronchodilator. In the same subject, the maximal FVC % predicted value was very close to normal ranges, leading to a significantly reduced FEV<sub>1</sub>/FVC (38%). Thus, the baseline FEV<sub>1</sub> % predicted values of both SA 1 and SA 2 were small values, but the lung function of SA 1 (38%  $\uparrow$ ) is relatively reversible than that of SA 2 (6%  $\uparrow$ ). According to baseline and maximal PFTs, SA 2 is likely to have significant airway narrowing despite bronchodilator, whereas airways of SA 1 might have dilated with the aid of bronchodilator.

**3.2. CT-Based Structural and Functional Characteristics.** We compared structural quantities of  $Cr$  and  $D_h$  in two healthy subjects and two severe asthmatics (Figure 2). Figure 2(a) shows that  $Cr$  of two severe asthmatics was reduced compared to those of two healthy subjects. For example,  $Cr$  of Trachea, RMB, TriRUL, RLL7, RB6, RB9+10, and LMB in two severe asthmatics were deviated from those of the same airway segments in healthy subjects. Both SA 1 and SA 2 had the prominently reduced  $Cr$ , but only SA 2 demonstrated significantly smaller  $D_h$  compared with HS 1, HS 2, and SA 1 in CT-resolved airways (Figure 2(b)), which was also reflected in PFT measurements at postbronchodilator. The effect of reduced  $Cr$  in RMB and TriRUL is assessed between “HS 1, HS 2” and “SA 1, SA 2”. Next, the effect of constricted branch on particle deposition is mainly assessed with SA 2. In addition, SA 1 and SA 2 were characterized by reduced air-volume change in lower lungs along with elevated air-volume change in upper lungs, as compared with the healthy subjects, being quantified by the air-volume change in upper lobes to air-volume change in middle and lower lobes, i.e.,  $U/(M+L)|_V$  (Figure 3).

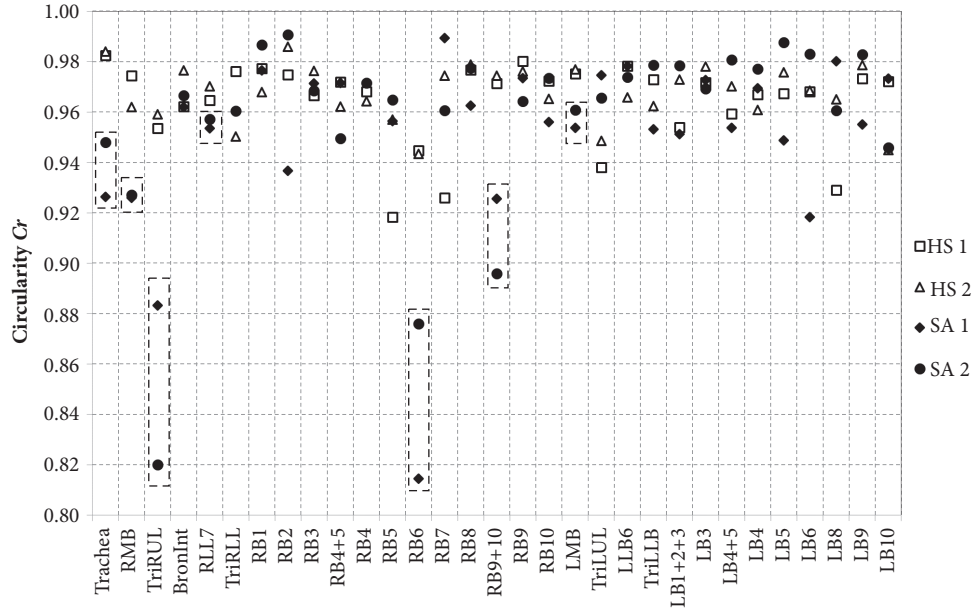
**3.3. Regional Volume Change vs. Particle Distribution.** Given the regional air-volume change, particle distribution was evaluated with three different particle sizes (Figure 3). With 2.5  $\mu\text{m}$  particles, the  $U/(M+L)|_{\text{dist}}$  (the particle distribution ratio of upper lobes to middle and lower lobes) was close to the ratio of air-volume changes ( $U/(M+L)|_V$ ), because small particles are likely to follow airflow streamlines. Next,  $U/(M+L)|_{\text{dist}}$  decreased as particle size increases due in part to the inertial effect that particles can easily move along with the flow to the lower lobes. Overall, SA 1 and SA 2 had an increased particle distribution to upper lobes compared with HS 1 and HS 2, being consistent with the alteration of air-volume change distribution in severe asthmatics. Furthermore, the particle distribution to upper lobes in severe asthmatics became more evident with decreasing particle size.

TABLE 2: Circularity  $Cr$ ,  $D_{\text{ave}}$ , and  $D_h$  of two healthy subjects (HS 1 and HS 2) and two severe asthmatics (SA 1 and SA 2) in RMB and TriRUL regions (see Figure 1(b)).

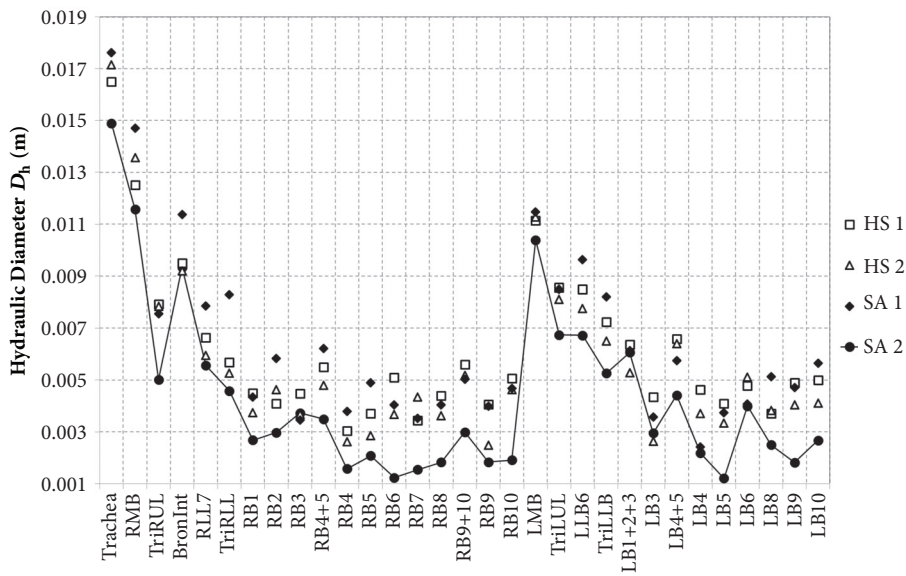
	Healthy subjects		Severe asthmatics	
	HS 1	HS 2	SA 1	SA 2
RMB				
$Cr$	0.974	0.962	0.926	0.927
$D_{\text{ave}}$ (mm)	12.8	14.1	15.9	12.5
$D_h$ (mm)	12.5	13.6	14.7	11.6
TriRUL				
$Cr$	0.953	0.959	0.883	0.820
$D_{\text{ave}}$ (mm)	8.3	8.2	8.5	6.1
$D_h$ (mm)	7.9	7.8	7.6	5.0

**3.4. Circularity and Particle Deposition.** Around RMB and TriRUL regions (Figure 1(b)), we compared particle depositions of two healthy subjects without elliptic shapes vs. two severe asthmatics with elliptic shapes, because SA 1 and SA 2 exhibit significantly decreased  $Cr$  in both RMB and TriRUL (Table 2). The two selected severe asthmatics (83° and 88° and 91°) at RMB, expecting similar particle depositions given the same range of Stk numbers. In Table 2,  $D_{\text{ave}}$  of TriRUL in SA 1 is the largest among four subjects, but  $D_h$  was slightly smaller than those of both HS 1 and HS 2 due to the reduced  $Cr$ . Figure 4(a) shows the increased particle deposition of SA 1 and SA 2 in TriRUL, as compared with HS 1 and HS 2 in the same Stk range of the parent branch (RMB). Note that the comparisons based on the same Stk numbers were made to control the effects of flow-rate and airway narrowing. Figure 5 also displays the distributions of particle deposition in TriRUL. Thus, an increase of particle deposition in both severe asthmatics was possibly due to the decreased airway  $Cr$ .

**3.5. Constriction vs. Particle Deposition.** Particle deposition efficiency of the branches based on Stk numbers, daughter branches of RB9+10 and LB10, were plotted in Figures 4(b) and 4(c), respectively. Figure 6(a) (around RB9+10) and Figure 6(b) (around LB10) show particle depositions of SA 2 with narrowed and elliptic airways. Compared with HS 1, HS 2, and SA 1, Stk is increased for SA 2 due to airway narrowing, because Stk is proportional to  $1/D_{\text{ave}}^3$  with a given flow-rate (see (5)). In the case of 5  $\mu\text{m}$  particles, particle deposition efficiency reached 60% and 90% for RB9+10 and LB10, respectively. For 10  $\mu\text{m}$  particles, particle deposition reached 100%; thus large particles could not ventilate beyond these airways. These results imply that particle deposition would be very sensitive to the reduced airway diameters due to airway constriction (see Figures 6(a) and 6(b)). We further investigated flow structure, wall shear stress, and pressure drop around LB10 (Figure 6(c)). In this airway, constriction-induced jet-flow, higher wall shear stress and large pressure drop were simultaneously observed.



(a)



(b)

FIGURE 2: Structural variability of (a)  $Cr$  and (b)  $D_h$  for 31 segmental airways after 1st generation in two healthy subjects and two severe asthmatics.

#### 4. Discussion

Our previous studies [8, 12] have demonstrated that air-volume change is smaller in lower lobes and larger in the upper lobes in severe asthmatics, as compared with healthy subjects. In addition, severe asthmatics were structurally characterized by smaller  $Cr$  and  $D_h$ . In this study, we focused on the effect of structural and functional alterations in severe asthmatics on particle depositions under a moderate inspiratory flow condition ( $\sim 20$  liters/min). The two severe asthmatics had altered lung function characterized by larger  $U/(M + L)|v$  than the two healthy subjects. Both SA 1 and

SA 2 had small  $FEV_1\%$  predicted values in the baseline lung function and showed smaller  $Cr$ , whereas only SA 2 subject had small  $FEV_1\%$  predicted in the maximal lung function and showed smaller  $D_h$  in CT-resolved regions. This observation implied that bronchodilator may help recover narrowed airways, but it may not recover noncircular airway shape. This emphasizes the importance of investigating airway shape besides airway diameter in particle delivery. In this study, SA 1 and SA 2 were used to evaluate the effect of  $Cr$  on particle deposition, and SA 2 was used to evaluate the effect of  $D_h$  on particle deposition.

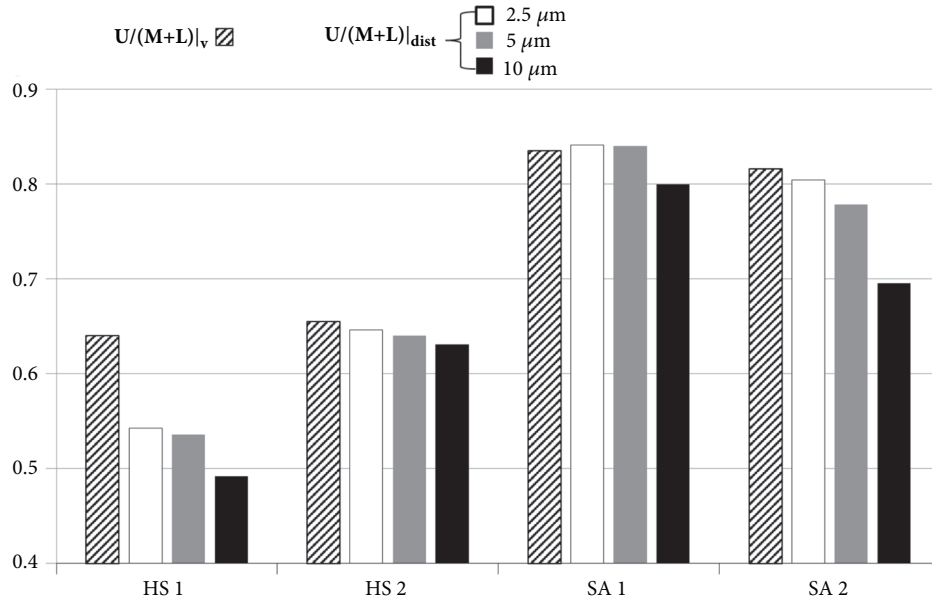


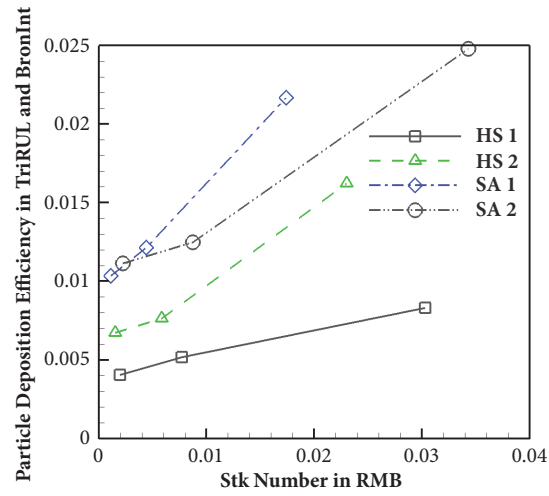
FIGURE 3:  $U/(M+L)|_v$  (the ratio of air-volume change in upper lobes to middle and lower lobes) and  $U/(M+L)|_{dist}$  (the distribution ratio of particles in upper lobes to middle and lower lobes) according to the particle sizes.

First, investigating characteristics of particle deposition in severe asthmatics is important for inhaled pharmaceutical drugs [21, 34], airborne bacteria, or air pollutants. Lobar distribution of small particles was consistent with air-volume distribution (Figure 3). With increasing particle size, the delivery of particles to lower lobes may increase because of an increased inertial effect of large particles. When targeting subject-specific treatments of aerosols, understanding the mechanism of particle distribution would be critical. For example, if lower lobar bronchi need be targeted for some specific subjects, relatively larger aerosol should be treated. However, one should also consider sizes of targeted branches, because larger aerosols could not be delivered to small airways with higher generation.

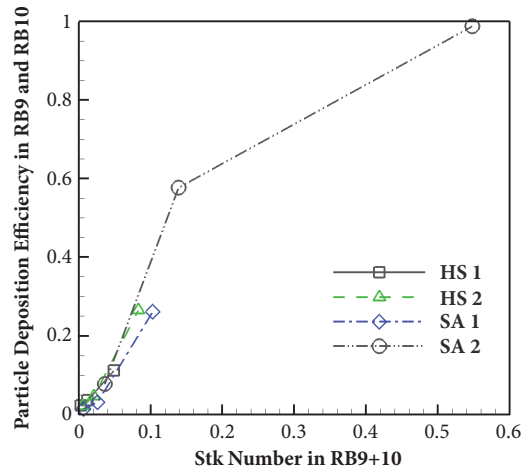
We previously found that in severe asthmatics  $Cr$  of RMB is significantly smaller [13], so we investigated the effect of smaller  $Cr$  on particle deposition. With the same  $Stk$  and similar bifurcation angle of RMB, particle depositions of SA 1 and SA 2 were greater in TriRUL than healthy subjects, which could be attributed to smaller  $Cr$ . Airway structures with smaller  $Cr$  might increase the sensitivity of bacterial inflammation due to particle deposition, which would potentially increase airway wall thickness. While both SA 1 and SA 2 demonstrated smaller  $Cr$ , only SA 2 had constricted airways, especially in lower lobes. Particle deposition efficiency is the function of  $1/D_{ave}^3$  based on  $Stk$  numbers, given flow-rate. In other words, airway constriction could be the most important structural characteristic in association with increased particle deposition efficiency. Thus, if airways are chronically constricted in a subject, the subject may have an increased exposure of pollutants, so further reducing airway diameters along with airway inflammation. Mechanisms among airway constriction, wall shear stress, pressure

drop, and particle deposition may be strongly coupled as described in Figure 6(c). First, constriction-induced high velocity creates high wall shear stress in association with high velocity gradient on the wall. A large pressure drop is required to overcome large wall shear stress. In addition, the constriction-induced high velocity might lead to an increase of particle deposition due to particle impaction in both constricted parent and daughter branches (Figures 6(a) and 6(b)). As a result, both high velocity and small  $D_{ave}$  may contribute to be a large  $Stk$  (see (5)), leading to an increase of particle deposition.

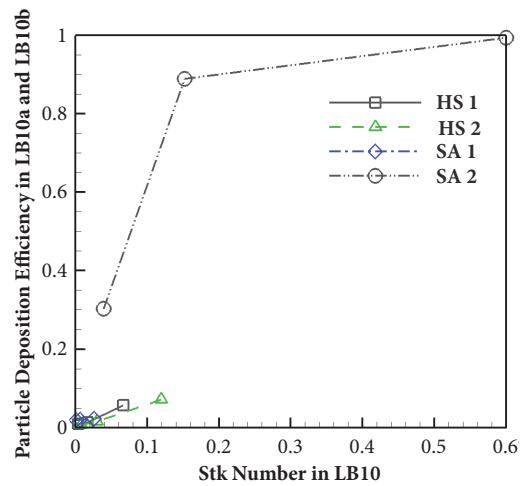
In this study, we only investigated two healthy subjects and two severe asthmatics, which could prevent statistical reliability, so a CFD-based population study is necessary. However, performing many CFD simulations to obtain normal distribution is computationally expensive. We have recently performed CT imaging-based clustering analysis and found clinically meaningful subgroups [35]. Since the clustering membership employed airway structure and lung function, each cluster has similar airway structure and lung function. We believe that such an approach using clustering analysis possibly reduces the number of samples by transitioning an interest from intersubject study to intercluster study. In this study, we imposed the same flow-rate on trachea inlet, due to a lack of subject-specific flow-rate information. If the subject-specific flow-rate is measured, we would further improve the comparison between healthy subjects and severe asthmatics. Furthermore, we have recently investigated airway resistance with symmetric branching angles up to the 20th generation for inspiration and expiration [36]. Then an empirical airway resistance model was introduced to estimate pressure drop due to kinetic energy and viscous dissipation. However, we have not discussed airway resistance



(a)



(b)



(c)

FIGURE 4: Particle deposition efficiency in (a) TriRUL based on Stk in RMB, (b) RB9 and RB10 based on Stk in RB9+10, and (c) LB10a and LB10b based on Stk in LB10.

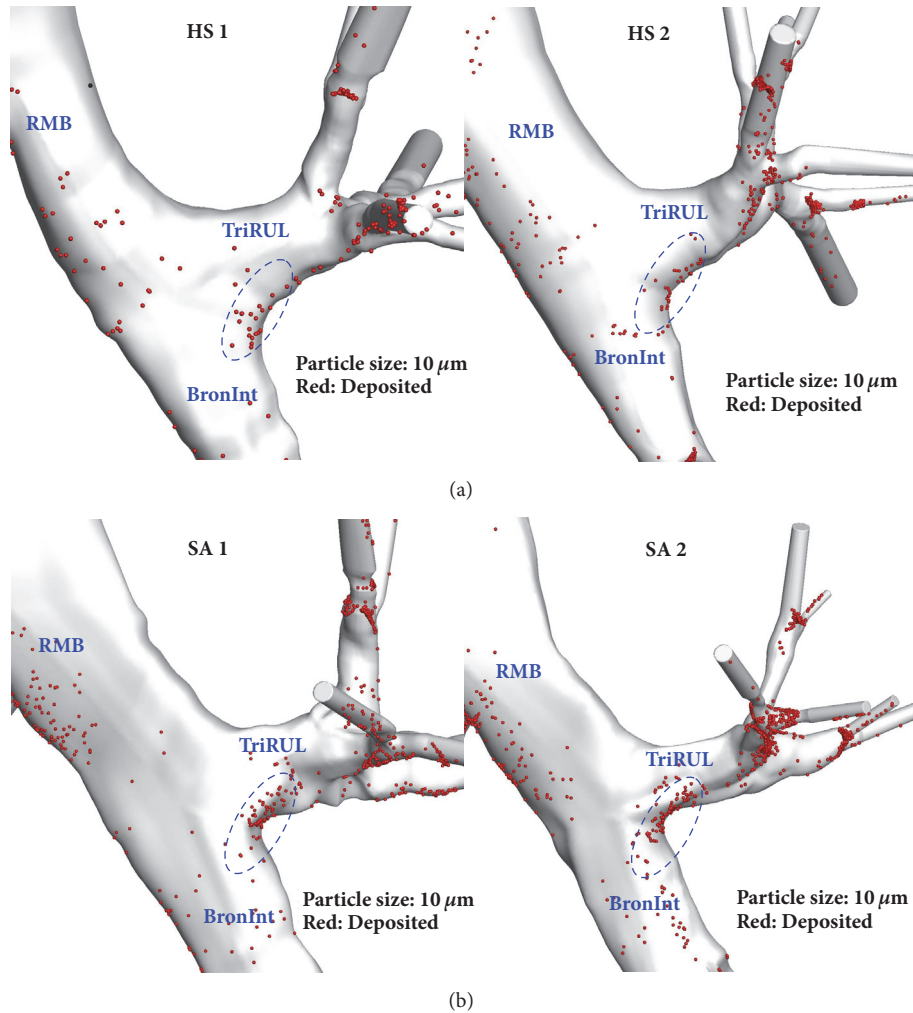


FIGURE 5: Relationships among noncircularity and particle deposition in RMB, TriRUL, and BronInt regions between (a) healthy subjects and (b) severe asthmatics. All of the images are plotted as backside-view.

in this study, because the number of airways was limited to investigate airway resistance. In the future, airway resistance study of severe asthmatics with realistic multiscale airways would be desirable.

In conclusion, we applied a high-fidelity CFD model together with CT image-based airway models to study particle deposition in both healthy and severe asthmatic lungs. With the aid of image registration technique, the subject-specific physiologically realistic-flow boundary condition is derived based on air-volume difference between two CT lung images of the same human subject. As expected from flow-rate distribution, particle distribution to upper lobes was larger in severe asthmatics, relative to healthy subjects. This phenomenon was more prominent when using smaller particles. In both healthy subjects and severe asthmatics, with increasing particle size, particles are distributed more toward lower lobar regions due to inertial effects. Alterations of airway  $Cr$  and  $D_h$  were found to be associated with particle deposition. With the same  $Stk$ , reduced  $Cr$  increases particle deposition. On the other hand, reduced  $D_h$  significantly elevates  $Stk$ , resulting in greater deposition efficiency. The

constricted airways contribute to high wall shear stress, elevated pressure drop, and significantly increased particle deposition. It is concluded that  $U/(M+L)|v$ ,  $Cr$ , and  $D_h$  shall be carefully considered to target subject-specific aerosols.

## Disclosure

Preliminary results of the current manuscript were presented as an abstract in the following link: <http://meetings.aps.org/Meeting/DFD14/Session/E15.1>.

## Conflicts of Interest

The authors declare that they have no conflicts of interest.

## Acknowledgments

The authors thank Drs. Eric A Hoffman, Sally E Wenzel, and Jiwoong Choi for assisting in imaging data acquisition and analysis. Computational time was supported by XSEDE

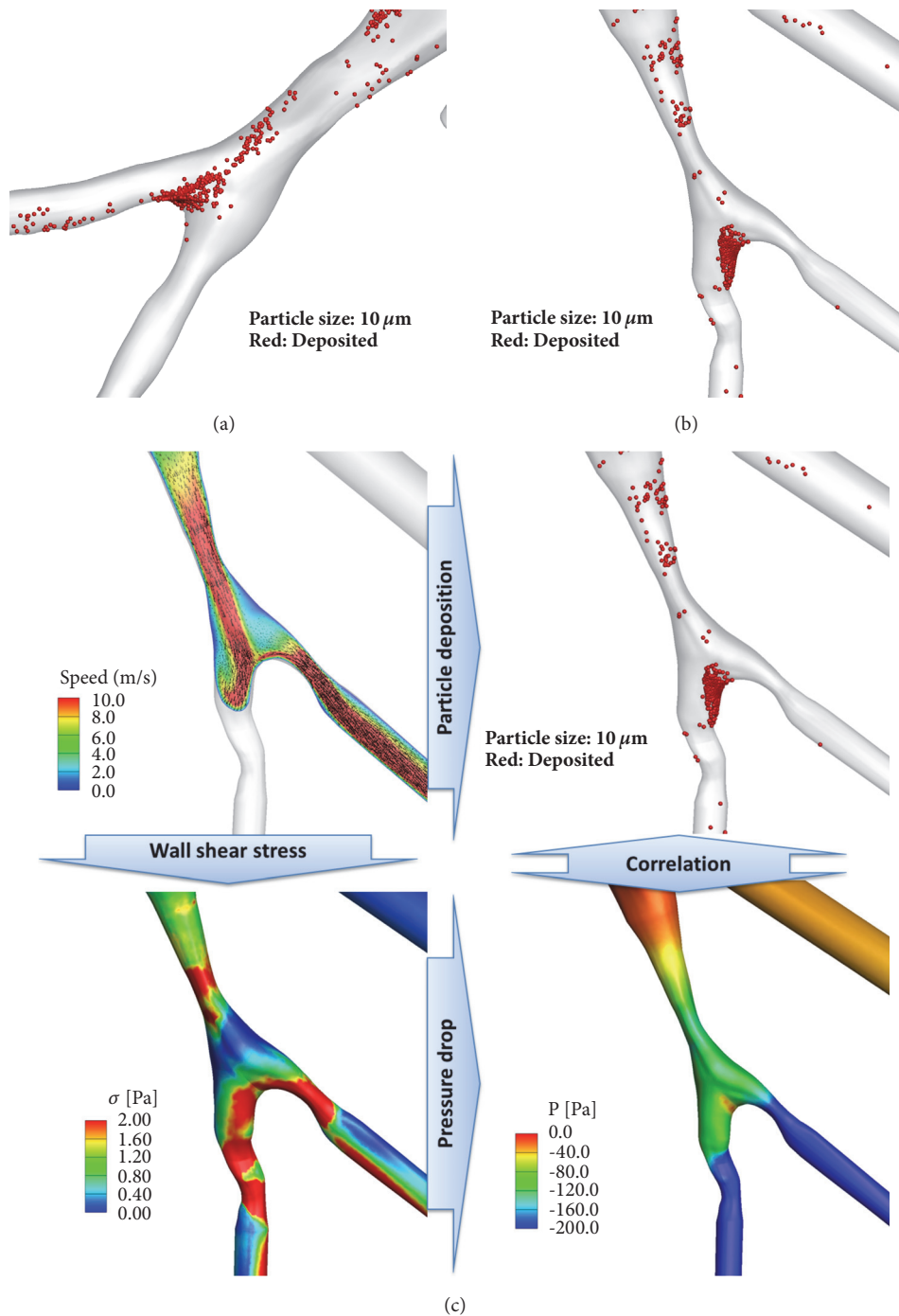


FIGURE 6: Two representative constricted regions of (a) RB9+10 and (b) LB10 in lower lobes in SA 2 subject and (c) correlations among airway constriction, wall shear stress, pressure drop, and particle deposition.

and by the National Institute of Supercomputing and Network/Korea Institute of Science and Technology Information with supercomputing resources including technical support (KSC-2017-S1-0021). This study was supported in part by NIH Grants U01 HL114494, R01 HL094315, and S10 RR022421 and in part by Basic Science Research Program through the National Research Foundation of Korea (NRF) funded by the Ministry of Education (NRF-2017R1D1A1B03034157).

## References

- [1] W. W. Busse and R. F. Lemanske Jr., "Asthma," *The New England Journal of Medicine*, vol. 344, no. 5, pp. 350–362, 2001.
- [2] R. S. Harris, H. Fujii-Rios, T. Winkler, G. Musch, M. F. Vidal Melo, and J. G. Venegas, "Ventilation Defect Formation in Healthy and Asthma Subjects Is Determined by Lung Inflation," *PLoS ONE*, vol. 7, no. 12, Article ID e53216, 2012.

- [3] G. G. King, B. Harris, and S. Mahadev, "V/Q SPECT: Utility for investigation of pulmonary physiology," *Seminars in Nuclear Medicine*, vol. 40, no. 6, pp. 467–473, 2010.
- [4] J. G. Venegas, T. Schroeder, S. Harris, R. T. Winkler, and M. F. Vidal Melo, "The distribution of ventilation during bronchoconstriction is patchy and bimodal: A PET imaging study," *Respiratory Physiology & Neurobiology*, vol. 148, no. 1-2, pp. 57–64, 2005.
- [5] M. Montaudon, M. Lederlin, S. Reich et al., "Bronchial measurements in patients with asthma: Comparison of quantitative thin-section CT findings with those in healthy subjects and correlation with pathologic findings," *Radiology*, vol. 253, no. 3, pp. 844–853, 2009.
- [6] A. Busacker, J. D. Newell Jr., T. Keefe et al., "A multivariate analysis of risk factors for the air-trapping asthmatic phenotype as measured by quantitative CT analysis," *CHEST*, vol. 135, no. 1, pp. 48–56, 2009.
- [7] R. S. Aysola, E. A. Hoffman, D. Gierada et al., "Airway remodeling measured by multidetector CT is increased in severe asthma and correlates with pathology," *CHEST*, vol. 134, no. 6, pp. 1183–1191, 2008.
- [8] S. Choi, E. A. Hoffman, S. E. Wenzel, M. Castro, and C.-L. Lin, "Improved CT-based estimate of pulmonary gas trapping accounting for scanner and lung-volume variations in a multicenter asthmatic study," *Journal of Applied Physiology*, vol. 117, no. 6, pp. 593–603, 2014.
- [9] Y. Yin, E. A. Hoffman, and C.-L. Lin, "Mass preserving nonrigid registration of CT lung images using cubic B-spline," *Medical Physics*, vol. 36, no. 9, pp. 4213–4222, 2009.
- [10] J. M. Reinhardt, K. Ding, K. Cao, G. E. Christensen, E. A. Hoffman, and S. V. Bodas, "Registration-based estimates of local lung tissue expansion compared to xenon CT measures of specific ventilation," *Medical Image Analysis*, vol. 12, no. 6, pp. 752–763, 2008.
- [11] C. J. Galbán, M. K. Han, J. L. Boes et al., "Computed tomography-based biomarker provides unique signature for diagnosis of COPD phenotypes and disease progression," *Nature Medicine*, vol. 18, no. 11, pp. 1711–1715, 2012.
- [12] S. Choi, E. A. Hoffman, S. E. Wenzel et al., "Registration-based assessment of regional lung function via volumetric CT images of normal subjects vs. severe asthmatics," *Journal of Applied Physiology*, vol. 115, no. 5, pp. 730–742, 2013.
- [13] S. Choi, E. A. Hoffman, S. E. Wenzel et al., "Quantitative assessment of multiscale structural and functional alterations in asthmatic populations," *Journal of Applied Physiology*, vol. 118, no. 10, pp. 1286–1298, 2015.
- [14] H. Zhang and G. Papadakis, "Computational analysis of flow structure and particle deposition in a single asthmatic human airway bifurcation," *Journal of Biomechanics*, vol. 43, no. 13, pp. 2453–2459, 2010.
- [15] K. Inthavong, J. Tu, Y. Ye, S. Ding, A. Subic, and F. Thien, "Effects of airway obstruction induced by asthma attack on particle deposition," *Journal of Aerosol Science*, vol. 41, no. 6, pp. 587–601, 2010.
- [16] J. W. De Backer, W. G. Vos, A. Devolder et al., "Computational fluid dynamics can detect changes in airway resistance in asthmatics after acute bronchodilation," *Journal of Biomechanics*, vol. 41, no. 1, pp. 106–113, 2008.
- [17] A. F. Heenan, E. Matida, A. Pollard, and W. H. Finlay, "Experimental measurements and computational modeling of the flow field in an idealized human oropharynx," *Experiments in Fluids*, vol. 35, no. 1, pp. 70–84, 2003.
- [18] S. T. Jayaraju, M. Brouns, C. Lacor, B. Belkasssem, and S. Verbanck, "Large eddy and detached eddy simulations of fluid flow and particle deposition in a human mouth-throat," *Journal of Aerosol Science*, vol. 39, no. 10, pp. 862–875, 2008.
- [19] P. W. Longest, M. Hindle, S. D. Choudhuri, and P. R. Byron, "Numerical simulations of capillary aerosol generation: CFD model development and comparisons with experimental data," *Aerosol Science and Technology*, vol. 41, no. 10, pp. 952–973, 2007.
- [20] G. Tian, P. W. Longest, G. Su, R. L. Walenga, and M. Hindle, "Development of a stochastic individual path (SIP) model for predicting the tracheobronchial deposition of pharmaceutical aerosols: Effects of transient inhalation and sampling the airways," *Journal of Aerosol Science*, vol. 42, no. 11, pp. 781–799, 2011.
- [21] S. Vinchurkar, L. De Backer, W. Vos, C. Van Holsbeke, J. De Backer, and W. De Backer, "A case series on lung deposition analysis of inhaled medication using functional imaging based computational fluid dynamics in asthmatic patients: Effect of upper airway morphology and comparison with in vivo data," *Inhalation Toxicology*, vol. 24, no. 2, pp. 81–88, 2012.
- [22] J. W. De Backer, W. G. Vos, S. C. Vinchurkar et al., "Validation of computational fluid dynamics in CT-based airway models with SPECT/CT," *Radiology*, vol. 257, no. 3, pp. 854–862, 2010.
- [23] S. Miyawaki, M. H. Tawhai, E. A. Hoffman, S. E. Wenzel, and C.-L. Lin, "Automatic construction of subject-specific human airway geometry including trifurcations based on a CT-segmented airway skeleton and surface," *Biomechanics and Modeling in Mechanobiology*, vol. 16, no. 2, pp. 583–596, 2017.
- [24] S. E. Wenzel and W. W. Busse, "Severe asthma: Lessons from the Severe Asthma Research Program," *The Journal of Allergy and Clinical Immunology*, vol. 119, no. 1, pp. 14–21, 2007.
- [25] A. W. Vreman, "An eddy-viscosity subgrid-scale model for turbulent shear flow: algebraic theory and applications," *Physics of Fluids*, vol. 16, no. 10, pp. 3670–3681, 2004.
- [26] C.-L. Lin, H. Lee, T. Lee, and L. J. Weber, "A level set characteristic Galerkin finite element method for free surface flows," *International Journal for Numerical Methods in Fluids*, vol. 49, no. 5, pp. 521–547, 2005.
- [27] M. Howatson Tawhai, A. J. Pullan, and P. J. Hunter, "Generation of an Anatomically Based Three-Dimensional Model of the Conducting Airways," *Annals of Biomedical Engineering*, vol. 28, no. 7, pp. 793–802, 2000.
- [28] C. Geuzaine and J. F. Remacle, "Gmsh: A 3-D finite element mesh generator with built-in pre- and post-processing facilities," *International Journal for Numerical Methods in Engineering*, vol. 79, no. 11, pp. 1309–1331, 2009.
- [29] S. Miyawaki, E. A. Hoffman, and C.-L. Lin, "Numerical simulations of aerosol delivery to the human lung with an idealized laryngeal model, image-based airway model, and automatic meshing algorithm," *Computers & Fluids*, vol. 148, pp. 1–9, 2017.
- [30] S. Miyawaki, M. H. Tawhai, E. A. Hoffman, and C.-L. Lin, "Effect of carrier gas properties on aerosol distribution in a CT-based human airway numerical model," *Annals of Biomedical Engineering*, vol. 40, no. 7, pp. 1495–1507, 2012.
- [31] M. R. Maxey and J. J. Riley, "Equation of motion for a small rigid sphere in a nonuniform flow," *Physics of Fluids*, vol. 26, no. 4, pp. 883–889, 1983.
- [32] P. W. Longest, G. Tian, R. L. Walenga, and M. Hindle, "Comparing MDI and DPI aerosol deposition using in vitro experiments and a new stochastic individual path (SIP) model of the conducting airways," *Pharmaceutical Research*, vol. 29, no. 6, pp. 1670–1688, 2012.

- [33] R. L. Sorkness, E. R. Bleecker, W. W. Busse et al., “Lung function in adults with stable but severe asthma: Air trapping and incomplete reversal of obstruction with bronchodilation,” *Journal of Applied Physiology*, vol. 104, no. 2, pp. 394–403, 2008.
- [34] R. L. Walenga and P. W. Longest, “Current Inhalers Deliver Very Small Doses to the Lower Tracheobronchial Airways: Assessment of Healthy and Constricted Lungs,” *Journal of Pharmaceutical Sciences*, vol. 105, no. 1, pp. 147–159, 2016.
- [35] S. Choi, E. A. Hoffman, S. E. Wenzel et al., “Quantitative computed tomographic imaging–based clustering differentiates asthmatic subgroups with distinctive clinical phenotypes,” *The Journal of Allergy and Clinical Immunology*, vol. 140, no. 3, pp. 690–700.e8, 2017.
- [36] S. Choi, J. Choi, and C.-L. Lin, “Contributions of Kinetic Energy and Viscous Dissipation to Airway Resistance in Pulmonary Inspiratory and Expiratory Airflows in Successive Symmetric Airway Models with Various Bifurcation Angles,” *Journal of Biomechanical Engineering*, vol. 140, no. 1, 2018.

## Research Article

# Numerical Simulations of the Motion and Deformation of Three RBCs during Poiseuille Flow through a Constricted Vessel Using IB-LBM

Rongyang Wang <sup>1,2</sup>, Yikun Wei <sup>1</sup>, Chuanyu Wu <sup>1</sup>, Liang Sun,<sup>1</sup> and Wenguang Zheng<sup>1,3</sup>

<sup>1</sup>Faculty of Mechanical Engineering and Automation, Zhejiang Sci-Tech University, Hangzhou 310018, China

<sup>2</sup>College of Mechanical and Electrical Engineering, Huzhou Vocational and Technical College, Huzhou 313000, China

<sup>3</sup>School of Mechanical Engineering and Automation, University of Science and Technology Liaoning, Anshan 114051, China

Correspondence should be addressed to Yikun Wei; [ykun\\_wei@sina.com](mailto:ykun_wei@sina.com) and Chuanyu Wu; [cywu@zstu.edu.cn](mailto:cywu@zstu.edu.cn)

Received 15 November 2017; Revised 19 January 2018; Accepted 23 January 2018; Published 21 February 2018

Academic Editor: Xiaole Chen

Copyright © 2018 Rongyang Wang et al. This is an open access article distributed under the Creative Commons Attribution License, which permits unrestricted use, distribution, and reproduction in any medium, provided the original work is properly cited.

The immersed boundary-lattice Boltzmann method (IB-LBM) was used to examine the motion and deformation of three elastic red blood cells (RBCs) during Poiseuille flow through constricted microchannels. The objective was to determine the effects of the degree of constriction and the Reynolds ( $Re$ ) number of the flow on the physical characteristics of the RBCs. It was found that, with decreasing constriction ratio, the RBCs experienced greater forced deformation as they squeezed through the constriction area compared to at other parts of the microchannel. It was also observed that a longer time was required for the RBCs to squeeze through a narrower constriction. The RBCs subsequently regained a stable shape and gradually migrated toward the centerline of the flow beyond the constriction area. However, a sick RBC was observed to be incapable of passing through a constricted vessel with a constriction ratio  $\leq 1/3$  for  $Re$  numbers below 0.40.

## 1. Introduction

Red blood cells (RBCs) play an important role in blood flow in the human body, particularly in the transportation of oxygen from the lungs to every cell of the body. An adult RBC has a biconcave shape of diameter  $6\ \mu\text{m}$  and thickness  $2\ \mu\text{m}$  [1–6]. The RBC membrane is highly deformable, which enables the passage of RBCs through a blood vessel with a diameter smaller than that of the RBCs [7, 8]. The flow of RBCs through a blood vessel represents a typical fluid-structure interaction (FSI) problem, involving a complex interplay of fluid dynamics, elastic body, and a moving boundary [9]. A variety of accurate and efficient numerical methods have been proposed for the solution of a FSI problem involving a complex geometry, such as the arbitrary Lagrangian–Eulerian method [10], immersed interface method [11], immersed finite element method [12], immersed boundary method [13], and immersed boundary-lattice Boltzmann method (IB-LBM) [14–18].

Previous studies on the IB-LBM emphasized its potential advantages for the solution of FSI problems, namely,

its simplicity, parallelizability, intrinsic kinetic and explicit calculations, and essential relative simplicity for handling complex, moving, and deformable geometries [14–18]. In recent years, the numerical investigation of the motion and deformation of RBCs in capillaries and arteries has received considerable attention [15, 16]. Zhang et al. [4] presented a numerical IB-LBM algorithm for investigating the microscopic hemodynamic and hemorheological behaviors of discrete RBCs in shear flows. Dadvand et al. [9] used the IB-LBM to numerically investigate the motion and deformation of healthy and sick RBCs in viscous shear flows. Shi et al. [19] proposed a two-dimensional (2D) elastic spring model of the RBC membrane based on the immersed boundary method, which was first introduced by Peskin [20] for the investigation of blood flow through heart valves. Krüger et al. [21] used a hybrid LB-IB-finite element method to simulate the tumbling and tank-treading-like motion of dense suspended RBCs in an external shear flow. The transient motion and deformation of healthy RBCs and PF-RBCs at different stages were examined in a simple 2D microchannel, with the RBCs moving along the center line of the channel [22, 23].

Sui et al. [24–26] used a combination of the IBM, a multi-block lattice Boltzmann model, and membrane mechanics to investigate the transient behaviors of elastic capsules and the deformation and aggregation of RBCs in a shear flow. Ma et al. [27] proposed an IB-LBM that considered the ultrasonic effect for the simulation of RBC aggregation and deformation in an ultrasonic field. They found that the action of the ultrasound waves on the pure plasma could induce a recirculation flow. The IB-LBM has also been used to numerically investigate the effect of the RBC deformability on the dispersion of the cells at physiological flow rates with respect to the hematocrit [28]. Further, the IB-LBM has been applied to quantitative analyses of the motion and deformation of the RBC membrane in a Poiseuille flow and its compression during passage through a stenotic microvessel, with a focus on the cell-cell interaction strength [2, 3, 29]. The flow of multiple RBCs through a microvascular bifurcation has also been simulated by the 2D IB-LBM and an RBC spring model [30, 31]. Other methods have been used for the same purpose, such as by Stamou and Buick [32] and Wang et al. [33]. Alizadeh et al. [17, 18] also used a hybrid IB-LBM to investigate the dynamics of healthy and sick RBCs during flows through a constricted vessel. The foregoing shows that the IB-LBM is effective for investigating the dynamics of RBCs in flows through constricted vessels and in relevant biomedical applications.

The present study represents further work about certain previous studies [30, 31], namely, an examination of the motion and deformation of RBCs by numerical simulation using the IB-LBM. The primary objective was a qualitative analysis of the effects of the degree of constriction in the vessel and the Re number on the physical characteristics of flowing RBCs. The RBC dynamics were extensively analyzed with respect to the degree of constriction, Re number, elastic modulus, and bending modulus. The IB-LBM was specifically used to examine the physical characteristics of three elastic RBCs. Flows through a simple straight vessel and a vessel with an annular bump were considered. The rest of this paper is organized as follows. Section 2 briefly describes the employed governing equations and numerical method. The detailed numerical results are presented and discussed in Section 3. Finally, the conclusions drawn from the study and the scope for further study are presented in Section 4.

## 2. Governing Equations and Numerical Method

**2.1. Governing Equations.** Consider an RBC with curved boundary  $\Gamma$  immersed in the 2D viscous fluid domain  $\Omega$ . The point on RBC boundary  $\Gamma$  is characterized by the Lagrangian parameters  $\mathbf{X}(s, t)$ , and the fluid domain  $\Omega$  is represented by the Eulerian coordinates  $\mathbf{x}$ . The equations governing the incompressible flow and elasticity of the RBCs in an external force field are as follows [17, 18]:

$$\rho \left( \frac{\partial \mathbf{u}}{\partial t} + \mathbf{u} \cdot \nabla \mathbf{u} \right) = -\nabla p + \mu \nabla^2 \mathbf{u} + \mathbf{f}(\mathbf{x}, t) \quad (1)$$

$$\nabla \cdot \mathbf{u} = 0 \quad (2)$$

$$\mathbf{f}(\mathbf{x}, t) = \int_{\Gamma} \mathbf{F}(s, t) \cdot \delta(\mathbf{x} - \mathbf{X}(s, t)) ds. \quad (3)$$

In the above equations,  $\rho$ ,  $\mathbf{u}$ ,  $p$ , and  $\mu$ , respectively, denote the fluid density, fluid velocity, fluid pressure, and dynamic viscosity;  $\mathbf{f}(\mathbf{x}, t)$  and  $\mathbf{F}(s, t)$  are, respectively, the membrane forces acting on the RBCs at the Eulerian point  $\mathbf{x}(x, t)$  and Lagrangian point  $\mathbf{X}(s, t)$ ; and  $\delta(\mathbf{x} - \mathbf{X}(s, t))$  is a nondimensional Dirac delta function.

**2.2. Immersed Boundary-Lattice Boltzmann Method (IB-LBM).** A popular kinetic model, namely, the discrete Boltzmann equation in the Bhatnagar–Gross–Krook (BGK) model with a single relaxation time under an external force, may be reproduced as follows [9, 18, 22, 27, 29]:

$$f_{\alpha}(\mathbf{x} + \mathbf{e}_{\alpha} \delta_t, t + \delta_t) - f_{\alpha}(\mathbf{x}, t) = -\frac{1}{\tau} [f_{\alpha}(\mathbf{x}, t) - f_{\alpha}^{\text{eq}}(\mathbf{x}, t)] + \delta_t \cdot G_{\alpha} \quad (4)$$

$$G_{\alpha} = \left( 1 - \frac{1}{2\tau} \right) \cdot \omega_{\alpha} \cdot \left( \frac{\mathbf{e}_{\alpha} \cdot \mathbf{u}}{c_s^2} + \frac{\mathbf{e}_{\alpha} \cdot \mathbf{u}}{c_s^4} \right) \cdot \mathbf{f}, \quad (5)$$

where  $f_{\alpha}^{\text{eq}}$  is the equilibrium distribution function,  $f_{\alpha}$  is the distribution function,  $\tau$  is the single relaxation parameter,  $\delta_t$  is the time interval,  $\mathbf{e}_{\alpha}$  is the particle velocity, and  $\omega_{\alpha}$  is a weight coefficient that is determined by the selected lattice velocity model. In the present study, a 2D lattice with nine velocity components, referred to as D2Q9, was employed. The formation of the D2Q9 lattice is illustrated in Figure 2.

The discrete velocity vectors of the 2D square lattice of D2Q9 can be expressed as

$$\mathbf{e}_{\alpha} = \begin{cases} (0, 0) & \alpha = 0 \\ c \left( \cos \left[ (\alpha - 1) \frac{\pi}{2} \right], \sin \left[ (\alpha - 1) \frac{\pi}{2} \right] \right) & \alpha = 1, 2, 3, 4 \\ \sqrt{2}c \left( \cos \left[ (2\alpha - 1) \frac{\pi}{4} \right], \sin \left[ (2\alpha - 1) \frac{\pi}{4} \right] \right) & \alpha = 5, 6, 7, 8, \end{cases} \quad (6)$$

where  $c (= \delta_x / \delta_t)$  is the lattice speed and  $\delta_x$  is the lattice constant.  $\omega_{\alpha}$  are the weight coefficients with the following values:

$$\omega_{\alpha} = \begin{cases} \frac{4}{9} & \alpha = 0 \\ \frac{1}{9} & \alpha = 1, 2, 3, 4 \\ \frac{1}{36} & \alpha = 5, 6, 7, 8. \end{cases} \quad (7)$$

The equilibrium distribution function  $f_{\alpha}^{\text{eq}}$  was chosen from the nine-velocity set model for 2D problems, as follows:

$$f_{\alpha}^{\text{eq}} = \rho \omega_{\alpha} \left[ 1 + \frac{\mathbf{e}_{\alpha} \cdot \mathbf{u}}{c_s^2} + \frac{(\mathbf{e}_{\alpha} \cdot \mathbf{u})^2}{2c_s^4} - \frac{|\mathbf{u}|^2}{2c_s^2} \right], \quad (8)$$

where  $c_s = 1/\sqrt{3} \cdot c$  is the speed of sound.

An immersed boundary treatment of a nonslip boundary condition was adopted, wherein the boundary force is spread

to the lattice points and the fluid lattice velocity is interpolated to the boundary points [18]. Figure 3 illustrates a 2D part of the membrane and the surrounding fluid. The interaction between the blood and the RBCs can be considered based on the relationship between the Lagrangian and Eulerian points using the following interaction equations [8, 9]:

$$\mathbf{f}(x, t) = \int_0^l \mathbf{F}(s, t) \delta(\mathbf{x} - \mathbf{X}(s, t)) ds$$

$$\mathbf{U}(s, t) = \mathbf{u}(\mathbf{X}(s, t), t) = \int_{\Gamma} \mathbf{u}(\mathbf{x}, t) \delta(\mathbf{X}(s, t) - \mathbf{x}) d\mathbf{x} \quad (9)$$

$$\delta_h(\mathbf{x}) = \delta_h(x) \cdot \delta_h(y),$$

where  $\mathbf{F}(s, t)$  is the Eulerian force of the fluid flow,  $\mathbf{f}(x, t)$  is the Lagrangian force of the immersed boundary, and  $l$  represents the cross-sectional profile of the immersed boundary of a discrete RBC.  $\delta(\mathbf{x} - \mathbf{X}(s, t))$  can be smoothly approximated by a continuous kernel distribution  $\delta(x)$ , as proposed by Peskin [20]:

$$\delta(x) = \begin{cases} 1 - |x| & 0 \leq |x| \leq \Delta x \\ 0 & \Delta x \leq |x|. \end{cases} \quad (10)$$

The position of the RBC is updated explicitly:

$$\frac{\partial \mathbf{X}(s, t)}{\partial t} = \mathbf{U}(s, t). \quad (11)$$

The macroscopic density is evaluated as  $\rho = \sum_{\alpha} f_{\alpha}$ , the velocity as  $\mathbf{u} = (1/\rho) \sum_{\alpha} f_{\alpha} \mathbf{e}_{\alpha}$ , the pressure as  $p = \rho c_s^2$ , and the viscosity as  $\nu = (\tau - 1/2)c_s^2 \cdot \delta_t$ .

Equation (4) can be decomposed into the two following distinct parts that can be executed in succession.

Collision is

$$f_{\alpha}^*(\mathbf{x}, t + \delta_t) = f_{\alpha}(\mathbf{x}, t) - \frac{1}{\tau} (f_{\alpha}(\mathbf{x}, t) - f_{\alpha}^{\text{eq}}(\mathbf{x}, t)). \quad (12)$$

Streaming is

$$f_{\alpha}(\mathbf{x} + c_{\alpha} \cdot \delta_t, t + \delta_t) = f_{\alpha}^*(\mathbf{x}, t + \delta_t). \quad (13)$$

Here,  $f_{\alpha}^*(\mathbf{x}, t + \delta_t)$  represents the distribution function after the collision, with its execution followed by streaming of the resulting distribution  $f_{\alpha}^*(\mathbf{x}, t + \delta_t)$  to neighboring nodes.

A Chapman–Enskog expansion can be used to obtain the equations of the density and momentum from (4). To derive the classical fluid equations ((1) and (2)), two macroscopic time scales ( $t_1 = \epsilon t$  and  $t_2 = \epsilon^2 t$ ) and a macroscopic length scale ( $x_1 = \epsilon x$ ) are required. An execution of the streaming operation on the left-hand side of each of the classical fluid equations ((1) and (2)) obtained by the Chapman–Enskog expansion can be used to determine the inertial terms.

**2.3. RBC Model.** A natural undeformed human RBC has a biconcave disk shape. The  $x$ - $y$  coordinates of the RBC cross-sectional profile can be described by the following equation [15]:

$$\bar{y} = 0.5 \times (1 - \bar{x}^2)^{1/2} \times (c_0 + c_1 \bar{x}^2 + c_2 \bar{x}^4), \quad (14)$$

$$-1 \leq \bar{x} \leq 1,$$

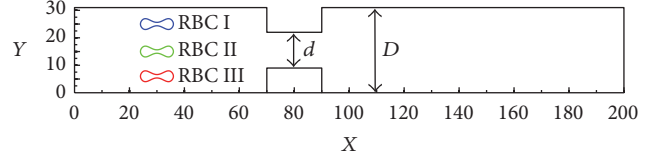


FIGURE 1: Schematic descriptions of the physical RBC models.

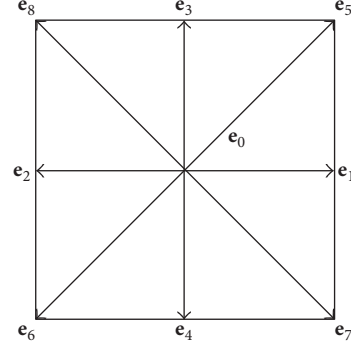


FIGURE 2: D2Q9 lattice.

where  $c_0 = 0.207$ ,  $c_1 = 2.002$ , and  $c_2 = 1.122$ . A physical model of the cross-sectional profile of an RBC is shown in Figure 4.

**2.4. Boundary Conditions.** Three different boundary conditions were implemented in this study. A periodic boundary condition was applied to both the vessel inlet and outlet [1, 4, 18, 23, 29]; a nonslip boundary condition was applied to the solid-wall boundary of the vessel [7]; and a half-way bounce-back boundary condition was applied to the straight vessel walls.

The boundary conditions of the bottom and top walls are, respectively, expressed by the following equations:

$$\begin{aligned} f_3'(x_f, t + \delta_t) &= f_4(x_f, t), \\ f_5'(x_f, t + \delta_t) &= f_6(x_f, t), \\ f_8'(x_f, t + \delta_t) &= f_7(x_f, t), \\ f_4'(x_f, t + \delta_t) &= f_3(x_f, t), \\ f_6'(x_f, t + \delta_t) &= f_5(x_f, t), \\ f_7'(x_f, t + \delta_t) &= f_8(x_f, t). \end{aligned} \quad (15)$$

The no-slip boundary condition on the fluid-solid interface is satisfied by making the velocity of any point on the solid surface equal to that of the adjacent fluid particle [9, 17, 25, 26].

### 3. Simulation Results and Discussions

A model of a microvessel with an annular bump was constructed as shown in Figure 1. Numerical calculations were

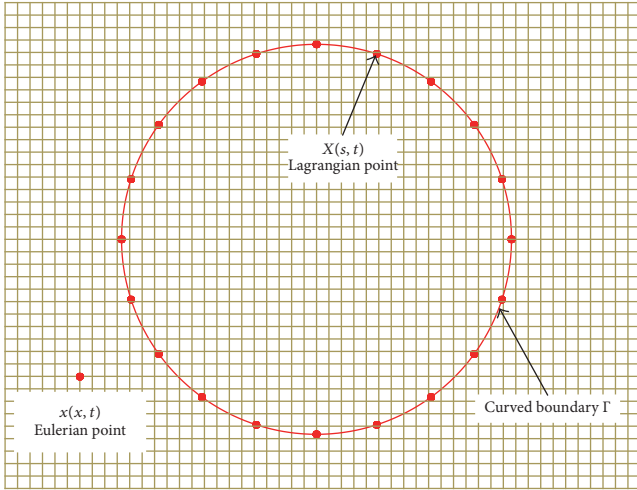


FIGURE 3: Structural boundary immersed in the 2D computational domain.

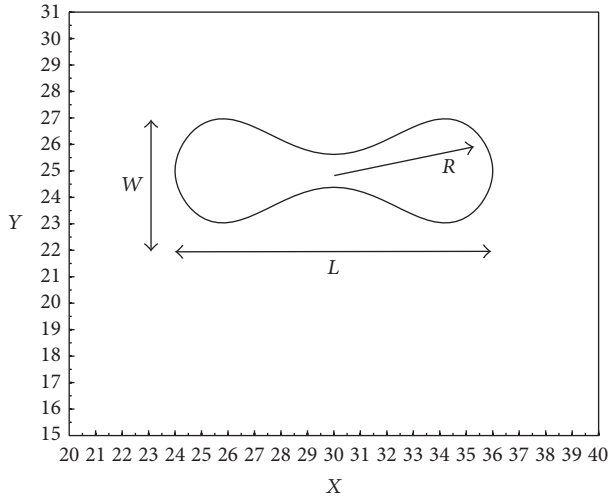
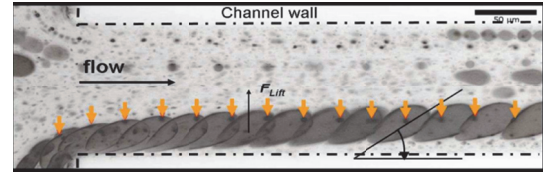
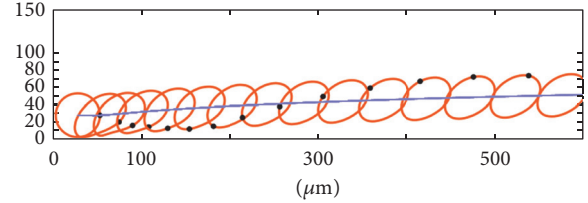


FIGURE 4: Physical model of the cross-sectional profile of an RBC of length  $L$ , width  $W$ , and radius  $R$ .

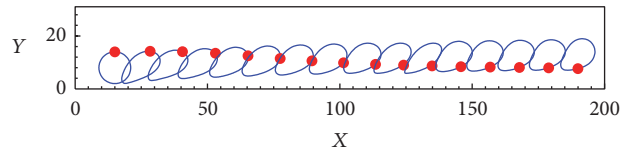
performed over  $200 \times 32$  lattice nodes covering a physical space of  $100 \mu\text{m} \times 15 \mu\text{m}$ . A uniform square mesh with a nondimensional unit of  $dx = dy = 1$  was employed. The membrane of an RBC of  $\approx 6 \mu\text{m}$  in diameter and  $\approx 2 \mu\text{m}$  in thickness was represented by 100 elastic elements. The elastic modulus  $E_s$  and bending modulus  $E_b$  were, respectively, set to  $6.0 \times 10^{-3} \text{ Pa}\cdot\text{s}$  and  $2.0 \times 10^{-19} \text{ Pa}\cdot\text{s}$  for a healthy RBC and  $6.0 \times 10^{-2} \text{ Pa}\cdot\text{s}$  and  $2.0 \times 10^{-18} \text{ Pa}\cdot\text{s}$  for a sick RBC, while the nondimensional unit conditions  $E_b$  and  $E_s$  were set to 0.1 and 0.001 for a healthy RBC, respectively. The nonslip boundary condition was applied to the solid-wall boundary of the channel, while the immersed RBC elastic boundary and the periodic boundary conditions were, respectively, applied to the inlet and outlet of the channel. The physical problem is governed by the nondimensional Re number defined by  $\text{Re} = \rho R^2 \gamma / \mu$ , where  $R$  is the RBCs radius and  $\gamma$  is the flow shear rate. The Re number was 0.1. To examine the motion



(a)



(b)



(c)

FIGURE 5: The rotational motions of an initially spherical vesicle in Poiseuille flows: (a) series of snapshots from experimental data [34], (b) numerical simulation by the FE-LBM [35], and (c) current numerical simulation.

and deformation of the three considered RBCs during flows through constricted vessels, five cases involving different degrees of constriction values ( $=d/D$ ) were investigated. The initial positions of RBC I (upper), RBC II (middle), and RBC III (lower) were (25, 30), (15, 30), and (2, 30), respectively (see Figure 1).

**3.1. Motion and Deformations of “Healthy” and “Sick” RBCs in a Straight Vessel.** The motions and deformations of healthy and sick RBCs in a straight vessel were compared. The elastic RBCs were placed asymmetrically in a Poiseuille shear flow near the wall of the channel.

Figure 5 shows the rotational motions of an initially spherical vesicle in Poiseuille flows, it is evident that the spherical membrane will rotate clockwise and is dragged toward the centerline of the channel, and the red bold point illustrates the rotation (Figure 5(c)). The comparison reveals a good agreement among the experimental results [34] (Figure 5(a)), numerical simulation by the FE-IBM [35] (Figure 5(b)), and the present numerical results (Figure 5(c)).

The time evolutions of the rotational motions of a healthy and sick RBC initially positioned vertically are plotted in Figure 6: (a) healthy RBC, (b) sick RBC, and (c) numerical simulation by the FE-LBM [35]. It can be observed from Figure 6(a) that a healthy RBC undergoes deformation and an unsteady tank-treading motion toward the center of the channel, attributable to the shearing effect of the Poiseuille flow. Figure 6(b) shows profile snapshots of the sick RBC during its deformation. The sick RBC exhibits an almost steady tumbling-rotating behavior accompanied by periodical shape

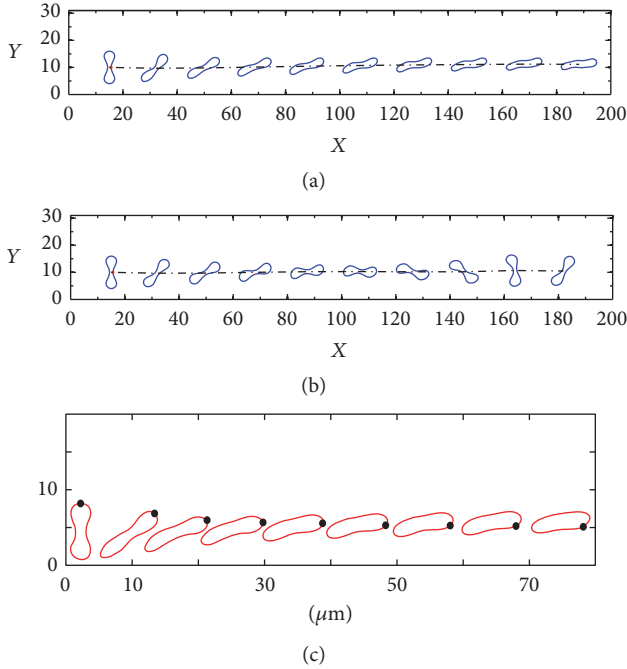


FIGURE 6: The time evolutions of the motions of RBC in Poiseuille flows, the initially vertical RBCs are positioned near the bottom lateral wall of the channel. (a) Healthy RBC, (b) sick RBC, and (c) numerical simulation by the FE-LBM [35].

deformation. It rotates clockwise and preserves its shape. The above observations are well consistent with the findings of previous studies [7, 9, 26, 27, 35].

Figure 7 shows snapshots of the deformation of healthy and sick RBCs initially positioned thwart-wise ((a) and (b): current numerical simulation; (c) and (d): numerical results of [9]). The comparison reveals that the current numerical simulation results (Figures 7(a) and 7(b)) are in line with the numerical simulation by Dadvand et al. (Figures 7(c) and 7(d)) [9, 35]. Comparison of the cases of different initial states in Figures 6 and 7 suggests that the elastic modulus significantly impacts the overall mechanical characteristics of the tank-treading and tumbling-rotating motions of an RBC.

The spatial-temporal evolutions of the motions, deformations, and shapes of three healthy RBCs along the channel are shown in Figure 8. It can be observed that RBC II moves over a longer distance compared to RBCs I and III. RBC II assumes a typical arrow-like shape, whereas RBCs I and III acquire a diagonal configuration. This may be attributed to RBC II being located near the centerline of the channel, where the pressure is higher. RBCs I and III gradually migrate toward the centerline of the channel, although the latter migrates further and is more elongated.

To investigate the effect of the Re number on the variation of the barycentric coordinates, four different Re numbers, namely, 0.10, 0.15, 0.20, and 0.25, were considered. The vertical movements of the RBCs for the different Re numbers are described in Figure 9, the relationship of  $t$  and vertical distance is shown in Figure 9(a), and Figure 9(b) reveals the effect of Re on the barycentric coordinates. Firstly, the vertical

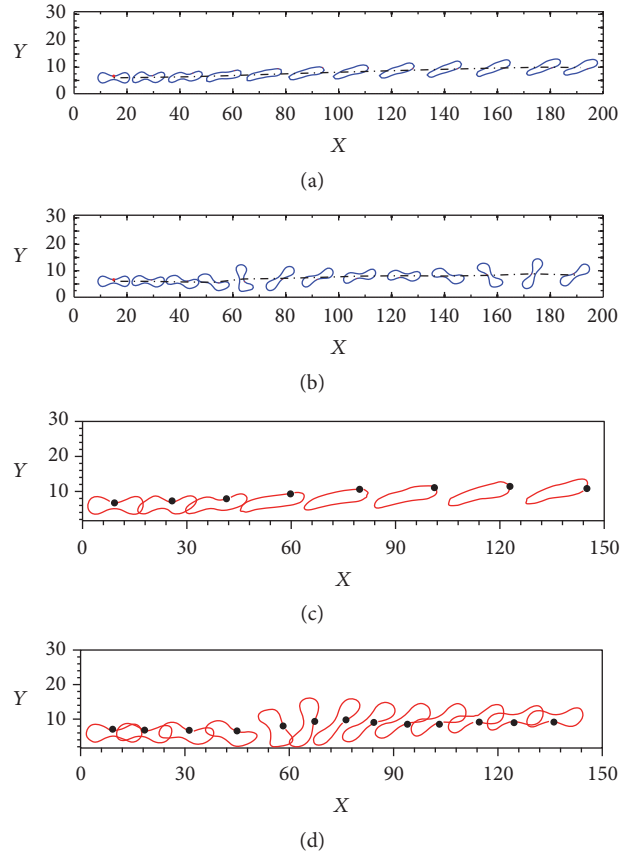


FIGURE 7: Rotational motions of healthy RBC ((a) and (c)) and sick RBC ((b) and (d)) in Poiseuille flows. The initially thwart-wise RBCs are positioned near the bottom lateral wall of the channel. ((a) and (b)) Current numerical simulation and ((c) and (d)) numerical results of [9].

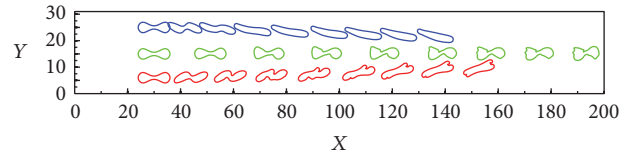


FIGURE 8: Rotational motions of three healthy RBCs asymmetrically positioned in the channel.

distance increases with increasing Re number, accompanied by farther migration toward to the centerline of the channel, to reduce the flow resistance. Secondly, in a certain position, the Re has little effect on the barycentric coordinates, and the position of X direction has important influence on the longitudinal displacement.

3.2. Motion and Deformation of Three RBCs in a Constricted Vessel. The spatial-temporal evolutions of the motions and deformations of three healthy RBCs in various constricted vessels are shown in Figures 10(a)–10(f), which, respectively, correspond to cases of  $d/D = 30/30$  at  $t = 45$  ms,  $d/D = 24/30$  at  $t = 47$  ms,  $d/D = 20/30$  at  $t = 51$  ms,  $d/D = 16/30$  at  $t = 59.5$  ms,  $d/D = 12/30$  at  $t = 85$  ms, and  $d/D = 10/30$  at  $t =$

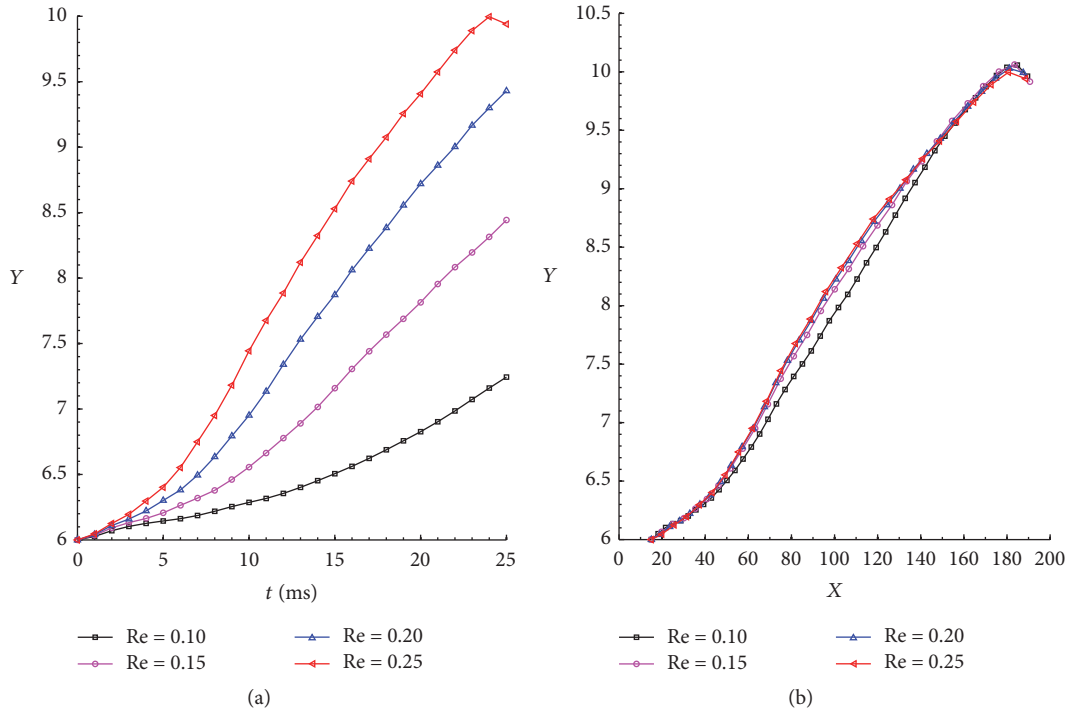


FIGURE 9: Variation of the RBC vertical movements with respect to the Re number of the flow: (a) the relationship of  $t$  and vertical distance and (b) the effect of Re on the barycentric coordinates.

116.5 ms. It can be seen that the RBCs in the vessel would deform and pass through the constricted part easily. Ahead of the constriction, the RBCs are swept by the fluid flow with minimal deformation. As they approach the constriction, they rotate toward the center of the flow and gradually assume an approximately horizontal orientation. The RBCs are relaxed and vibrate elastically, although the vibration rapidly decays under the viscous damping of the surrounding fluid. The RBCs subsequently regain their stable shape within a short time.

Comparison of the six constriction cases suggests that, with increasing constriction, the RBCs are forced to exhibit higher deformability than in other parts of the microchannel to squeeze through the constriction. In addition, a longer time is required for the RBCs to squeeze through a narrower constriction, attributable to the greater deformation required. It is also noteworthy that the initial position of the RBCs is not on the centerline of the channel, although they migrate toward the centerline, assuming a diagonal configuration to reduce the flow resistance.

In contrast with a healthy RBC, the elastic modulus of a sick RBC is reduced to 0.05 while the other parameters are maintained constant. Figure 11 shows the spatial-temporal evolutions of the motions and deformations of three sick RBCs in a constricted vessel. Figures 11(b)–11(e) reveal that the sick RBCs easily pass through the constriction and no obstruction will occur during the process, and the overall characteristics of the motions are similar consistent with healthy RBCs. However, the ultimate shape of the sick RBCs significantly differs from that of the healthy RBCs in Figures 10(b)–10(e), and this is attributed to the variations of the

pressure along the flow direction. It can also be seen that the sick RBCs move slower than the healthy one due to its larger elastic module. Moreover, for a low constriction ratio of  $d/D = 1/3$  in Figure 11(f), only the sick RBC II emerges from the constriction zone, with the sick RBCs I and III touching the boundary of the constriction, and this touching phenomenon can produce friction, which caused the RBCs aggregating at the constriction area.

The deformations and motions of three sick RBCs in a constricted vessel with  $d/D = 1/3$  are shown in Figure 12. It can be observed that, with increasing Re number up to 0.40, the RBCs pass through the constriction region and gradually migrate toward the centerline of the channel. This is due to the fact that, with the Re number increasing, the shear force acting on the RBCs could undergo a bigger growth, and then the RBCs will experience more deformation. People who have suffered a hypertensive disease experienced a crucial augment in blood velocity, which maybe caused fractures and lacerations. Heart disease may cause a reduction in blood velocity, under the low-speed vessels which maybe caused deoxygenation [18]. In addition, the elastic modulus, blood pressure, flow velocity, and Re number significantly impact the passage of the RBCs passing through a constricted vessel.

### 3.3. Effect of Constriction Ratio on RBC Mechanical Behavior.

To examine the effects of the degree of constriction on the motion and deformation of the RBCs, six cases with  $d/D$  values of 30/30, 24/30, 20/30, 16/30, 12/30, and 10/30 were, respectively, considered. The nondimensional ratios width-to-length ( $W/L$ ), width-to-diameter ( $W/R$ ), and length-to-diameter ( $L/R$ ) were evaluated, where  $W$ ,  $L$ , and  $R$  are the

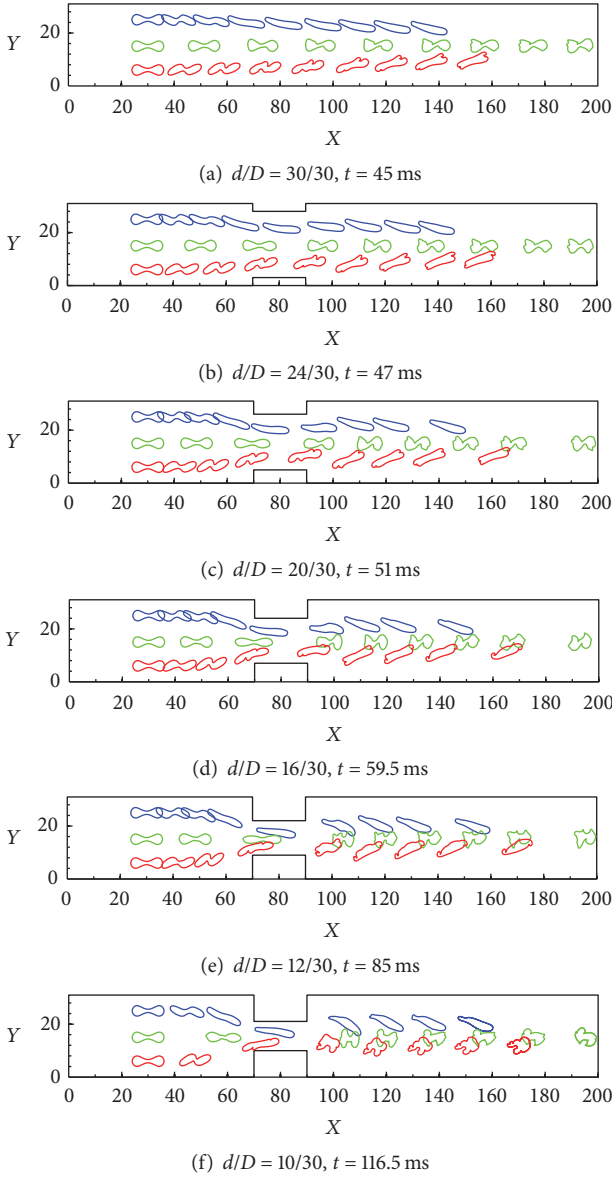


FIGURE 10: Transient deformations and motions of three healthy RBCs during Poiseuille flow through a constricted vessel: (a)  $d/D = 30/30$  at  $t = 45$  ms, (b)  $d/D = 24/30$  at  $t = 47$  ms, (c)  $d/D = 20/30$  at  $t = 51$  ms, (d)  $d/D = 16/30$  at  $t = 59.5$  ms, (e)  $d/D = 12/30$  at  $t = 85$  ms, and (f)  $d/D = 10/30$  at  $t = 116.5$  ms.

length, width, and radius of the RBCs, respectively (see Figure 4).

Figure 13 shows the variations of the ratios  $L/R$  and  $W/R$  for different degrees of constriction of the microchannel. It can be seen that the values of  $L/R$  and  $W/R$  were positively correlated with constriction ratio; the constriction area has a significant effect on the nondimensional parameters, and the RBCs undergo greater forced deformation compared to other areas of the microchannel to squeeze through the constriction. The peak position indicates that the RBCs have entered the constriction area. With the constriction ratio increasing, a longer time is required for the RBCs to squeeze through the constriction. When the RBCs pass through the

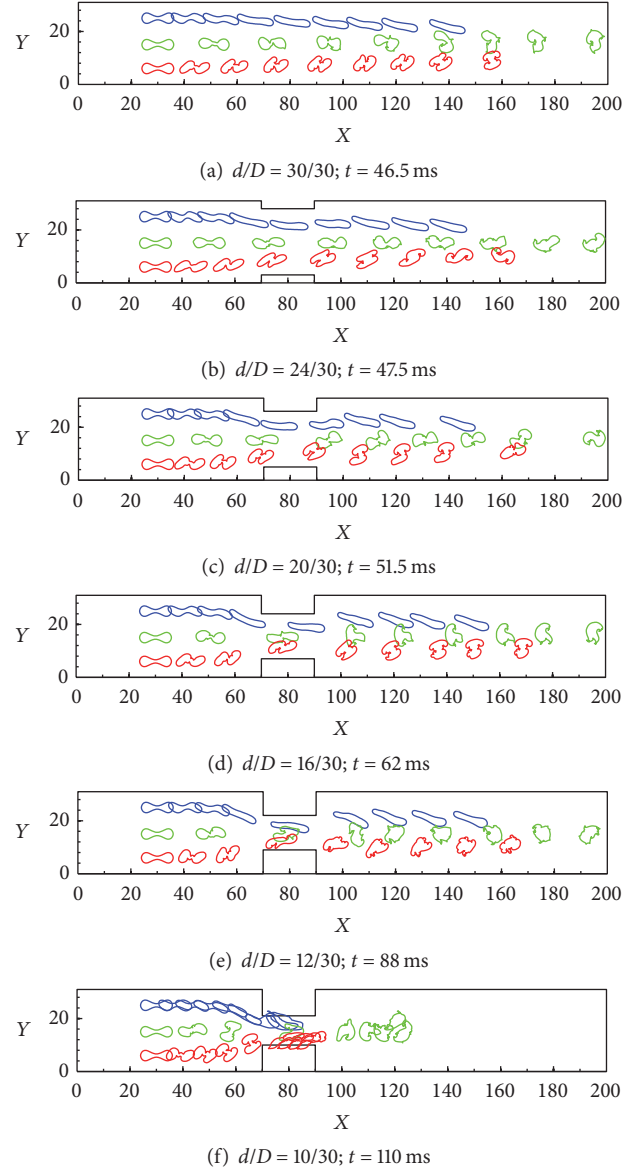


FIGURE 11: Transient deformations and motions of three sick RBCs during Poiseuille flow through a contracted vessel with  $Re = 0.10$ : (a)  $d/D = 30/30$  at  $t = 46.5$  ms, (b)  $d/D = 24/30$  at  $t = 47.5$  ms, (c)  $d/D = 20/30$  at  $t = 51.5$  ms, (d)  $d/D = 16/30$  at  $t = 62$  ms, (e)  $d/D = 12/30$  at  $t = 88$  ms, and (f)  $d/D = 10/30$  at  $t = 110$  ms.

constriction section, the RBCs regain a stable shape beyond the constriction area.

Figures 14(a)–14(f) show the variations of the ratio  $W/L$  of healthy RBCs for  $d/D$  values of 30/30, 24/30, 20/30, 16/30, 12/30, and 10/30, respectively. It can be seen from the figures that RBC II undergoes greater deformation and flows faster than RBCs I and III, and the peak position also indicates that the RBCs have entered the constriction area. This may be attributed to the shearing effect of the Poiseuille flow. Figures 14(b)–14(f) reveal that as the RBCs approach the constriction section, the nondimensional parameter  $W/L$  of RBCs has a substantial change until they leave the constriction area. RBC II (middle) moves quicker than RBC I and RBC

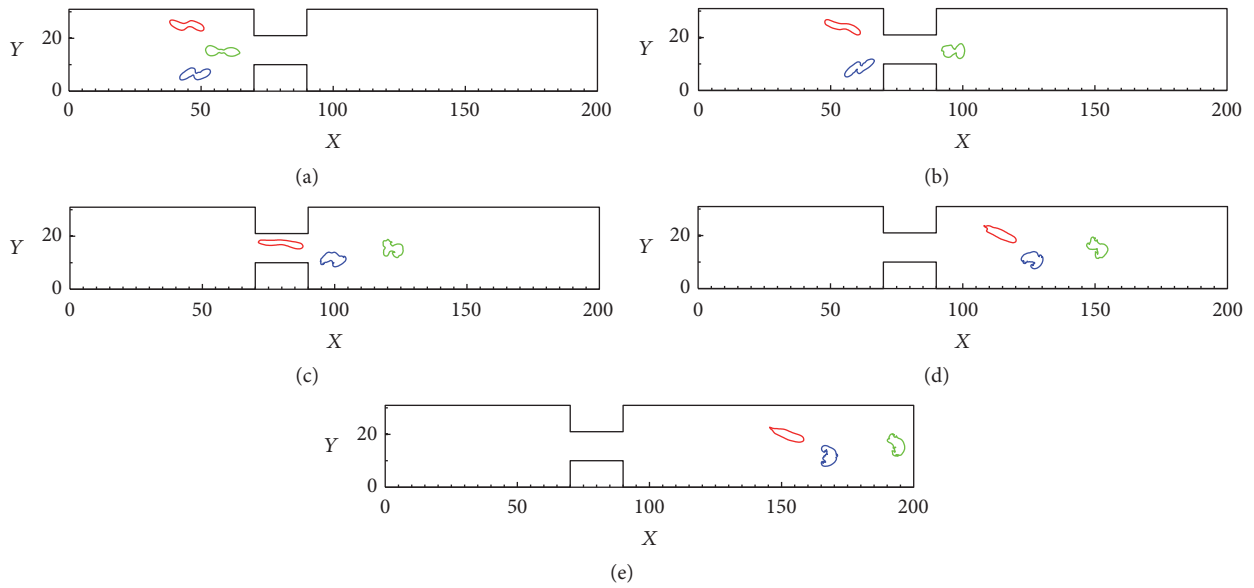


FIGURE 12: Deformations and motions of three sick RBCs in a constricted vessel ( $d/D = 10/30$ ) with  $Re = 0.4$ .

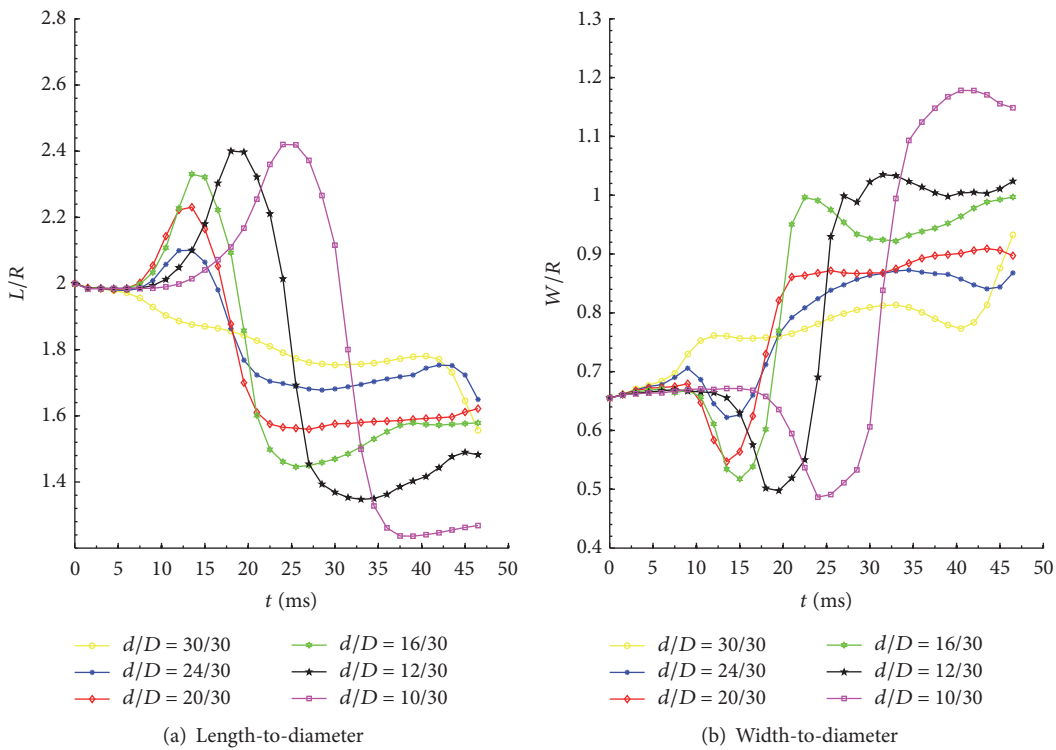


FIGURE 13: Variations of the (a) length-to-diameter and (b) width-to-diameter ratios of healthy RBCs during Poiseuille flow through microchannels with different degrees of constriction.

III (lower), attributed to the effect of the Poiseuille flow. Another interesting phenomenon is that, with RBCs leaving constriction area, the  $W/L$  of RBC II has minor change, while the values for RBCs I and III abruptly decrease owing to the boundary effect.

The variations of  $L/R$  ratio for the healthy and sick RBCs II for different degrees of constriction are shown in Figure 15. It can be seen from the figures that the healthy RBC has a

lower  $L/R$  ratio than the sick RBC. In addition, the variation of the  $L/R$  ratio of the healthy RBC is regular, whereas that of the sick RBC is irregular and oscillates.

#### 4. Conclusions

The motions and deformations of three RBCs in a Poiseuille flow through a constricted microchannel were numerically

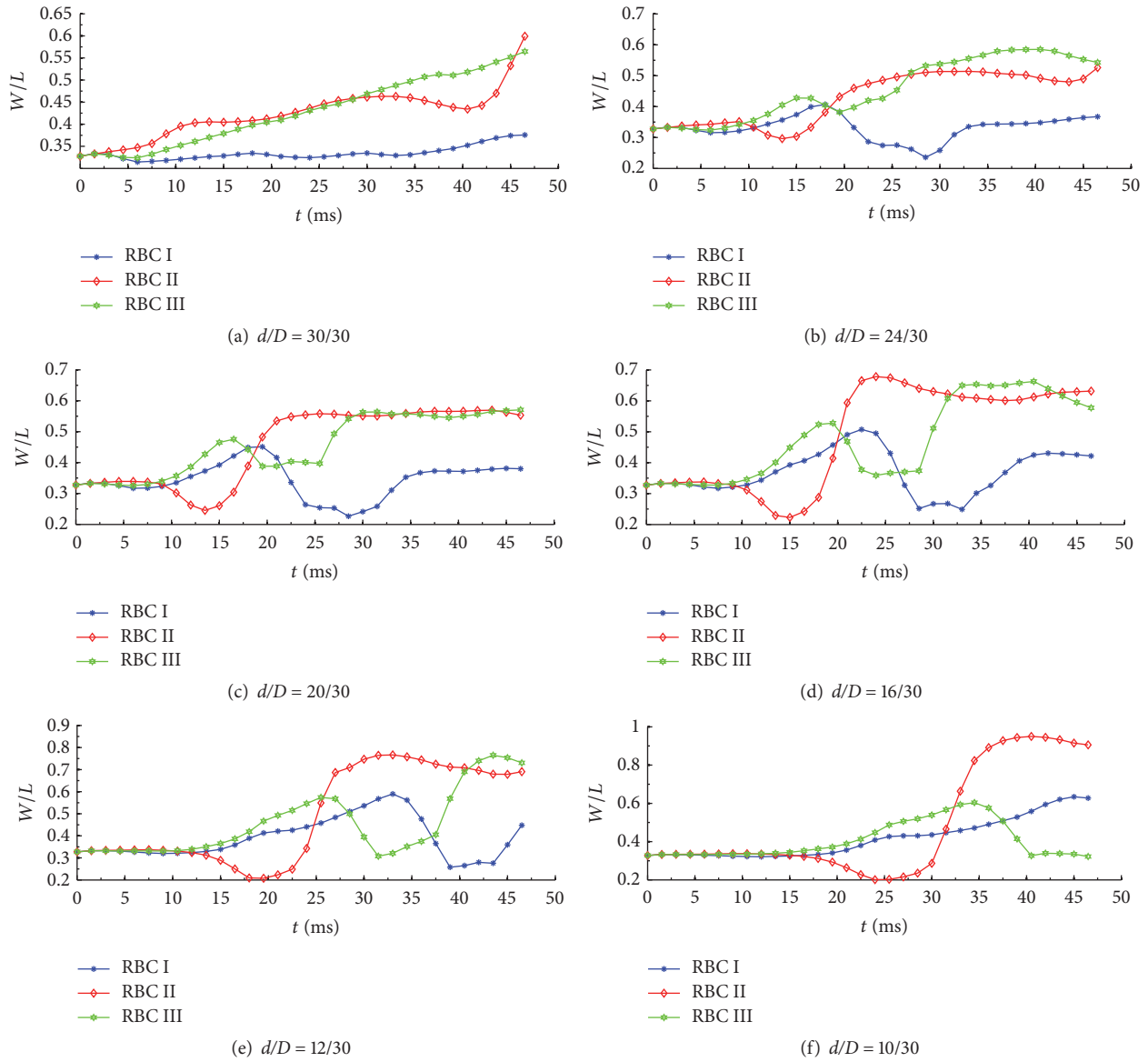


FIGURE 14: Variations of the width-to-length ratio for healthy RBCs during Poiseuille flow through microchannels with different degrees of constriction represented by  $d/D$  values of 30/30, 24/30, 20/30, 16/30, 12/30, and 10/30, respectively.

investigated using the IB-LBM. The dynamics of the RBCs with respect to the degree of constriction of the microchannel, the  $Re$  number of the flow, and the elastic and bending moduli of the cells in the flow field were analyzed in detail. Following is a summary of the conclusions drawn from the observations.

Firstly, when the RBCs are located off the axis of symmetry of the microchannel, the shearing effect of the Poiseuille flow increases the forces acting on them, inducing their migration toward the centerline of the microchannel. Secondly, healthy RBCs exhibit higher deformability than sick RBCs during passage through a constriction area. In the process, the length-to-radius ratios of healthy RBCs vary regularly, whereas those of sick RBCs vary irregularly and oscillate. Thirdly, the width-to-radius and length-to-radius

ratios of the RBCs increase with decreasing constriction ratio, with a longer time required for the RBCs to squeeze through a narrower constriction. However, the RBCs regain their stable shape beyond the constriction area. Furthermore, for sick RBCs in a microchannel with a constriction ratio as low as 1/3, adjustment of the flow parameters such as increasing the  $Re$  number to about 0.4 is required, given which they are able to pass and gradually migrate toward the centerline of the channel. This is particularly applicable to practical health conditions such as hemangioma and hypertension.

It is noteworthy that the present study only examined the effects of the degree of constriction of the channel and the  $Re$  number of the flow on the mechanical behavior of RBCs. Further study is required to examine the aggregation behavior of the cells and the elastic and viscoelastic effects

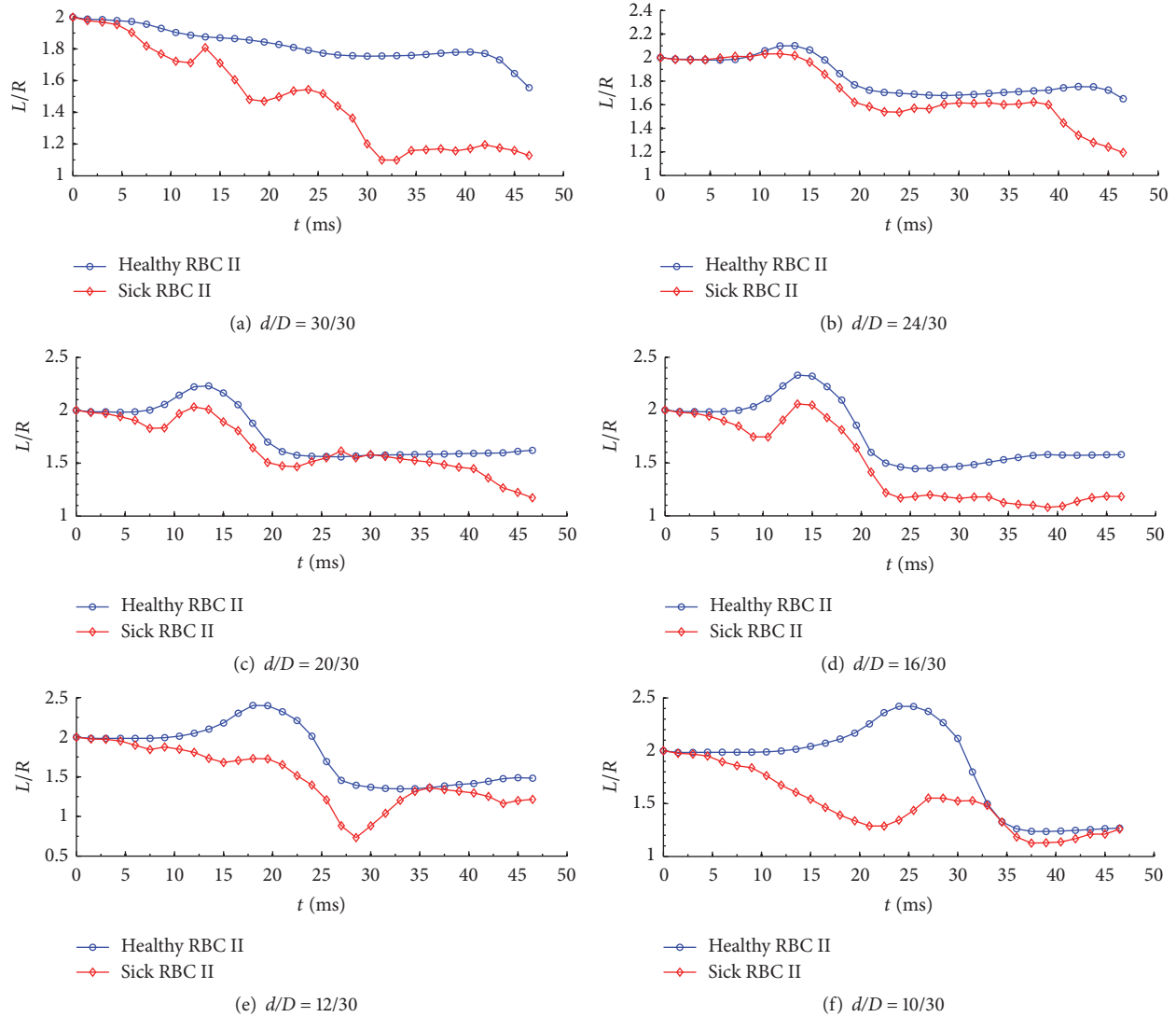


FIGURE 15: Variations of the length-to-radius ratio of the healthy and sick RBC II during Poiseuille flow through microchannels with different degrees of constriction represented by  $d/D$  values of 30/30, 24/30, 20/30, 16/30, 12/30, and 10/30, respectively.

of the channel. Additionally, for more accurate results, more sophisticated 3D models with more complex geometries such as bifurcation should be adopted for the simulations.

## Disclosure

Due consideration has been given to the protection of intellectual property associated with this work and there are no impediments to this publication, including the timing of the publication, with respect to intellectual property. In so doing, the authors confirm that they have followed the regulations of their institutions concerning intellectual property.

## Conflicts of Interest

The authors declare that there are no known conflicts of interest associated with this publication. No significant financial support of the work was received that could have influenced its outcome.

## Authors' Contributions

Rongyang Wang, Yikun Wei, and Chuanyu Wu conceived of, designed, and performed the experiments of this study; Liang Sun and Wenguang Zheng analyzed the data; and Rongyang Wang wrote the paper. Yikun Wei and Chuanyu Wu contributed equally to this work. The paper has been read and approved by all the named authors and there is no other person who satisfies the criteria for authorship of the same. The listing order of the authors on this paper has been approved by all the authors.

## Acknowledgments

This work was supported by the National Natural Science Foundation of China (Grant nos. 51675488 and 11502237), the Major Science and Technology Projects of Zhejiang Province (Grant no. 2015C02001), Zhejiang Provincial Natural Science Foundation of China (Grant nos. LGN18E050002,

LY18A020010), and Huzhou Public Welfare Application Research Project (Grant no. 2015GZ02).

## References

- [1] J. Zhang, P. C. Johnson, and A. S. Popel, "An immersed boundary lattice Boltzmann approach to simulate deformable liquid capsules and its application to microscopic blood flows," *Physical Biology*, vol. 4, no. 4, pp. 285–295, 2007.
- [2] K. Vahidkhan and N. Fatourae, "Numerical simulation of red blood cell behavior in a stenosed arteriole using the immersed boundary-lattice Boltzmann method," *International Journal for Numerical Methods in Biomedical Engineering*, vol. 28, no. 2, pp. 239–256, 2012.
- [3] Y.-Q. Xu, F.-B. Tian, and Y.-L. Deng, "An efficient red blood cell model in the frame of IB-LBM and its application," *International Journal of Biomathematics*, vol. 6, no. 1, Article ID 1250061, pp. 1–22, 2013.
- [4] J. F. Zhang, P. C. Johnson, and A. S. Popel, "Red blood cell aggregation and dissociation in shear flows simulated by lattice Boltzmann method," *Journal of Biomechanics*, vol. 41, no. 1, pp. 47–55, 2008.
- [5] K.-I. Tsubota and S. Wada, "Elastic force of red blood cell membrane during tank-treading motion: Consideration of the membrane's natural state," *International Journal of Mechanical Sciences*, vol. 52, no. 2, pp. 356–364, 2010.
- [6] W. Xiong and J. Zhang, "Two-dimensional lattice Boltzmann study of red blood cell motion through microvascular bifurcation: Cell deformability and suspending viscosity effects," *Biomechanics and Modeling in Mechanobiology*, vol. 11, no. 3-4, pp. 575–583, 2012.
- [7] A. Ghafouri and A. Hassanzadeh, "Numerical study of red blood cell motion and deformation through a microchannel using lattice Boltzmann-immersed boundary method," *Journal of the Brazilian Society of Mechanical Sciences and Engineering*, vol. 39, no. 6, pp. 1873–1882, 2017.
- [8] Z. L. Wu, Y. Chen, M. Wang et al., "Continuous inertial microparticle and blood cell separation in straight channels with local microstructures," *Lab on a Chip*, vol. 16, pp. 532–542, 2016.
- [9] A. Dadvand, M. Baghalnezhad, I. Mirzaee, B. C. Khoo, and S. Ghoreishi, "An immersed boundary-lattice Boltzmann approach to study the dynamics of elastic membranes in viscous shear flows," *Journal of Computational Science*, vol. 5, no. 5, pp. 709–718, 2014.
- [10] H. H. Hu, N. A. Patankar, and M. Y. Zhu, "Direct Numerical Simulations of Fluid-Solid Systems Using the Arbitrary Lagrangian-Eulerian Technique," *Journal of Computational Physics*, vol. 169, no. 2, pp. 427–462, 2001.
- [11] S. Xu and Z. J. Wang, "An immersed interface method for simulating the interaction of a fluid with moving boundaries," *Journal of Computational Physics*, vol. 216, no. 2, pp. 454–493, 2006.
- [12] W. K. Liu, D. W. Kim, and S. Tang, "Mathematical foundations of the immersed finite element method," *Computational Mechanics*, vol. 39, no. 3, pp. 211–222, 2007.
- [13] F.-B. Tian, H. Dai, H. Luo, J. F. Doyle, and B. Rousseau, "Fluid-structure interaction involving large deformations: 3D simulations and applications to biological systems," *Journal of Computational Physics*, vol. 258, pp. 451–469, 2014.
- [14] F.-B. Tian, "Deformation of a capsule in a power-law shear flow," *Computational and Mathematical Methods in Medicine*, vol. 2016, Article ID 7981386, 9 pages, 2016.
- [15] Q. Wei, Y. Q. Xu, F. B. Tian et al., "IB-LBM simulation on blood cell sorting with a micro-fence structure," *Bio-Medical Materials and Engineering*, vol. 24, pp. 475–481, 2014.
- [16] T. Krüger, F. Varnik, and D. Raabe, "Efficient and accurate simulations of deformable particles immersed in a fluid using a combined immersed boundary lattice Boltzmann finite element method," *Computers & Mathematics with Applications*, vol. 61, no. 12, pp. 3485–3505, 2011.
- [17] A. Alizadeh and A. Dadvand, "Simulation of the motion of two elastic membranes in Poiseuille shear flow via a combined immersed boundary-lattice Boltzmann method," *Journal of Computational Science*, vol. 12, pp. 51–61, 2016.
- [18] A. Hassanzadeh, N. Pourmahmoud, and A. Dadvand, "Numerical simulation of motion and deformation of healthy and sick red blood cell through a constricted vessel using hybrid lattice Boltzmann-immersed boundary method," *Computer Methods in Biomechanics and Biomedical Engineering*, vol. 20, no. 7, pp. 1–13, 2017.
- [19] L. Shi, T.-W. Pan, and R. Glowinski, "Numerical simulation of lateral migration of red blood cells in Poiseuille flows," *International Journal for Numerical Methods in Fluids*, vol. 68, no. 11, pp. 1393–1408, 2012.
- [20] C. S. Peskin, "Numerical analysis of blood flow in the heart," *Journal of Computational Physics*, vol. 25, no. 3, pp. 220–252, 1977.
- [21] T. Krüger, M. Gross, D. Raabe, and F. Varnik, "Crossover from tumbling to tank-treading-like motion in dense simulated suspensions of red blood cells," *Soft Matter*, vol. 9, no. 37, pp. 9008–9015, 2013.
- [22] M. Navidbakhsh and M. Rezazadeh, "An immersed boundary-lattice Boltzmann model for simulation of malaria-infected red blood cell in micro-channel," *Scientia Iranica*, vol. 19, no. 5, pp. 1329–1336, 2012.
- [23] M. Navidbakhsh and M. Rezazadeh, "A computational study of a capsule lateral migration in microchannel flow," *Acta Mechanica Sinica*, vol. 29, no. 4, pp. 513–525, 2013.
- [24] Y. Sui, Y. T. Chew, P. Roy, and H. T. Low, "A hybrid method to study flow-induced deformation of three-dimensional capsules," *Journal of Computational Physics*, vol. 227, no. 12, pp. 6351–6371, 2008.
- [25] Y. Sui, Y. T. Chew, P. Roy, and H. T. Low, "Inertia effect on the transient deformation of elastic capsules in simple shear flow," *Computers & Fluids*, vol. 38, no. 1, pp. 49–59, 2009.
- [26] H.-T. Low, M. Ju, Y. Sui, T. Nazir, B. Namgung, and S. Kim, "Numerical simulations of deformation and aggregation of red blood cells in shear flow," *Critical Reviews in Biomedical Engineering*, vol. 41, no. 4-5, pp. 425–434, 2013.
- [27] X. Ma, B. Huang, G. Wang, X. Fu, and S. Qiu, "Numerical simulation of the red blood cell aggregation and deformation behaviors in ultrasonic field," *Ultrasonics Sonochemistry*, vol. 38, pp. 604–613, 2017.
- [28] M. Ju, H. L. Leo, and S. Kim, "Numerical investigation on red blood cell dynamics in microflow: Effect of cell deformability," *Clinical Hemorheology and Microcirculation*, vol. 65, no. 2, pp. 105–117, 2017.
- [29] Y. Q. Xu, X. Y. Tang, F. B. Tian, Y. H. Peng, Y. Xu, and Y. J. Zeng, "IB-LBM simulation of the haemocyte dynamics in a stenotic capillary," *Computer Methods in Biomechanics and Biomedical Engineering*, vol. 17, no. 9, pp. 978–985, 2014.

- [30] Z.-Y. Shen and Y. He, "A lattice Boltzmann method for simulating the separation of red blood cells at microvascular bifurcations," *Chinese Physics Letters*, vol. 29, no. 2, Article ID 024703, 2012.
- [31] X. Yin, T. Thomas, and J. Zhang, "Multiple red blood cell flows through microvascular bifurcations: Cell free layer, cell trajectory, and hematocrit separation," *Microvascular Research*, vol. 89, pp. 47–56, 2013.
- [32] A. C. Stamou and J. M. Buick, "An LBM based model for initial stenosis development in the carotid artery," *Journal of Physics A: Mathematical and Theoretical*, vol. 49, no. 19, Article ID 195602, 2016.
- [33] T. Wang, Y. Tao, U. Rongin, and Z. Xing, "A Two-Dimensional Numerical Investigation of Transport of Malaria-Infected Red Blood Cells in Stenotic Microchannels," *BioMed Research International*, vol. 2016, Article ID 1801403, 2016.
- [34] T. Franke and H. Schmid, "Tank-trading motion of red blood cell membranes in viscometric flow: behavior of intracellular and extracellular markers," *Blood Cells*, vol. 3, pp. 351–365, 1997.
- [35] T. Franke, R. H. W. Hoppe, C. Linsenmann, L. Schmid, C. Willbold, and A. Wixforth, "Numerical simulation of the motion of red blood cells and vesicles in microfluidic flows," *Computing and Visualization in Science*, vol. 14, no. 4, pp. 167–180, 2011.

## Research Article

# Analysis and Numerical Simulations of a Stochastic SEIQR Epidemic System with Quarantine-Adjusted Incidence and Imperfect Vaccination

Fei Li,<sup>1</sup> Xinzhu Meng ,<sup>1,2</sup> and Xinzeng Wang<sup>1,2</sup>

<sup>1</sup>College of Mathematics and Systems Science, Shandong University of Science and Technology, Qingdao 266590, China

<sup>2</sup>State Key Laboratory of Mining Disaster Prevention and Control Co-Founded by Shandong Province and the Ministry of Science and Technology, Shandong University of Science and Technology, Qingdao 266590, China

Correspondence should be addressed to Xinzhu Meng; mxz721106@sdust.edu.cn

Received 21 October 2017; Accepted 28 January 2018; Published 20 February 2018

Academic Editor: Xiaole Chen

Copyright © 2018 Fei Li et al. This is an open access article distributed under the Creative Commons Attribution License, which permits unrestricted use, distribution, and reproduction in any medium, provided the original work is properly cited.

This paper considers a high-dimensional stochastic SEIQR (susceptible-exposed-infected-quarantined-recovered) epidemic model with quarantine-adjusted incidence and the imperfect vaccination. The main aim of this study is to investigate stochastic effects on the SEIQR epidemic model and obtain its thresholds. We first obtain the sufficient condition for extinction of the disease of the stochastic system. Then, by using the theory of Hasminskii and the Lyapunov analysis methods, we show there is a unique stationary distribution of the stochastic system and it has an ergodic property, which means the infectious disease is prevalent. This implies that the stochastic disturbance is conducive to epidemic diseases control. At last, computer numerical simulations are carried out to illustrate our theoretical results.

## 1. Introduction

Mathematical models for differential equations have been widely applied in various fields [1–7]. Specifically, they have had a realistic significance to analyze the dynamical behaviors in the field of mathematical biology [8–17], which obtained some novel results.

In fact, the main meaning of the research of infectious disease dynamics is to make people more comprehensively and deeply understand the epidemic regularity of infectious disease; then more effective control strategies are adopted to provide better theoretical support for the prevention and control of epidemics. To this end, many mathematical biology workers considered more realistic factors in the course of the study, such as population size change, migration, cross infection, and other practical factors. In the course of epidemics and outbreaks of infectious diseases, people always take various measures to control the epidemic in order to minimize the harm of epidemic diseases. Quarantine is one of the important means to prevent and control epidemic diseases; it has been used to control contagious diseases

with some success. Specifically, during the severe acute respiratory syndrome (SARS) outbreak in 2002, remarkable results were also achieved. Among them, mathematical models have been used to investigate their impact on the dynamics of infectious diseases under quarantine [18–22], which attracts deep research interest of many mathematicians and biologists. Recently, Hethcote et al. [21] considered an SIQR (susceptible-infected-quarantined-recovered) model with quarantine-adjusted incidence. The system can be expressed as follows:

$$\begin{aligned}\dot{S} &= \Lambda - \frac{\beta SI}{\bar{N} - Q} - \mu S, \\ \dot{I} &= \frac{\beta SI}{\bar{N} - Q} - (\lambda + \varepsilon_1 + \gamma + \mu) I, \\ \dot{Q} &= \lambda I - (\varphi + \varepsilon_2 + \mu) Q, \\ \dot{R} &= \gamma I + \varphi Q - \mu R,\end{aligned}\tag{1}$$

where the total population size is given by  $\bar{N}(t) = S(t) + I(t) + Q(t) + R(t)$ ,  $\Lambda$  is the inflow rate corresponding to birth

and immigration, and  $\mu$  is the outflow rate corresponding to natural death and emigration. Since the quarantine process, using the standard incidence  $(\beta I/\bar{N})S$ , the contact rate  $\beta Q/\bar{N}$  with the quarantined fraction  $Q/\bar{N}$  does not occur. Hence the standard incidence is replaced by  $\beta SI/(\bar{N} - Q)$  (it is called quarantine-adjusted incidence); here  $\beta$  is the transmission coefficient between susceptible individuals and infected individuals.  $\lambda$  is the quarantine rate of infected individuals,  $\varphi$  is the recovery rate of quarantined individuals, and  $\varepsilon_1$  and  $\varepsilon_2$  stand for the rate of disease-related death of infected and quarantined individuals, respectively.  $\gamma$  is the recovery rate of infected individuals. Furthermore, all the parameters are positive and the region  $\bar{D} = \{(S, I, Q, R) \mid S \geq 0, I \geq 0, Q \geq 0, R \geq 0, S + I + Q + R \leq \Lambda/\mu\}$  is a positively invariant set of system (1). In the region  $\bar{D}$ , they established the basic reproduction number  $R_0$ , which determines disease extinction or permanence, where

$$R_0 = \frac{\beta}{\lambda + \varepsilon_1 + \gamma + \mu}. \quad (2)$$

Meanwhile, they analyzed the global dynamics of system (1) and derived the equilibria (including the disease-free equilibrium and the endemic equilibrium) and their global stability. In addition, the parameter conditions for the existence of a Hopf bifurcation are obtained.

In the real world, with the development of modern medicine, vaccination has become an important strategy for disease prevention and control in addition to quarantine, and numerous scholars have investigated the effect of vaccination on disease [23–30]. For another, many infectious diseases incubate inside the hosts for a period of time before becoming infectious, so it is very meaningful to consider the effect of the incubation period. Motivated by the aforementioned work, this paper considers an SEIQR (susceptible-exposed-infected-quarantined-recovered) epidemic model with imperfect vaccination, which is described by the following system:

$$\begin{aligned} \dot{S} &= \Lambda - \frac{(1-\delta)\beta SI}{N-Q} - \frac{\delta(1-p)\beta SI}{N-Q} - (\delta p + \mu)S, \\ \dot{E} &= \frac{(1-\delta)\beta SI}{N-Q} + \frac{\delta(1-p)\beta SI}{N-Q} - (\alpha + \mu)E, \\ \dot{I} &= \alpha E - (\lambda + \varepsilon_1 + \gamma + \mu)I, \\ \dot{Q} &= \lambda I - (\varphi + \varepsilon_2 + \mu)Q, \\ \dot{R} &= \delta p S + \gamma I + \varphi Q - \mu R, \end{aligned} \quad (3)$$

where the total population size is given by  $N(t) = S(t) + E(t) + I(t) + Q(t) + R(t)$ ,  $\delta$  ( $0 \leq \delta < 1$ ) is the vaccine coverage rate,  $p$  ( $0 \leq p \leq 1$ ) is the vaccine efficacy, and  $\alpha$  is the rate at which the exposed individuals become infected individuals. Other parameters are the same as in system (1). Now we assume that all the parameters are positive constants here except that  $\delta, p$  are nonnegative constants. Clearly, the region  $D = \{(S, E, I, Q, R) \mid S \geq 0, E \geq 0, I \geq 0, Q \geq 0, R \geq 0,$

$S + E + I + Q + R \leq \Lambda/\mu\}$  is a positively invariant set of system (3). For system (3), the basic reproduction number is

$$R_1 = \frac{\mu(1-\delta p)\beta\alpha}{(\delta p + \mu)(\alpha + \mu)(\lambda + \varepsilon_1 + \gamma + \mu)} \quad (4)$$

and it has the following properties:

- (1) When  $R_1 \leq 1$  holds, system (3) has a unique disease-free equilibrium  $E_0 = (S_0, 0, 0, 0, R_0) = (\Lambda/(\delta p + \mu), 0, 0, 0, \delta p \Lambda/\mu(\delta p + \mu))$  which is globally asymptotically stable in the region  $D$ . That means the epidemic diseases will die out and the total individuals will become the susceptible and recovered individuals.
- (2) When  $R_1 > 1$  holds, system (3) has a unique globally asymptotically stable positive equilibrium  $E^* = (S^*, E^*, I^*, Q^*, R^*)$  in the region  $D$ , which means the epidemic diseases will persist.

In the natural world, deterministic model is not enough to describe the species activities. Sometimes, the species activities may be disturbed by uncertain environmental noises. Consequently, some parameters should be stochastic [31–40]. There is no denying that this phenomenon is ubiquitous in the ecosystem. Therefore numerous scholars have introduced the effect of stochastic perturbation on diseases [41–50]. To the best of our knowledge, the research on global dynamics of the stochastic SEIQR epidemic model with imperfect vaccination is not too much yet. In this paper, to make system (3) more reasonable and realistic, we assume the environmental noise is directly proportional to  $S(t)$ ,  $E(t)$ ,  $I(t)$ ,  $Q(t)$ , and  $R(t)$ . Then corresponding to system (3), a stochastic version can be reached by

$$\begin{aligned} dS &= \left[ \Lambda - \frac{(1-\delta)\beta SI}{N-Q} - \frac{\delta(1-p)\beta SI}{N-Q} - (\delta p + \mu)S \right] dt \\ &\quad + \sigma_1 S dB_1(t), \\ dE &= \left[ \frac{(1-\delta)\beta SI}{N-Q} + \frac{\delta(1-p)\beta SI}{N-Q} - (\alpha + \mu)E \right] dt \\ &\quad + \sigma_2 E dB_2(t), \\ dI &= [\alpha E - (\lambda + \varepsilon_1 + \gamma + \mu)I] dt + \sigma_3 I dB_3(t), \\ dQ &= [\lambda I - (\varphi + \varepsilon_2 + \mu)Q] dt + \sigma_4 Q dB_4(t), \\ dR &= (\delta p S + \gamma I + \varphi Q - \mu R) dt + \sigma_5 R dB_5(t), \end{aligned} \quad (5)$$

where  $B_i(t)$  ( $i = 1, 2, 3, 4, 5$ ) is the mutually independent standard Wiener process with  $B_i(0) = 0$  a.s.  $\sigma_i(t)$  ( $i = 1, 2, 3, 4, 5$ ) is a continuous and bounded function for any  $t \geq 0$  and  $\sigma_i^2(t)$  ( $i = 1, 2, 3, 4, 5$ ) are the intensities of Wiener processes.

In this paper, we are mainly concerned with two interesting problems as follows:

- (P1) Under what parameter conditions, will the disease die out?  
 (P2) Under what conditions, will system (5) have a unique ergodic stationary distribution?

Throughout this paper, let  $(\Omega, \mathcal{F}, \{\mathcal{F}_t\}_{t \geq 0}, \mathbb{P})$  be a complete probability space with a filtration  $\{\mathcal{F}_t\}_{t \geq 0}$  satisfying the usual conditions (i.e., it is increasing and right continuous while  $\mathcal{F}_0$  contains all  $\mathbb{P}$ -null sets). Further  $B_i(t)$  ( $i = 1, 2, 3, 4, 5$ ) is defined on the complete probability space.

For simplicity and convenience, we introduce the following notations:

- (1)  $\mathbb{R}_+ = [0, +\infty)$ ,  $\mathbb{R}_+^5 = \{x = (x_1, x_2, x_3, x_4, x_5) \in \mathbb{R}^5 : x_i > 0 \ (i = 1, 2, 3, 4, 5)\}$ .  
 (2) For an integrable function  $x(t) \in [0, +\infty)$ ,  $\langle x(t) \rangle = (1/t) \int_0^t x(r) dr$ .  
 (3)  $a \wedge b = \min\{a, b\}$ ,  $a \vee b = \max\{a, b\}$ .

## 2. Global Positive Solution

To investigate the dynamical behaviors of a population system, we first concern the global existence and positivity of the solutions of system (5).

**Lemma 1.** *For any given initial value  $(S(0), E(0), I(0), Q(0), R(0)) \in \mathbb{R}_+^5$ , system (5) has a unique positive local solution  $(S(t), E(t), I(t), Q(t), R(t))$  for  $t \in [-\omega, \tau_e)$ , where  $\tau_e$  is the explosion time [51].*

**Theorem 2.** *For any given initial value  $(S(0), E(0), I(0), Q(0), R(0)) \in \mathbb{R}_+^5$ , system (5) has a unique positive solution  $(S(t), E(t), I(t), Q(t), R(t)) \in \mathbb{R}_+^5$  on  $t \geq 0$  a.s.*

*Proof.* The following proof is divided into two parts.

*Part I.* By Lemma 1, it is easy to see that system (5) has a unique positive local solution  $(S(t), E(t), I(t), Q(t), R(t))$  for any given initial value  $(S(0), E(0), I(0), Q(0), R(0)) \in \mathbb{R}_+^5$ .

*Part II.* Now we prove that the positive solution is global, that is,  $\tau_e = \infty$  a.s. Let  $k_0 \geq 0$  be sufficiently large such that  $S(0), E(0), I(0), Q(0)$ , and  $R(0)$  all lie in  $[1/k_0, k_0]$ . For each integer  $k \geq k_0$ , let us define the stopping time as follows:

$$\begin{aligned} \tau_k = \inf \left\{ t \in [-\omega, \tau_e) : S(t) \notin \left( \frac{1}{k}, k \right), E(t) \right. \\ \left. \notin \left( \frac{1}{k}, k \right), I(t) \notin \left( \frac{1}{k}, k \right), Q(t) \notin \left( \frac{1}{k}, k \right) \text{ or } R(t) \right. \\ \left. \notin \left( \frac{1}{k}, k \right) \right\}, \end{aligned} \quad (6)$$

where we define  $\inf \emptyset = \infty$  ( $\emptyset$  represents the empty set). Evidently,  $\tau_k$  is strictly increasing when  $k \rightarrow \infty$ . Let  $\tau_\infty = \lim_{k \rightarrow \infty} \tau_k$ ; thus  $\tau_\infty \leq \tau_e$  a.s. So we just need to show that

$\tau_\infty = \infty$  a.s. If  $\tau_\infty = \infty$  is untrue, then there exist two constants  $T > 0$  and  $\varsigma \in (0, 1)$  such that  $\mathbb{P}\{\tau_\infty \leq T\} > \varsigma$ . Thus there exists  $k_1 \geq k_0$  ( $k_1 \in \mathbb{N}_+$ ) such that

$$\mathbb{P}\{\tau_k \leq T\} \geq \varsigma, \quad k \geq k_1. \quad (7)$$

Define a  $C^2$ -function  $\widehat{V} : \mathbb{R}_+^5 \rightarrow \mathbb{R}_+$  by

$$\begin{aligned} \widehat{V}(S, E, I, Q, R) = S - 1 - \ln S + E - 1 - \ln E + I - 1 \\ - \ln I + Q - 1 - \ln Q + R - 1 \\ - \ln R. \end{aligned} \quad (8)$$

Applying Itô's formula and system (5), we have

$$\begin{aligned} d\widehat{V} = \mathcal{L}\widehat{V}dt + \sigma_1(S-1)dB_1(t) + \sigma_2(E-1)dB_2(t) \\ + \sigma_3(I-1)dB_3(t) + \sigma_4(Q-1)dB_4(t) \\ + \sigma_5(R-1)dB_5(t), \end{aligned} \quad (9)$$

where

$$\begin{aligned} \mathcal{L}\widehat{V} = & \left(1 - \frac{1}{S}\right) \\ & \cdot \left[ \Lambda - \frac{(1-\delta)\beta SI}{N-Q} - \frac{\delta(1-p)\beta SI}{N-Q} - (\delta p + \mu)S \right] \\ & + \left(1 - \frac{1}{E}\right) \\ & \cdot \left[ \frac{(1-\delta)\beta SI}{N-Q} + \frac{\delta(1-p)\beta SI}{N-Q} - (\alpha + \mu)E \right] \\ & + \left(1 - \frac{1}{I}\right) [\alpha E - (\lambda + \varepsilon_1 + \gamma + \mu)I] + \left(1 - \frac{1}{Q}\right) \\ & \cdot [\lambda I - (\varphi + \varepsilon_2 + \mu)Q] + \left(1 - \frac{1}{R}\right) \\ & \cdot (\delta p S + \gamma I + \varphi Q - \mu R) \\ & + \frac{1}{2} (\sigma_1^2 + \sigma_2^2 + \sigma_3^2 + \sigma_4^2 + \sigma_5^2) = \Lambda + \delta p + \alpha + \lambda \\ & + \gamma + \varphi + \varepsilon_1 + \varepsilon_2 + 5\mu + \frac{(1-\delta p)\beta I}{S+E+I+R} \\ & - \mu(S+E+I+Q+R) - \varepsilon_1 I - \varepsilon_1 Q - \frac{\Lambda}{S} \\ & - \frac{(1-\delta p)\beta SI}{E(S+E+I+R)} - \frac{\alpha E}{I} - \frac{\lambda I}{Q} - \frac{\delta p S}{R} - \frac{\gamma I}{R} \\ & - \frac{\varphi Q}{R} + \frac{1}{2} (\sigma_1^2 + \sigma_2^2 + \sigma_3^2 + \sigma_4^2 + \sigma_5^2) \leq \Lambda + \delta p + \alpha \\ & + \lambda + \gamma + \varphi + \varepsilon_1 + \varepsilon_2 + 5\mu + (1-\delta p)\beta \\ & + \frac{1}{2} (\sigma_1^2 + \sigma_2^2 + \sigma_3^2 + \sigma_4^2 + \sigma_5^2) = M_0, \end{aligned} \quad (10)$$

and here  $M_0$  is a positive constant. Hence

$$\begin{aligned} d\widehat{V} &\leq M_0 dt + \sigma_1 (S - 1) dB_1(t) + \sigma_2 (E - 1) dB_2(t) \\ &\quad + \sigma_3 (I - 1) dB_3(t) + \sigma_4 (Q - 1) dB_4(t) \\ &\quad + \sigma_5 (R - 1) dB_5(t). \end{aligned} \quad (11)$$

Integrating both sides of (11) from 0 to  $\tau_k \wedge T$  and then taking the expectation, we have

$$\begin{aligned} \mathbb{E}\widehat{V}(S(\tau_k \wedge T), E(\tau_k \wedge T), I(\tau_k \wedge T), Q(\tau_k \wedge T), \\ R(\tau_k \wedge T)) &\leq \widehat{V}(S(0), E(0), I(0), Q(0), R(0)) \\ &\quad + \mathbb{E} \int_0^{\tau_k \wedge T} M_0 dt \leq \widehat{V}(S(0), E(0), I(0), Q(0), R(0)) \\ &\quad + M_0 T. \end{aligned} \quad (12)$$

Set  $\Omega_k = \{\tau_k \leq T\}$ ,  $k \geq k_1$  and by (7) we can get that  $P(\Omega_k) \geq \varsigma$ . Notice that, for every  $\omega \in \Omega_k$ , there exists  $S(\tau_k, \omega)$ ,  $E(\tau_k, \omega)$ ,  $I(\tau_k, \omega)$ ,  $Q(\tau_k, \omega)$ , or  $R(\tau_k, \omega)$  which equals either  $1/k$  or  $k$ . Thus

$$\begin{aligned} \widehat{V}(S(\tau_k, \omega), E(\tau_k, \omega), I(\tau_k, \omega), Q(\tau_k, \omega), R(\tau_k, \omega)) \\ \geq \left(\frac{1}{k} - 1 - \ln \frac{1}{k}\right) \wedge (k - 1 - \ln k). \end{aligned} \quad (13)$$

By virtue of (12) and (13), one has

$$\begin{aligned} \widehat{V}(S(0), E(0), I(0), Q(0), R(0)) + M_0 T \\ \geq \mathbb{E} \left[ 1_{\Omega_k(\omega)} \widehat{V}(S(\tau_k, \omega), E(\tau_k, \omega), I(\tau_k, \omega), \right. \\ \left. Q(\tau_k, \omega), R(\tau_k, \omega)) \right] \geq \varsigma \left[ \left(\frac{1}{k} - 1 - \ln \frac{1}{k}\right) \wedge (k - 1 \right. \\ \left. - \ln k) \right], \end{aligned} \quad (14)$$

and here  $1_{\Omega_k(\omega)}$  is the indicator function of  $\Omega_k(\omega)$ . Let  $k \rightarrow \infty$ , which implies

$$\infty > \widehat{V}(S(0), E(0), I(0), Q(0), R(0)) + M_0 T = \infty \quad (15)$$

is a contradiction. Obviously, we get that  $\tau_\infty = \infty$ . This completes the proof of Theorem 2.  $\square$

### 3. Extinction

In this section, we mainly explore the parameter conditions for extinction of the disease in system (5). Before proving the main results, we first give a useful lemma as follows.

**Lemma 3.** For any given initial value  $(S(0), E(0), I(0), Q(0), R(0)) \in \mathbb{R}_+^5$ , the solution  $(S(t), E(t), I(t), Q(t), R(t))$  of the system (5) has the following properties:

$$\begin{aligned} \lim_{t \rightarrow \infty} \frac{S(t)}{t} &= 0, \\ \lim_{t \rightarrow \infty} \frac{E(t)}{t} &= 0, \\ \lim_{t \rightarrow \infty} \frac{I(t)}{t} &= 0, \\ \lim_{t \rightarrow \infty} \frac{Q(t)}{t} &= 0, \\ \lim_{t \rightarrow \infty} \frac{R(t)}{t} &= 0 \end{aligned} \quad (16)$$

a.s.

Furthermore, when  $\mu > (1/2)(\sigma_1^2 \vee \sigma_2^2 \vee \sigma_3^2 \vee \sigma_4^2 \vee \sigma_5^2)$  holds, then

$$\begin{aligned} \lim_{t \rightarrow \infty} \frac{1}{t} \int_0^t S(r) dB_1(r) &= 0, \\ \lim_{t \rightarrow \infty} \frac{1}{t} \int_0^t E(r) dB_2(r) &= 0, \\ \lim_{t \rightarrow \infty} \frac{1}{t} \int_0^t I(r) dB_3(r) &= 0, \\ \lim_{t \rightarrow \infty} \frac{1}{t} \int_0^t Q(r) dB_4(r) &= 0, \\ \lim_{t \rightarrow \infty} \frac{1}{t} \int_0^t R(r) dB_5(r) &= 0 \end{aligned} \quad (17)$$

a.s.

*Proof.* The proof of Lemma 3 is similar to [25, 41]; thus we omit it here.  $\square$

**Theorem 4.** Let  $\mu > (1/2)(\sigma_1^2 \vee \sigma_2^2 \vee \sigma_3^2 \vee \sigma_4^2 \vee \sigma_5^2)$ . For any given initial value  $(S(0), E(0), I(0), Q(0), R(0)) \in \mathbb{R}_+^5$ , if

$$\tilde{R}^* := \frac{2\alpha(1 - \delta p)\beta(\alpha + \mu)}{(\lambda + \varepsilon_1 + \gamma + \mu + \sigma_3^2/2)(\alpha + \mu)^2 \wedge (\alpha^2 \sigma_2^2/2)} \quad (18)$$

$< 1$

holds, then

$$\lim_{t \rightarrow \infty} E(t) = \lim_{t \rightarrow \infty} I(t) = \lim_{t \rightarrow \infty} Q(t) = 0 \quad a.s. \quad (19)$$

Moreover,

$$\begin{aligned} \lim_{t \rightarrow \infty} \langle S \rangle &= \frac{\Lambda}{\delta p + \mu} = S_0, \\ \lim_{t \rightarrow \infty} \langle R \rangle &= \frac{\delta p \Lambda}{\mu(\delta p + \mu)} = R_0 \end{aligned} \quad (20)$$

a.s.

*Proof.* Define a differentiable function  $V_0$  by

$$V_0 = \ln [\alpha E(t) + (\alpha + \mu) I(t)]. \quad (21)$$

From Itô's formula and system (5), we have

$$\begin{aligned}
dV_0 &= \left\{ \frac{\alpha(1-\delta p)\beta SI/(S+E+I+R) - (\alpha+\mu)(\lambda+\varepsilon_1+\gamma+\mu)I}{\alpha E + (\alpha+\mu)I} - \frac{\alpha^2\sigma_2^2 E^2 + (\alpha+\mu)^2\sigma_3^2 I^2}{2[\alpha E + (\alpha+\mu)I]^2} \right\} dt \\
&\quad + \frac{\alpha\sigma_2 E}{\alpha E + (\alpha+\mu)I} dB_2(t) + \frac{(\alpha+\mu)\sigma_3 I}{\alpha E + (\alpha+\mu)I} dB_3(t) \\
&\leq \left\{ \frac{\alpha(1-\delta p)\beta}{\alpha+\mu} - \frac{(\lambda+\varepsilon_1+\gamma+\mu+\sigma_3^2/2)(\alpha+\mu)^2 I^2 + (\alpha^2\sigma_2^2/2)E^2}{[\alpha E + (\alpha+\mu)I]^2} \right\} dt + \frac{\alpha\sigma_2 E}{\alpha E + (\alpha+\mu)I} dB_2(t) \\
&\quad + \frac{(\alpha+\mu)\sigma_3 I}{\alpha E + (\alpha+\mu)I} dB_3(t) \\
&\leq \left\{ \frac{\alpha(1-\delta p)\beta}{\alpha+\mu} - \frac{(\lambda+\varepsilon_1+\gamma+\mu+\sigma_3^2/2)(\alpha+\mu)^2 \wedge (\alpha^2\sigma_2^2/2)}{2(\alpha+\mu)^2} \right\} dt + \frac{\alpha\sigma_2 E}{\alpha E + (\alpha+\mu)I} dB_2(t) \\
&\quad + \frac{(\alpha+\mu)\sigma_3 I}{\alpha E + (\alpha+\mu)I} dB_3(t).
\end{aligned} \tag{22}$$

Integrating from 0 to  $t$  and dividing by  $t$  on both sides of (22), we have

$$\begin{aligned}
&\frac{\ln[\alpha E(t) + (\alpha+\mu)I(t)]}{t} \\
&\leq \frac{\alpha(1-\delta p)\beta}{\alpha+\mu} \\
&\quad - \frac{(\lambda+\varepsilon_1+\gamma+\mu+\sigma_3^2/2)(\alpha+\mu)^2 \wedge (\alpha^2\sigma_2^2/2)}{2(\alpha+\mu)^2} \\
&\quad + \frac{\ln[\alpha E(0) + (\alpha+\mu)I(0)]}{t} \\
&\quad + \frac{\alpha\sigma_2}{t} \int_0^t \frac{E(r)}{\alpha E(r) + (\alpha+\mu)I(r)} dB_2(r) \\
&\quad + \frac{(\alpha+\mu)\sigma_3}{t} \int_0^t \frac{I(r)}{\alpha E(r) + (\alpha+\mu)I(r)} dB_3(r).
\end{aligned} \tag{23}$$

Making use of Lemma 3, we have

$$\begin{aligned}
&\limsup_{t \rightarrow \infty} \frac{\ln[\alpha E(t) + (\alpha+\mu)I(t)]}{t} \\
&\leq \frac{\alpha(1-\delta p)\beta}{\alpha+\mu} \\
&\quad - \frac{(\lambda+\varepsilon_1+\gamma+\mu+\sigma_3^2/2)(\alpha+\mu)^2 \wedge (\alpha^2\sigma_2^2/2)}{2(\alpha+\mu)^2} \\
&< 0 \quad \text{a.s.},
\end{aligned} \tag{24}$$

which shows that

$$\begin{aligned}
&\lim_{t \rightarrow \infty} E(t) = 0, \\
&\lim_{t \rightarrow \infty} I(t) = 0 \\
&\quad \text{a.s.}
\end{aligned} \tag{25}$$

From the fourth equation of system (5), it is easy to get that

$$\lim_{t \rightarrow \infty} Q(t) = 0 \quad \text{a.s.} \tag{26}$$

Moreover, integrating from 0 to  $t$  and dividing by  $t$  on both sides of the first equation of system (5) yield

$$\begin{aligned}
\frac{S(t) - S(0)}{t} &= \Lambda - (1-\delta p)\beta \left\langle \frac{SI}{N-Q} \right\rangle \\
&\quad - (\delta p + \mu) \langle S \rangle + \frac{\sigma_1}{t} \int_0^t S(r) dB_1(r),
\end{aligned} \tag{27}$$

and considering (25), (26), and Lemma 3, it then follows that

$$\lim_{t \rightarrow \infty} \langle S \rangle = \frac{\Lambda}{\delta p + \mu} = S_0 \quad \text{a.s.} \tag{28}$$

Similarly, we also get

$$\lim_{t \rightarrow \infty} \langle R \rangle = \frac{\delta p \Lambda}{\mu(\delta p + \mu)} = R_0 \quad \text{a.s.} \tag{29}$$

The proof of Theorem 4 is complete.  $\square$

#### 4. Stationary Distribution and Ergodicity

Ergodicity is a significant property in a population system. Recently, it attracts deep research interest of numerous

scholars [52, 53]. In this section, based on the theory of Hasminskii et al. [54] and the Lyapunov analysis methods, we study the conditions of the existence of an ergodic stationary distribution.

Assume  $X(t)$  as a time-homogeneous Markov process in  $\mathbb{E}_n \subset \mathbb{R}^n$ , which is described by the stochastic differential equation

$$dX(t) = b(X) dt + \sum_{\eta=1}^n \sigma_{\eta}(X) dB_{\eta}(t), \quad (30)$$

and here  $\mathbb{E}_n$  stands for a  $n$ -dimensional Euclidean space. The diffusion matrix takes the following form:

$$\tilde{A}(x) = (a_{ij}(x)), \quad a_{ij}(x) = \sum_{\eta=1}^n \sigma_{\eta}^i(x) \sigma_{\eta}^j(x). \quad (31)$$

*Assumption 5.* Assume that there is a bounded domain  $U \subset \mathbb{E}_n$  with regular boundary  $\Gamma$  such that  $\bar{U} \subset \mathbb{E}_n$  ( $\bar{U}$  is the closure of  $U$ ), satisfying the following properties:

- (i) In the domain  $U$  and some neighborhood thereof, the smallest eigenvalue of the diffusion matrix  $\tilde{A}(x)$  is bounded away from zero.
- (ii) If  $x \in \mathbb{E}_n \setminus U$ , the mean time  $\tau$  at which a path issuing from  $x$  reaches the set  $U$  is finite, and  $\sup_{x \in \Theta} \mathbb{E}_x \tau < \infty$  for every compact subset  $\Theta \subset \mathbb{E}_n$ .

**Lemma 6** (see [54]). *When Assumption 5 holds, then the Markov process  $X(t)$  has a stationary distribution  $\pi(\cdot)$ . Furthermore, when  $f(\cdot)$  is a function integrable with respect to the measure  $\pi$ , then*

$$\mathbb{P}_x \left\{ \lim_{T \rightarrow \infty} \frac{1}{T} \int_0^T f(X(t)) dt = \int_{\mathbb{E}_n} f(x) \pi(dx) \right\} = 1 \quad (32)$$

for all  $x \in \mathbb{E}_n$ .

*Remark 7.* To demonstrate Assumption 5(i) [55], it suffices to demonstrate that  $F$  is uniformly elliptical in any bounded domain  $H$ ; here

$$Fu = b(x) u_x + \frac{1}{2} \text{trace}(A(x) u_{xx}); \quad (33)$$

namely, there exists a positive number  $Z$  such that

$$\sum_{i,j=1}^n a_{ij}(x) \xi_i \xi_j \geq Z |\xi|^2, \quad x \in \bar{H}, \quad \xi \in \mathbb{R}^n. \quad (34)$$

To verify Assumption 5(ii) [56], it suffices to demonstrate that there exist some neighborhood  $U$  and a nonnegative  $C^2$ -function  $V$  such that  $\forall x \in \mathbb{E}_n \setminus U, LV(x) < 0$ .

Using Lemma 6, we can get the following main results.

**Theorem 8.** *For any given initial value  $(S(0), E(0), I(0), Q(0), R(0)) \in \mathbb{R}_+^5$ . If*

$$R^* := \frac{\mu(1-\delta p)\beta\alpha}{(\delta p + \mu + \sigma_1^2/2)(\alpha + \mu + \sigma_2^2/2)(\lambda + \varepsilon_1 + \gamma + \mu + \sigma_3^2/2)} > 1 \quad (35)$$

holds, then system (5) has a unique stationary distribution  $\pi(\cdot)$  and it has ergodic property.

*Proof.* Define a  $C^2$ -function  $\bar{V}: \mathbb{R}_+^5 \rightarrow \mathbb{R}$  by

$$\begin{aligned} \bar{V}(S, E, I, Q, R) &= Y(S + E + I + Q + R - a_1 \ln S - a_2 \ln E - a_3 \ln I) \\ &\quad + \frac{1}{\varrho + 1} (S + E + I + Q + R)^{\varrho+1} - \ln S - \ln E \\ &\quad - \ln Q - \ln R + (S + E + I + Q + R) \\ &:= YV_1 + V_2 + V_3 + V_4 + V_5 + V_6 + V_7, \end{aligned} \quad (36)$$

and here  $\varrho$  and  $a_i$  ( $i = 1, 2, 3$ ) are positive constants satisfying the following conditions:

$$\begin{aligned} 0 < \varrho < \frac{2\mu}{\sigma_1^2 \vee \sigma_2^2 \vee \sigma_3^2 \vee \sigma_4^2 \vee \sigma_5^2}, \\ a_1 &= \frac{\Lambda}{\delta p + \mu + \sigma_1^2/2}, \\ a_2 &= \frac{\Lambda}{\alpha + \mu + \sigma_2^2/2}, \\ a_3 &= \frac{\Lambda}{\lambda + \varepsilon_1 + \gamma + \mu + \sigma_3^2/2}, \end{aligned} \quad (37)$$

and we take  $Y > 0$  large enough such that

$$-Y\phi + M \leq -2; \quad (38)$$

here

$$\begin{aligned} \phi &:= 4\Lambda \left[ (R^*)^{1/4} - 1 \right], \\ M &:= \Lambda + \Gamma + \delta p + \alpha + \varphi + \varepsilon_2 + 4\mu + \frac{\sigma_1^2}{2} + \frac{\sigma_2^2}{2} + \frac{\sigma_4^2}{2} \\ &\quad + \frac{\sigma_5^2}{2}. \end{aligned} \quad (39)$$

Obviously,

$$\liminf_{w \rightarrow \infty, (S, E, I, Q, R) \in \mathbb{R}_+^5 \setminus U_w} \bar{V}(S, E, I, Q, R) = \infty, \quad (40)$$

and here  $U_w = (1/w, w) \times (1/w, w) \times (1/w, w) \times (1/w, w) \times (1/w, w)$ . Since  $\bar{V}(S, E, I, Q, R)$  is a continuous function, then there exists a unique point  $(S^*, E^*, I^*, Q^*, R^*)$  in  $\mathbb{R}_+^5$  which is the minimum point of  $\bar{V}(S, E, I, Q, R)$ . Therefore let us construct a positive-definite  $C^2$ -function  $V: \mathbb{R}_+^5 \rightarrow \mathbb{R}_+$  by

$$\begin{aligned} V(S, E, I, Q, R) &= \bar{V}(S, E, I, Q, R) \\ &\quad - \bar{V}(S^*, E^*, I^*, Q^*, R^*). \end{aligned} \quad (41)$$

From Itô's formula, we have

$$\begin{aligned}
\mathcal{L}V_1 &= -\mu(S + E + I + Q + R) - \frac{a_1\Lambda}{S} - \frac{a_2(1-\delta)\beta SI}{E(N-Q)} - \frac{a_2\delta(1-p)\beta SI}{E(N-Q)} - \frac{a_3\alpha E}{I} + \frac{a_1(1-\delta)\beta I}{N-Q} + \frac{a_1\delta(1-p)\beta I}{N-Q} \\
&\quad + \Lambda + a_1\left(\delta p + \mu + \frac{\sigma_1^2}{2}\right) + a_2\left(\alpha + \mu + \frac{\sigma_2^2}{2}\right) + a_3\left(\lambda + \varepsilon_1 + \gamma + \mu + \frac{\sigma_3^2}{2}\right) - \varepsilon_1 I - \varepsilon_2 Q \\
&\leq -\mu(S + E + I + Q + R) - \frac{a_1\Lambda}{S} - \frac{a_2(1-\delta p)\beta SI}{E(S+E+I+Q+R)} - \frac{a_3\alpha E}{I} + \frac{a_1(1-\delta p)\beta I}{S+E+I+R} + \Lambda + a_1\left(\delta p + \mu + \frac{\sigma_1^2}{2}\right) \\
&\quad + a_2\left(\alpha + \mu + \frac{\sigma_2^2}{2}\right) + a_3\left(\lambda + \varepsilon_1 + \gamma + \mu + \frac{\sigma_3^2}{2}\right) \leq -4(a_1 a_2 a_3 \Lambda \mu (1-\delta p) \beta \alpha)^{1/4} + \frac{a_1(1-\delta p)\beta I}{S+E+I+R} + 4\Lambda \\
&= -4\Lambda \left[ \left( \frac{\mu(1-\delta p)\beta \alpha}{(\delta p + \mu + \sigma_1^2/2)(\alpha + \mu + \sigma_2^2/2)(\lambda + \varepsilon_1 + \gamma + \mu + \sigma_3^2/2)} \right)^{1/4} - 1 \right] + \frac{a_1(1-\delta p)\beta I}{S+E+I+R} \\
&= -4\Lambda \left[ (R^*)^{1/4} - 1 \right] + \frac{a_1(1-\delta p)\beta I}{S+E+I+R} = -\phi + \frac{a_1(1-\delta p)\beta I}{S+E+I+R}.
\end{aligned} \tag{42}$$

Similarly,

$$\begin{aligned}
\mathcal{L}V_2 &= (S + E + I + Q + R)^{\varrho} \\
&\quad \cdot [\Lambda - \mu(S + E + I + Q + R) - \varepsilon_1 I - \varepsilon_2 Q] \\
&\quad + \frac{\varrho(S + E + I + Q + R)^{\varrho-1}}{2} \\
&\quad \times (\sigma_1^2 S^2 + \sigma_2^2 E^2 + \sigma_3^2 I^2 + \sigma_4^2 Q^2 + \sigma_5^2 R^2) \\
&\leq \Lambda(S + E + I + Q + R)^{\varrho} \\
&\quad - \left[ \mu - \frac{\varrho}{2} (\sigma_1^2 \vee \sigma_2^2 \vee \sigma_3^2 \vee \sigma_4^2 \vee \sigma_5^2) \right] \\
&\quad \cdot (S + E + I + Q + R)^{\varrho+1} \leq \Gamma \\
&\quad - \frac{1}{2} \left[ \mu - \frac{\varrho}{2} (\sigma_1^2 \vee \sigma_2^2 \vee \sigma_3^2 \vee \sigma_4^2 \vee \sigma_5^2) \right] \\
&\quad \cdot (S + E + I + Q + R)^{\varrho+1} \leq \Gamma \\
&\quad - \frac{1}{2} \left[ \mu - \frac{\varrho}{2} (\sigma_1^2 \vee \sigma_2^2 \vee \sigma_3^2 \vee \sigma_4^2 \vee \sigma_5^2) \right] \\
&\quad \cdot (S^{\varrho+1} + E^{\varrho+1} + I^{\varrho+1} + Q^{\varrho+1} + R^{\varrho+1}),
\end{aligned} \tag{43}$$

and here

$$\begin{aligned}
\Gamma &= \sup_{(S,E,I,Q,R) \in \mathbb{R}_+^5} \left\{ \Lambda(S + E + I + Q + R)^{\varrho} \right. \\
&\quad \left. - \frac{1}{2} \left[ \mu - \frac{\varrho}{2} (\sigma_1^2 \vee \sigma_2^2 \vee \sigma_3^2 \vee \sigma_4^2 \vee \sigma_5^2) \right] \right. \\
&\quad \left. \times (S + E + I + Q + R)^{\varrho+1} \right\} < \infty.
\end{aligned} \tag{44}$$

We also have

$$\begin{aligned}
\mathcal{L}V_3 &= -\frac{\Lambda}{S} + \frac{(1-\delta p)\beta I}{S+E+I+R} + \delta p + \mu + \frac{\sigma_1^2}{2}, \\
\mathcal{L}V_4 &\leq -\frac{(1-\delta p)\beta SI}{E(S+E+I+Q+R)} + \alpha + \mu + \frac{\sigma_2^2}{2}, \\
\mathcal{L}V_5 &= -\frac{\lambda I}{Q} + \varphi + \varepsilon_2 + \mu + \frac{\sigma_4^2}{2}, \\
\mathcal{L}V_6 &= -\frac{\delta p S + \gamma I + \varphi Q}{R} + \mu + \frac{\sigma_5^2}{2}, \\
\mathcal{L}V_7 &\leq \Lambda - \mu(S + E + I + Q + R).
\end{aligned} \tag{45}$$

Therefore,

$$\begin{aligned}
\mathcal{L}V &\leq -Y\phi + \frac{Ya_1(1-\delta p)\beta I}{S+E+I+R} + \frac{(1-\delta p)\beta I}{S+E+I+R} \\
&\quad - \frac{1}{2} \left[ \mu - \frac{\varrho}{2} (\sigma_1^2 \vee \sigma_2^2 \vee \sigma_3^2 \vee \sigma_4^2 \vee \sigma_5^2) \right] \\
&\quad \times (S^{\varrho+1} + E^{\varrho+1} + I^{\varrho+1} + Q^{\varrho+1} + R^{\varrho+1}) - \frac{\Lambda}{S} \\
&\quad - \frac{(1-\delta p)\beta SI}{E(S+E+I+Q+R)} - \mu(S + E + I + Q + R) \\
&\quad - \frac{\lambda I}{Q} - \frac{\delta p S + \gamma I + \varphi Q}{R} + \Lambda + \Gamma + \delta p + \alpha + \varphi + \varepsilon_2 \\
&\quad + 4\mu + \frac{\sigma_1^2}{2} + \frac{\sigma_2^2}{2} + \frac{\sigma_4^2}{2} + \frac{\sigma_5^2}{2} \leq -Y\phi \\
&\quad + \frac{(Ya_1 + 1)(1-\delta p)\beta I}{S+E+I+R}
\end{aligned}$$

$$\begin{aligned}
& -\frac{1}{2} \left[ \mu - \frac{\rho}{2} (\sigma_1^2 \vee \sigma_2^2 \vee \sigma_3^2 \vee \sigma_4^2 \vee \sigma_5^2) \right] \\
& \cdot (S^{e+1} + E^{e+1} + I^{e+1} + Q^{e+1} + R^{e+1}) - \frac{\Lambda}{S} \\
& - 2 \left( \frac{\mu(1-\delta p)\beta SI}{E} \right)^{1/2} - \frac{\lambda I}{Q} - \frac{\delta p S + \gamma I + \varphi Q}{R} \\
& + M,
\end{aligned} \tag{46}$$

where  $M = \Lambda + \Gamma + \delta p + \alpha + \varphi + \varepsilon_2 + 4\mu + \sigma_1^2/2 + \sigma_2^2/2 + \sigma_4^2/2 + \sigma_5^2/2$ .  
Next let us consider the following compact subset  $D$ :

$$\begin{aligned}
D = \left\{ \epsilon \leq S \leq \frac{1}{\epsilon}, \epsilon^4 \leq E \leq \frac{1}{\epsilon^4}, \epsilon^2 \leq I \leq \frac{1}{\epsilon^2}, \epsilon^3 \leq Q \right. \\
\left. \leq \frac{1}{\epsilon^3}, \epsilon^4 \leq R \leq \frac{1}{\epsilon^4} \right\},
\end{aligned} \tag{47}$$

and here  $\epsilon$  is a sufficiently small constant satisfying the following conditions:

$$-\frac{\Lambda}{\epsilon} + (\Upsilon a_1 + 1)(1 - \delta p)\beta + M \leq -1, \tag{48}$$

$$\begin{aligned}
-2 \left( \frac{\mu(1-\delta p)\beta}{\epsilon} \right)^{1/2} + (\Upsilon a_1 + 1)(1 - \delta p)\beta \\
+ M \leq -1,
\end{aligned} \tag{49}$$

$$-\Upsilon\phi + (\Upsilon a_1 + 1)(1 - \delta p)\beta\epsilon + M \leq -1, \tag{50}$$

$$-\frac{\lambda}{\epsilon} + (\Upsilon a_1 + 1)(1 - \delta p)\beta + M \leq -1, \tag{51}$$

$$-\frac{\delta p}{\epsilon^3} - \frac{\gamma}{\epsilon^2} - \frac{\varphi}{\epsilon} + (\Upsilon a_1 + 1)(1 - \delta p)\beta + M \leq -1, \tag{52}$$

$$-\frac{1}{2} \left[ \mu - \frac{\rho}{2} (\sigma_1^2 \vee \sigma_2^2 \vee \sigma_3^2 \vee \sigma_4^2 \vee \sigma_5^2) \right] \frac{1}{\epsilon^{e+1}} \tag{53}$$

$$+ (\Upsilon a_1 + 1)(1 - \delta p)\beta + M \leq -1,$$

$$-\frac{1}{2} \left[ \mu - \frac{\rho}{2} (\sigma_1^2 \vee \sigma_2^2 \vee \sigma_3^2 \vee \sigma_4^2 \vee \sigma_5^2) \right] \frac{1}{\epsilon^{4(e+1)}} \tag{54}$$

$$+ (\Upsilon a_1 + 1)(1 - \delta p)\beta + M \leq -1,$$

$$-\frac{1}{2} \left[ \mu - \frac{\rho}{2} (\sigma_1^2 \vee \sigma_2^2 \vee \sigma_3^2 \vee \sigma_4^2 \vee \sigma_5^2) \right] \frac{1}{\epsilon^{2(e+1)}} \tag{55}$$

$$+ (\Upsilon a_1 + 1)(1 - \delta p)\beta + M \leq -1,$$

$$-\frac{1}{2} \left[ \mu - \frac{\rho}{2} (\sigma_1^2 \vee \sigma_2^2 \vee \sigma_3^2 \vee \sigma_4^2 \vee \sigma_5^2) \right] \frac{1}{\epsilon^{3(e+1)}} \tag{56}$$

$$+ (\Upsilon a_1 + 1)(1 - \delta p)\beta + M \leq -1.$$

Then

$$\begin{aligned}
\mathbb{R}_+^5 \setminus D = D_1 \cup D_2 \cup D_3 \cup D_4 \cup D_5 \cup D_6 \cup D_7 \cup D_8 \\
\cup D_9 \cup D_{10},
\end{aligned} \tag{57}$$

with

$$D_1 = \{(S, E, I, Q, R) \in \mathbb{R}_+^5 \mid 0 < S < \epsilon\},$$

$$D_2 = \{(S, E, I, Q, R) \in \mathbb{R}_+^5 \mid S \geq \epsilon, I \geq \epsilon^2, 0 < E < \epsilon^4\},$$

$$D_3 = \{(S, E, I, Q, R) \in \mathbb{R}_+^5 \mid S \geq \epsilon, 0 < I < \epsilon^2\},$$

$$D_4 = \{(S, E, I, Q, R) \in \mathbb{R}_+^5 \mid I \geq \epsilon^2, 0 < Q < \epsilon^3\},$$

$$D_5 = \{(S, E, I, Q, R) \in \mathbb{R}_+^5 \mid S \geq \epsilon, I \geq \epsilon^2, Q \geq \epsilon^3, 0 < R < \epsilon^4\},$$

$$D_6 = \{(S, E, I, Q, R) \in \mathbb{R}_+^5 \mid S > \frac{1}{\epsilon}\}, \tag{58}$$

$$D_7 = \{(S, E, I, Q, R) \in \mathbb{R}_+^5 \mid E > \frac{1}{\epsilon^4}\},$$

$$D_8 = \{(S, E, I, Q, R) \in \mathbb{R}_+^5 \mid I > \frac{1}{\epsilon^2}\},$$

$$D_9 = \{(S, E, I, Q, R) \in \mathbb{R}_+^5 \mid Q > \frac{1}{\epsilon^3}\},$$

$$D_{10} = \{(S, E, I, Q, R) \in \mathbb{R}_+^5 \mid R > \frac{1}{\epsilon^4}\}.$$

Now we analyze the negativity of  $\mathcal{L}V$  for any  $(S, E, I, Q, R) \in \mathbb{R}_+^5 \setminus D$ .

*Case I.* If  $(S, I, Q, R) \in D_1$ , (46) and (48) derive that

$$\begin{aligned}
\mathcal{L}V & \leq -\frac{\Lambda}{S} + \frac{(\Upsilon a_1 + 1)(1 - \delta p)\beta I}{S + E + I + R} + M \\
& \leq -\frac{\Lambda}{\epsilon} + (\Upsilon a_1 + 1)(1 - \delta p)\beta + M \leq -1.
\end{aligned} \tag{59}$$

*Case II.* If  $(S, I, Q, R) \in D_2$ , (46) and (49) imply that

$$\begin{aligned}
\mathcal{L}V & \leq -2 \left( \frac{\mu(1-\delta p)\beta SI}{E} \right)^{1/2} \\
& + \frac{(\Upsilon a_1 + 1)(1 - \delta p)\beta I}{S + E + I + R} + M \\
& \leq -2 \left( \frac{\mu(1-\delta p)\beta}{\epsilon} \right)^{1/2} + (\Upsilon a_1 + 1)(1 - \delta p)\beta \\
& + M \leq -1.
\end{aligned} \tag{60}$$

*Case III.* If  $(S, I, Q, R) \in D_3$ , it follows from (46) and (50) that

$$\begin{aligned}
\mathcal{L}V & \leq -\Upsilon\phi + \frac{(\Upsilon a_1 + 1)(1 - \delta p)\beta I}{S + E + I + R} + M \\
& \leq -\Upsilon\phi + \frac{(\Upsilon a_1 + 1)(1 - \delta p)\beta I}{S} + M \\
& \leq -\Upsilon\phi + (\Upsilon a_1 + 1)(1 - \delta p)\beta\epsilon + M \leq -1.
\end{aligned} \tag{61}$$

Case IV. If  $(S, I, Q, R) \in D_4$ , (46) and (51) yield that

$$\begin{aligned} \mathcal{L}V &\leq -\frac{\lambda I}{Q} + \frac{(\Upsilon a_1 + 1)(1 - \delta p)\beta I}{S + E + I + R} + M \\ &\leq -\frac{\lambda}{\epsilon} + (\Upsilon a_1 + 1)(1 - \delta p)\beta + M \leq -1. \end{aligned} \quad (62)$$

Case V. If  $(S, I, Q, R) \in D_5$ , it follows from (46) and (52) that

$$\begin{aligned} \mathcal{L}V &\leq -\frac{\delta p S + \gamma I + \varphi Q}{R} + \frac{(\Upsilon a_1 + 1)(1 - \delta p)\beta I}{S + E + I + R} \\ &\quad + M \\ &\leq -\frac{\delta p}{\epsilon^3} - \frac{\gamma}{\epsilon^2} - \frac{\varphi}{\epsilon} + (\Upsilon a_1 + 1)(1 - \delta p)\beta + M \\ &\leq -1. \end{aligned} \quad (63)$$

Case VI. If  $(S, I, Q, R) \in D_6$ , (46) and (53) lead to

$$\begin{aligned} \mathcal{L}V &\leq -\frac{1}{2} \left[ \mu - \frac{\varrho}{2} (\sigma_1^2 \vee \sigma_2^2 \vee \sigma_3^2 \vee \sigma_4^2 \vee \sigma_5^2) \right] S^{\varrho+1} \\ &\quad + \frac{(\Upsilon a_1 + 1)(1 - \delta p)\beta I}{S + E + I + R} + M \\ &\leq -\frac{1}{2} \left[ \mu - \frac{\varrho}{2} (\sigma_1^2 \vee \sigma_2^2 \vee \sigma_3^2 \vee \sigma_4^2 \vee \sigma_5^2) \right] \frac{1}{\epsilon^{\varrho+1}} \\ &\quad + (\Upsilon a_1 + 1)(1 - \delta p)\beta + M \leq -1. \end{aligned} \quad (64)$$

Case VII. If  $(S, I, Q, R) \in D_7$ , (46) and (54) derive that

$$\begin{aligned} \mathcal{L}V &\leq -\frac{1}{2} \left[ \mu - \frac{\varrho}{2} (\sigma_1^2 \vee \sigma_2^2 \vee \sigma_3^2 \vee \sigma_4^2 \vee \sigma_5^2) \right] E^{\varrho+1} \\ &\quad + \frac{(\Upsilon a_1 + 1)(1 - \delta p)\beta I}{S + E + I + R} + M \\ &\leq -\frac{1}{2} \left[ \mu - \frac{\varrho}{2} (\sigma_1^2 \vee \sigma_2^2 \vee \sigma_3^2 \vee \sigma_4^2 \vee \sigma_5^2) \right] \frac{1}{\epsilon^{4(\varrho+1)}} \\ &\quad + (\Upsilon a_1 + 1)(1 - \delta p)\beta + M \leq -1. \end{aligned} \quad (65)$$

Case VIII. If  $(S, I, Q, R) \in D_8$ , it follows from (46) and (55) that

$$\begin{aligned} \mathcal{L}V &\leq -\frac{1}{2} \left[ \mu - \frac{\varrho}{2} (\sigma_1^2 \vee \sigma_2^2 \vee \sigma_3^2 \vee \sigma_4^2 \vee \sigma_5^2) \right] I^{\varrho+1} \\ &\quad + \frac{(\Upsilon a_1 + 1)(1 - \delta p)\beta I}{S + E + I + R} + M \\ &\leq -\frac{1}{2} \left[ \mu - \frac{\varrho}{2} (\sigma_1^2 \vee \sigma_2^2 \vee \sigma_3^2 \vee \sigma_4^2 \vee \sigma_5^2) \right] \frac{1}{\epsilon^{2(\varrho+1)}} \\ &\quad + (\Upsilon a_1 + 1)(1 - \delta p)\beta + M \leq -1. \end{aligned} \quad (66)$$

Case IX. If  $(S, I, Q, R) \in D_9$ , (46) and (56) derive that

$$\begin{aligned} \mathcal{L}V &\leq -\frac{1}{2} \left[ \mu - \frac{\varrho}{2} (\sigma_1^2 \vee \sigma_2^2 \vee \sigma_3^2 \vee \sigma_4^2 \vee \sigma_5^2) \right] Q^{\varrho+1} \\ &\quad + \frac{(\Upsilon a_1 + 1)(1 - \delta p)\beta I}{S + E + I + R} + M \\ &\leq -\frac{1}{2} \left[ \mu - \frac{\varrho}{2} (\sigma_1^2 \vee \sigma_2^2 \vee \sigma_3^2 \vee \sigma_4^2 \vee \sigma_5^2) \right] \frac{1}{\epsilon^{3(\varrho+1)}} \\ &\quad + (\Upsilon a_1 + 1)(1 - \delta p)\beta + M \leq -1. \end{aligned} \quad (67)$$

Case X. If  $(S, I, Q, R) \in D_{10}$ , it follows from (46) and (54) that

$$\begin{aligned} \mathcal{L}V &\leq -\frac{1}{2} \left[ \mu - \frac{\varrho}{2} (\sigma_1^2 \vee \sigma_2^2 \vee \sigma_3^2 \vee \sigma_4^2 \vee \sigma_5^2) \right] R^{\varrho+1} \\ &\quad + \frac{(\Upsilon a_1 + 1)(1 - \delta p)\beta I}{S + E + I + R} + M \\ &\leq -\frac{1}{2} \left[ \mu - \frac{\varrho}{2} (\sigma_1^2 \vee \sigma_2^2 \vee \sigma_3^2 \vee \sigma_4^2 \vee \sigma_5^2) \right] \frac{1}{\epsilon^{4(\varrho+1)}} \\ &\quad + (\Upsilon a_1 + 1)(1 - \delta p)\beta + M \leq -1. \end{aligned} \quad (68)$$

Clearly, from the discussion of the above ten cases, one sees that, for a sufficiently small  $\epsilon$ ,

$$\mathcal{L}V \leq -1 \quad \forall (S, E, I, Q, R) \in \mathbb{R}_+^5 \setminus D, \quad (69)$$

which shows that Assumption 5(ii) is satisfied. In addition, the diffusion matrix of system (5) takes the following form:

$$\bar{A} = \begin{pmatrix} \sigma_1^2 S^2 & 0 & 0 & 0 & 0 \\ 0 & \sigma_2^2 E^2 & 0 & 0 & 0 \\ 0 & 0 & \sigma_3^2 I^2 & 0 & 0 \\ 0 & 0 & 0 & \sigma_4^2 Q^2 & 0 \\ 0 & 0 & 0 & 0 & \sigma_5^2 R^2 \end{pmatrix}. \quad (70)$$

There exists a positive number

$$Z = \min_{(S, E, I, Q, R) \in \bar{D}} \{ \sigma_1^2 S^2, \sigma_2^2 E^2, \sigma_3^2 I^2, \sigma_4^2 Q^2, \sigma_5^2 R^2 \} \quad (71)$$

such that

$$\begin{aligned} \sum_{i,j=1}^5 a_{ij} \xi_i \xi_j &= \sigma_1^2 S^2 \xi_1^2 + \sigma_2^2 E^2 \xi_2^2 + \sigma_3^2 I^2 \xi_3^2 + \sigma_4^2 Q^2 \xi_4^2 \\ &\quad + \sigma_5^2 R^2 \xi_5^2 \geq Z |\xi|^2, \end{aligned} \quad (72)$$

$$(S, E, I, Q, R) \in \bar{D}, \quad \xi \in \mathbb{R}^5,$$

which shows that Assumption 5(i) is satisfied. Consequently, system (5) has a unique stationary distribution  $\pi(\cdot)$  and it has ergodic property. The proof of Theorem 8 is complete.  $\square$

*Remark 9.* From Theorem 8, we see that if  $R^* > 1$  holds, then system (5) has a unique ergodic stationary distribution. It is worthwhile noting that if  $\sigma_i = 0$  ( $i = 1, 2, 3, 4, 5$ ), the expression of  $R^*$  coincides with the basic reproduction number  $R_1$  of system (3). This shows that we generalize the results of system (3). For another, this theorem also shows that the disease can resist a small environmental noise to maintain the original persistence.

## 5. Conclusions and Simulations

This paper studies the stochastic SEIQR epidemic model with quarantine-adjusted incidence and imperfect vaccination and obtains two thresholds which govern the extinction and the spread of the epidemic disease. Firstly, the existence of a unique positive solution of system (5) with any positive initial value is proved. Then, from Theorems 4 and 8, the sufficient conditions for extinction of the disease and existence of ergodic stationary distribution of the stochastic system are derived by using the theory of Hasminskii and the Lyapunov analysis methods, which means the infectious disease is prevalent. This implies that the stochastic disturbance is conducive to epidemic diseases control. Now we summarize the main conclusions as follows:

- (I) When  $\mu > (1/2)(\sigma_1^2 \vee \sigma_2^2 \vee \sigma_3^2 \vee \sigma_4^2 \vee \sigma_5^2)$  and  $\tilde{R}^* = (2\alpha(1-\delta p)\beta(\alpha+\mu))/((\lambda+\varepsilon_1+\gamma+\mu+\sigma_3^2/2)(\alpha+\mu)^2 \wedge (\alpha^2\sigma_2^2/2)) < 1$  hold, then the infected individuals go to extinction almost surely.
- (II) When  $R^* = (\mu(1-\delta p)\beta\alpha)/((\delta p+\mu+\sigma_1^2/2)(\alpha+\mu+\sigma_2^2/2)(\lambda+\varepsilon_1+\gamma+\mu+\sigma_3^2/2)) > 1$  holds, then system (5) has a unique stationary distribution  $\pi(\cdot)$  and it has ergodic property.

To illustrate the results of the above theorems, we next carry out some numerical simulations by the Matlab software. Let us consider the following discretization equations of system (5):

$$\begin{aligned}
S_{k+1} &= S_k + \left[ \Lambda - \frac{(1-\delta)\beta S_k I_k}{S_k + E_k + I_k + R_k} - \frac{\delta(1-p)\beta S_k I_k}{S_k + E_k + I_k + R_k} - (\delta p + \mu) S_k \right] \Delta t \\
&\quad + \sigma_1 S_k \sqrt{\Delta t} \zeta_{1,k} + \frac{\sigma_1^2}{2} S_k (\zeta_{1,k}^2 - 1) \Delta t, \\
E_{k+1} &= E_k + \left[ \frac{(1-\delta)\beta S_k I_k}{S_k + E_k + I_k + R_k} + \frac{\delta(1-p)\beta S_k I_k}{S_k + E_k + I_k + R_k} - (\alpha + \mu) E_k \right] \Delta t \\
&\quad + \sigma_2 E_k \sqrt{\Delta t} \zeta_{2,k} + \frac{\sigma_2^2}{2} E_k (\zeta_{2,k}^2 - 1) \Delta t, \\
I_{k+1} &= I_k + [\alpha E_k - (\lambda + \varepsilon_1 + \gamma + \mu) I_k] \Delta t \\
&\quad + \sigma_3 I_k \sqrt{\Delta t} \zeta_{3,k} + \frac{\sigma_3^2}{2} I_k (\zeta_{3,k}^2 - 1) \Delta t, \\
Q_{k+1} &= Q_k + [\lambda I_k - (\varphi + \varepsilon_2 + \mu) Q_k] \Delta t \\
&\quad + \sigma_4 Q_k \sqrt{\Delta t} \zeta_{4,k} + \frac{\sigma_4^2}{2} Q_k (\zeta_{4,k}^2 - 1) \Delta t, \\
R_{k+1} &= R_k + (\delta p S_k + \gamma I_k + \varphi Q_k - \mu R_k) \Delta t \\
&\quad + \sigma_5 R_k \sqrt{\Delta t} \zeta_{5,k} + \frac{\sigma_5^2}{2} R_k (\zeta_{5,k}^2 - 1) \Delta t,
\end{aligned} \tag{73}$$

and here  $\zeta_{i,k}$  ( $i = 1, 2, 3, 4, 5$ ;  $k = 1, 2, \dots, n$ ) stands for  $N(0, 1)$  distributed independent random variables and time increment  $\Delta t > 0$ .

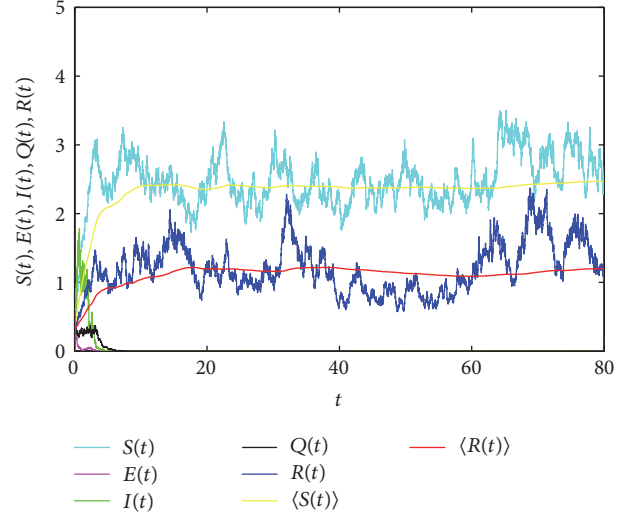


FIGURE 1: Time sequence diagram of system (5) for extinction of the disease.

In Figure 1, take  $S(0) = E(0) = I(0) = Q(0) = R(0) = 0.3$ ,  $\Lambda = 2$ ,  $\mu = 0.55$ ,  $\beta = 0.25$ ,  $\gamma = 0.2$ ,  $\alpha = 2.5$ ,  $\delta = 0.5$ ,  $p = 0.5$ ,  $\varepsilon_1 = 0.1$ ,  $\varepsilon_2 = 0.1$ ,  $\lambda = 0.18$ ,  $\varphi = 0.15$ ,  $\sigma_1 = 0.15$ ,  $\sigma_2 = 1$ ,  $\sigma_3 = 1$ ,  $\sigma_4 = 0.5$ ,  $\sigma_5 = 0.25$ , and  $\Delta t = 0.01$ . Then

$$\mu = 0.55 > \frac{1}{2} (\sigma_1^2 \vee \sigma_2^2 \vee \sigma_3^2 \vee \sigma_4^2 \vee \sigma_5^2) = 0.5,$$

$$\begin{aligned}
\tilde{R}^* &= \frac{2\alpha(1-\delta p)\beta(\alpha+\mu)}{(\lambda+\varepsilon_1+\gamma+\mu+\sigma_3^2/2)(\alpha+\mu)^2 \wedge (\alpha^2\sigma_2^2/2)} \\
&= 0.9150 < 1
\end{aligned} \tag{74}$$

satisfy the conditions in Theorem 4; we can obtain that the exposed, infected, and quarantined individuals go to extinction almost surely. Moreover,

$$\lim_{t \rightarrow \infty} \langle S \rangle = \frac{\Lambda}{\delta p + \mu} = 2.5,$$

$$\lim_{t \rightarrow \infty} \langle R \rangle = \frac{\delta p \Lambda}{\mu(\delta p + \mu)} = 1.1364 \tag{75}$$

a.s.

Obviously, Figure 1 supports our results of Theorem 4.

In Figure 2, take  $S(0) = E(0) = I(0) = Q(0) = R(0) = 0.5$ ,  $\Lambda = 0.3$ ,  $\mu = 0.1$ ,  $\beta = 1.5$ ,  $\gamma = 0.2$ ,  $\alpha = 0.3$ ,  $\delta = 0.1$ ,  $p = 0.2$ ,  $\varepsilon_1 = 0.05$ ,  $\varepsilon_2 = 0.05$ ,  $\lambda = 0.18$ ,  $\varphi = 0.15$ ,  $\sigma_1 = \sigma_2 = \sigma_3 = \sigma_4 = \sigma_5 = 0.03$ , and  $\Delta t = 0.01$ . Then

$$\begin{aligned}
R^* &= \frac{\mu(1-\delta p)\beta\alpha}{(\delta p + \mu + \sigma_1^2/2)(\alpha + \mu + \sigma_2^2/2)(\lambda + \varepsilon_1 + \gamma + \mu + \sigma_3^2/2)} \\
&= 1.7236 > 1
\end{aligned} \tag{76}$$

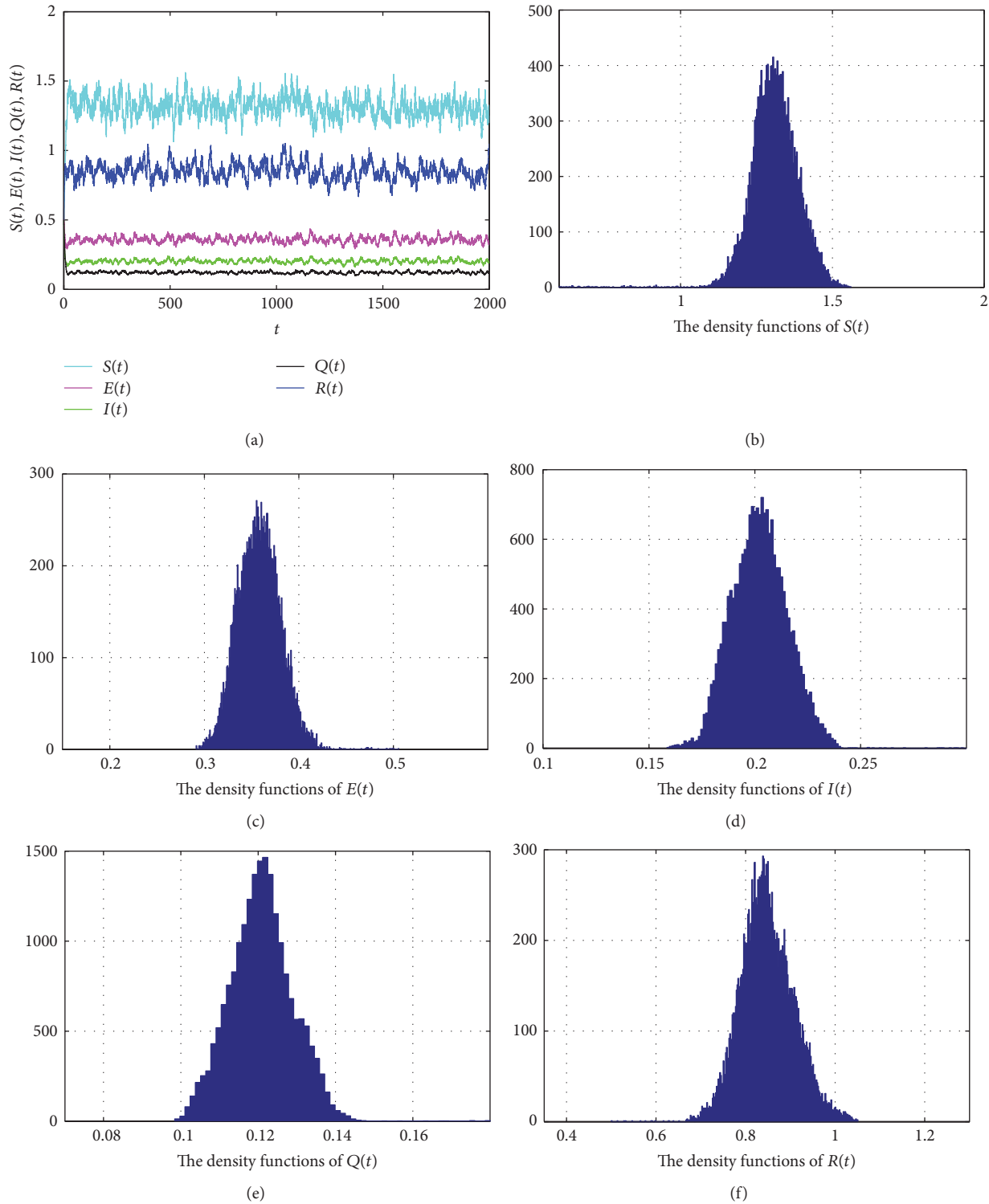


FIGURE 2: (a) represents the solutions of system (5); (b)–(f) stand for the density functions of  $S(t)$ ,  $E(t)$ ,  $I(t)$ ,  $Q(t)$ , and  $R(t)$ , respectively.

satisfies the condition in Theorem 8; we can obtain that system (5) has a unique stationary distribution  $\pi(\cdot)$  and it has ergodic property. Figure 2 shows that the solution of system (5) swings up and down in a small neighborhood. According to the density functions in Figures 2(b)–2(f), we can see that

there exists a stationary distribution. As expected, Figure 2 confirms our results of Theorem 8.

In Figure 3, take  $S(0) = E(0) = I(0) = Q(0) = R(0) = 0.1$ ,  $\Lambda = 0.2$ ,  $\mu = 0.55$ ,  $\beta = 2.65$ ,  $\gamma = 0.2$ ,  $\alpha = 2.5$ ,  $\delta = 0.1$ ,  $p = 0.1$ ,  $\varepsilon_1 = 0.1$ ,  $\varepsilon_2 = 0.1$ ,  $\lambda = 0.18$ ,  $\varphi = 0.15$ , and  $\Delta t = 0.01$ .

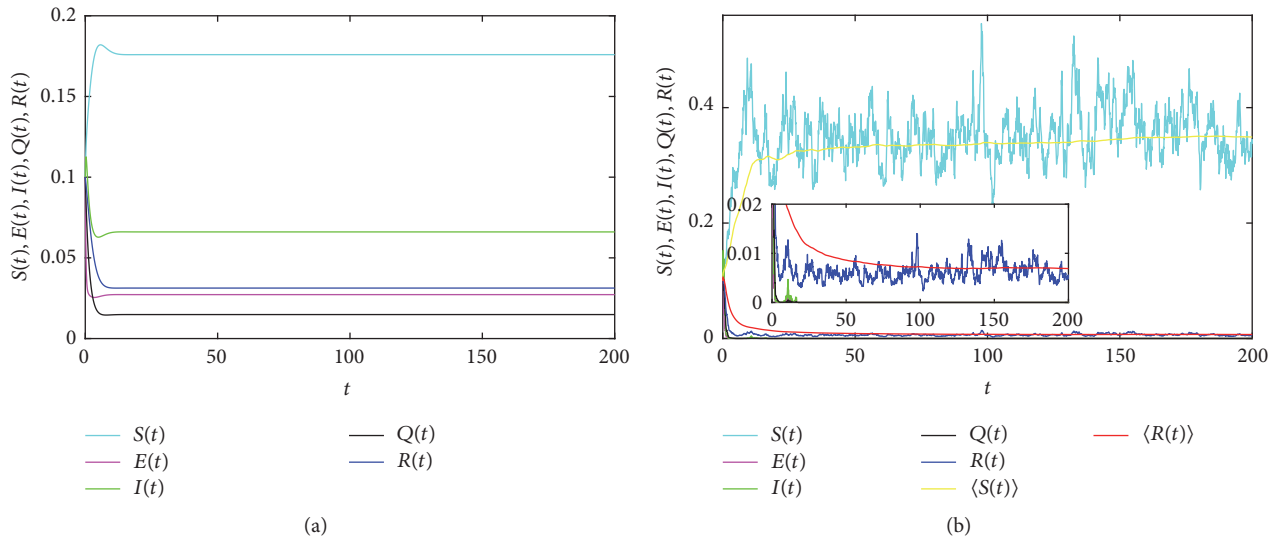


FIGURE 3: Time sequence diagram of system (5) for persistence and extinction of the disease.

In Figure 3(a), take  $\sigma_i = 0$  ( $i = 1, 2, 3, 4, 5$ ); then

$$R_1 = \frac{\mu(1 - \delta p)\beta\alpha}{(\delta p + \mu)(\alpha + \mu)(\lambda + \varepsilon_1 + \gamma + \mu)} = 2.0505 > 1, \quad (77)$$

which means the disease will persist. As expected, Figure 3(a) shows the disease persists in real life.

Synchronously, in Figure 3(b), take  $\sigma_1 = 0.15$ ,  $\sigma_2 = 1$ ,  $\sigma_3 = 1$ ,  $\sigma_4 = 0.5$ ,  $\sigma_5 = 0.25$ . Obviously, Figure 3(b) shows the exposed, infected, and quarantined individuals go to extinction and we can get that the permanent disease of system (3) can die out under stochastic effects. This implies that the stochastic disturbance is conducive to epidemic diseases control.

## Conflicts of Interest

The authors declare that there are no conflicts of interest regarding the publication of this paper.

## Acknowledgments

This work was supported by the National Natural Science Foundation of China (11371230), the SDUST Research Fund (2014TDJH102), and Shandong Provincial Natural Science Foundation, China (ZR2015AQ001).

## References

- [1] L. Hörmander, "Hypoelliptic second order differential equations," *Acta Mathematica*, vol. 119, pp. 147–171, 1967.
- [2] J. J. Nieto and D. O'Regan, "Variational approach to impulsive differential equations," *Nonlinear Analysis: Real World Applications*, vol. 10, no. 2, pp. 680–690, 2009.
- [3] Z. Bai and H. Lü, "Positive solutions for boundary value problem of nonlinear fractional differential equation," *Journal of Mathematical Analysis and Applications*, vol. 311, pp. 495–505, 2005.
- [4] J. Mierczynski, "Instability in linear cooperative systems of ordinary differential equations," *SIAM Review*, vol. 59, pp. 649–670, 2017.
- [5] X. Dong, Z. Bai, and S. Zhang, "Positive solutions to boundary value problems of p-Laplacian with fractional derivative," *Boundary Value Problems*, vol. 2017, no. 5, 2017.
- [6] Y. Cui, "Uniqueness of solution for boundary value problems for fractional differential equations," *Applied Mathematics Letters*, vol. 51, pp. 48–54, 2016.
- [7] Y. Zhang, H. Dong, X. Zhang, and H. Yang, "Rational solutions and lump solutions to the generalized (3+1)-dimensional Shallow Water-like equation," *Computers & Mathematics with Applications*, vol. 73, pp. 246–252, 2017.
- [8] L. Liu and X. Meng, "Optimal harvesting control and dynamics of two-species stochastic model with delays," *Advances in Difference Equations*, vol. 2017, no. 18, 2017.
- [9] Y. Cai, Y. Kang, M. Banerjee, and W. Wang, "A stochastic SIRS epidemic model with infectious force under intervention strategies," *Journal of Differential Equations*, vol. 259, no. 12, pp. 7463–7502, 2015.
- [10] T. Zhang, X. Meng, and T. Zhang, "Global analysis for a delayed SIV model with direct and environmental transmissions," *Journal of Applied Analysis and Computation*, vol. 6, no. 2, pp. 479–491, 2016.
- [11] Z. Qiu, "The complete classification for dynamics of an SIS STD model in terms of four parameters," *Nonlinear Analysis: Real World Applications*, vol. 11, no. 4, pp. 2875–2887, 2010.
- [12] W. Ma, M. Song, and Y. Takeuchi, "Global stability of an SIR epidemic model with time delay," *Applied Mathematics Letters*, vol. 17, no. 10, pp. 1141–1145, 2004.
- [13] S. Zhang, X. Meng, T. Feng, and T. Zhang, "Dynamics analysis and numerical simulations of a stochastic non-autonomous predator-prey system with impulsive effects," *Nonlinear Analysis: Hybrid Systems*, vol. 26, pp. 19–37, 2017.
- [14] H. Cheng and T. Zhang, "A new predator-prey model with a profitless delay of digestion and impulsive perturbation on the prey," *Applied Mathematics and Computation*, vol. 217, no. 22, pp. 9198–9208, 2011.

- [15] L. Liu, X. Meng, and T. Zhang, "Optimal control strategy for an impulsive stochastic competition system with time delays and jumps," *Physica A: Statistical Mechanics and its Applications*, vol. 477, pp. 99–113, 2017.
- [16] Y. He, S. Gao, and D. Xie, "An SIR epidemic model with time-varying pulse control schemes and saturated infectious force," *Applied Mathematical Modelling*, vol. 37, no. 16-17, pp. 8131–8140, 2013.
- [17] T. Zhang, W. Ma, and X. Meng, "Global dynamics of a delayed chemostat model with harvest by impulsive flocculant input," *Advances in Difference Equations*, vol. 2017, no. 115, 2017.
- [18] L. Wu and Z. Feng, "Homoclinic bifurcation in an SIQR model for childhood diseases," *Journal of Differential Equations*, vol. 168, pp. 150–167, 2000.
- [19] S. Li, M. Fan, and X. Rong, "Global threshold dynamics of SIQS epidemic model in time fluctuating environment," *International Journal of Biomathematics*, vol. 10, no. 4, Article ID 1750060, 22 pages, 2017.
- [20] Z. Feng and H. Thieme, "Recurrent outbreaks of childhood diseases revisited: The impact of isolation," *Mathematical Biosciences*, vol. 123, pp. 93–130, 1995.
- [21] H. Hethcote, M. Zhien, and L. Shengbing, "Effects of quarantine in six endemic models for infectious diseases," *Mathematical Biosciences*, vol. 180, pp. 141–160, 2002.
- [22] M. Erdem, M. Safan, and C. Castillo-Chavez, "Mathematical analysis of an SIQR influenza model with imperfect quarantine," *Bulletin of Mathematical Biology*, vol. 79, no. 7, pp. 1612–1636, 2017.
- [23] C. Sun and Y.-H. Hsieh, "Global analysis of an SEIR model with varying population size and vaccination," *Applied Mathematical Modelling*, vol. 34, no. 10, pp. 2685–2697, 2010.
- [24] Z. Qiu and Z. Feng, "Transmission dynamics of an influenza model with vaccination and antiviral treatment," *Bulletin of Mathematical Biology*, vol. 72, no. 1, pp. 1–33, 2010.
- [25] Y. Zhao and D. Jiang, "The threshold of a stochastic SIS epidemic model with vaccination," *Applied Mathematics and Computation*, vol. 243, pp. 718–727, 2014.
- [26] X. Leng, T. Feng, and X. Meng, "Stochastic inequalities and applications to dynamics analysis of a novel SIVS epidemic model with jumps," *Journal of Inequalities and Applications*, vol. 2017, no. 138, 2017.
- [27] S. Gao, L. Chen, J. J. Nieto, and A. Torres, "Analysis of a delayed epidemic model with pulse vaccination and saturation incidence," *Vaccine*, vol. 24, no. 35-36, pp. 6037–6045, 2006.
- [28] X. Meng, L. Chen, and B. Wu, "A delay SIR epidemic model with pulse vaccination and incubation times," *Nonlinear Analysis: Real World Applications*, vol. 11, no. 1, pp. 88–98, 2010.
- [29] J. Jiao, S. Cai, and L. Li, "Impulsive vaccination and dispersal on dynamics of an SIR epidemic model with restricting infected individuals boarding transports," *Physica A: Statistical Mechanics and its Applications*, vol. 449, pp. 145–159, 2016.
- [30] T. Zhang, X. Meng, Y. Song, and T. Zhang, "A stage-structured predator-prey SI model with disease in the prey and impulsive effects," *Mathematical Modelling and Analysis*, vol. 18, no. 4, pp. 505–528, 2013.
- [31] L. Wang and D. Jiang, "A note on the stationary distribution of the stochastic chemostat model with general response functions," *Applied Mathematics Letters*, vol. 73, pp. 22–28, 2017.
- [32] M. Liu and M. Fan, "Permanence of stochastic Lotka-Volterra systems," *Journal of Nonlinear Science*, vol. 27, no. 2, pp. 425–452, 2017.
- [33] X. Liu, Y. Li, and W. Zhang, "Stochastic linear quadratic optimal control with constraint for discrete-time systems," *Applied Mathematics and Computation*, vol. 228, pp. 264–270, 2014.
- [34] M. Liu, C. Bai, and Y. Jin, "Population dynamical behavior of a two-predator one-prey stochastic model with time delay," *Discrete and Continuous Dynamical Systems - Series A*, vol. 37, no. 5, pp. 2513–2538, 2017.
- [35] M. Liu and M. Fan, "Stability in distribution of a three-species stochastic cascade predator-prey system with time delays," *IMA Journal of Applied Mathematics*, vol. 82, no. 2, pp. 396–423, 2017.
- [36] H. Ma and Y. Jia, "Stability analysis for stochastic differential equations with infinite Markovian switchings," *Journal of Mathematical Analysis and Applications*, vol. 435, no. 1, pp. 593–605, 2016.
- [37] G. Liu, X. Wang, X. Meng, and S. Gao, "Extinction and persistence in mean of a novel delay impulsive stochastic infected predator-prey system with jumps," *Complexity*, vol. 2017, Article ID 1950970, pp. 1–15, 2017.
- [38] C. Tan and W. Zhang, "On observability and detectability of continuous-time stochastic Markov jump systems," *Journal of Systems Science & Complexity*, vol. 28, no. 4, pp. 830–847, 2015.
- [39] Y. Zhao and W. Zhang, "Observer-based controller design for singular stochastic Markov jump systems with state dependent noise," *Journal of Systems Science & Complexity*, vol. 29, no. 4, pp. 946–958, 2016.
- [40] Q. Liu, D. Jiang, N. Shi, T. Hayat, and A. Alsaedi, "Dynamics of a stochastic tuberculosis model with constant recruitment and varying total population size," *Physica A: Statistical Mechanics and its Applications*, vol. 469, pp. 518–530, 2017.
- [41] X. Meng, S. Zhao, T. Feng, and T. Zhang, "Dynamics of a novel nonlinear stochastic SIS epidemic model with double epidemic hypothesis," *Journal of Mathematical Analysis and Applications*, vol. 433, no. 1, pp. 227–242, 2016.
- [42] A. Miao, J. Zhang, T. Zhang, and B. G. S. A. Pradeep, "Threshold Dynamics of a Stochastic SIR Model with Vertical Transmission and Vaccination," *Computational and Mathematical Methods in Medicine*, vol. 2017, Article ID 4820183, 2017.
- [43] L. Wang, Z. Teng, T. Tang, and Z. Li, "Threshold Dynamics in Stochastic SIRS Epidemic Models with Nonlinear Incidence and Vaccination," *Computational and Mathematical Methods in Medicine*, vol. 2017, Article ID 7294761, 2017.
- [44] Y. Chen, B. Wen, and Z. Teng, "The global dynamics for a stochastic SIS epidemic model with isolation," *Physica A: Statistical Mechanics and its Applications*, vol. 492, pp. 1604–1624, 2018.
- [45] Y. Zhang, K. Fan, S. Gao, and S. Chen, "A remark on stationary distribution of a stochastic SIR epidemic model with double saturated rates," *Applied Mathematics Letters*, vol. 76, pp. 46–52, 2018.
- [46] A. Miao, X. Wang, T. Zhang, W. Wang, and B. Sampath Aruna Pradeep, "Dynamical analysis of a stochastic SIS epidemic model with nonlinear incidence rate and double epidemic hypothesis," *Advances in Difference Equations*, vol. 2017, no. 226, 2017.
- [47] T. Feng, X. Meng, L. Liu, and S. Gao, "Application of inequalities technique to dynamics analysis of a stochastic eco-epidemiology model," *Journal of Inequalities and Applications*, vol. 2016, no. 327, 2016.
- [48] H. Qi, L. Liu, and X. Meng, "Dynamics of a non-autonomous stochastic SIS epidemic model with double epidemic hypothesis," *Complexity*, vol. 2017, no. 14, 2017.

- [49] F. Wang, B. Chen, C. Lin, and X. Li, “Distributed adaptive neural control for stochastic nonlinear multiagent systems,” *IEEE Transactions on Cybernetics*, vol. 47, no. 7, pp. 1795–1803, 2017.
- [50] X. Lv, L. Wang, and X. Meng, “Global analysis of a new nonlinear stochastic differential competition system with impulsive effect,” *Advances in Difference Equations*, vol. 2017, no. 296, 2017.
- [51] X. Mao, *Stochastic Differential Equations and Applications*, Woodhead Publishing, Cambridge, UK, 2007.
- [52] Y. Zhao, S. Yuan, and T. Zhang, “The stationary distribution and ergodicity of a stochastic phytoplankton allelopathy model under regime switching,” *Communications in Nonlinear Science and Numerical Simulation*, vol. 37, pp. 131–142, 2016.
- [53] J. Yu and M. Liu, “Stationary distribution and ergodicity of a stochastic food-chain model with Lévy jumps,” *Physica A: Statistical Mechanics and its Applications*, vol. 482, pp. 14–28, 2017.
- [54] R. Hasminskii, G. Milstein, and M. Nevelon, *Stochastic Stability of Differential Equations*, Springer-Verlag, Berlin, Germany, 2012.
- [55] T. Gard, *Introduction to Stochastic Differential Equations*, Dekker, New York, NY, USA, 1988.
- [56] C. Zhu and G. Yin, “Asymptotic properties of hybrid diffusion systems,” *SIAM Journal on Control and Optimization*, vol. 46, no. 4, pp. 1155–1179, 2007.